UNIVERSITY OF Southampton

University of Southampton Research Repository

Copyright © and Moral Rights for this thesis and, where applicable, any accompanying data are retained by the author and/or other copyright owners. A copy can be downloaded for personal non-commercial research or study, without prior permission or charge. This thesis and the accompanying data cannot be reproduced or quoted extensively from without first obtaining permission in writing from the copyright holder/s. The content of the thesis and accompanying research data (where applicable) must not be changed in any way or sold commercially in any format or medium without the formal permission of the copyright holder/s.

When referring to this thesis and any accompanying data, full bibliographic details must be given, e.g.

Thesis: Author (Year of Submission) "Full thesis title", University of Southampton, name of the University Faculty or School or Department, PhD Thesis, pagination.

Data: Author (Year) Title. URI [dataset]

University of Southampton

Faculty of Engineering and Physical Science

School of Chemistry

X-ray Absorption Spectroscopy and Electrochemical Studies of Pt-Sn Electrocatalysts

by

Haoliang Huang

ORCID ID: 0000-0002-0993-1536

Thesis for the degree of Doctor of Philosophy

October 2020

University of Southampton

Abstract

Faculty of Engineering and Physical Science

School of Chemistry

Doctor of Philosophy

X-ray Absorption Spectroscopy and Electrochemical Studies of Pt-Sn Electrocatalysts

by

Haoliang Huang

The addition of a second metal to form bimetallic electrocatalysts offers a means of enhancing electrocatalytic activity through promotional effects. To establish the structure-activity relationship and ascertain details of the promotional mechanism, it is key to characterise the complex structure of bimetallic nanoparticles and acquire molecular-level information regarding the bonding between the adsorbate and the surface.

This thesis focuses on characterising Pt-Sn bimetallic electrocatalysts using X-ray absorption spectroscopy (XAS) and electrochemical measurements. The work starts with Pt_3Sn samples containing both SnO_2 and alloyed Sn, where the extent of alloying was examined by a variety of techniques. The presence of Sn did promote CO oxidation, but the extent of alloying showed little effects on CO oxidation activity. To deepen understanding of the promotional mechanism, Pt-Sn samples in which the Sn was present exclusively as either SnO_2 or as the Pt-Sn alloy were prepared, the structures of which were ascertained by both XAS and other methods. Both SnO_2 and alloyed Sn were found to promote CO oxidation mainly via the bifunctional mechanism, but with different active species and redox couples. Whilst a surface hydroxide of SnO_2 (Sn^{IV}-OH) generated from a Sn^{II}/Sn^{IV} reversible redox couple was proposed for Pt-SnO_2 using cyclic voltammograms, Pt-Sn-OH from water dissociation on surface Pt-Sn* sites was determined for the surface alloyed Sn using *in situ* XAS. Finally, through the collection of a library of Pt-Sn XAS data, a method for determination of the contraction of the surface atoms of Pt-Sn alloys was derived, with the contraction found to be proportional to the Pt-Sn coordination number.

Table of Contents

Research Thesis: Declaration of Authorship

Print name: Haoliang Huang

Title of thesis: X-ray Absorption Spectroscopy and Electrochemical Studies of Pt-Sn Electrocatalysts

I declare that this thesis and the work presented in it are my own and has been generated by me as the result of my own original research.

I confirm that:

1. This work was done wholly or mainly while in candidature for a research degree at this University;
2. Where any part of this thesis has previously been submitted for a degree or any other qualification at this University or any other institution, this has been clearly stated;
3. Where I have consulted the published work of others, this is always clearly attributed;
4. Where I have quoted from the work of others, the source is always given. With the exception of such quotations, this thesis is entirely my own work;
5. I have acknowledged all main sources of help;
6. Where the thesis is based on work done by myself jointly with others, I have made clear exactly what was done by others and what I have contributed myself;
7. Parts of this work have been published as:

[1] H. Huang, A. Nassr, V. Celorrio, S.F.R. Taylor, V.K. Puthiyapura, C. Hardacre, D.J.L. Brett, A.E. Russell, Effects of heat treatment atmosphere on the structure and activity of Pt_3Sn nanoparticle electrocatalysts: a characterisation case study, Faraday Discuss., 208 (2018) 555-573.

[2] H. Huang, A.E. Russell, Approaches to achieve surface sensitivity in the in situ XAS of electrocatalysts, Curr. Opin. Electrochem., 27 (2021) 100681.

Signature: ..... Date:.....

Acknowledgements

First and foremost, I would like to thank my supervisor Andrea Russell for the opportunity to study my PhD and for her continued support. Most importantly, under Andrea's supervision, I think I become able to grasp the truth of research and science.

I'd also like to thank:

- Level 6 members (Abu Bakr Nassr, David Inwood, Turgut Sönmez, Andy Leach, Danai Panagoulia, Alex Keeler, Hisham, Saifu, Firas and Gabriella) for their kindness and helping me get my life and research started in a foreign country.
- out-of-hour buddies (Hisham, Saifu, Alex Keeler, Alex Black and Firas) for their company in the evening and at the weekends.
- Nikolay Zhelev for helping me everything and inviting me to a Bulgarian Christmas meal.
- Veronica Celorrio for experiment preparation in B18 as a leader of BAG team or as a beamline scientist.
- UK Catalysis Hub and the BAG team for their contribution of all XAS experiments in this thesis.
- SuperSTEM and Fredrik for contribution of STEM experiments and for their professional.
- Project students (Ed, Hamza and Grace) for going through trial-and-errors with me.
- Cats for their company during my thesis writing months and on the way home,

Special thank goes to Tammy Nimmo for her 4-year company and helps in the lab.

Last but not least, I would like to thank China Scholarship Council for financial support and Chinese embassy in UK for a health package during the ongoing COVID pandemics.

Chapter 1 Introduction

1.1 Fuel cells electrocatalysts

Since the industrial revolution, fossil fuels have been the main energy source for various applications in our daily life, such as transportation, power plants and home heating. However, fossil fuels are not renewable, and its overconsumption and overreliance lead to energy crisis and serious environmental damages. Fuel cells are devices for direct conversion of chemical energy of fuels into electric energy without combustion, and the fuels can be H_2, methanol, and ethanol, etc, which can be generated from biomass or via other renewable energy. If H_2 is the fuel, H_2O and electricity and heat are the only products, with zero carbon emission. Compared to conventional combustion-based engines, fuel cells can offer superior efficiency and lower emission. Amongst fuel cells, Proton-exchange membrane fuel cells (PEMFCs) stand out for automotive application, due to high energy density, low operating temperature (50–100 °C) and rapid start-up[1, 2]. A typical PEMFCs diagram is shown in Figure 1-1. At the anode the fuel is oxidised to H^+ and CO_2 (if the fuel is alcohol), and at the cathode O_2 is reduced into H_2O with consumption of H^+ from the PEM that selectively transfers H^+ from the anode to the cathode. As both the oxidation of fuels (H_2 or alcohol) and the reduction of O_2 are on the corresponding catalyst layer, the properties of the electrocatalysts determine the performance of the PEMFC.

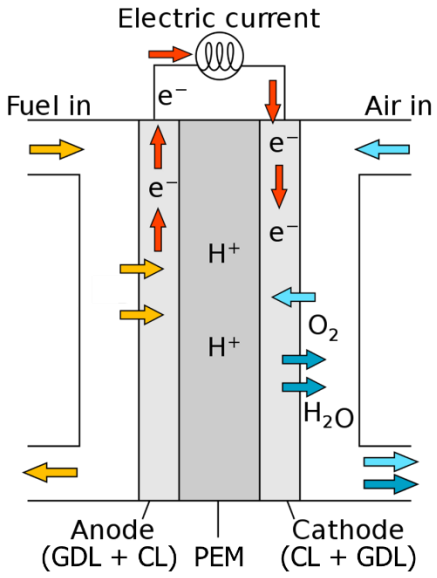

Figure 1-1 Schematic diagram of a PEMFC. The anode and the cathode are composed of a gas diffusion layer (GDL) and a catalyst layer (CL), and these two catalyst layers are separated by a proton-exchange membrane (PEM). The fuel can be H_2 and alcohols.

For both the anodic reactions and the cathodic reaction, Pt nanoparticles supported on high surface area carbon are the best monometallic electrocatalyst, but the activity is unsatisfactory and the Pt is scarce, which inhibits the wide commercialisation of PEMFC. Synthesising Pt-based bimetallic

electrocatalysts is a promising solution because the addition of a second metal offers a means of enhancing electrocatalytic activity through promotional effects and/or improving the atom-economy for Pt-based electrocatalysts. The promotional effects of the second component (which may or may not be active) to the catalytically active host metal are usually attributed to the following mechanisms, or a combination of them: (i) the ligand mechanism, where the electronic structure of the host metal is modified by the neighbouring second component, so that the interactions with adsorbates and reaction intermediates are changed [3-5]; (ii) the strain mechanism, where the atomic spacing of the host metal on the surface is altered by the second component underneath, producing similar effects as the ligand mechanism [6, 7]; (iii) the ensemble mechanism, where the surface ensemble of the host metal is diluted by the inert component, thus changing the reaction pathway[5, 8-11]; and (iv) the bifunctional mechanism, where the second component acts as a co-catalyst, providing one of the necessary reactive intermediates at potentials more negative than that on pure Pt [12-14]. Amongst these mechanisms, the bifunctional mechanism plays a major role in promoting sluggish anodic reactions on Pt, such as CO oxidation in acidic solution[15-20], which is the reaction of interest in this thesis.

In the following sections, I will firstly introduce the structure of bimetallic electrocatalyst to give a context about the possible arrangement of two metals in a particle, then introduce the use of X-ray adsorption spectroscopy for characterising bimetallic materials and propose it as the capable technique to clarify the structural and mechanical confusions of Pt-based bimetallic catalysts.

1.2 The structure of bimetallic electrocatalysts

Bimetallic nanoparticles (NPs), composed of two different metallic elements, are of great interest in heterogeneous catalysis, imaging and biomedical applications [21-24]. Compared to the monometallic counterpart, bimetallic NPs (A_mB_n) enable two more parameters to be manipulated, the ratio and mixing patterns of element A and element B, which allows fine tuning of the nanoparticle properties. Ideally, the mixing patterns of bimetallic NPs can be classified using the interaction of A and B into three main groups, aggregates mixtures, core-shell particles, and alloys (Figure 1-1).

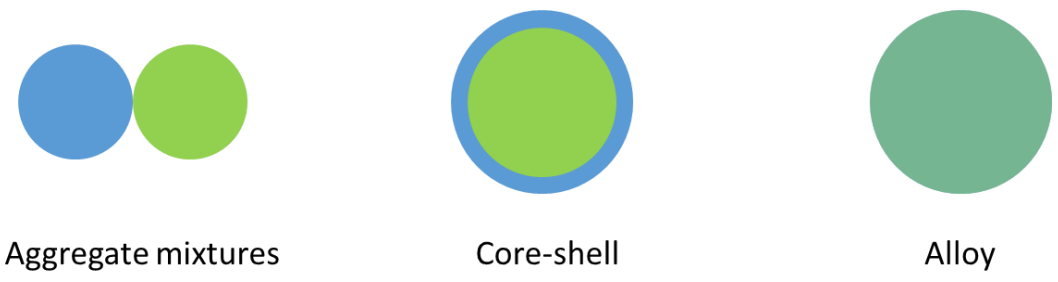

Figure 1-2 Schematic illustration of the three main mixing patterns of bimetallic nanoparticles (A_mB_n).

For practical bimetallic electrocatalysts, the mixing patterns may not be as simple as shown in Figure 1-1. Take Pt-based catalysts in acidic electrolyte as examples. If the second metal is a non-noble metal, such as Co, Ni or Cu, it is susceptible to be leached out until a protective Pt skin is formed, producing an alloy-core-Pt-shell configuration. If the second metal is oxophilic, such as Mo, Ru, and Sn, exposure to air and wet-chemical synthesis may lead to the formation of oxide phases. Such oxide phases, also considered as active species for the bifunctional mechanism [25-28], may or may not be reducible back to metal under operative/measurement condition. In addition, in both cases the surface structure/composition determining the electrocatalytic activity may or may not be the same measured as the one in the bulk, and the surface speciation may also vary due to the presence of adsorbates under working conditions.

To establish the structure-activity relationship and ascertain the promotional mechanism for bimetallic electrocatalysts, characterisation is required to solve the complex structure (speciation, mixing patterns and surface structure) and provide molecular-level information regarding the bonding between the adsorbate and the surface.

1.3 X-ray absorption spectroscopy (XAS)

XAS describes how X-rays are absorbed by an atom at near and above the core-level binding energies of that atom[29]. The XAS spectrum can be divided into three regions as depicted in Figure 1-2. At the absorption edge the energy of the incident X-ray is high enough to excite core-level electrons of an absorbing atom to unoccupied states (Figure 1-2) and, from approximately 50 eV above the edge, into the continuum producing photoelectrons, which can be scattered back by the neighbouring atoms. The outgoing photoelectron wave and the backscattered wave interfere, producing the oscillation of the absorbance or fluorescence signal above the edge (Figure 1-2). Arising from their physical origins, the X-ray absorption near edge (XANES) region is sensitive to the oxidation state and electronic structure of the absorber, whilst the extended X-ray absorption fine structure (EXAFS) offers information regarding local coordination of the absorber; the identity and coordination number of the neighbouring atoms and the distance between the absorber and the neighbours.

XAS has three unique advantages over other techniques in characterising bimetallic electrocatalysts; (i) the capability to probe the local structure regardless of the degree of crystallinity of the material, which is of particular importance for nanoparticles as they usually do not possess long-range order, especially on their surface; (ii) the ability to ascertain the mixing pattern/atomic arrangement of these two metals from perspective of local coordination of each element; and (iii) XAS measurements can be conducted under electrochemical control (*in situ* measurements) or in an environment very similar to that of the working device (operando measurements). In the following section, recent use of XAS

to probe the (surface) structure of bimetallic electrocatalysts and to understand the detailed mechanism of electrocatalytic reactions are reviewed.

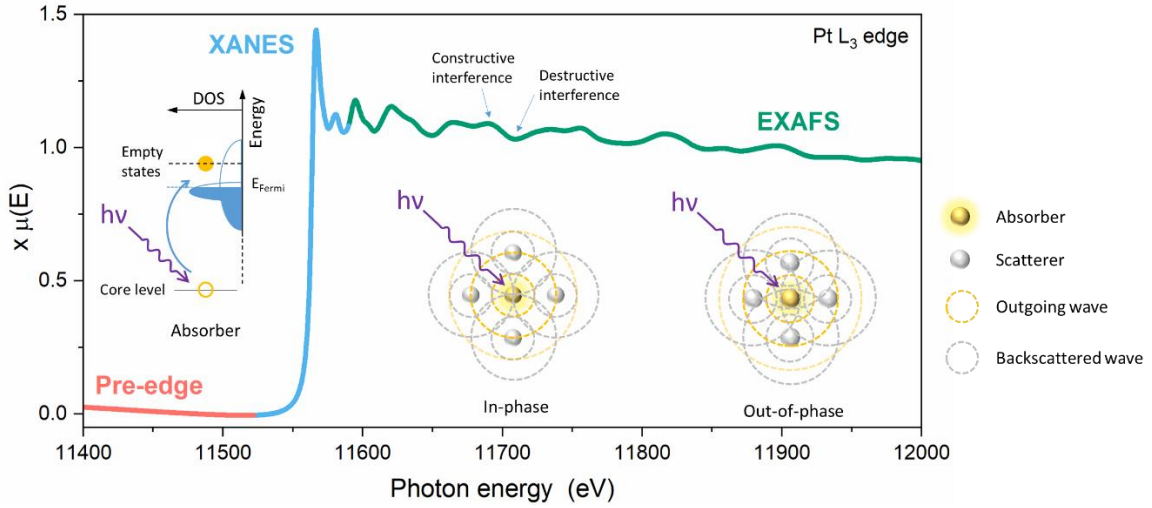

Figure 1-2 A XAS spectrum of Pt foil at the Pt L_3 edge, showing a XAS spectrum consists of three parts, the pre-edge (red), the XANES (cyan) and the EXAFS (green). The insets show the electron transition happening in the XANES, and the interference between photoelectrons and backscattered electrons in the EXAFS.

1.3.1 XAS to probe the structure of bimetallic electrocatalysts

Almeida *et al.*[30] studied the configuration of Pt_3Rh/C catalysts using EXAFS at both the Pt L_3-edge and the Rh K-edge. The Pt_3Rh/C catalysts were prepared by two different methods, a polyol synthesis and using Pb NPs as a sacrificial material, and although these two catalysts showed similar and broad diffraction peaks, the configuration was able to distinguish using EXAFS fitting. Whilst no heteroatomic scattering path (Rh–Pt or Pt–Rh) was found from the former catalyst, suggesting a bimetallic aggregate mixture (Figure 1-1), the latter catalyst was found to have the first-shell Rh–Pt and Pt–Rh with the coordination numbers (CNs) of 0.7 and 5, respectively, suggesting that the Pt and Rh were mixed to some extent. Alayoglu *et al.*[31] conducted a comparative study of PtRu alloy and Ru@Pt core-shell NPs using a combination of scanning transmission electron microscopy-energy dispersive spectroscopy (STEM-EDS) and XAS. By STEM-EDS line scans the different local compositions of these two samples were directly distinguished, and from EXAFS fitting the heteroatomic bonds, although found on both samples, showed significant differences in CN, with those of the core-shell configuration less than those of the alloy (~0.3 and ~0.4 *vs.* ~2.8 and ~4.0 for Pt–Ru and Ru–Pt, respectively). Furthermore, from comparison of the EXAFS fitting results with structural models of 4 nm Ru@Pt core-shell NPs, the author proposed that the Ru@Pt was comprised of ~3.0 nm Ru cores and 1~2 monolayer Pt shells.

To establish the relationship between the CN of the first-shell scattering paths and the general mixing patterns of bimetallic NPs (A_mB_n), Hwang *et al.*[32] developed 7 possible structure models and atomic distributions by introducing extents of alloying (*J*) from the perspective of both element A and element B (Figure 1-3). The extent of alloying of element A (J_A) was defined as the ratio of $P_{observed,\,A}$ and $P_{random,\,A}$ ($J_A = P_{observed,\,A}/P_{random,\,A}$), where the $P_{observed,\,A}$ was defined as the ratio between the coordination number of A–B ($N_{A–B}$) and the total coordination number of A ($N_{A\text{-}B} + N_{A\text{-}A}$, if other contributions were absent) and the $P_{random,\,A}$ was the P_A for completely random alloyed bimetallic nanoparticles, $P_{random,\,A} = n/(m + n)$, for A_mB_n bimetallic NPs. Thus,

$$J_A = \frac{P_{observed,A}}{P_{random,A}} = \frac{N_{A-B}/(N_{A-B} + N_{A-A})}{n/(m+n)}$$

$$J_B = \frac{P_{observed,B}}{P_{random,B}} = \frac{N_{B-A}/(N_{B-A} + N_{B-B})}{m/(m+n)}$$

By determining the values of J_A and J_B as shown in Figure 1-3, the corresponding structure model of a given sample can be easily obtained. Independent studies found consistent results using STEM-EDS and the *J* parameters[33, 34]. Using the *J* parameters and the derived structural models, the Pt_3Rh alloy NPs reported by Almeida *et al.*[30] ($J_{Pt} = 0.28$ and $J_{Rh} = 1.11$) were suggested to have a structure with a Pt rich core and a Rh rich shell.

It should be noted that the *J* parameter by definition is not applicable for intermetallic compounds, where the arrangement of A and B is in a specific order rather than random. A typical example of intermetallic compounds is Pt_3Sn (Figure 1-4), which is the electrocatalyst studied in this thesis. However, the $P_{random,}$, the reference point of *J*, can be adjusted to the P value obtained from the crystal structure of the intermetallic compound, and thus the *J* parameter of intermetallic compounds is defined as the extent of perfectness (to the corresponding crystal structure). For Pt_3Sn, $N_{Sn\text{-}Pt} = 12$, $N_{Sn\text{-}Sn} = 0$, $N_{Pt\text{-}Sn} = 4$ and $N_{Pt\text{-}Pt} = 8$ (Figure 1-4), and thus the $P_{perfect,\,Sn} = 1$ and $P_{perfect,\,Pt} = 1/3$. In addition to the *J* parameters, the ratio of total average coordination number ($N_{A\text{-}M} = N_{A\text{-}A} + N_{A\text{-}B}$ for element A) is a measure to determine the preferred location (core or shell), if there is no contribution from other elements and the saturated coordination numbers of element A and element B are equal. For example, $N_{A\text{-}M} > N_{B\text{-}M}$ indicates that element A segregates to the core of the nanoparticles and B to the surface.

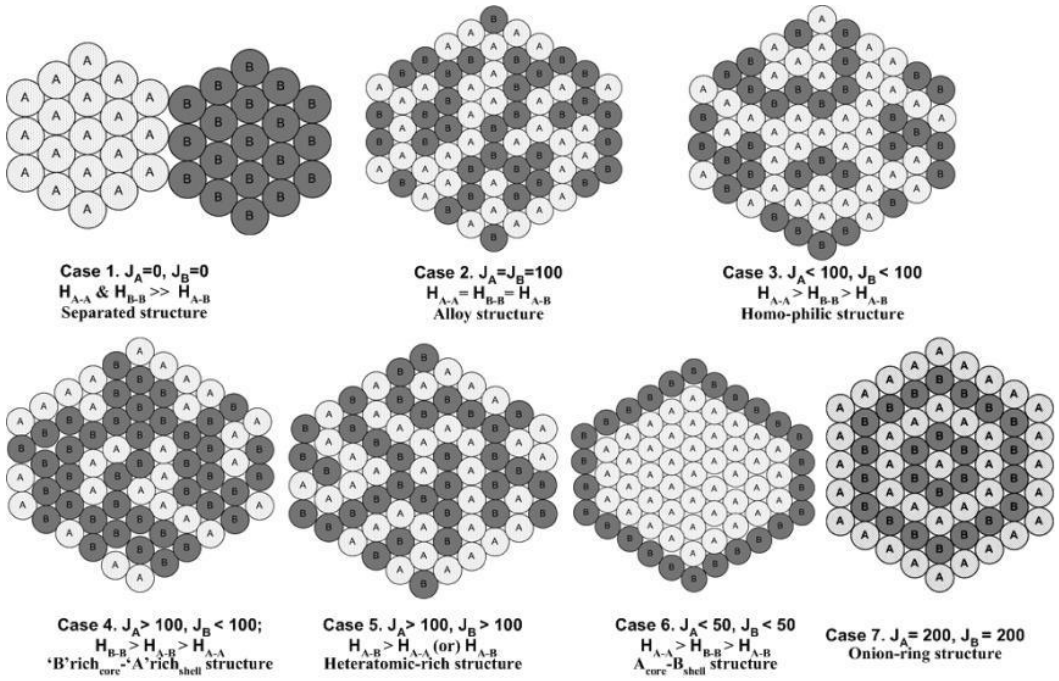

Figure 1-3 Schematic illustrations of bimetallic nanoparticles with different extent of mixing. J_A and J_B are the extent of alloying of element A and element B, respectively. H_{A-A} and H_{B-B} are the homoatomic interaction of A atoms and B atoms, respectively, and H_{A-B} is the heteroatomic interaction between A atoms and B atoms. Reproduced with permission from [32]. Copyright (2005) American Chemical Society.

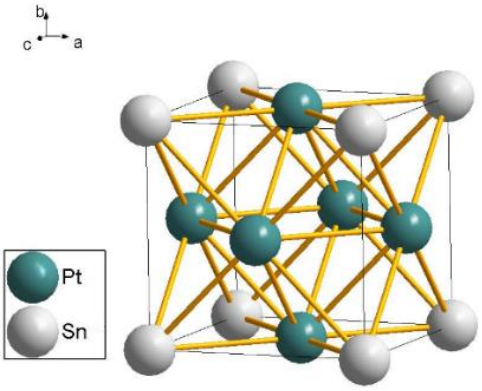

Figure 1-4 The unit cell of the Pt_3Sn intermetallic compound (ICSD No.105796), showing the coordination of Pt atoms (green) and Sn atoms (white).

In addition to the general elemental distribution, XAS can also provide further information regarding the atomic structure. Yang's group [35, 36] used *in situ* XAS to study the Pt skins of two Pt_3Ni nanoframe catalysts, which were synthesized using the same method, but produced different oxygen reduction reaction (ORR) activity. *In situ* XAS was used to characterise the particles after the dissolution of surface oxidized Ni, which mimics the ORR condition. Fits of the EXAFS spectra produced J_{Pt} = 82 and J_{Ni} = 82 for the sample with higher activity (Pt_3Ni-1), suggesting a homophilic structure (Case 3 in Figure 1-3), and J_{Pt} = 117 and J_{Ni} = 83 for the sample with lower activity (Pt_3Ni-

2), suggesting a structure with Pt-rich shell and Ni-rich core (Case 4 in Figure 1-3). From the total average coordination number of Ni and Pt (N_{Pt} = 8.5~8.7 and N_{Ni} = 10.3~10.4), both catalysts were suggested to have a Pt-rich shell. Combination of these two means of analysis on the obtained coordination number revealed that the Pt_3Ni-2 had a thicker Pt skin/shell than Pt_3Ni-1, as the J_{Pt} of Pt_3Ni-2 is lower than that of Pt_3Ni-1. This atomic structure was also supported by a control experiment where the surface Pt and Ni were deliberately oxidised by air exposure, and the XANES spectra showed more oxidized Ni in Pt_3Ni-1 whilst more oxidized Pt in Pt_3Ni-2.

The strain in the Pt skins of bimetallic electrocatalysts can be studied using *in situ* XAS. Jia *et al.*[37-39] varied the atomic composition of $PtCo_x$ nanoparticles (x = 0~3, 4–5 nm diameter), which shared similar structural parameters with the Pt_3Ni-2 nanoframes (N_{Pt} = 8~10, N_{Co} = ~12, J_{Pt} = 1.25~1.36 and J_{Co} = 0.88~1.07). It was found that the Pt-Pt bond length (R_{Pt-Pt}) decreased proportionally with the Co concentration whilst the ORR activity did the opposite. The authors correlated the Pt-Pt bond contraction with the compressive-strain effects and ORR activity, and proposed that the strain effect dominated the improved ORR activity of Pt_xCo NPs over Pt NPs, demonstrating that the R_{Pt-Pt} is the descriptor for both strain effect and the activity [37]. The linear relationship between ORR activity and the R_{Pt-Pt} was supported by the study of Kaito *et al.* of PtCo, PtCu and PtNi alloy NPs[40].

Although a wealth of information becomes available from XAS measurements, it should be acknowledged that the XAS is a bulk per-atom averaging technique, which is unable to obtain information specific to the surface, unless the XAS experiment is properly designed to take advantage of the element-specificity. Price *et al.*[41] studied the shell formation of Au@Cu core-shell nanoparticles, and monitored the underpotential deposition (upd) process of Cu on Au nanoparticles as a function of potential at both the Au L_3 and Cu K edges. Whilst no Cu neighbour was found from the Au edge data, XAS data at the Cu edge showed preferential Cu deposition at defect sites on the Au surface at -0.42 V vs. mercury-mercurous sulfate (MMS), as evidenced by a large coordination number of Cu-Au ($N_{Cu–Au}$ = 6 ± 2, no Cu-Cu), and bulk Cu deposition at -0.51 V_{MMS}, with the addition of Cu–Cu contribution ($N_{Cu–Cu}$ = 3 ± 1, Figure 1-5A). During bulk Cu deposition or Au@Cu core-shell formation, a decrease in $N_{Cu–Au}$ (2 ± 1) was also found, which suggested that the upd Cu at the Au nanoparticle surface yielded Cu clusters rather than a uniform shell. In addition, the Cu clusters were found to have a shortened R_{Cu-Cu} compared to that of the bulk Cu (~2.49 Å vs. ~2.56 Å).

Price *et al.*[42] also compared the surface composition of two Au@Pd core-shell nanoparticles, the Pd shells of which were prepared using different electrochemical approaches, galvanic displacement of the upd Cu layer (two steps) on Au nanoparticles and a Cu-upd-mediated deposition (one step). Like the above Au@Cu nanoparticles, deposited atoms (Pd in this case) were absent from the Au edge data, indicating a common Au-core structure for both samples. EXAFS fitting results at the Pd K edge suggested that the mixing patterns of the Pd shells were different, as evidenced by J_{Pd} (~64% for Cu-upd-mediated Au@Pd and ~49% for Cu-upd-displaced Au@Pd). More detailed structure was

revealed by $R_{Pd\text{-}Pd}$ at -0.665 V_{MMS}, a potential to allow H adsorption into Pd lattice. Although an increase of $R_{Pd\text{-}Pd}$ induced by the H adsorption was found for both samples, the extent of the increase was significantly higher for the Cu-upd-displaced Au@Pd, suggesting the formation of Pd clusters on Au surface using galvanic displacement method, whilst the Cu-upd-mediate method was likely to yield a Pd-Au alloyed shell (Figure 1-5B).

Friebel *et al.*[43, 44] deposited a 2D Pt monolayers (ML) on a Rh(111) single-crystal substrate and compared the data with that for Pt islands on Rh(111). Since on a perfect Rh(111) the Pt deposition is limited to the 3-fold hollow sites, the obtained coordination number of Pt can be directly used to determine the arrangement of the surface Pt atoms (Figure 1-5C). On 2D Pt/Rh(111), it was found that $N_{Pt\text{-}Pt}$ = ~6.5 and $N_{Pt\text{-}Rh}$ = ~3.2, in good agreement with the expected structure ($N_{Pt\text{-}Pt}$ = 6 and $N_{Pt\text{-}Rh}$ = 3, Figure 1-5C), whilst for Pt islands/Rh(111) $N_{Pt\text{-}Pt}$ = ~7.3 and $N_{Pt\text{-}Rh}$ = ~1.4 (Figure 1-5D). In addition, the surface strain of the Pt ML became available from EXAFS fitting, $R_{Pt\text{-}Pt}$ = ~2.72 Å, indicating compressive strain ($R_{Pt\text{-}Pt}$ = ~2.77 Å for bulk Pt).

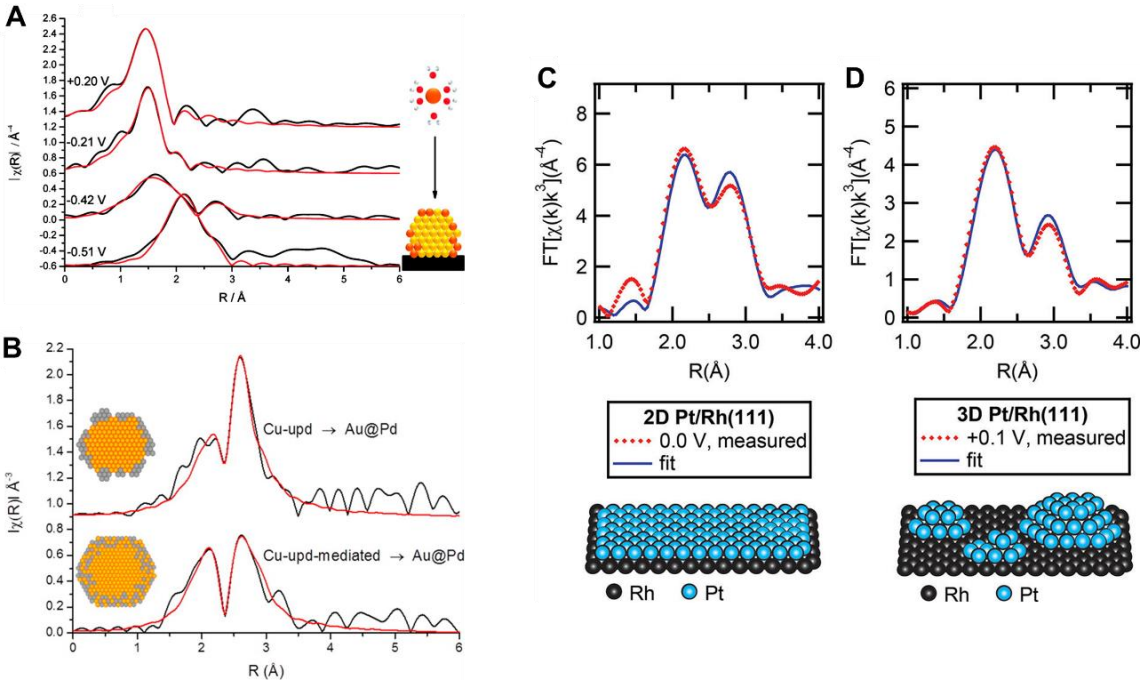

Figure 1-5 (A) k^2-weighted Fourier transforms of Cu K edge data (black) and the corresponding fit (red) for a Au/C electrode in 0.5 M H_2SO_4 and 2 mM $CuSO_4$ as a function of the applied potentials, with a schematic illustration of the Cu upd process (Cu atoms in orange and Au atoms in yellow). Reproduced from [41], which is licensed under ACS AuthorChoice. (B) k^3-weighted Fourier transforms of Pd K edge data (black) and the corresponding fit (red) for Au@Pd electrodes prepared using (the upper panel) Cu-upd-displaced method and (the lower panel) Cu-upd-mediated method in 0.5 M H_2SO_4 at –0.665 V, with schematic structure models showing the atomic arrangement of the Pd shell (silver) on the Au surface (yellow). Reproduced with permission from [42]. Copyright (2013) American Chemical Society. (C and D) k^3-weighted Fourier transforms of Pt L_3 edge data (red) and the corresponding fit (blue) for (C) 2D Pt/Rh(111) and (D) 3D Pt/Rh(111), with the corresponding schematic structure models at the bottom. Reproduced with permission from [44]. Copyright (2012) American Chemical Society.

1.3.2 *In situ* XAS to probe surface electrochemistry

Electrocatalytic reactions involve adsorption of either the reactants or intermediates on the electrode surface and electron transfer between these species and the electrode. Although the thermodynamics and kinetics of the electron transfer step can be analysed by electrochemical measurements, such measurements need to be supplemented by complimentary techniques that provide molecular-level information regarding the bonding between the adsorbate and the surface and structural information regarding the atomic arrangement and electronic structure of the surface atoms. XAS is one such technique that has found increasing use in the study of electrocatalysts[45, 46]. A successful example of coupling *in situ* XAS with electrochemical measurements is single-atom electrocatalysts, where metal atoms are atomically dispersed on suitable supporting materials (mostly carbon). Mukerjee's group [47-52] used *in situ* XAS to study Fe atoms embedded in nitrogen-doped carbon matrices (Fe-N-C) for ORR, and Osmieri *et al.*[53] recently extended the measurements to the membrane electrode assembly (MEA) level. They directly observed spectral changes corresponding to Fe^{2+}/Fe^{3+} redox (Figure 1-6A) and the simultaneous addition of one oxygen neighbour. The redox transition of the Fe active site was attributed to a Fe^{2+}-N_4 to (H)O-Fe^{3+}-N_4 transition, of which the O(H) can be from water activation or from ORR, with Fe^{2+}-N_4 considered as the active site for ORR. Using this notion, the fraction of active site as a function of potential was obtained from both the electrochemical and XANES analyses (Figure 1-6B) and found to be consistent with the kinetics-controlled part of ORR polarisation curves [52]. Further inspection of the average Fe-N bond length (R_{Fe-N}) by Mukerjee's group revealed that the geometry of the Fe^{2+}-N_4 active site can be either square-planar or out-of-plane, both of which switched to the other geometry with the Fe^{2+}/Fe^{3+} redox transition and the addition of an oxygen neighbour[49, 50]. This opposite structure-switching behaviour was used to explain the bond strength of Fe^{3+}-O, which results in the differences in redox potential and ORR activity[52].

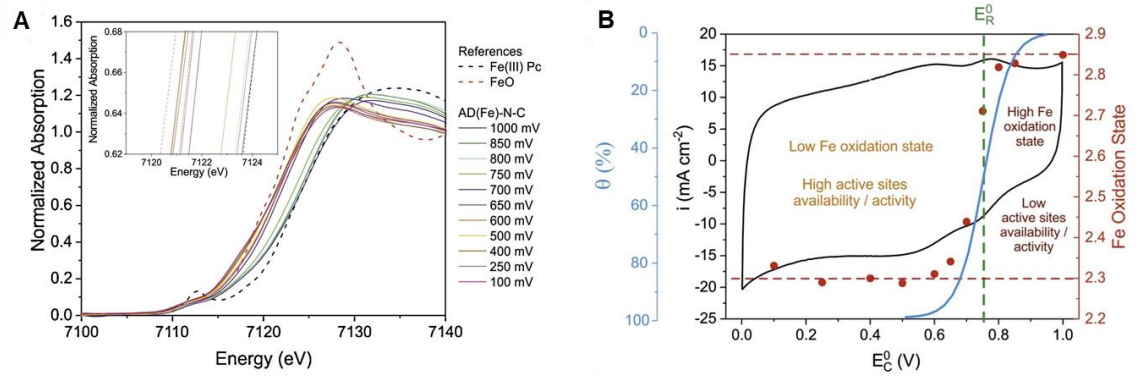

Figure 1-6 (A and B) *In situ* Fe K edge XAS measurements of a Fe-N-C catalyst. (A) XANES spectra of a Fe-N-C MEA electrode at cathode potentials of 0.1–1.0 V. The MEA electrode was measured at 80 °C, 100% RH, 1.5 atm with H_2/He flows at the anode/cathode, respectively. (B) Fe oxidation states (red) as a function of the cathode potential (E_c^0), obtained from linear combination fitting using the reference samples shown in A. CV (black) of cathode at 20 mV s^{-1}, showing the redox potential (E_R^0) of the Fe-N-C MEA (0.787 V). Theoretical fraction of active site (θ, blue), obtained from Nernst equation. Adapted from [53], Copyright (2019), with permission from Elsevier.

However, for metallic nanoparticles the XAS and electrochemical measurements may not probe the same parts (atoms) of the electrocatalyst. The electrochemical measurements are inherently a probe of the surface, whilst XAS is a bulk per-atom averaging technique (Figure 1-7) [54]. The spectator part in the core or underneath the surface dilutes the XAS signal from surface atoms, which are of electrochemical interest. This dilution may blur any potential- and adsorption-induced changes of the spectra and introduce large uncertainty to determine the structural parameters of adsorbed species. The key to solve this challenge is to increase the surface-to-bulk ratio to have sufficient surface signal, which aligned with the general requirement for practical electrocatalysts.

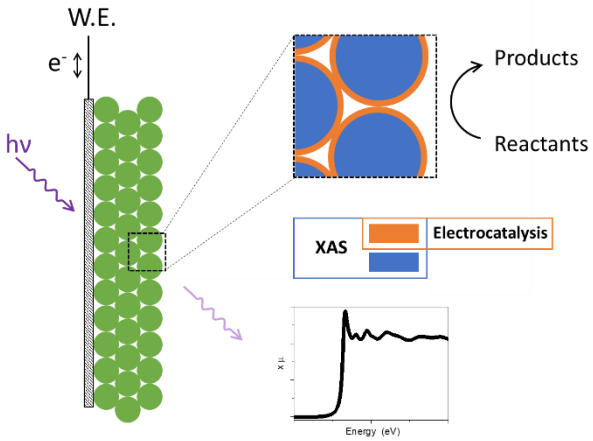

Figure 1-7 Schematic illustration of *in situ* XAS under potential control, showing the parts of the electrocatalysts probed by XAS and electrochemical measurements.

One of the strategies is to decrease the size of nanoparticles, normally to less than 3 nm corresponding to >50% atoms on the surface (Pt as an example[55]). Imai et al. [56] studied the oxidation of ~2 nm Pt nanoparticles (~60% surface atoms) at 1.4 V in 0.5 M H_2SO_4 using time-resolved XAS. Fits of the EXAFS spectra suggested a gradual development of oxygen coordinated Pt atoms (Figure 1-8A–C); at the initial stage OH_{ads}/H_2O_{ads} with a long Pt-O bond (R = 2.2–2.3 Å) was the dominant species, this species was then oxidized into α-PtO_2-like 2D oxides with a shorter Pt-O bond of ~2.0 Å and a new Pt-Pt scattering path at 3.1 Å, and finally the 2D oxides were transformed into β-PtO_2-like 3D oxides with an additional Pt-Pt scattering path at ~3.5 Å. Similar development of Pt oxide formation was also found by Merte et al.[57] on ~1.2 nm Pt nanoparticles (~80% surface atoms) with applied potentials from -0.04 V to 1.26 V using linear combination fitting of high-energy-resolution fluorescence-detected (HERFD) XANES spectra.

For nanoparticles with size larger than 5 nm, the electrochemistry-induced changes in the XAS spectra usually become subtle. Δμ methods, in which the bulk metal-metal interactions are removed by subtracting spectra at a reference potential from that at the potential of interest, are used to

emphasise the changes[58, 59]. Li et al.[60] studied the existence of surface adsorbed OH (OH_{ads}) on Ru/C (~8 nm) and PtRu/C in the hydrogen oxidation region. They found that the experimental Δμ, obtained by subtracting the XANES at 0.05 V, where the surface was covered by adsorbed H (H_{ads}), from that at 0.24 V, where CO stripping experiments suggested that OH_{ads} existed, matched with a theoretical Δμ obtained from FEFF calculations modelling the replacement of H_{ads} on top of a Ru_6 cluster by an OH_{ads} (Figure 1-8D–F). Similarly, Δ-EXAFS has also been used to detect adsorbate-induced changes on the surface of metallic particles [61, 62].

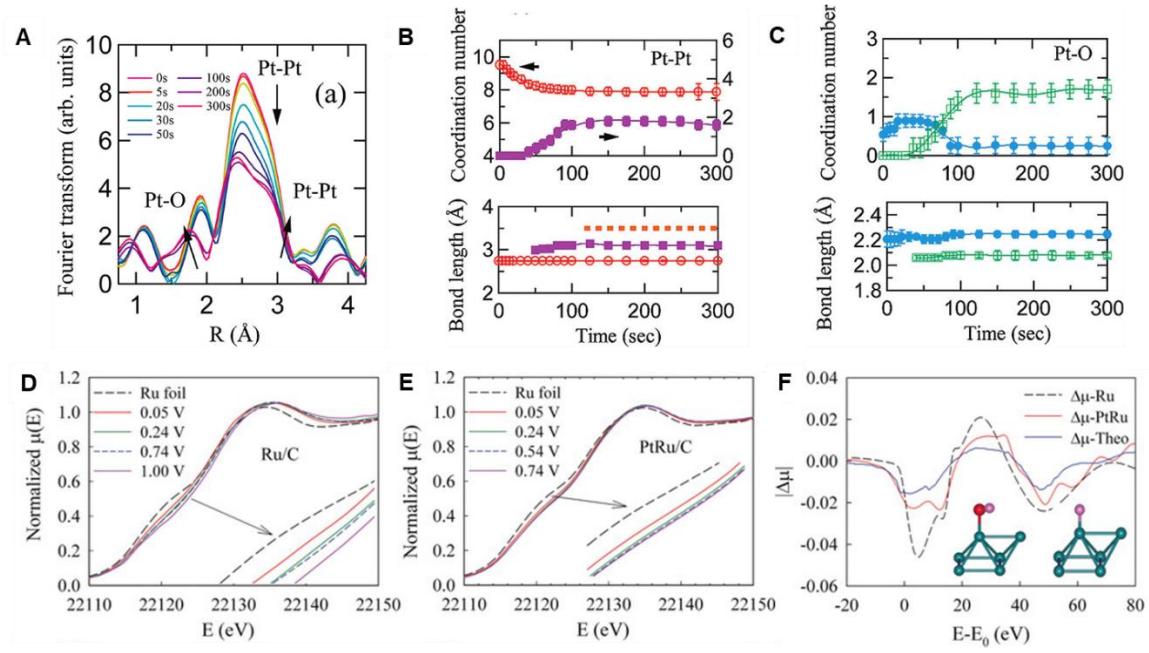

Figure 1-8 (A–F) in situ XAS studies on a Pt/C () during potential step at 1.4 V (A) k^3-weighted Fourier transforms of Pt-L_3 EXAFS spectra and variations of (B) Pt-Pt and (C) Pt-O scattering paths in terms of bond length and coordination numbers. Reproduced with permission from [56]. Copyright (2009) American Chemical Society. (D–F) A Δμ method used to emphasise electrochemistry-induced changes on nanoparticles. Ru K edge XANES spectra of (A) Ru/C (~8 nm) and (B) PtRu/C collected in H_2-saturated 0.1 M KOH solution under potential control. (C) Comparison of experimental Δμ signals, derived from the XANES spectra in A and B (Δμ = μ(0.24 V) - μ(0.05 V)), with A theoretical Δμ, modelled from clusters shown in the inset (Δμ-Theo = μ(Ru_6-OH) - μ(Ru_6-H)). Reproduced with permission from [60]. Copyright (2017) Wiley-VCH Verlag GmbH & Co. KGaA, Weinheim.

Another strategy for in situ XAS studies of metallic nanoparticles is to design core-shell bimetallic particles, or to deposit surface ad-atoms, wherein the element of interest is exclusively put on the surface of a second component, which may serve as an inert host or participate in structural or electronic modification of the surface atoms. Using this approach, the direct measurement of Pt surface oxidation using XAS can be achieved regardless of the particle size[44]. Sasaki et al.[55] prepared a Pt monolayer(ML) on Pd particles (4.2 nm, ~35% surface atoms) using the galvanic displacement of an underpotential deposited Cu ML. By linear combination fitting, they compared

the oxide percentage of this Pt_{ML}/Pd/C with that Pt/C (2.6 nm) per surface atoms (obtained using the fraction of surface atoms) as a function of applied potentials, and they found that the Pd core underneath significantly retarded the Pt oxidation.

The second component of Pt-based bimetallic electrocatalysts can also participate in electrochemical process. A good example is PtRu/C catalysts for anodic reactions of fuel cells, the Ru site of which can be an adsorption site of CO intermediate and an active site for OH_{ads} formation at low potentials. Rose *et al.*[63] probed the Ru-CO bond of CO adsorbed on a Ru-modified Pt/C catalyst (1.5 ML Ru on Pt surface), and they found 1.4 C neighbours at ~2.04 Å from the Ru K edge EXAFS data in the presence of CO. Pelliccione et al.[64] compared the potential dependence of Ru K-edge spectra on a Ru@Pt catalyst (0.3 ML Ru on Pt nanoparticles, ~10 nm) with or without the presence of methanol. In 0.1 M H_2SO_4, the Ru atoms were gradually oxidized with potential and started being transformed into RuO_2-like species at 0.575 V vs. Ag/AgCl (Figure 1-9), consistent with another *in situ* XAS study on Ru modified Pt/C in 1 M H_2SO_4 (0.7 V *vs.* RHE)[65]. In the presence of methanol, however, the oxidation state and coordination environment of the Ru atoms were more stable without the formation of the RuO_2-like species at high potentials but with additional Ru-CO species present at all the studied potentials (Figure 1-9)[64]. The authors attributed the different response to electrolyte to the dual role of Ru sites during methanol oxidation, providing OH_{ads} species and available sites for CO_{ads}.

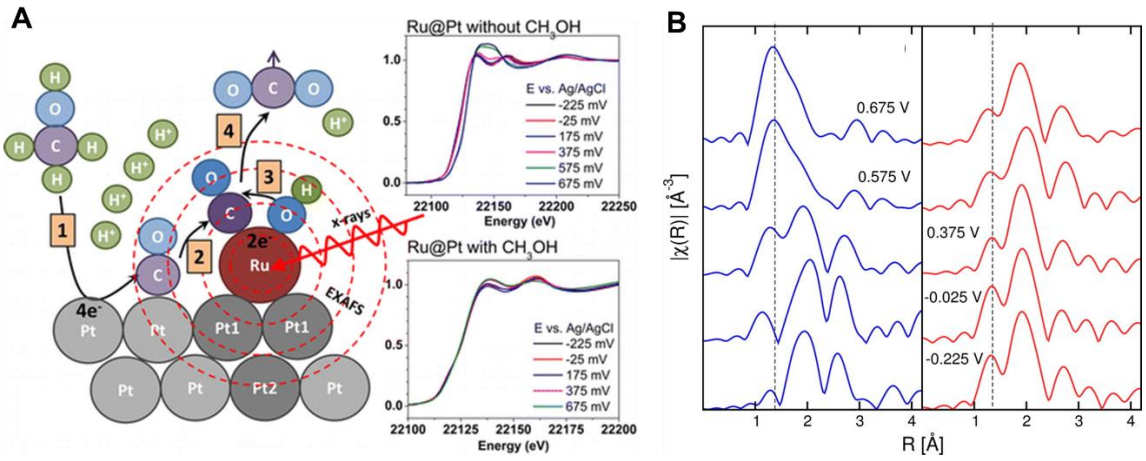

Figure 1-9 (A) XANES spectra and (B) Fourier transformed EXAFS spectra of the Ru@Pt catalyst as a function of applied potential (right top in A and left in B) without CH_3OH and (right bottom in A and right in B) with CH_3OH, with schematic illustration of the in situ Ru K-edge XAS experiment of Ru@Pt. Reproduced with permission from [64]. Copyright (2013) American Chemical Society.

1.4 Aims and thesis outline

XAS is a powerful technique to interrogate the structure of bimetallic electrocatalysts and to probe the dynamic electronic and coordination structure under working conditions. It should be acknowledged that XAS is intrinsically not surface sensitive, and care must be taken when designing experiments. With the advantages and limitations borne in mind, this thesis, combining XAS measurements and electrochemical measurements, is set out to (i) demonstrate the strength of XAS in characterising the speciation, extent of alloying and surface structure of Pt-Sn bimetallic electrocatalysts, (ii) study how these parameters affect the electrocatalytic activity of Pt-Sn, especially for CO oxidation reaction, (iii) clarify the active Sn species and details of the bifunctional mechanism for CO oxidation, and (iv) show how to achieve surface sensitivity of XAS and probe bimetallic surface structure by careful experiment design.

Chapter 2 covers the common experimental details, mainly characterisation, and data processing used in this thesis. Experiments specific to **Chapter 3–6** are provided in the experimental section of each chapter, such as catalyst synthesis.

Chapter 3 focuses on identification of the phases and atomic configurations of Pt-Sn bimetallic nanoparticles. The same carbon supported Pt_3Sn catalyst was annealed under air, Ar and H_2, resulting in variation of the extent of alloying of the two components, whilst retaining the same composition. The extent of alloying was characterised using a variety of methods including TEM, XRD, XPS, XANES, and EXAFS.

Chapter 4 investigates the role of SnO_2 in the bifunctional mechanism for CO oxidation. A carbon supported Pt-SnO_2 was carefully synthesized to avoid the formation of Pt-Sn alloy, the structure of which was confirmed by STEM and detailed XAS analysis. The CO oxidation voltammograms of the Pt-SnO_2/C and other SnO_2-modified Pt surfaces were used to ascertain the electrochemistry and the bifunctional mechanism of SnO_2.

Chapter 5 explores details of the bifunctional mechanism of CO oxidation on Pt-Sn bimetallic nanoparticles. A model Pt-Sn catalyst, where Sn ad-atoms are exclusively on the surface of Pt nanoparticles (Sn_{ad}-Pt/C), was prepared. The effects of the Sn ad-atoms on CO oxidation were studied as a function of Sn coverage. The active oxygenated species, the nature and surface electrochemistry of the Sn were identified by *in situ* XAS measurements.

Chapter 6 reveals the surface contraction of Pt-Sn bimetallic nanoparticles. Dealloyed Pt-Sn nanoparticles (a sample from **Chapter 3)**, where most Sn atoms were oxidized and segregated to the surface, were partly reduced to form a surface alloy in H_2 at room temperature, the XAS data of which was compared with that measured in air to ascertain the presence of a surface contraction on bimetallic nanoparticles. An improved fitting model combining the data measured in H_2 and in air

was devised to extract the structural information specifically of the surface from the averaged XAS results.

1.5 References

[1] M.K. Debe, Electrocatalyst approaches and challenges for automotive fuel cells, Nature, 486 (2012) 43-51.

[2] K. Jiao, M. Ni, Challenges and opportunities in modelling of proton exchange membrane fuel cells (PEMFC), International Journal of Energy Research, 41 (2017) 1793-1797.

[3] T. Bligaard, J.K. Nørskov, Ligand effects in heterogeneous catalysis and electrochemistry, Electrochim. Acta, 52 (2007) 5512-5516.

[4] F. Calle-Vallejo, M.T. Koper, A.S. Bandarenka, Tailoring the catalytic activity of electrodes with monolayer amounts of foreign metals, Chem. Soc. Rev., 42 (2013) 5210-5230.

[5] W.M.H. Sachtler, Ensemble and Ligand Effects in Metal Catalysis, Handbook of Heterogeneous Catalysis2008, pp. 1585-1593.

[6] M. Luo, S. Guo, Strain-controlled electrocatalysis on multimetallic nanomaterials, Nat. Rev. Mater., 2 (2017) 17059.

[7] Z. Xia, S. Guo, Strain engineering of metal-based nanomaterials for energy electrocatalysis, Chem. Soc. Rev., 48 (2019) 3265-3278.

[8] A. Cuesta, At least three contiguous atoms are necessary for CO formation during methanol electrooxidation on platinum, J. Am. Chem. Soc., 128 (2006) 13332-13333.

[9] A. Cuesta, M. Escudero, B. Lanova, H. Baltruschat, Cyclic voltammetry, FTIRS, and DEMS study of the electrooxidation of carbon monoxide, formic acid, and methanol on cyanide-modified Pt(111) electrodes, Langmuir, 25 (2009) 6500-6507.

[10] R. Wang, C. Wang, W.B. Cai, Y. Ding, Ultralow-platinum-loading high-performance nanoporous electrocatalysts with nanoengineered surface structures, Adv. Mater., 22 (2010) 1845-1848.

[11] Q.S. Chen, Z.Y. Zhou, F.J. Vidal-Iglesias, J. Solla-Gullon, J.M. Feliu, S.G. Sun, Significantly enhancing catalytic activity of tetrahexahedral Pt nanocrystals by Bi adatom decoration, J. Am. Chem. Soc., 133 (2011) 12930-12933.

[12] M. Watanabe, S. Motoo, Electrocatalysis by ad-atoms, J. Electroanal. Chem. Interfacial Electrochem., 60 (1975) 267-273.

[13] M. Watanabe, M. Shibata, S. Motoo, Electrocatalysis by ad-atoms, J. Electroanal. Chem. Interfacial Electrochem., 187 (1985) 161-174.

[14] B.E. Hayden, M.E. Rendall, O. South, Electro-oxidation of carbon monoxide on well-ordered Pt(111)/Sn surface alloys, J. Am. Chem. Soc., 125 (2003) 7738-7742.

[15] C. Lu, C. Rice, R.I. Masel, P.K. Babu, P. Waszczuk, H.S. Kim, E. Oldfield, A. Wieckowski, UHV, Electrochemical NMR, and Electrochemical Studies of Platinum/Ruthenium Fuel Cell Catalysts, J. Phys. Chem. B, 106 (2002) 9581-9589.

[16] Mechanistic aspects of carbon monoxide oxidation, Handbook of Fuel Cells2010.

[17] H. Wang, Z. Jusys, R.J. Behm, H.D. Abruña, New Insights into the Mechanism and Kinetics of Adsorbed CO Electrooxidation on Platinum: Online Mass Spectrometry and Kinetic Monte Carlo Simulation Studies, J. Phys. Chem. C, 116 (2012) 11040-11053.

[18] M.T.M. Koper, S.C.S. Lai, E. Herrero, Mechanisms of the Oxidation of Carbon Monoxide and Small Organic Molecules at Metal Electrodes, Fuel Cell Catalysis2009, pp. 159-207.

[19] N. Markovic, Surface science studies of model fuel cell electrocatalysts, Surf. Sci. Rep., 45 (2002) 117-229.

[20] S. Gilman, The Mechanism of Electrochemical Oxidation of Carbon Monoxide and Methanol on Platinum. II. The "Reactant-Pair" Mechanism for Electrochemical Oxidation of Carbon Monoxide and Methanol, J. Phys. Chem., 68 (1964) 70-80.

[21] K. Loza, M. Heggen, M. Epple, Synthesis, Structure, Properties, and Applications of Bimetallic Nanoparticles of Noble Metals, Adv. Funct. Mater., 30 (2020) 1909260.

[22] R. Ferrando, J. Jellinek, R.L. Johnston, Nanoalloys: from theory to applications of alloy clusters and nanoparticles, Chem. Rev., 108 (2008) 845-910.

[23] N. Toshima, T. Yonezawa, Bimetallic nanoparticles—novel materials for chemical and physical applications, New J. Chem., 22 (1998) 1179-1201.

[24] D. Medina-Cruz, B. Saleh, A. Vernet-Crua, A. Nieto-Argüello, D. Lomelí-Marroquín, L.Y. Vélez-Escamilla, J.L. Cholula-Díaz, J.M. García-Martín, T. Webster, Bimetallic Nanoparticles for Biomedical Applications: A Review, in: B. Li, T.F. Moriarty, T. Webster, M. Xing (Eds.) Racing for the Surface: Antimicrobial and Interface Tissue Engineering, Springer International Publishing, Cham, 2020, pp. 397-434.

[25] M. Arenz, V. Stamenkovic, B. Blizanac, K. Mayrhofer, N. Markovic, P. Ross, Carbon-supported Pt–Sn electrocatalysts for the anodic oxidation of H_2, CO, and H_2/CO mixtures.Part II: The structure–activity relationship, J. Catal., 232 (2005) 402-410.

[26] F. Ye, J. Li, T. Wang, Y. Liu, H. Wei, J. Li, X. Wang, Electrocatalytic Properties of Platinum Catalysts Prepared by Pulse Electrodeposition Method Using SnO_2 as an Assisting Reagent, J. Phys. Chem. C, 112 (2008) 12894-12898.

[27] E.M. Crabb, R. Marshall, D. Thompsett, Carbon Monoxide Electro-oxidation Properties of Carbon-Supported PtSn Catalysts Prepared Using Surface Organometallic Chemistry, J. Electrochem. Soc., 147 (2000) 4440-4447.

[28] W.-P. Zhou, W. An, D. Su, R. Palomino, P. Liu, M.G. White, R.R. Adzic, Electrooxidation of Methanol at SnO_x–Pt Interface: A Tunable Activity of Tin Oxide Nanoparticles, J. Phys. Chem. Lett., 3 (2012) 3286-3290.

[29] M. Newville, Fundamentals of XAFS, 2014.

[30] C.V.S. Almeida, D.S. Ferreira, H. Huang, A.C. Gaiotti, G.A. Camara, A.E. Russell, K.I.B. Eguiluz, G.R. Salazar-Banda, Highly active Pt3Rh/C nanoparticles towards ethanol electrooxidation. Influence of the catalyst structure, Appl. Catal., B, 254 (2019) 113-127.

[31] S. Alayoglu, P. Zavalij, B. Eichhorn, Q. Wang, A.I. Frenkel, P. Chupas, Structural and architectural evaluation of bimetallic nanoparticles: a case study of Pt-Ru core-shell and alloy nanoparticles, ACS Nano, 3 (2009) 3127-3137.

[32] B.J. Hwang, L.S. Sarma, J.M. Chen, C.H. Chen, S.C. Shih, G.R. Wang, D.G. Liu, J.F. Lee, M.T. Tang, Structural models and atomic distribution of bimetallic nanoparticles as investigated by X-ray absorption spectroscopy, J. Am. Chem. Soc., 127 (2005) 11140-11145.

[33] G.Y. Chen, K.A. Kuttiyiel, D. Su, M. Li, C.H. Wang, D. Buceta, C.Y. Du, Y.Z. Gao, G.P. Yin, K. Sasaki, M.B. Vukmirovic, R.R. Adzic, Oxygen Reduction Kinetics on Pt Monolayer Shell Highly Affected by the Structure of Bimetallic AuNi Cores, Chem. Mater., 28 (2016) 5274-5281.

[34] J.E.S. van der Hoeven, T.A.J. Welling, T.A.G. Silva, J.E. van den Reijen, C. La Fontaine, X. Carrier, C. Louis, A. van Blaaderen, P.E. de Jongh, In Situ Observation of Atomic Redistribution in Alloying Gold-Silver Nanorods, ACS Nano, 12 (2018) 8467-8476.

[35] N. Becknell, Y. Kang, C. Chen, J. Resasco, N. Kornienko, J. Guo, N.M. Markovic, G.A. Somorjai, V.R. Stamenkovic, P. Yang, Atomic Structure of Pt_3Ni Nanoframe Electrocatalysts by in Situ X-ray Absorption Spectroscopy, J. Am. Chem. Soc., 137 (2015) 15817-15824.

[36] C. Chen, Y. Kang, Z. Huo, Z. Zhu, W. Huang, H.L. Xin, J.D. Snyder, D. Li, J.A. Herron, M. Mavrikakis, M. Chi, K.L. More, Y. Li, N.M. Markovic, G.A. Somorjai, P. Yang, V.R. Stamenkovic, Highly crystalline multimetallic nanoframes with three-dimensional electrocatalytic surfaces, Science, 343 (2014) 1339-1343.

[37] Q. Jia, W. Liang, M.K. Bates, P. Mani, W. Lee, S. Mukerjee, Activity descriptor identification for oxygen reduction on platinum-based bimetallic nanoparticles: in situ observation of the linear composition-strain-activity relationship, ACS Nano, 9 (2015) 387-400.

[38] Q. Jia, K. Caldwell, D.E. Ramaker, J.M. Ziegelbauer, Z. Liu, Z. Yu, M. Trahan, S. Mukerjee, In Situ Spectroscopic Evidence for Ordered Core–Ultrathin Shell Pt_1Co_1 Nanoparticles with Enhanced Activity and Stability as Oxygen Reduction Electrocatalysts, J. Phys. Chem. C, 118 (2014) 20496-20503.

[39] Q. Jia, K. Caldwell, K. Strickland, J.M. Ziegelbauer, Z. Liu, Z. Yu, D.E. Ramaker, S. Mukerjee, Improved Oxygen Reduction Activity and Durability of Dealloyed $PtCo_x$ Catalysts for Proton Exchange Membrane Fuel Cells: Strain, Ligand, and Particle Size Effects, ACS Catal., 5 (2015) 176-186.

[40] T. Kaito, H. Tanaka, H. Mitsumoto, S. Sugawara, K. Shinohara, H. Ariga, H. Uehara, S. Takakusagi, K. Asakura, In Situ X-ray Absorption Fine Structure Analysis of PtCo, PtCu, and PtNi Alloy Electrocatalysts: The Correlation of Enhanced Oxygen Reduction Reaction Activity and Structure, J. Phys. Chem. C, 120 (2016) 11519-11527.

[41] S.W. Price, J.D. Speed, P. Kannan, A.E. Russell, Exploring the first steps in core-shell electrocatalyst preparation: in situ characterization of the underpotential deposition of Cu on supported Au nanoparticles, J. Am. Chem. Soc., 133 (2011) 19448-19458.

[42] S.W.T. Price, J.M. Rhodes, L. Calvillo, A.E. Russell, Revealing the Details of the Surface Composition of Electrochemically Prepared Au@Pd Core@Shell Nanoparticles with in Situ EXAFS, J. Phys. Chem. C, 117 (2013) 24858-24865.

[43] D. Friebel, D.J. Miller, C.P. O'Grady, T. Anniyev, J. Bargar, U. Bergmann, H. Ogasawara, K.T. Wikfeldt, L.G. Pettersson, A. Nilsson, In situ X-ray probing reveals fingerprints of surface platinum oxide, Phys. Chem. Chem. Phys., 13 (2011) 262-266.

[44] D. Friebel, V. Viswanathan, D.J. Miller, T. Anniyev, H. Ogasawara, A.H. Larsen, C.P. O'Grady, J.K. Norskov, A. Nilsson, Balance of nanostructure and bimetallic interactions in Pt model fuel cell catalysts: in situ XAS and DFT study, J. Am. Chem. Soc., 134 (2012) 9664-9671.

[45] J. Li, J. Gong, Operando characterization techniques for electrocatalysis, Energy Environ. Sci., 13 (2020) 3748-3779.

[46] M. Wang, L. Árnadóttir, Z.J. Xu, Z. Feng, In situ X-ray absorption spectroscopy studies of nanoscale electrocatalysts, Nano-Micro Lett., 11 (2019) 47.

[47] Q. Jia, N. Ramaswamy, U. Tylus, K. Strickland, J. Li, A. Serov, K. Artyushkova, P. Atanassov, J. Anibal, C. Gumeci, S.C. Barton, M.-T. Sougrati, F. Jaouen, B. Halevi, S. Mukerjee, Spectroscopic insights into the nature of active sites in iron–nitrogen–carbon electrocatalysts for oxygen reduction in acid, Nano Energy, 29 (2016) 65-82.

[48] Q. Jia, E. Liu, L. Jiao, S. Pann, S. Mukerjee, X-Ray absorption spectroscopy characterizations on PGM-free electrocatalysts: justification, advantages, and limitations, Adv. Mater., 31 (2019) e1805157.

[49] Q. Jia, N. Ramaswamy, H. Hafiz, U. Tylus, K. Strickland, G. Wu, B. Barbiellini, A. Bansil, E.F. Holby, P. Zelenay, S. Mukerjee, Experimental observation of redox-induced Fe-N switching behavior as a determinant role for oxygen reduction activity, ACS Nano, 9 (2015) 12496-12505.

[50] J. Li, S. Ghoshal, W. Liang, M.-T. Sougrati, F. Jaouen, B. Halevi, S. McKinney, G. McCool, C. Ma, X. Yuan, Z.-F. Ma, S. Mukerjee, Q. Jia, Structural and mechanistic basis for the high activity of Fe-N-C catalysts toward oxygen reduction, Energy Environ. Sci., 9 (2016) 2418-2432.

[51] M. Xiao, J. Zhu, L. Ma, Z. Jin, J. Ge, X. Deng, Y. Hou, Q. He, J. Li, Q. Jia, S. Mukerjee, R. Yang, Z. Jiang, D. Su, C. Liu, W. Xing, Microporous framework induced synthesis of single-atom dispersed Fe-N-C acidic ORR catalyst and its in situ reduced Fe-N_4 active site identification revealed by X-ray absorption spectroscopy, ACS Catal., 8 (2018) 2824-2832.

[52] J. Li, A. Alsudairi, Z.F. Ma, S. Mukerjee, Q. Jia, Asymmetric volcano trend in oxygen reduction activity of Pt and non-Pt catalysts: in situ identification of the site-blocking effect, J. Am. Chem. Soc., 139 (2017) 1384-1387.

[53] L. Osmieri, R.K. Ahluwalia, X. Wang, H.T. Chung, X. Yin, A.J. Kropf, J. Park, D.A. Cullen, K.L. More, P. Zelenay, D.J. Myers, K.C. Neyerlin, Elucidation of Fe-N-C electrocatalyst active site functionality via in-situ X-ray absorption and operando determination of oxygen reduction reaction kinetics in a PEFC, Appl. Catal., B, 257 (2019) 117929.

[54] A.E. Russell, A. Rose, X-ray absorption spectroscopy of low temperature fuel cell catalysts, Chem. Rev., 104 (2004) 4613-4636.

[55] K. Sasaki, N. Marinkovic, H.S. Isaacs, R.R. Adzic, Synchrotron-based in situ characterization of carbon-supported platinum and platinum monolayer electrocatalysts, ACS Catal., 6 (2015) 69-76.

[56] H. Imai, K. Izumi, M. Matsumoto, Y. Kubo, K. Kato, Y. Imai, In situ and real-time monitoring of oxide growth in a few monolayers at surfaces of platinum nanoparticles in aqueous media, J. Am. Chem. Soc., 131 (2009) 6293-6300.

[57] L.R. Merte, F. Behafarid, D.J. Miller, D. Friebel, S. Cho, F. Mbuga, D. Sokaras, R. Alonso-Mori, T.-C. Weng, D. Nordlund, A. Nilsson, B. Roldan Cuenya, Electrochemical oxidation of size-selected Pt nanoparticles studied using in situ high-energy-resolution X-ray absorption spectroscopy, ACS Catal., 2 (2012) 2371-2376.

[58] D.E. Ramaker, D.C. Koningsberger, The atomic AXAFS and Δμ XANES techniques as applied to heterogeneous catalysis and electrocatalysis, Phys. Chem. Chem. Phys., 12 (2010) 5514-5534.

[59] M. Teliska, W.E. O'Grady, D.E. Ramaker, Determination of O and OH adsorption sites and coverage in situ on Pt electrodes from Pt $L_{2,3}$ X-ray absorption spectroscopy, J. Phys. Chem. B, 109 (2005) 8076-8084.

[60] J. Li, S. Ghoshal, M.K. Bates, T.E. Miller, V. Davies, E. Stavitski, K. Attenkofer, S. Mukerjee, Z.F. Ma, Q. Jia, Experimental proof of the bifunctional mechanism for the hydrogen oxidation in alkaline media, Angew. Chem., Int. Ed., 56 (2017) 15594-15598.

[61] C.S. Spanjers, T.P. Senftle, A.C. van Duin, M.J. Janik, A.I. Frenkel, R.M. Rioux, Illuminating surface atoms in nanoclusters by differential X-ray absorption spectroscopy, Phys. Chem. Chem. Phys., 16 (2014) 26528-26538.

[62] S. Maniguet, R.J. Mathew, A.E. Russell, EXAFS of carbon monoxide oxidation on supported Pt fuel cell electrocatalysts, J. Phys. Chem. B, 104 (2000) 1998-2004.

[63] A. Rose, R. Bilsborrow, C.R. King, M.K. Ravikumar, Y. Qian, R.J.K. Wiltshire, E.M. Crabb, A.E. Russell, In situ Ru K-edge EXAFS of CO adsorption on a Ru modified Pt/C fuel cell catalyst, Electrochim. Acta, 54 (2009) 5262-5266.

[64] C.J. Pelliccione, E.V. Timofeeva, J.P. Katsoudas, C.U. Segre, In situ Ru K-edge X-ray absorption spectroscopy study of methanol oxidation mechanisms on model submonolayer ru on Pt nanoparticle electrocatalyst, J. Phys. Chem. C, 117 (2013) 18904-18912.

[65] A. Rose, E.M. Crabb, Y.D. Qian, M.K. Ravikumar, P.P. Wells, R.J.K. Wiltshire, J. Yao, R. Bilsborrow, F. Mosselmans, A.E. Russell, Potential dependence of segregation and surface alloy formation of a Ru modified carbon supported Pt catalyst, Electrochim. Acta, 52 (2007) 5556-5564.

Chapter 2 Experimental section

2.1 X-ray diffraction measurements

X-ray diffraction (XRD) patterns were collected using a Bruker D2 Phaser diffractometer with a Cu K_α radiation (λ = 1.5418 Å, 30 kV, 10 mA) and a LYNXEYE detector. The measurements were carried out with the step size of 0.02° counting 0.3 s per step. A home-made sample holder (shown in figure 1), comprising a 3D printed base and an glass sample holder, was found to contribute insignificant background in the patterns and to require much less sample than the standard sample holder provided.

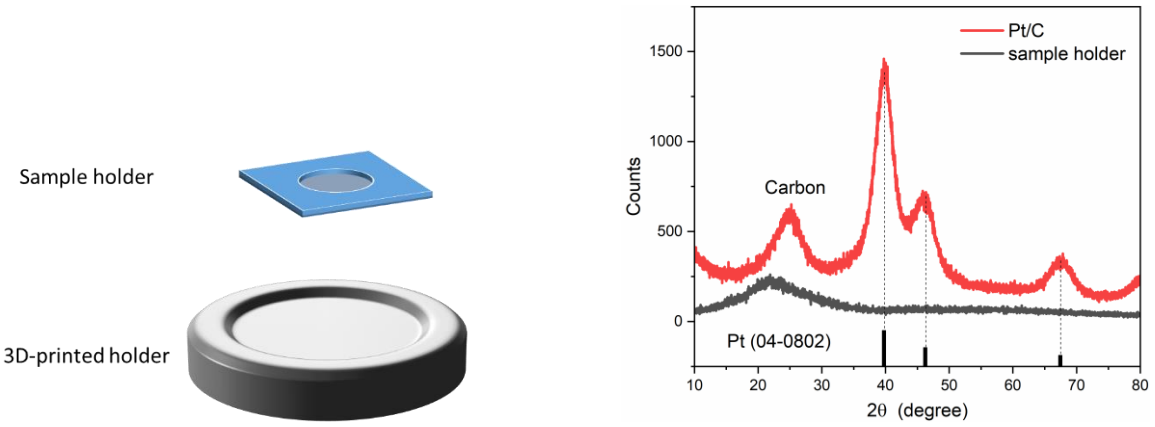

Figure 2-1 (Left) Schematic illustration for a customised sample holder used for the D2 Phaser. The base was 3D-printed using ABS plastic, and the sample holder was cut from a microscope slide and engineered to have a flat-bottom hole in the middle. (Right) XRD patterns of the sample holder with and without a Pt/C sample (20 wt%, Johnson Matthey), showing that the contribution of the sample holder in the pattern is negligible.

2.2 TEM and STEM-EELS microanalysis

Scanning transmission electron microscopy (STEM) measurements, together with electron energy loss spectroscopy (EELS), were carried out on an aberration-corrected Nion UltraSTEM™ 100MC at the SuperSTEM laboratory (Daresbury, UK). The accelerating voltage was 60 kV. TEM images were recorded on an FEI Tecnai 12 at 80 kV (Biomedical imaging unit, University of Southampton). The STEM and TEM samples were prepared by dropcasting a drop of diluted catalyst ink (alcohol aqueous solution) on a carbon coated Cu grid (400 meshes). The samples were allowed to dry overnight and stored in a Cu grid box.

2.2.1 STEM-EELS Data processing

The STEM-EELS data processing was carried out using the Gatan Microscopy Suite® (GMS) software (version 3.31), which is free of charge on computers not attached to microscope or image acquisition hardware. Whilst STEM images can be presented without being processed (Figure 2-2A), STEM-EELS microanalysis requires spectra extraction and signal processing from the spectral images, each pixel of which contains an EELS spectrum. The spectra can be merged if multiple pixels are selected (3×3 pixels in Figure 2-2B). Background subtraction was carried out on the raw spectra obtained using a power law model on energy range selected before the edge of interest (Figure 2-2C). By defining energy range as the signal on the background-subtracted spectrum, the distribution of the signal intensity across the spectral image can be mapped (Figure 2-2D). Another STEM-EELS measurement was carried out at a different edge but on the same particle (Figure 2-2E) allowing a colormix map can to be plotted, which shows the relative distribution of these two signals (Figure 2-2F).

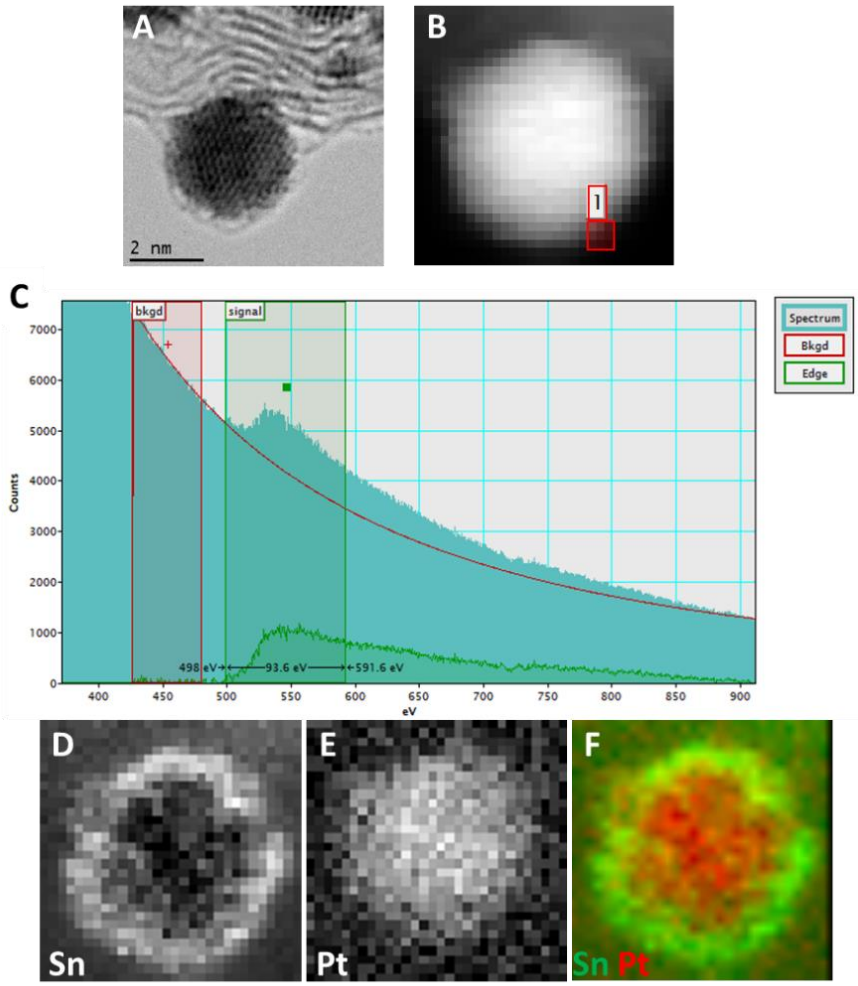

Figure 2-2 STEM-EELS analysis on a Pt-Sn core shell sample. (A) A BF-STEM image, (B) A spectral image focusing on the particle shown in A, (C) EELS spectra of the selected area of B at the Sn $M_{4,5}$ edge, showing the raw spectrum, the background, and the background-subtracted spectrum, (D) a STEM-EELS mapping image of Sn using the signal range defined in C, (E) a STEM-EELS mapping image at the Pt $M_{4,5}$ edge, and (F) a colormix image of D and E.

2.3 X-ray photoelectron spectra

X-ray photoelectron spectra (XPS) were acquired on a Kratos Axis Ultra Hybrid spectrometer (Queen's University Belfast). XPS data deconvolution was performed using XPSPEAK 4.1. The background was corrected using the Shirley method[1] and the percentage of Gaussian contribution in peak shape was fixed in a range of 20% to 30%. XPS spectra were calibrated using the C 1s peak associated with adventitious carbon at 284.8 eV. In the Pt 4f spectra, the spin-orbit spitting energy and the ratio of the peak area between Pt $4f_{7/2}$ and $Pt4f_{5/2}$ are constrained to be 3.35 eV and 4:3, respectively. For the Sn 3d spectra, the spin orbit spitting energy and the ratio of the peak area between Sn $3d_{5/2}$ and Sn $3d_{3/2}$ are constrained to be 8.4 eV and 3:2, respectively.

2.4 Electrochemical measurements

2.4.1 Electrochemical cell and thin-film preparation

Electrochemical measurements were performed in a standard three-electrode cell at room temperature or at 25 ± 1 °C when a jacketed cell and water bath were used. A Pt gauze was used as the counter electrode, and a reversible hydrogen electrode (RHE, HydroFlex, Gaskatel GmbH) equipped with a Luggin capillary as the reference electrode (Figure 2-3). The values of potential in the text are referenced against RHE, unless stated otherwise.

The working electrode was prepared by drop-casting 10 μL of a catalyst ink onto an inverted polished glassy carbon (GC) electrode (5 mm diameter, Pine) and drying at 700 rpm and under an IR lamp (250 W) to obtain an even thin film (Figure 2-4). The GC electrode was polished using Al_2O_3 paste (0.1 μm diameter), and the catalyst ink (2 mg mL^{-1}) was prepared by dispersing a sample into isopropanol alcohol (IPA) aqueous solution (25 vol% of IPA) using an ultrasonic bath for >20 min. For some catalysts such as Pt/C the even thin film can be easily obtained using this procedure, but for as-prepared samples such as Pt-Sn/C samples after heat treatment it may be more difficult; generally, 2 out of 5 electrodes with even thin film can be obtained.

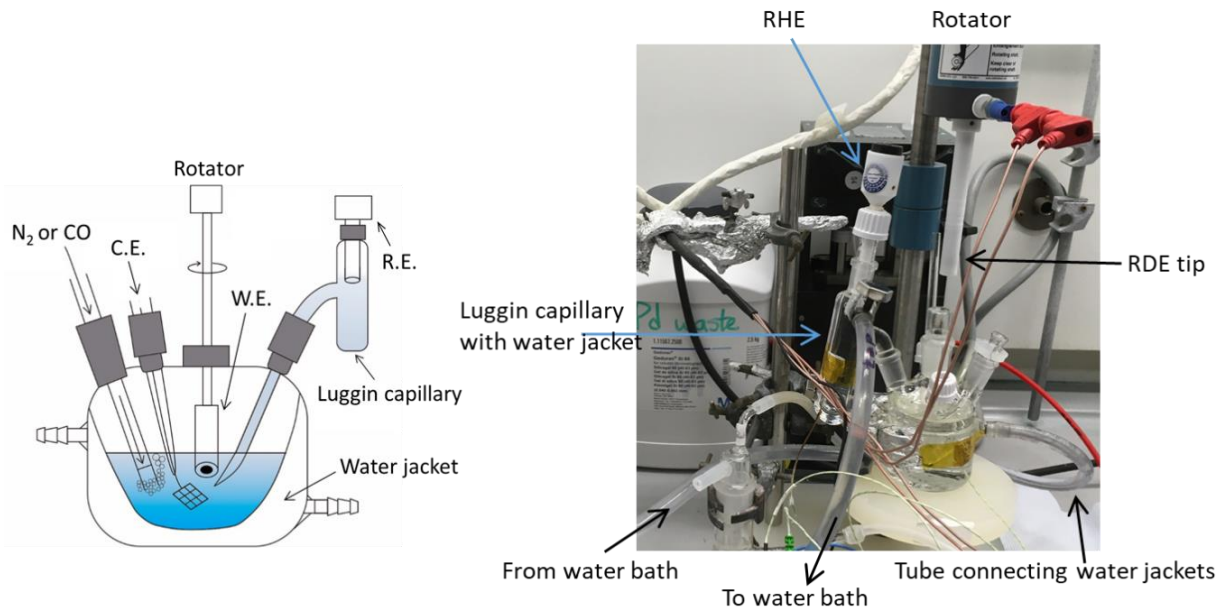

Figure 2-3 (Left) Schematic illustration of the three-electrode electrochemistry setup. The water jacket of the Luggin capillary is not shown. (Right) A picture of the setup used in this thesis. The thermostatic water goes from the water jacket of the main compartment to that of Luggin capillary to ensure both are at the same temperature.

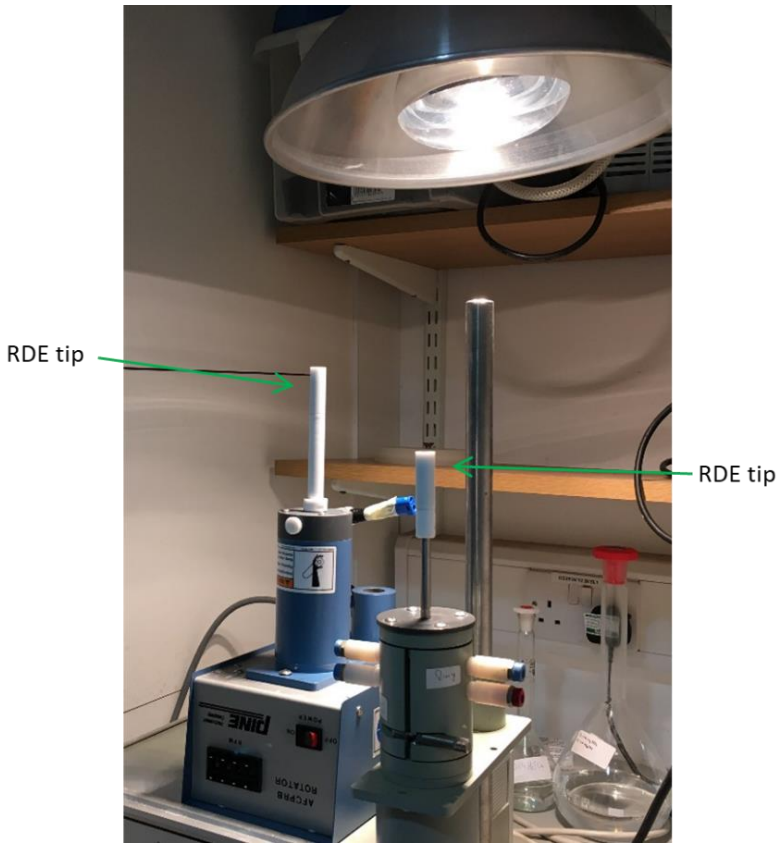

Figure 2-4 A setup for drying catalyst ink under rotation to obtain an even thin film on a RDE tip.

2.4.2 Cyclic voltammetry

In this thesis, cyclic voltammetry is used to study the surface electrochemistry of Pt-Sn bimetallic electrocatalysts. The potential vs. time triangle waveform used for cyclic voltammetry can be manipulated in terms of scan rates and potential limits (Figure 2-5). Figure 2-6 shows effects of these two parameters on the typical cyclic voltammograms (CV) of Pt in acid. The Pt CV consists of three parts, a H underpotential deposition (H_{upd}) region for H adsorption/desorption on Pt surface (0.05~0.4 V), an oxide region for Pt surface oxide formation and reduction (>0.8 V in the forward scan and ~0.8 V in the backward scan) and a double-layer (DL) region (0.4~0.8 V in the forward scan). The currents of the H_{upd} region and the oxide region are proportional to the scan rate (the inset of Figure 2-6), indicating that the electrochemical reactions are related to surface bound species. Also, the nearly constant peak potentials of the H_{upd} at high scan rates indicate the fast kinetics of H_{upd} on Pt. Assuming the coverage of H_{upd} on Pt is one monolayer, the electrochemical active surface area can be obtained by integrating the charge of H_{upd} and dividing the charge by a commonly accepted value (0.21 mC cm^{-2})[2].

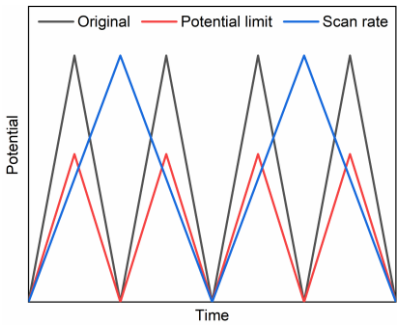

Figure 2-5 Potential plotted as triangle functions of time used in cyclic voltammetry, showing the common parameters of CV measurements.

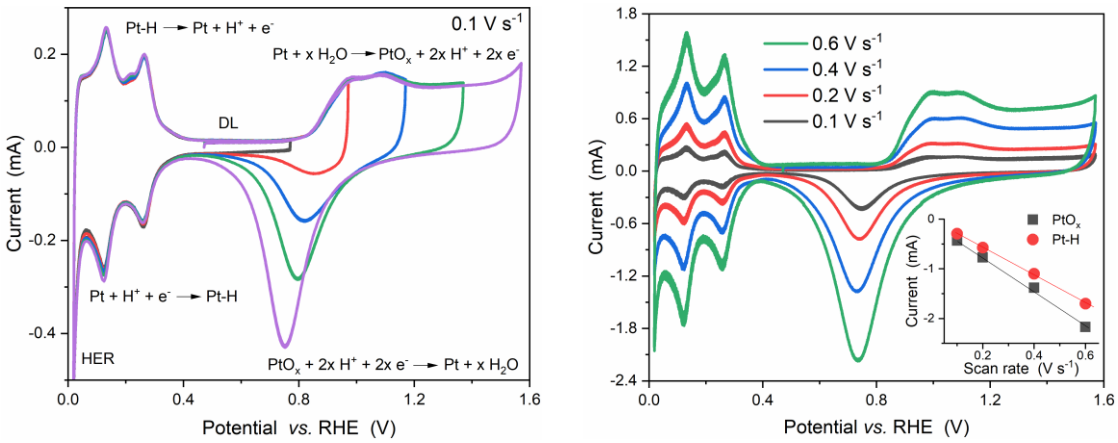

Figure 2-6 Cyclic voltammograms of Pt (8 mm diameter) in N_2-saturated 1 M H_2SO_4 (left) with different upper limits and (right) with different scan rates. The inset plots the peak current of PtO_x reduction and H adsorption on Pt (~0.12 V) as a function of scan rate, showing a linear relationship.

2.5 XAS

X-ray absorption spectra (XAS) were acquired at the B18 beamline of Diamond Light Source (UK) using a Quick EXAFS mode with a ring energy of 3.0 GeV and an average ring current of 300 mA. The XAS spectra can be measured in transmission using ionization chambers and in fluorescence using a 36-element Ge detector, along with the corresponding foil in the reference channel for energy calibration (Figure 2-7).

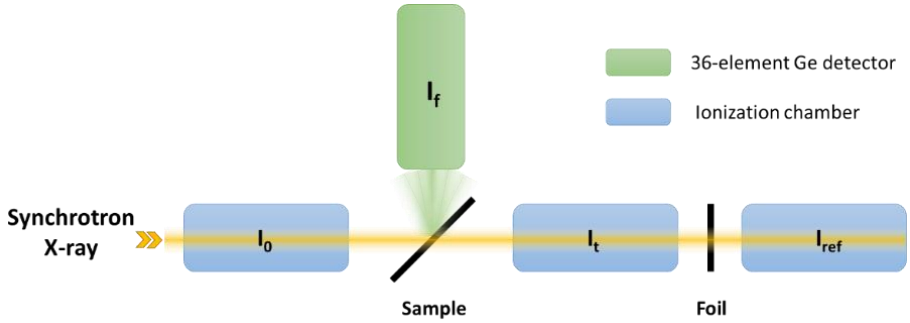

Figure 2-7 Schematic illustration of XAS measurements in transmission and in fluorescence.

2.5.1 *Ex situ* XAS measurements

For *ex situ* measurements, each sample was finely ground and mixed with boron nitride to form a homogeneous mixture, and then compressed into a pellet (~5 ton). For samples intended to be measured in transmission, the edge jump is recommended to be closed to 1 by adjusting the sample mass, whilst maintaining the total absorption less than 2.5. For samples intended to be measured in fluorescence (the calculated edge jump < 0.1), further dilution using boron nitride may be required to avoid self-absorption effects. The pellets were loaded in a 3D-printed rack for samples only to be measured in air, or a leak-tested airtight gas cell (Figure 2-8), which allows the measurements to be conducted in air and in H_2(g). For measurements performed in H_2(g), the air inside the cell was first replaced by flowing N_2 for 30 min **(FIRE RISK, never let Pt nanoparticles meet H_2 and air at the same time)**. Then, the gas was switched to H_2(g) and maintained in constant H_2 flow for 30 min, followed by the closure of the pipes. Following the measurements the cell was once again purged with N_2 prior to opening to air.

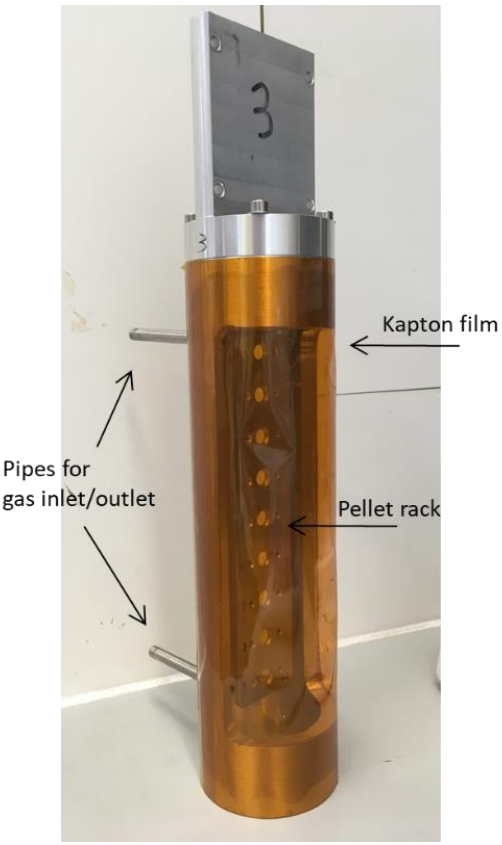

Figure 2-8 The gas cell for XAS measurements in H_2(g), using which XAS spectra in both transmission and fluorescence can be obtained simultaneously. Valves on the pipes are not shown.

2.5.2 *In situ* XAS

XAS spectra as a function of applied potentials were collected using a customized spectro-electrochemistry cell[3] (Figure 2-9). A flattened Au wire was used as the contact to a catalyst-painted electrode, and a Pt coil and a commercial RHE electrode (HydroFlex, Gaskatel GmbH) were used as the counter electrode and the reference electrode, respectively. Before being loaded in the cell, each electrode was flooded by water in a vacuum desiccator. The N_2-purged 1 M $HClO_4$ (TraceSELECT, Honeywell) was circulated through the cell using a peristaltic pump. Using this setup, typical cyclic voltammograms of Pt in acid can be obtained (Figure 2-10).

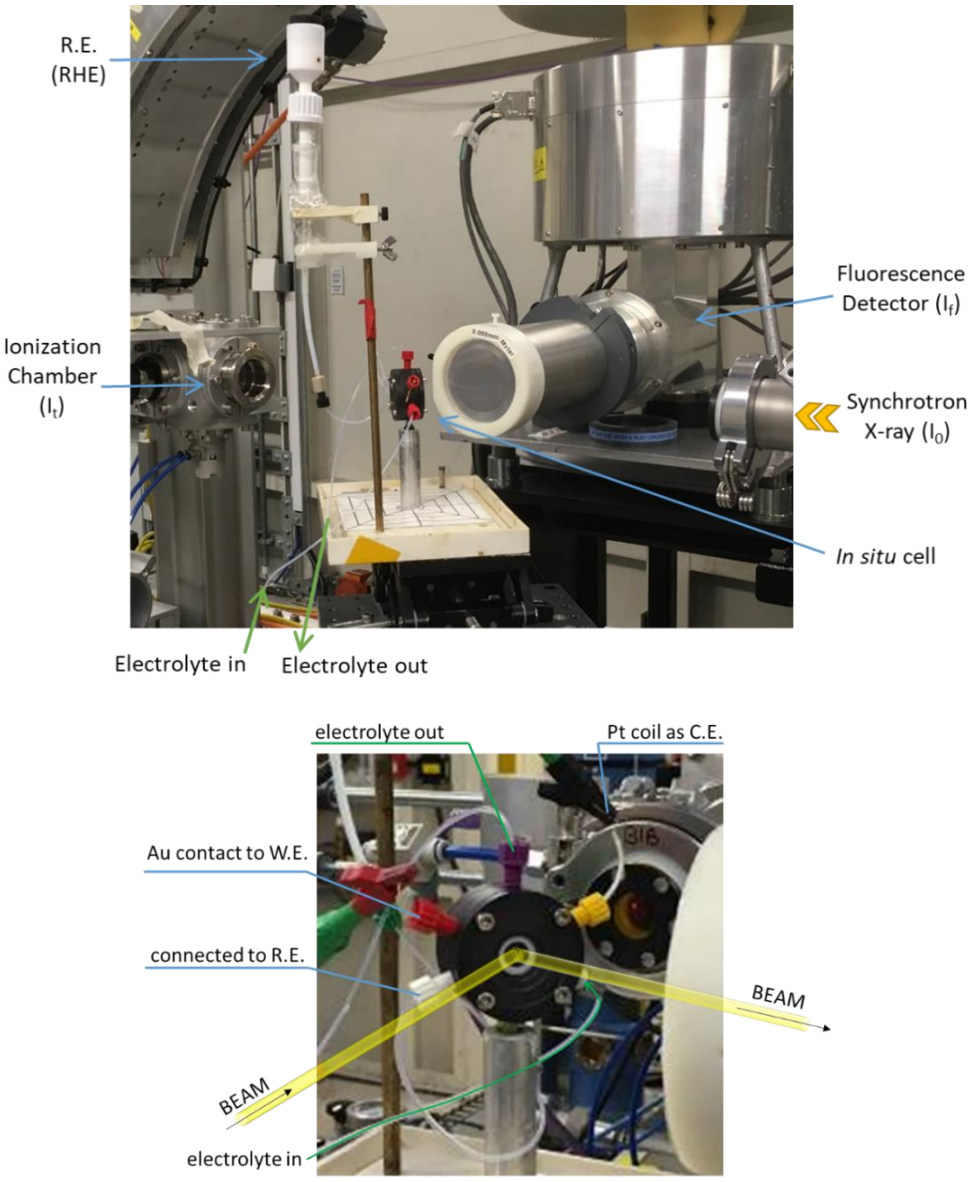

Figure 2-9 (top) The configuration of the *in situ* experiments inside the experimental hub, and (middle) the front view of the *in situ* electrochemistry cell, showing each part of the cell.

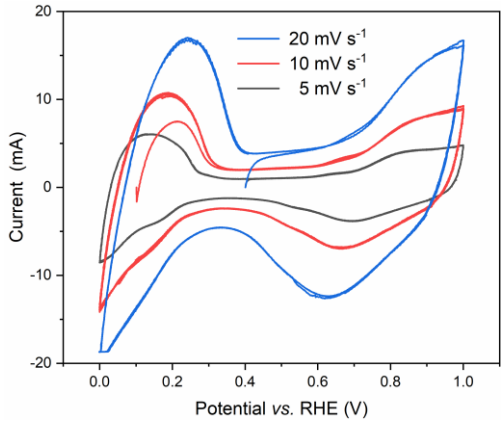

Figure 2-10 Cyclic voltammograms carried out using the *in situ* cell on a carbon paper electrode painted with Pt/C (60 wt%) with a Pt loading of ~0.97 mg_{Pt} cm^{-2} in 1 M $HClO_4$ solution with scan rates of 5, 10 and 20 mV s^{-1}.

2.5.3 Data reduction

The measured XAS spectra, $x \cdot \mu(E)$, were processed to extract X-ray absorption near-edge structure (XANES) spectra and extended X-ray absorption fine structure (EXAFS) spectra using ATHENA in Demeter software package[4]. The data reduction for XANES spectra involves the following steps:

(1) Merge repetition scans: XAS spectra were collected for 3~5 repetitions and merged for better signal-to-noise. Before being merged, the spectrum from each scan, including that of reference foil if available, was compared to make sure that there was no significant change in terms of energy shift and spectral features between scans.

(2) Calibrate energy shifts: The energy shift of each merged spectrum was calibrated using the corresponding reference foil, the E_0 of which was known and provided by ATHENA. The E_0 of both the sample spectrum and the reference spectrum were chosen as the first peak in the derivative, or the zero crossing of the second derivative (Figure 2-11).

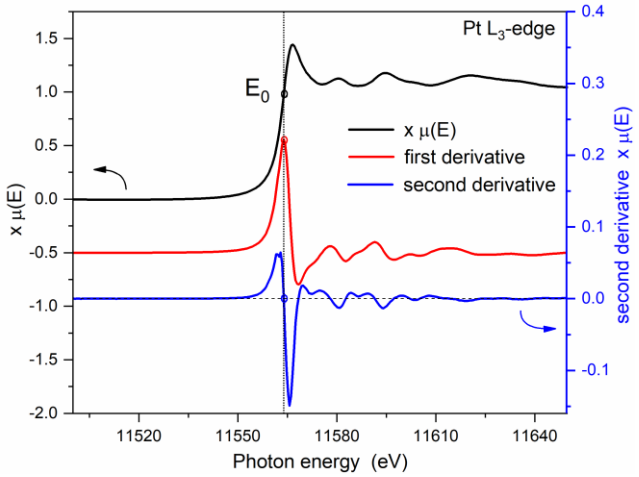

Figure 2-11 XANES spectrum of Pt foil at Pt L_3-edge (black, left y-axis), its derivative (red) and its second derivative (blue, right y-axis), showing the selection of E_0 in these three spectra

(3) Normalization: Normalization transforms the measured XAS spectra (Figure 2-12, top) data to a per-atom basis, regardless of total absorption, sample preparation, instrumental settings and other aspects from measurement. Normalization contains three steps: subtract a pre-edge line, normalize an edge step, $\Delta\mu(E_0)$, and flatten a post-edge line to y = 1 (Figure 2-12). The pre-edge line is the flat part before the rising edge, the post-edge line is generated from a quadratic polynomial regressing all the data selected within a chosen post-edge range (called normalization range in ATHENA), and the edge step, $\Delta\mu(E_0)$, is obtained by subtracting the E_0-crossing of pre-edge line from that of post-edge line.

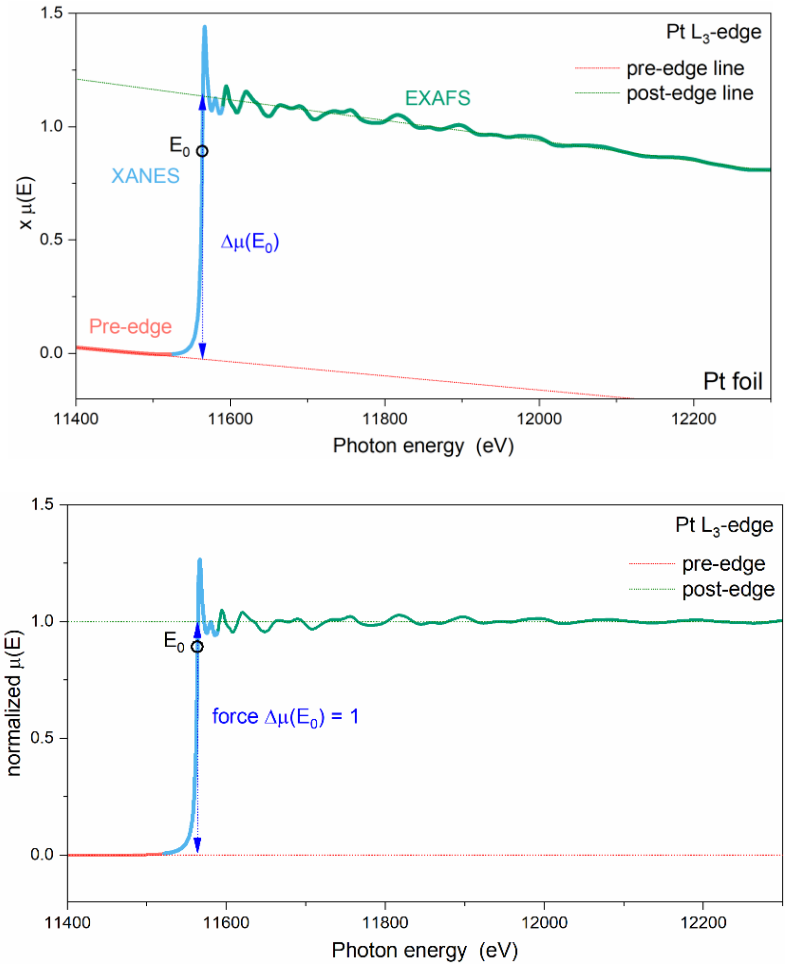

Figure 2-12 An example showing procedures of normalization. (top) A raw spectrum of Pt foil at the Pt L_3 edge, with a pre-edge line, a post-edge line and the resulting edge step, and (bottom) the normalized spectrum.

To obtain an EXAFS spectrum, the oscillation part after the absorption edge, $\chi(E)$, was extracted from the whole absorption spectrum, $\mu(E)$ (Figure 2-13). For a normalized spectrum, $\chi(E)$ and $\mu(E)$ are in relation of:

$$\chi(E) = \mu(E)_{\text{normalized}} - \mu_0(E)_{\text{normalized}} \qquad \text{(Equation 1)}$$

Where $\mu_0(E)$, the absorption of an atom without any neighbouring atoms, is the background of EXAFS spectra. In ATHENA, the background $\mu_0(E)$ is approximated using AUTOBKG algorithm[5], a spline function (a piecewise fourth-order polynomial) with knots equally spaced in *k* space. In AUTOBKG, R_{bkg} is a cutoff parameter to minimize the low frequency component in EXAFS spectra, the reasonable value of which was about half the distance of the first shell peak in *R* space according to the manual of ATHENA. For noisy data, decreasing the upper limit of the spline for several eV is helpful to allow AUTOBKG reasonably follow the end part of the spectra.

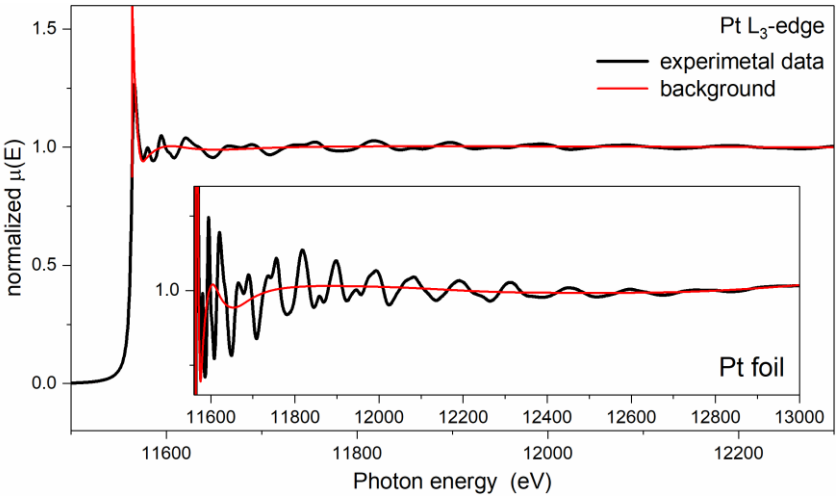

Figure 2-13 A normalised XAS spectrum of Pt foil at Pt L_3-edge, showing a background function following the oscillation part of the data. The inset enlarged the post-edge region.

Then, $\chi(E)$ is converted $\chi(k)$, from energy space (in eV) to k space (in $Å^{-1}$), to spread out the oscillation (Figure 2-14A), using the following relationship

$$k = \sqrt{2m_e(E - E_0)}/\hbar \qquad \text{(Equation 2)}$$

Where m_e is the mass of an electron, and $\hbar$ is the reduce Planck constant. The relation is approximate to

$$E - E_0 \approx 3.810\, k^2 \qquad \text{(Equation 3)}$$

As the amplitude of $\chi(k)$ is attenuated with k (Figure 2-14B), the data are usually multiplied by k, k^2 or k^3 to compensate the dampened undulation at the high k region. The k^n-weighted $\chi(k)$ spectra are usually Fourier-transformed into R space to show the different coordination shells from back-scattering. The Fourier transform is a complex function, interpreting selected $\chi(k)$ region using a magnitude and a phase or, equivalently, using the real part and the imaginary part (Figure 2-15). In this thesis, $\chi(R)$ spectra are mainly presented as the magnitude and the real part.

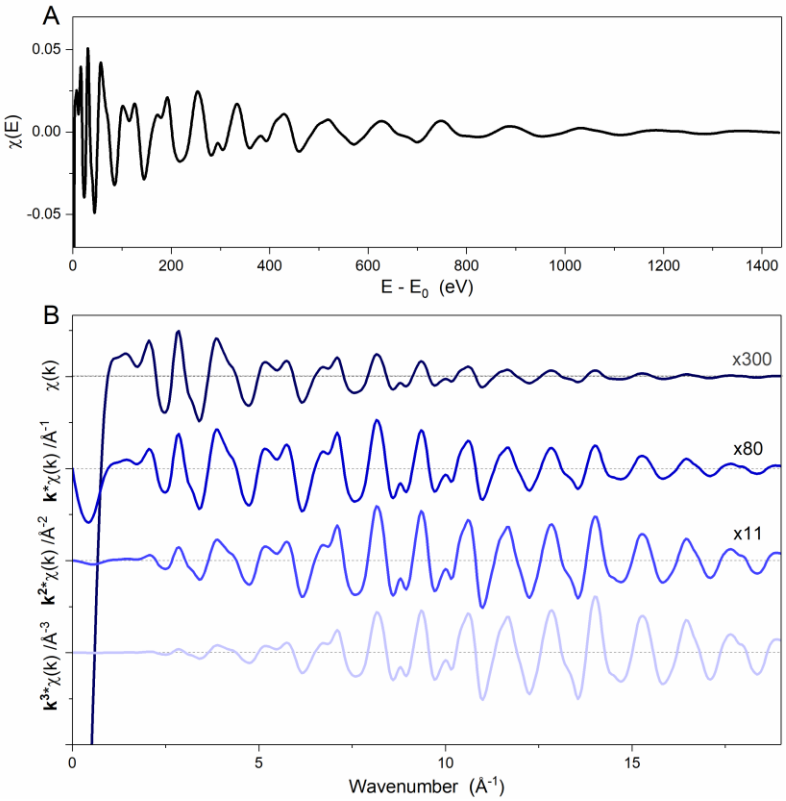

Figure 2-14 (A) The χ(*E*) spectrum of Figure 2-13 after the background removal, and (B) the corresponding χ(*k*) spectra with each k-weight of 0, 1, 2 or 3 (from top to bottom), illustrating the effect of *k*-weighting in plotting χ(*k*) spectra. The amplitudes of χ(*k*) with different *k*-weights are offset and scaled for comparison.

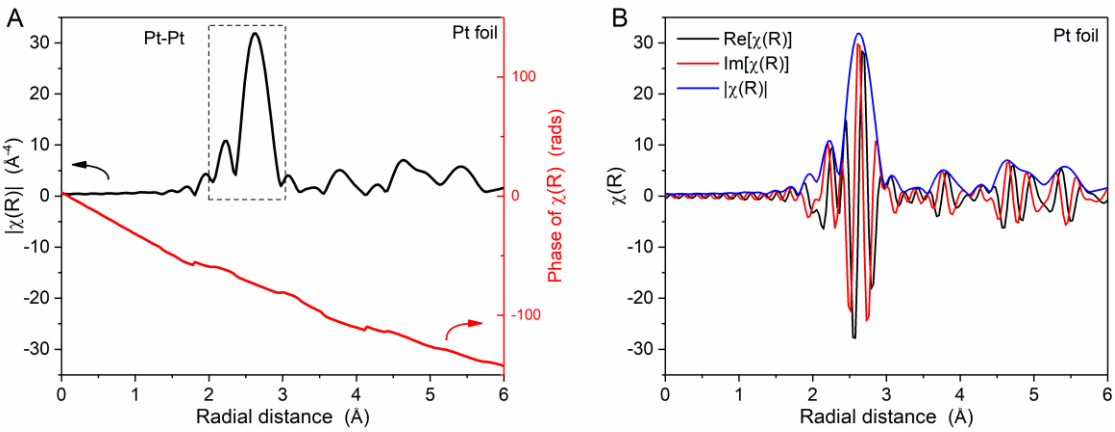

Figure 2-15 k^3-weighted χ(*R*) of Pt foil, plotting (A) as the magnitude, |χ(*R*)|, and the phase of χ(*R*), and (B) as the real part, Re[χ(*R*)], and the imaginary part of χ(*R*), Im[χ(*R*)].

2.5.4 EXAFS analysis

To extract structural parameters from the processed spectra, EXAFS fitting was carried out using ARTEMIS[4]. At the start of the fitting process, an educated guess for the structure of the sample was made to generate a standard EXAFS spectrum using the EXAFS equation (Equation 4),

$$\chi(k) = \sum_i \chi_i(k)$$

$$\chi_i(k) = {S_0}^2 \, N_i \, \frac{F_{eff_i}(k)}{kR_i^2} \, e^{-\frac{2R_i}{\lambda(k)}} \, e^{-2k^2\sigma_i{}^2} \sin\left[2kR_i + \delta_i(k)\right] \qquad \text{(Equation 4)}$$

Where $= \sqrt{2\mathrm{m_e}(E - \mathrm{E_0} - \Delta E_0)}/\hbar$, as in equation 2 and $R_i = R_{i,reff} + \Delta R_i$

$\boldsymbol{F_{eff}(k)}$ is the effective scattering amplitude of the photoelectron, $\boldsymbol{\lambda(k)}$ the mean-free-path of the photoelectron, and $\boldsymbol{\delta(k)}$ the phase shift of the photoelectron, all of which were calculated from the input guess by FEFF6 in ARTEMIS. For a scattering path i, $\boldsymbol{N}$ is the degeneracy, $\boldsymbol{R}$ (in Å) and $\boldsymbol{\Delta E_o}$ (in eV) the differences between the guess in the effective photoelectron half path length and in energy, respectively, σ^2 (in Å^2) for the mean square relative displacement of the *R*, all of which were allowed for small changes during the fitting of the measured data. ${S_0}^2$ is the amplitude reduction factor and considered as transferable within species of an element.

Since *N* and ${S_0}^2$ are highly correlated as shown in the EXAFS equation, ${S_0}^2$ of each element of interest is a prerequisite for EXAFS fitting. In this thesis, Pt foil and SnO_2 were used to obtain the S_0 of Pt and Sn, respectively, because the N of Pt foil and SnO_2 in each scattering path can be obtained from their crystal structure. Take the ${S_0}^2$ of Pt for example. The *N* of each scattering path was transferred from the face-centred cubic (fcc) structure of Pt, and a constrained model based on the symmetry of the fcc structure was used to minimises the number of variables[6] (Figure 2-16 and Table 2-1). The fit yielded a R factor (the goodness of the fit) of 1.6%, and 0.84 ± 0.03 for the S_0 of Pt, which will be used as a known constant, unless stated otherwise. Likewise, the ${S_0}^2$ of Sn was 1.03 ± 0.04, obtained from a two-shell fit of a SnO_2 reference.

Transferring the ${S_0}^2$ of Pt to a first-shell fit of a Pt/C sample yields structural parameters of the Pt nanoparticles (~2 nm, Figure 2-17). Comparison with Pt foil, the Pt nanoparticles show decreased coordination number of Pt-Pt from 12 to ~9.1, decreased bond length of Pt-Pt from ~2.765 Å to 2.756 Å, and increased Debye-Waller factor (disorder term) from ~4.9×10^{-3} Å^2 to ~6.2×10^{-3} Å^2, all of which are expected for Pt nanoparticles.

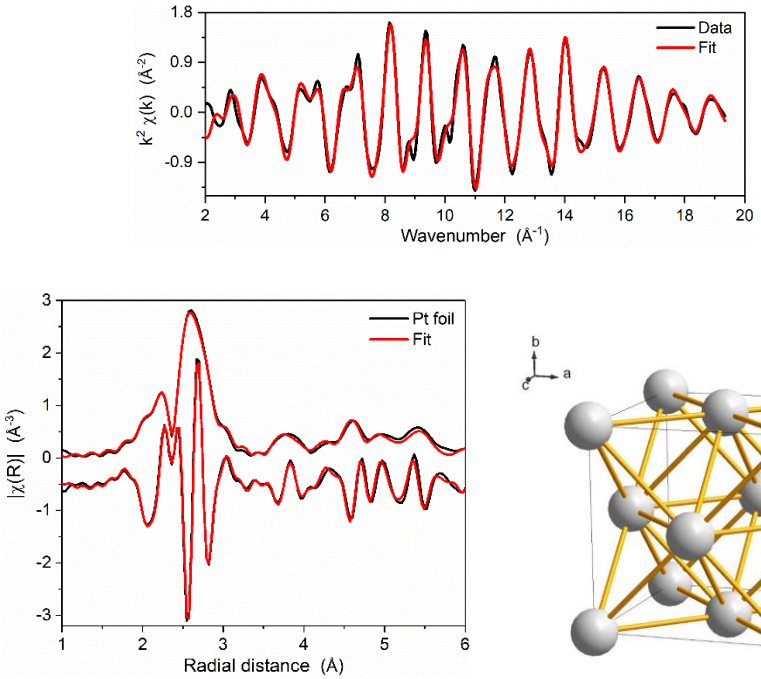

Figure 2-16 A fit of Pt foil to find the S_0^2 of Pt. (top) a k^2-weighted EXAFS spectrum at Pt L_3-edge, (bottom left) its Fourier transform in the magnitude and in the real part (offset by -0.5 $Å^{-3}$ for clarity), and (bottom right) the unit cell of face-centred cubic Pt (ICSD code: 52250) used to generate the input file and the constraints. The Fourier-transformation was carried out over a k range of 3.0–17.0 $Å^{-1}$, and the fit was conducted over a R range of 1.5 – 6.4 Å. The structural parameters obtained are shown in Table 2-2 and Table 2-3.

Table 2-1 Constrains used in fitting the EXAFS spectra of Pt foil (Figure 2-16)[6] to obtain S_0.

Scattering path[1]	**N^2**	**S_0**	**ΔE_0**	**ΔR^2**	**σ^2**
Pt_{abs}-Pt_1-Pt_{abs}	12	amp	enot	α*reff	ss1
Pt_{abs}-Pt_2-Pt_{abs}	6	amp	enot	α*reff	ss2
Pt_{abs}-Pt_1-Pt_1-Pt_{abs} (acute triangle)	48	amp	enot	α*reff	1.5*ss1
Pt_{abs}-Pt_3- Pt_{abs}	24	amp	enot	α*reff	ss3
Pt_{abs}-Pt_1-Pt_1- Pt_{abs} (obtuse triangle)	48	amp	enot	α*reff	ss1+0.5*ss3
Pt_{abs}-Pt_1-Pt_3- Pt_{abs} (obtuse triangle)	96	amp	enot	α*reff	ss1+0.5*ss3
Pt_{abs}-Pt_4- Pt_{abs}	12	amp	enot	α*reff	ss4
Pt_{abs}-Pt_1-Pt_1-Pt_{abs} (non-forward linear)	12	amp	enot	α*reff	2*ss1
Pt_{abs}-Pt_1-Pt_4-Pt_{abs} (forward)	24	amp	enot	α*reff	ss4
Pt_{abs}-Pt_1-Pt_{abs}-Pt_1-Pt_{abs} (forward through absorber)	12	amp	enot	α*reff	2*ss1

Table 2-1 (continued)

Pt_{abs}-Pt_1-Pt_4-Pt_1-Pt_{abs} (double forward)	**12**	**amp**	**enot**	**α*reff**	**ss4**
Pt_{abs}-Pt_1-Pt_3-Pt_1-Pt_{abs} (dog-leg)	48	amp	enot	α*reff	4*ss1
Pt_{abs}-Pt_5-Pt_{abs}	24	amp	enot	α*reff	ss5
Pt_{abs}-Pt_1-Pt_5-Pt_{abs} (obtuse triangle)	48	amp	enot	α*reff	0.5*(ss1+ss2+ss5)
Pt_{abs}-Pt_2-Pt_5-Pt_{abs} (obtuse triangle)	48	amp	enot	α*reff	0.5*(ss1+ss2+ss5)

[1] the subscript represents the shell around the absorbed atom (Pt_{abs})

[2] reff is the half scattering path calculated from the fcc Pt structure (ICSD No. 52250) using Feff.

Table 2-2 The fitting results of Pt foils using constrains listed in Table 2-1.

Parameters	amp	enot	α ($x10^3$)	ss1 ($x10^3$)	ss2 ($x10^3$)	ss3 ($x10^3$)	ss4 ($x10^3$)	ss5 ($x10^3$)	R-factor(%)
Pt/C	0.84(3)	7.2(3)	-3.5(5)	4.9(1)	6.9(8)	7.2(4)	8.4(6)	8.5(1)	1.6

Table 2-3 Structural parameters obtained from EXAFS fit of Pt foil (Figure 2-16) and Pt/C (Figure 2-17)

Sample	Scattering path*	R (Å)	N	σ^2 ($x10^3$ Å^2)	ΔE_0 (eV)	R factor (%)
Pt/C	Pt – Pt_1	2.756(2)	9.1(3)	6.2(2)	6.8(4)	0.25
Pt foil	Pt – Pt_1	2.765(1)	12**	4.9(1)	7.2(3)	1.6

* only the first-shell Pt–Pt scattering path is shown.

** not allowed to vary, to obtain S_0^2.

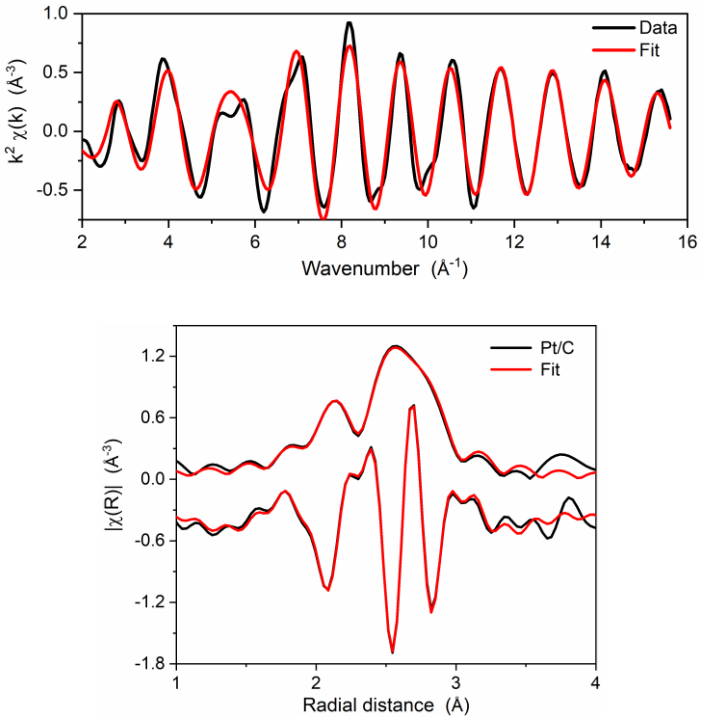

Figure 2-17 A first-shell fit of a Pt/C sample (~2 nm Pt nanoparticles, characterised by TEM and XRD). (Top) a k^2-weighted EXAFS spectrum at Pt L_3-edge, and (bottom) the magnitude and real parts of the Fourier tranform (offset by -0.4 Å^{-3} for clarity). The Fourier transformation was carried out over a k range of 3.6 – 15.0 Å^{-1}, and the fit was conducted over a R range of 1.5 – 3.2 Å. The obtained structural parameters are shown in Table 2-3.

2.6 References

[1] D.A. Shirley, High-Resolution X-Ray Photoemission Spectrum of the Valence Bands of Gold, Phys. Rev. B, 5 (1972) 4709-4714.

[2] M. Łukaszewski, Electrochemical Methods of Real Surface Area Determination of Noble Metal Electrodes – an Overview, Int. J. Electrochem. Sci., 11 (2016) 4442-4469.

[3] A.M. Wise, P.W. Richardson, S.W.T. Price, G. Chouchelamane, L. Calvillo, P.J. Hendra, M.F. Toney, A.E. Russell, Inhibitive effect of Pt on Pd-hydride formation of Pd@Pt core-shell electrocatalysts: An in situ EXAFS and XRD study, Electrochim. Acta, 262 (2018) 27-38.

[4] B. Ravel, M. Newville, ATHENA, ARTEMIS, HEPHAESTUS: data analysis for X-ray absorption spectroscopy using IFEFFIT, J. Synchrotron Radiat., 12 (2005) 537-541.

[5] M. Newville, P. Līviņš, Y. Yacoby, J.J. Rehr, E.A. Stern, Near-edge x-ray-absorption fine structure of Pb: A comparison of theory and experiment, Phys. Rev. B, 47 (1993) 14126-14131.

[6] D.W. Inwood, X-ray and electrochemical studies of bimetallic Pt-based oxygen reduction electrocatalysts, University of Southampton, 2017, pp. 228.

Chapter 3 Effects of heat treatment atmosphere on the structure and activity of Pt_3Sn nanoparticle electrocatalysts: a characterisation case study

3.1 Introduction

PtSn bimetallic nanoparticles (NPs) have attracted considerable attention in fuel cell catalyst research, both as more CO tolerant catalysts for reformate fuelled H_2 PEM fuel cells and as anode catalysts for direct alcohol fuel cells. Fundamental studies have shown that CO oxidation occurs at reduced overpotentials at Sn and SnO_2 (or its hydrated form) modified Pt[1-4] and at Pt_3Sn [5-8] compared to Pt electrodes. Similarly, Sn modified Pt surfaces and Pt_3Sn catalysts have also shown enhanced activity over Pt for methanol[9-11], ethanol[12-15], and butanol[16] oxidation. In each case the nature of the Sn species, SnO_2 or metallic Sn, and the extent of mixing of the Pt and Sn, alloy formation and the resulting Pt:Sn ratio at the surface, may play a role in determining the activities of the electrocatalysts. An understanding of these parameters is important in developing structure-property relationships.

Generally, Pt-Sn bimetallic nanoparticles can be synthesized using the general approach as other bimetallic system, that is, reduction of the Pt and Sn ions[17], where the typical reducing agents can be H_2, borohydride, formic acid and ethylene glycol, and where the reduction can be carried out at the same time or in a stepwise manner[18]. Using this approach, Pt-Sn nanoparticles with different Pt:Sn ratios[15, 19-22] morphologies[23, 24], phases[24-26] and/or configurations[15, 24, 27] can be achieved. However, the simultaneous control of composition and structure is difficult for such nanoparticle bimetallic catalysts. One recent approach has been to take a parent Pt_xSn catalyst with a defined Pt:Sn ratio and then to subject this to heat treatment/annealing under various atmospheres such as air to induce surface oxidation or H_2(g) to cause reduction. Wang et al.[28] prepared a Pt-SnO_x/C catalysts using a polyol method with limited amount of alloyed Sn phase, which was greatly increased by subsequent reduction treatment in 5% H_2/Ar at 250 °C but with obvious particle growth and agglomeration. Godoi et al.[29] controlled the ratios of Sn oxides and alloyed Sn phase of Pt-Sn/C catalysts with nearly identical particle size by heat treatment in either N_2 or pure H_2 atmosphere at a lower temperature than Wang et al. (150 °C). They found that the presence of oxidised Sn has an enhancement effect for ethanol oxidation, which can be further increased by converting the oxide phase into the alloyed phase. Du et al.[27] further investigated the effects of structure (non-alloy and alloy) on the ethanol oxidation activity using a CO_2 microelectrode to monitor CO_2 generation. They prepared non-alloyed Pt-Sn nanoparticles with a SnO_2 shell-rich and Pt core-rich structure, which

can be converted to Pt-Sn intermetallic compounds by annealing at 450 °C in Ar/H_2 flow (cause particle agglomeration), and they found that compared to the intermetallic sample, the non-alloyed sample show the worse kinetics but higher amount of CO_2 generation for ethanol oxidation.

Structural characterisation of Pt_xSn catalysts seeks to determine the extent of alloy formation, any variations in lattice parameters, determine the extent of surface segregation of either of the components, and to identify the presence or absence of a separate SnO_2 phase. Various structural methods such as transmission electron microscopy (TEM), X-ray diffraction (XRD), X-ray photoelectron spectroscopy (XPS), and X-ray absorption spectroscopy (XAS) may each be used, but each will has its own limitations and will, therefore, provide a different perspective.

An often-noted limitation of XRD is that only the crystalline components are observed. The SnO_2 in PtSn bimetallic catalysts are sometimes found to be "XRD amorphous". For example, Colmati *et al*.[22] investigated a range of compositions for Pt_xSn alloy catalysts prepared via formic acid reduction and studied their structures via XRD. The formation of Pt-Sn alloys and extent of alloy formation were suggested by an expanded Pt lattice parameter, and no tin oxides were found. Similarly, Lim et al.[30] prepared Pt_xSn catalysts over a wider range of atomic ratios using borohydride (a much stronger reductant than formic acid) reduction and subsequent hydrothermal treatment. These PtSn NPs exhibited expanded Pt lattice parameters similar to those measured by Colmati *et al.*, implying a similar extent of alloy formation. However, a set of obvious diffraction peaks from SnO_2 were also found by Lim *et al.* over the entire composition range explored. The "XRD amorphous" SnO_2 implied from Colmati's study is not a unique case in the literature and can also be found in studies of Pt-SnO_2 core-shell structures[27] and, more commonly, for catalysts with low Sn content[20, 29, 31].

Kim *et al*.[20] applied XRD, XPS, XANES, and EXAFS to investigate the influence of Sn content in carbon supported Pt_xSn catalysts. Like Colmati's and Lim's studies above, the expansion of the Pt lattice from XRD was found to be proportional to the amount of Sn used in the preparation, indicating alloy formation. In contrast, only oxidised Sn was found in the XPS spectra, and the coordination number of the Pt-Sn scattering path from EXAFS fitting did not vary systematically with composition. Such mismatches between XRD and other techniques were also found in our previous study[15]. We calculated the alloying degree of a Pt_3Sn alloy NPs (3~4 nm) to be ~90% from the lattice parameters according to Vegard's law[32, 33], but XPS and XANES spectra indicated at least 50% Sn atoms are oxidized.

In this chapter, the variation in heat treatment atmosphere approach described above is taken to provide a series of related PtSn catalysts with a nominal composition of Pt_3Sn. A variety of structural characterisation methods were then employed to characterise the resulting nanoparticles and the results compared. The alloy phase and SnO_2 were preliminarily characterised via high-resolution transmission electron microscopy (HRTEM) and conventional XRD. XPS, XANES (X-ray

absorption near edge structure) and EXAFS (extended X-ray absorption fine structure) spectra then were used to acquire additional information regarding the oxidation state and atomic environment, respectively. The CO, methanol, ethanol, and 1-butanol oxidation activities of the catalysts were measured in H_2SO_4 solution. Activity enhancements attributed to alloyed Sn and SnO_2 are then discussed.

3.2 Experimental section

Pt_3Sn nanoparticles were deposited on a carbon support to yield a loading of 20 wt% metals via a conventional polyol method[34, 35]. Vulcan XC-72R carbon black was functionalized by refluxing in nitric acid[36]. 200 mg of the functionalized carbon black was dispersed into 50 ml H_2O/ethylene glycol (1:3 v/v) containing 200 mg sodium hydroxide by 15 min stirring and sonication. To this mixture, 110 mg $H_2PtCl_6 \cdot 6H_2O$ and 16 mg $SnCl_2 \cdot 2H_2O$ were added, followed by stirring for 1 hour and then sonicating for 15 min. The suspension was heated to 160 ℃ in an oil bath and maintained at this temperature for 2 hours. The mixture was then cooled down to room temperature and 50 ml isopropanol was added to precipitate nanoparticles. The catalyst was then collected by centrifuge, washed with 50% ethanol aqueous solution and dried under vacuum at 80 °C. SEM-EDX (FEI XL30 ESEM equipped with UltraDry detector) was used to verify the composition, which was found to be $Pt_{2.43}Sn$, which is close to the nominal ratio of Pt_3Sn. The as-prepared Pt_3Sn/C catalyst was then divided into four parts and three parts were treated by annealing at 250 °C under either air, Ar, or H_2 (5%, balanced with N_2). The three treated samples are denoted as the air, Ar and H_2 samples. A 20 wt% Pt/C reference catalyst, supplied by Johnson Matthey, with an average particle size of ~2.8 nm (by TEM) was used for comparison.

Transmission electron microscopy (TEM) and high-resolution transmission electron microscopy (HRTEM) were performed on a FEI Tecnai 12 at 80 kV and a JEOL JEM 2010 at 200 kV (Bristol University), respectively. Power X-ray diffraction (PXRD) patterns were acquired on a Bruker D2 PHASER diffractometer using Cu K_α radiation (λ=1.5418 Å) at a voltage of 30 kV and a current of 10 mA.

X-ray photoelectron spectra (XPS) were acquired on a Kratos Axis Ultra Hybrid spectrometer (Queen's University Belfast). XPS data deconvolution was performed using XPSPEAK 4.1. The background was corrected using the Shirley method[37] and the percentage of Gaussian contribution in peak shape was fixed in range of 20% to 30%. XPS spectra were calibrated using the C 1s peak associated with adventitious carbon at 284.8 eV. In the Pt 4f spectra, the spin-orbit spitting energy and the ratio of the peak area between Pt $4f_{7/2}$ and $Pt4f_{5/2}$ are constrained to be 3.35 eV and 4:3, respectively. For the Sn 3d spectra, the spin orbit spitting energy and the ratio of the peak area between Sn $3d_{5/2}$ and Sn $3d_{3/2}$ are constrained to be 8.4 eV and 3:2, respectively.

First-shell fitting of the extended X-ray absorption fine structure (EXAFS) was performed in ARTEMIS. The Pt L_3-edge and Sn K-edge spectra of each sample were co-analysed with the half scattering path (R, referred as bond length for a single-scattering path) and mean square relative displacement (σ^2) of Pt-Sn and Sn-Pt first single scattering path ($R_{Pt\text{-}Sn} = R_{Sn\text{-}Pt}$, $\sigma_{Pt\text{-}Sn}^2 = \sigma_{Sn\text{-}Pt}^2$) set to be equal at both edges. Fits were carried out in an R-range of 1.1-3.3 Å at Pt L_3-edge, and 1.1-3.1 Å at Sn K-edge. Values for amplitude reduction factor were determined to be 0.872 for Pt and 1.034 for Sn extracted from fitting the Pt foil and SnO_2 standards, respectively.

The electrochemical measurements were conducted in a standard three-electrode cell connected to PGSTAT12 potentiostat (Metrohm Autolab). A Pt mesh electrode was used as the counter electrode, and a $Hg|Hg_2SO_4$ electrode (MMS) in 1M H_2SO_4 was used as the reference electrode and equipped with a Luggin capillary. The potentials reported here are with respect to the reversible hydrogen electrode (RHE) for convenience. The working electrode was prepared by drop casting 10 μL of catalyst ink on the surface of a glassy carbon electrode (5 mm diameter) and drying at room temperature. The catalyst ink was prepared by dispersing the sample powder, 2 mg cm^{-3}, in a mixture of water, isopropyl alcohol and Nafion solution (5 wt%, Sigma Aldrich) with a volume ratio of 8:2:0.01.

All the electrochemical experiments were performed in O_2-free (N_2 purged) 0.1 mol dm^{-3} H_2SO_4 solution at room temperature. The electrochemical active surface area (ECSA) was measured using CO-stripping cyclic voltammetry. Before the measurement, 20 cycles between 0.05 and 0.8 V *vs.* RHE were performed. High-purity CO (99.9%) was then bubbled through the electrolyte for 20 min while the potential was held at 0.2 V *vs.* RHE. N_2 was then bubbled to remove the free CO in the electrolyte. After that, the potential was swept to 1.0 V *vs.* RHE to oxidize the absorbed CO and then cycled between 0.05 and 1.0 V *vs.* RHE to confirm the complete removal of CO_{ads}. The electrochemical behaviour for alcohol oxidation was evaluated using cyclic voltammetry in 0.1 mol dm^{-3} of the alcohol (methanol, ethanol, or 1-butanol) + 0.1 mol dm^{-3} H_2SO_4 electrolyte. The potential was cycled between 0.1 and 1 V *vs.* RHE for at least 20 cycles, and the peak currents for the 10^{th} cycle were used to compare the activities.

3.3 Results and discussion

3.3.1 TEM and XRD

The morphologies of the heat treated Pt_3Sn catalysts were characterized using TEM (Figure 3-1). The images show good dispersion of the nanoparticles on the carbon support, and that the diameters of nanoparticles show some dependency on the annealing atmosphere: average particle diameters were ~3 nm for the sample annealed under air, ~5 nm for Ar and ~6 nm for H_2. The approximate compositions of these nanoparticles were then measured using the spacing of lattice fringes observed in HRTEM images (top inset of Figure 3-1). The spacing was interpreted in Fourier-transformed

space. The distance from the resulting bright spots to the centre, which is the reciprocal of the spacing, was measured and indexed to possible crystal facets with the help of centrosymmetric rings (bottom inset of Figure 3-1). Whilst the (111) plane and the (200) facet (for the air sample) of face-centric cubic (fcc) Pt or Pt_3Sn alloy are observed in all samples, the (110) facet of rutile SnO_2 was only be found for the Ar and air samples. Pt and the Pt_3Sn alloy have similar crystal structures, which cannot be distinguished from each other in HRTEM images.

The powder XRD for each of the treated catalysts are shown in Figure 3-2. The Pt_3Sn catalysts annealed under different atmospheres show features similar to the fcc structure of platinum, with strong diffraction peaks at ~39°, ~46°, ~67° and ~80°, in agreement with lattice fringes observed in HRTEM images. The XRD pattern of the air annealed sample more closely matches that of Pt standard (JCPDS no. 04-0802) with additional peaks present at ~29° and ~34° attributed to SnO_2. The latter peak is not present in the XRD for the Ar and H_2 annealed samples. The peak positions for the H_2 annealed sample more closely match those of the Pt_3Sn standard (JCPDS no. 35-1360), with the positions of the peaks for the Ar sample lying between those of the air and H_2 annealed samples (inset of Figure 3-2). The lattice parameters were calculated using the peak positions of (220) plane and found to be 3.996 Å for the H_2 annealed sample, 3.971 Å for the Ar sample, and 3.951 for Å for the air sample.

Combining the results from HRTEM images and XRD patterns, the existence of SnO_2 phase is still ambiguous and only clearly confirmed for the air annealed sample. The existence of SnO_2 in the H_2 and Ar annealed samples cannot be excluded, as Sn is relatively dilute (~3 wt%) and amorphous SnO_2, would not be detected in the XRD as previously noted in the introduction.

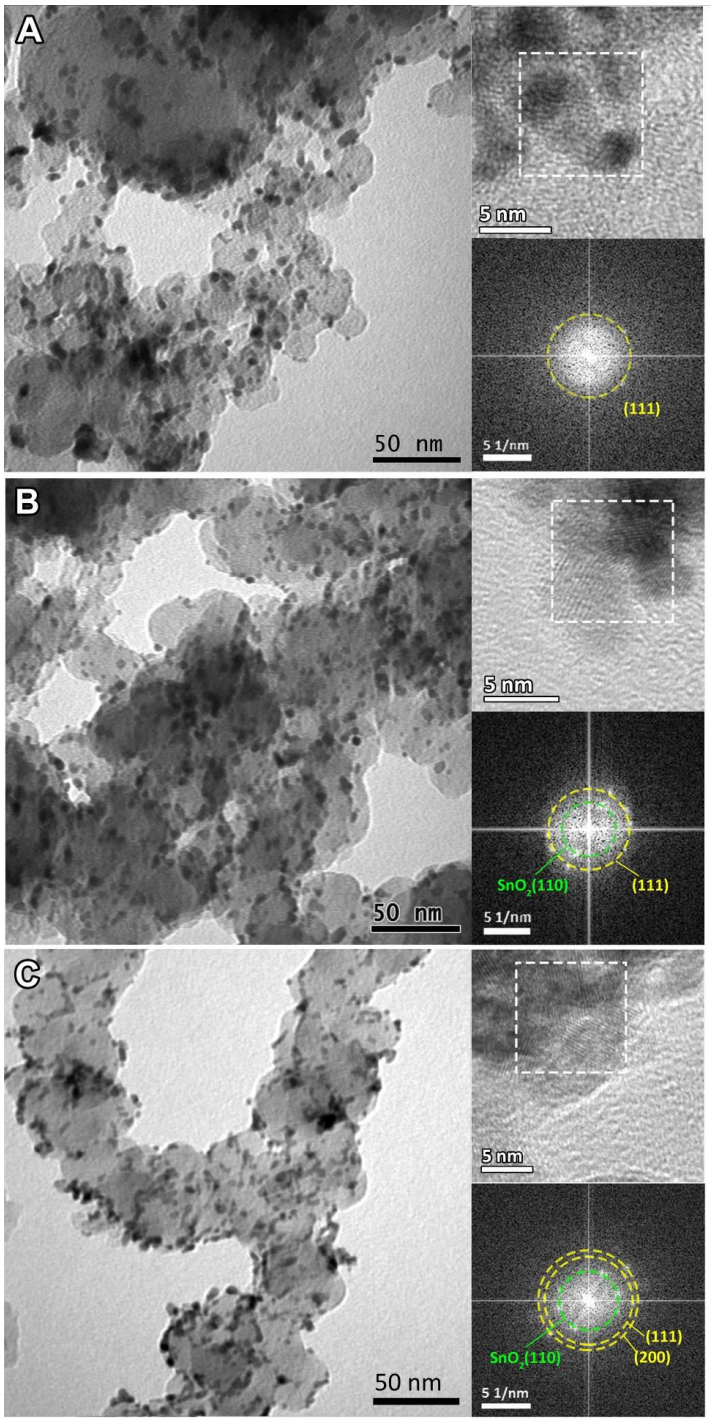

Figure 3-1 TEM images of Pt_3Sn nanoparticles annealed under (A) H_2, (B) Ar and (C) air. The upper insets are the corresponding HRTEM images and the bottom insets are the fast-Fourier transform patterns on the selected area (white dashed square) in the corresponding HRTEM images. The dashed rings are drawn to connect bright spots at the same distance to the centre and represent the lattice fringes of the selected areas.

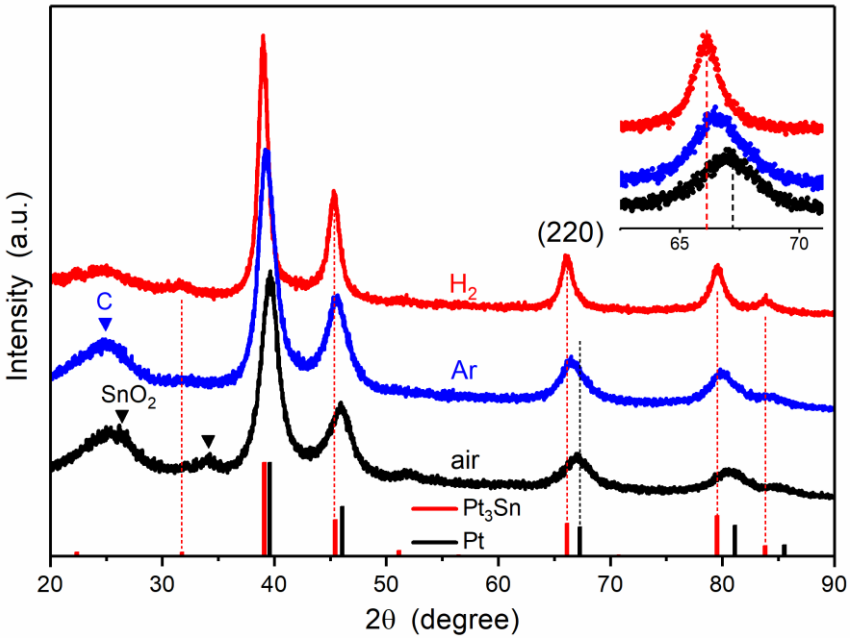

Figure 3-2 XRD patterns of Pt_3Sn nanoparticles annealed under H_2, Ar and air. The inset shows the magnified region of (220) peak. The standard patterns of Pt_3Sn (35-1360) and Pt (04-0802) were obtained from JCPDS database.

3.3.2 XPS

The presence of SnO_2 and speciation of the Sn at the surface of the nanoparticles was further investigated using X-ray photoelectron spectroscopy (XPS). The Sn 3d spectra (Figure 3-3) show two peaks corresponding to Sn $3d_{3/2}$ and Sn $3d_{5/2}$ states. These peaks are deconvoluted into two doublets of Sn^0 (green) and Sn^{IV} (blue) with some constraints (see experimental section), and a peak at the high energy side of Sn $3d_{3/2}$ (red) related to the loss feature of metallic tin. The deconvoluted peaks clearly show that the Sn species present on the surface of the nanoparticles are composed of Sn^{IV} and Sn^0, with the ratio of the species dependent on the annealing conditions. The ratios of the peak areas for Sn^0/Sn^{IV} are summarised in Table 3-1. The large values, 11:1 for the H_2 annealed sample and 2.6:1 for the Ar annealed sample, are likely to be an overestimate of the Sn^0 component due to a combination of the measurement condition and the deconvolution. Ultrahigh vacuum (UHV), in which the XPS measurements were conducted, may cause deoxygenation and reduction of the surface Sn^{IV} species, as these species are amorphous (suggested by XRD, and further analysed in Chapter 6) and may not be stable under UHV[38, 39]. In the data deconvolution Sn^{II} was not included, because the binding energies of Sn^{II} and Sn^{IV} are very similar and the 3d peak does not discriminate between these two peaks adequately. In addition, due to the high heterogeneity of nanoparticles the valence states of the Sn species are probably not as simple as Sn^0, Sn^{II} and Sn^{IV}, and the actual peak shape and peak position of these three valence state are not certain and may vary with samples. Thus, the absolute quantification of Sn species using XPS can produce problematic results, but the relative Sn^0/Sn^{IV} ratios obtained agree with the trend obtained from both the XRD and HRTEM results.

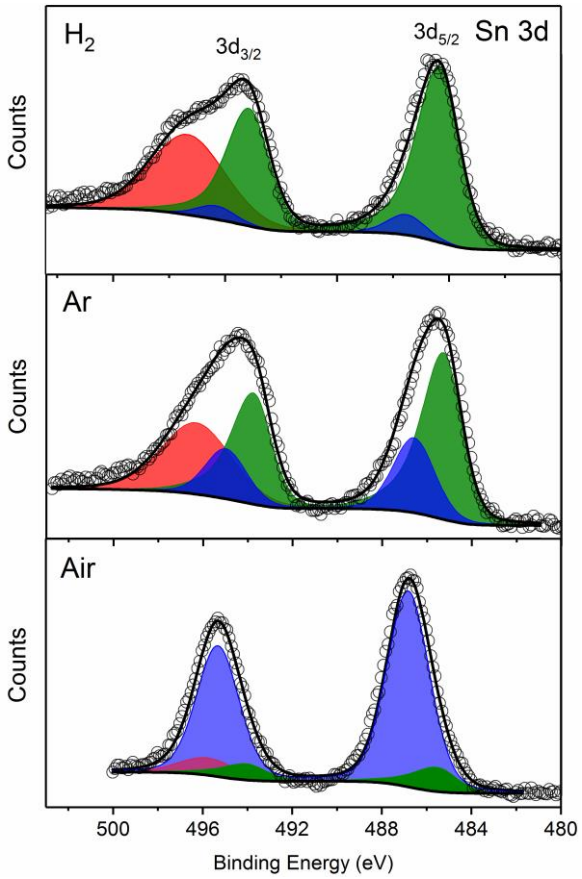

Figure 3-3 Sn 3d XPS spectra of samples synthesized under H_2/N_2, Ar or air. Peak deconvolution shown corresponding to Sn^0 (green), Sn^{IV} (blue), and metallic Sn $3d_{3/2}$ (red).

Table 3-1 Atomic ratios of Sn^0/Sn^{IV} determined by deconvolution of the XPS data (Figure 3-3) and linear combination fitting of the Sn K-edge XANES spectra (Figure 3-4B and C).

Samples	**Sn^0/Sn^{IV} from XPS**	**Sn^0/Sn^{IV} from XANES using Sn foil and SnO_2 as references**	**Sn^0/Sn^{IV} from XANES using Pt_3Sn[a] and SnO_2 as references**
H_2	11	0.54	1.4
Ar	2.6	0.22	0.43
air	0.16	0.08	0.10

[a] the H_2 treated sample collected under H_2

3.3.3 XAS

X-ray absorption near edge structure (XANES) spectra obtained at the Sn K-edge also provide speciation of the Sn, but on a per-atom basis. Figure 3-4A shows the Sn K-edge spectra of the heat treated samples compared to SnO_2 and Sn foil as references. The K-edge represents the transition of Sn 1s electrons to unoccupied 5p orbitals. The different electronic structures of Sn and SnO_2 (Sn^0: $[Kr]5s^25p^2$; Sn^{4+}:$[Kr]5s^05p^0$) are evident as shifts in the energy required to allow the K-edge transition

or edge position and a change in the intensity of the peak at the edge, which is related to the availability of suitable orbitals. The edge position, defined here as the maximum of the first derivative of XANES spectra (inset of Figure 3-4A), for the Ar and air samples are similar to that for SnO_2. The derivative of the XANES spectra for H_2 sample shows a broadened maximum, with a shoulder at lower energy. This suggests that more Sn atoms are alloyed with Pt following annealing in H_2, in agreement with the Pt_3Sn alloy phase detected by XRD. The intensities of the peak at the edge for the heat-treated samples approach that of SnO_2 and follow the order, air > Ar > H_2.

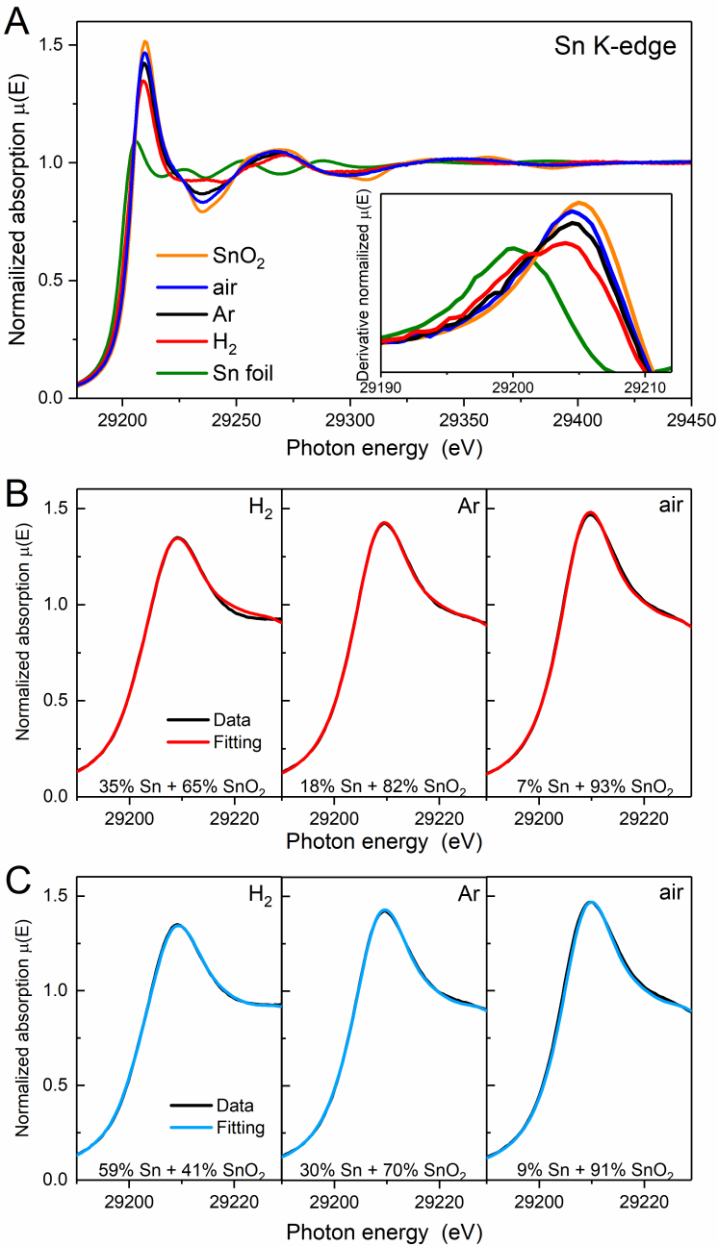

Figure 3-4 (A) XANES spectra and their first derivative (inset of A) of as-prepared samples and references on Sn K-edge. (B and C) linear combination fitting (LCF) of the peak. SnO_2 and (B) Sn foil (red line) or (C) the Sn K-edge spectra of the H_2 treated sample collected under H_2 (cyan line) are used as references for the fittings. The goodness of fit (R-factors) for the fits with Sn foil and Pt_3Sn are H_2 treated 0.9% and 0.08%, Ar treated 0.1% and 0.2%, air treated 0.5% and 0.6%.

The Sn^0/Sn^{IV} atomic ratio can be estimated by XANES linear combination fitting (LCF, Figure 3-4B) using the Sn foil and SnO_2 samples as the reference spectra and the results are shown in Table 3-1. Using Sn foil as the Sn^0 reference spectrum will provide an underestimate of the Sn^0. The electronic structure of Sn in the foil is not the same as in the Pt_3Sn alloy as electron transfer from Sn to Pt in the alloy increase the d-band occupancy of Pt (Pt XANES data not shown) and also will decrease the occupancy of the p-orbitals in Sn. To account for these effects, a second estimate was obtained using the XANES spectrum of the H_2 treated sample, collected in H_2(g) to minimise the contributions of surface oxides, and the results are also shown in Figure 3-4C and Table 3-1. As the Sn K-edge EXAFS data (discussed further below) show the presence of oxygen neighbours, this ratio is likely to be an over-estimate of the Sn^0. The Sn^0/Sn^{IV} ratios obtained from LCF are significantly less than those from XPS deconvolution, especially for the H_2 sample and the Ar sample. This can be attributed to the potential deoxygenation of Sn oxide species under UHV and the intrinsic defects of XPS deconvolution, and the LCF of XANES do not have these problems, as XAS spectra are measured in air and the LCF process is to find out the similarity between the sample spectrum with the reference spectra, containing less arbitrary parameters and uncertainty than the XPS deconvolution. Thus, we believe that the Sn^0/Sn^{IV} ratios obtained from LCF are more reliable than those from XPS.

The EXAFS data at the Pt L_3 and Sn K edges provide further characterisation of the average local coordination environments of each atom in the samples. The spectra and corresponding Fourier transforms are shown in Figure. 3-5 along with the corresponding first shell fits. The spectra were fitted simultaneously at the Sn K-edge and Pt L_3-edge using input parameters from theoretical models (rutile tin oxide and Pt_3Sn for Sn, platinum oxide and Pt_3Sn for Pt). The coordination parameters obtained are shown in (Table 3-2), all with a good R-factors < 2%. Pt-O scattering paths with low coordination numbers are found for all the samples for the spectra collected in air and are attributed to the slight surface oxidation of PtSn bimetallic nanoparticles. Such surface oxidation is confirmed by comparison with spectra collected under H_2 (g).

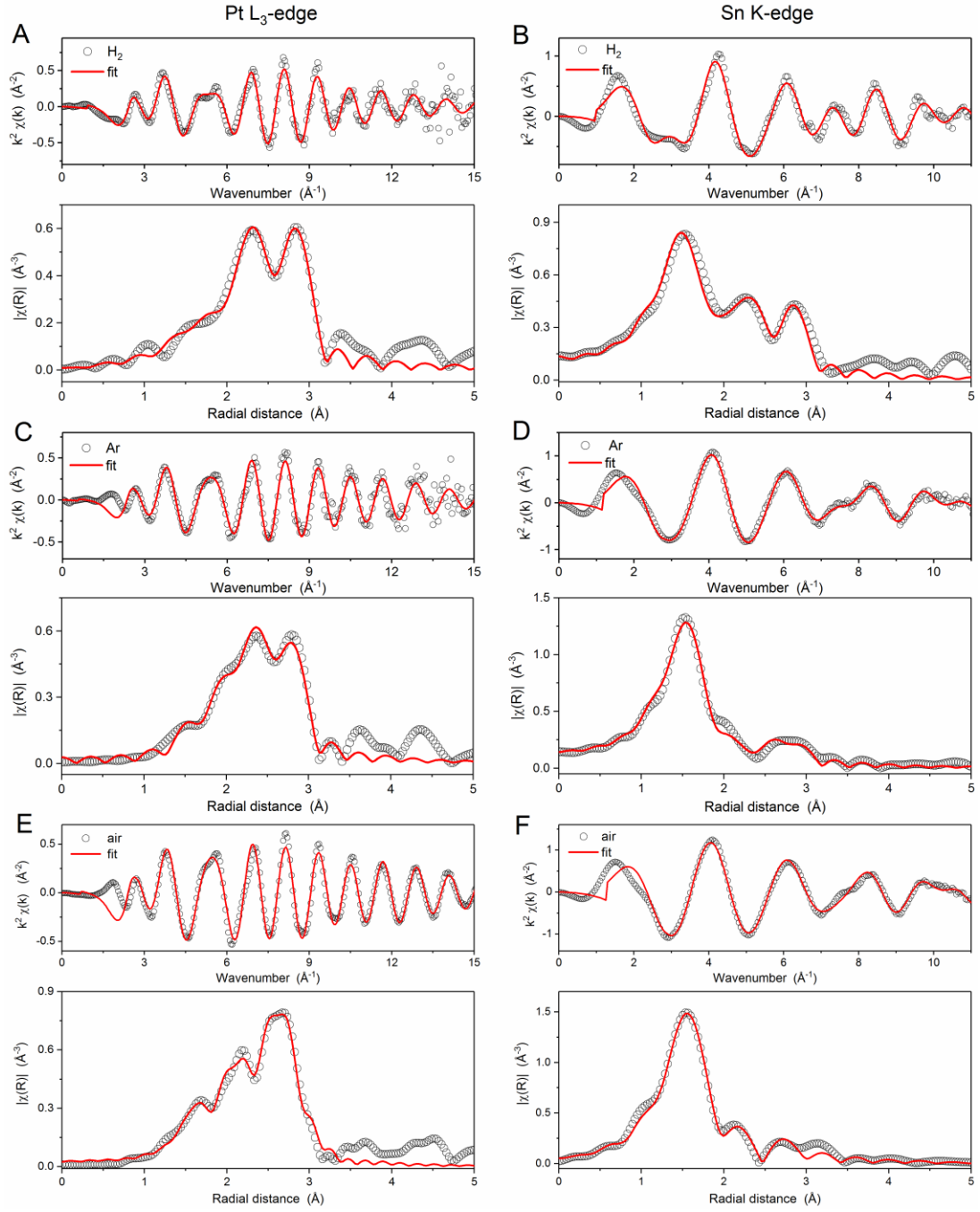

Figure. 3-5 k^2-weighted EXAFS spectra and their Fourier transforms (not phase corrected) of (A and B) Pt_3Sn NPs annealed under H_2, (C and D) Ar, and (E and F) air. Spectra at Pt L_3-edge and Sn K-edge are on the left and right column, respectively. The data points and the fittings are plotted as empty dots and red lines, respectively.

Table 3-2 EXAFS data fitting results of as-prepared samples and Pt foil. All spectra collected as BN pellets in air unless otherwise indicated.

Samples	Shell	N	R(Å)	$\sigma^2 \times 10^2$ (Å)	J_{Pt-Sn} (%)	R-factor (%)
Pt foil	Pt-Pt	12.0	2.764(1)	0.50(1)	N. A.	0.75
H_2 collected in H_2(g)	Pt-Pt	7.8(2)	2.779(2)	0.68(2)	60	0.56
	Pt-Sn	2.0(2)	2.788(5)	1.07(9)		
	Sn-O	1.2(3)	2.03(1)	0.6(4)		
	Sn-Pt	8.1(8)	2.788(5)	1.07(9)		
H_2	Pt-O	0.4(4)	1.99(6)	0(1)	55	1.19
	Pt-Pt	8(2)	2.78(1)	0.9(2)		
	Pt-Sn	1.7(7)	2.812(9)	1.0(1)		
	Sn-O	3.0(3)	2.025(8)	0.7(2)		
	Sn-Pt	6.9(9)	2.812(9)	1.0(1)		
Ar	Pt-O	0.3(3)	1.99(6)	0(1)	15	1.40
	Pt-Pt	8(2)	2.75(1)	0.9(2)		
	Pt-Sn	0.4(6)	2.83(1)	0.7(2)		
	Sn-O	4.5(3)	2.061(8)	0.6(1)		
	Sn-Pt	2.6(7)	2.83(1)	0.7(2)		
air	Pt-O	0.55(9)	1.974(9)	0.3(2)	9	1.11
	Pt-Pt	9.2(6)	2.739(4)	0.99(9)		
	Pt-Sn	0.3(1)	2.856(8)	0.08(8)		
	Sn-O	5.0(4)	2.06(1)	0.5(1)		
	Sn-Pt	0.8(3)	2.856(8)	0.08(8)		

N, the coordination number for the absorber-backscatterer pair; R, the average absorber-backscatterer distance; σ^2,the mean square relative displacement.

3.3.4 Extent of alloying from characterisation methods

Comparison of the parameters obtained from the EXAFS fitting provides further insight into the structure of the nanoparticles and the effects of heat treatment conditions. From the perspective of the coordination numbers (N_{Pt-Sn}, N_{Sn-Pt} and N_{Sn-O}, where the first element represents the edge and the second the neighbouring atom), the H_2 annealed sample shows the lowest N_{Sn-O} (3.0±0.3) and the highest N_{Pt-Sn} and N_{Sn-Pt} (1.7±0.7 and 6.9±0.9) among the Pt-Sn samples, indicating greatest mixing of the Pt and Sn in the H_2 annealed nanoparticles. For the Ar annealed sample and the air annealed

samples, their values in N_{Sn-O}, N_{Pt-Sn} and N_{Sn-Pt} are not significantly different considering the fitting error, but they follow the trend that air > Ar in N_{Sn-O} and Ar > air in N_{Pt-Sn} and N_{Sn-Pt}. From the perspective of the Pt-Pt bond length (R_{Pt-Pt}), a similar trend can also be observed, with the largest value found for the H_2-treated sample (2.78±0.01 Å) and relatively close values for the Ar-treated sample (2.75±0.01 Å) and the air-treated sample (2.739±0.004 Å). As the R_{Pt-Pt} values are expected to increase from 2.77 Å for metallic Pt[40] to 2.83 Å for Pt_3Sn[41], the shorter R_{Pt-Pt} observed for all the heat treated samples, compared to those from Pt and Pt_3Sn, are attributed to effects of the nanoparticle size of the catalysts[42, 43], which is supported by the shorter R_{Pt-Pt} observed for Pt/C (~2.756 Å) than Pt foil (Table 2-3, Chapter 2). These EXAFS results, combined with those from XANES, indicate that heat treatment under H_2 promotes the formation of an alloy, but heat treatment under air leads to de-alloying and phase-segregation of SnO_2. As this chapter is focusing on the extent of alloying, further discussion regarding the configuration of the Pt-Sn nanoparticles and the potential surface segregation due to the annealing in air will be holistically analysed with the XAS data measured in H_2, presented in Chapter 6.

As alloying Sn in Pt lattice forms Pt-Sn bonds (metallic Sn-Sn bonds were not found), the fraction of Sn atoms bonded with Pt can also be used to represent the extent of alloying. Thus, assuming the contents of Pt oxides of the Pt-Sn samples are approximate or negligible, J_{Pt-Sn} values, proposed by Hwang *et al*.[44], were used to quantify the extend of alloying from the perspective of CN.

$$J_{Pt-Sn} = \frac{P_{observed}}{P_{random}} \times 100\% \qquad \text{(eq. 1)}$$

where $P = N_{Pt-Sn}/(N_{Pt-Sn} + N_{Pt-Pt})$, $P_{observed}$ are the results from EXAFS fitting, and P_{random} is the ratio expected for a perfectly alloyed Pt_3Sn particle. The $P_{observed}$ directly represents the fraction of Sn neighbours in the first-shell neighbours of Pt, otherwise we cannot quantify the extents of intermixing using the obtained coordination number or compare them with the value from other techniques or approaches. It should be noted that unlike the original purpose devised from Hwang et al. the use of *J* parameter in this chapter is not intended to study the configuration of bimetallic nanoparticles, and another required parameter J_{Sn-Pt} cannot be obtained due to the interference from the presence of SnO_2 (the content is significantly different in each Pt-Sn sample). As shown in Table 3-2, the alloying degree of as-prepared Pt_3Sn nanoparticles is 9% in the air samples and reaches a maximum of 55% in the H_2-treated sample.

The extent of alloying was then also calculated from the perspective of the each of the other various structural characterisation techniques described above. For the XPS and XANES data the extent of alloying is defined as the fraction of Sn present as Sn^0 from the perspective of oxidation state. For the XRD and EXAFS data the fractional composition of alloyed Sn was obtained from the measured lattice parameters and R_{Pt-Pt} using the Vegard's law, which is widely used to estimate the alloying degree, and then scaled by the actual composition of the catalyst obtained from the EDX analysis, $Pt_{2.43}Sn$. The results of the various calculations are shown in Table 3. Whilst the trend in the extent

of alloying is the same for all of the methods H_2 > Ar > air annealed, the values differ significantly. As we have mentioned above, that the extents of alloying obtained from XPS suffers from the UHV measurement condition and intrinsic defects of data analysis, and those estimated from R and lattice parameters using the Vegard's law may also not be validated. This is because the Vegard's law is only an empirical finding for solid solutions, and the Pt_3Sn phase in our samples is a typical intermetallic compound, in which the arrangement of Pt and Sn is in a specific order rather than random as solid solutions. This suggests that the Vegard's law is not an appropriate approach to quantify the actual extent of alloying from lattice parameters and $R_{Pt\text{-}Pt}$, although it has been used widely in Pt-Sn materials. In contrast, the extents of alloying estimated from LCF and $J_{Pt\text{-}Sn}$ from EXAFS were obtained in a more straightforward way and contain less arbitrary parameters in data analysis, compared to other methods. In addition, the XAS measurements were bulk-sensitive and carried out in the ambient condition. These enable the extent of alloying obtained from LCF and $J_{Pt\text{-}Sn}$ represent better the actual value than other methods and produce similar value, given the error of $J_{Pt\text{-}Sn}$ is estimated roughly as >10 % due to the uncertainty of CN.

Table 3-3 Extent of alloying calculated using the various structural characterisation methods.

Characterisation method	H_2	Ar	air
$J_{Pt\text{-}Sn}$ from EXAFS	55%	15%	9%
XPS	92%	72%	14%
XANES[a]	35-59%	18-30%	7-9%
XRD	68%	41%	19%
EXAFS	79%	31%	12%

[a] using the Sn foil (lower end of range) or Pt_3Sn data (upper end of range) as one of the reference spectra.

3.3.5 CO stripping voltammetry

The effects of the extent of alloying on the electrocatalytic activities of the series of heat treated Pt_3Sn nanoparticles were then investigated taking the oxidation of a monolayer of CO, which is a known contaminant present in H_2(g) produced by reforming hydrocarbons, and methanol, which is the simplest alcohol used as a fuel in direct alcohol fuel cells. The data are compared to those obtained for a 20 wt% Pt/C reference catalyst supplied by Johnson Matthey.

The CO oxidation voltammograms are shown in Figure 3-6. Blocking of the H_{ads} sites and additional current associated with oxidation of the adsorbed CO monolayer are observed for all of the catalysts.

One measure of the enhanced activity of the bimetallic catalysts is the reduction in the onset potential for CO oxidation. This is defined in the data shown as the crossing of the first cycle (red line) with the second cycle (black line). As shown in Figure 3-6, the onset potentials shift dramatically from 0.69 V *vs.* RHE for Pt/C to 0.39 V *vs.* RHE for the air annealed sample, 0.36 V *vs.* RHE for the Ar sample, and 0.35 V *vs.* RHE for the H_2 sample.

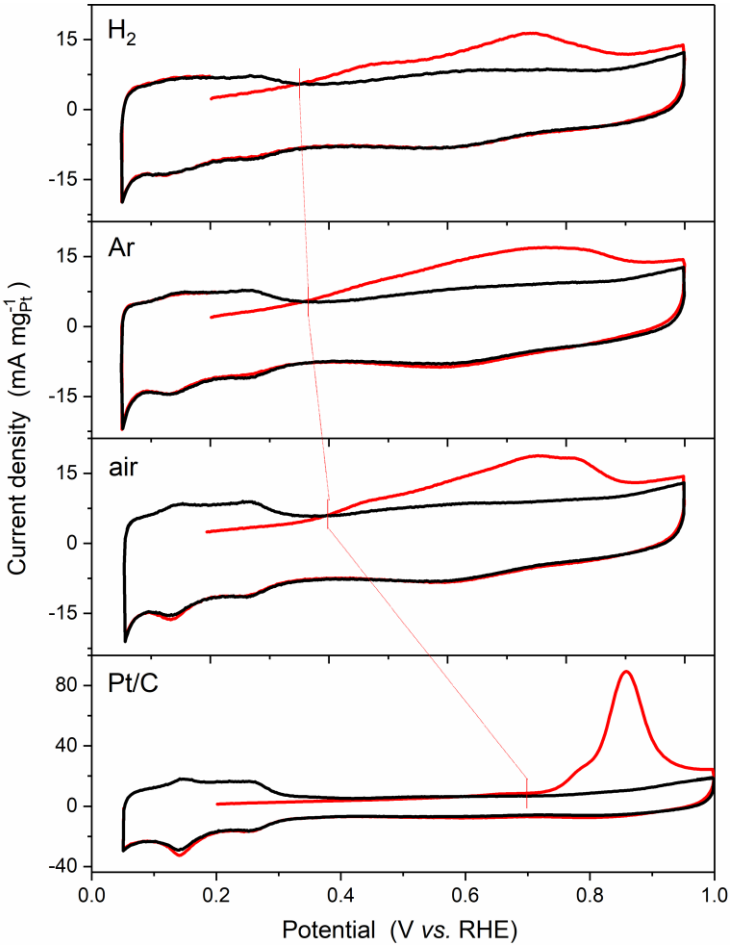

Figure 3-6 CO stripping voltammograms of as-prepared PtSn nanoparticles and commercial Pt/C (20 wt%, JM). A monolayer of CO is absorbed at 0.2 V *vs.* RHE. The first cycles, starting at 0.2 V, are shown in red and the third cycle is shown in black. Measurements were carried out in 1 mol dm^{-3} H_2SO_4 at 25 °C with a scan rate of 20 mV s^{-1}. The onset potentials of CO oxidation as defined in the text are marked by red bars.

The CO stripping voltammograms are commonly used to determine the electrochemically accessible surface areas (ECSA) of Pt based electrocatalysts using a charge density of 420 μC cm_{Pt}^{-2}.[45] Similarly, the ECSA may be calculated from the H_{upd} peaks using a charge density of 210 μC cm_{Pt}^{-2}. The ECSA values obtained using both methods are shown in Table 4 along with the ratio of the two. If the two methods are providing a measurement of the same surface area, the ratio of the two values should be 1 within the error of the measurement, and indeed this is the case for the Pt/C reference catalyst. Significant deviations are observed, however, for all of the PtSn catalysts. The origins of

which are two-fold. Firstly, as shown in Figure 3-6, formation of the alloy results in a decrease in the H_{upd} peaks, which would result in an under estimate of the ECSA. This decrease may be attributed blocking of the H adsorption sites by Sn at the surface of the nanoparticles. Rizo *et al.*[3] have recently shown that each Sn atom adsorbed on the surface of Pt(111) single crystal electrodes blocks the H adsorption sites for three Pt atoms, suggesting that the Sn adsorbs in the three-fold hollow sites on the Pt(111) surface in agreement with previous work[9]. Secondly, CO may either adsorb on the Sn sites on the surface of the nanoparticles or is not blocked at the Pt sites by the formation of the alloy as found for H adsorption. DFT calculations by Zheng *et al.*[46] strongly support the latter, as adsorbed CO was not found to be stable at any of the adsorption sites involving Sn atoms. The smaller ECSA-CO values obtained for all of the PtSn catalysts compared to the Pt/C reference catalyst are attributed to a combination of the larger average size of the nanoparticles and the proportional decrease in the Pt sites on the surface of the catalyst nanoparticles with increased incorporation of Sn.

Table 3-4 Comparison of ECSA calculated from the charge related to CO stripping and Pt-H desorption

Samples	ECSA-CO ($m^2 \cdot g_{Pt}^{-1}$)	ECSA-H ($m^2 \cdot g_{Pt}^{-1}$)	ECSA-CO/ECSA-H
H_2	25.1	7.4	3.4
Ar	26.1	8.4	3.1
air	29.5	12.8	2.3
Pt/C	67.2	60.7	1.1

The broad CO oxidation peaks observed on all the Pt_3Sn catalysts may be compared to the recent study by Rizo *et al.*[3] of Sn modified Pt(111) surfaces, who reported two distinct CO stripping peaks, a pre-peak below 0.5 V vs. RHE and a larger main peak at approximately 0.7 V. They attributed the pre-peak to oxidation of CO adsorbed on Pt with adjacent Sn sites at which water is activated, whilst that at higher potentials to promotion of CO oxidation by OH adsorbed on Sn that are not in direct contact with Pt. Closer examination of the CVs in Figure 3-6 show a more distinct pre-peak between 0.4 and 0.5 V for the H_2 annealed sample. As this sample has the greatest extent of alloying there should be a greater number of Sn sites at which water can be activated adjacent to Pt sites on the surface of the nanoparticles.

3.3.6 Alcohol oxidation

The methanol oxidation activity is similarly evaluated using cyclic voltammetry in 0.1 M methanol with 0.1 M sulfuric acid as electrolyte. The current densities have been normalised to the equivalent

area of Pt using the ECSA-CO values in Table 3-4 in Figure 3-7A and the mass of Pt in Figure 3-7B, representing the specific and Pt mass activities of the catalysts, respectively. The cyclic voltammograms of the heat treated Pt_3Sn NPs share the same features with Pt/C, with oxidation peaks appearing in both the forward sweep and the reverse sweep. Across the potential range of these peaks, the Pt_3Sn NPs, particularly the H_2 sample, show larger specific activities (Figure 3-7A) than that for Pt/C. The specific activity enhancement would appear to be even greater if the ECSA-H values had been used, but we suggest that such a comparison is inappropriate, as H adsorption is unlikely to be a good model of the methanol adsorption sites. In contrast, when the Pt mass activities are compared (Figure 3-7B**)**, only the H_2 annealed sample shows enhanced activity.

The ethanol and butanol specific and mass activities of the Pt_3Sn catalysts are also shown in Figure 3-7 The specific activities of all the catalysts, assessed by comparison of the maximum current density, for ethanol oxidation are approximately half and those for 1-butanol oxidation are approximately one quarter of those observed for methanol oxidation. Only the H_2 annealed catalyst shows enhanced specific activity for ethanol and 1-butanol oxidation compared to that for the Pt/C reference catalyst. When the mass activities are compared, none of the Pt_3Sn catalysts show enhanced current densities at the maximum.

The relative activities of the catalysts for oxidation of the three alcohols may also be assessed by comparison of the onset potential, which is the potential at which the current density starts to increase significantly, with the more active catalyst having the lowest onset potential. This is more difficult to define for the alcohol oxidation CVs than for the case of CO shown above and should only be used to provide a ranking of catalyst activity. No improvement in onset potential with alloy formation is observed for methanol oxidation. A slight improvement, by approximately -0.1 V, is seen for the air annealed catalyst for ethanol oxidation, and all of the Pt_3Sn catalysts show a similar -0.1 V improvement for 1-butanol oxidation.

Enhancements of activity of bimetallic Pt-based catalysts for CO oxidation have long been attributed to a bifunctional effect in which OH adsorbed on Sn provides active O species which facilitate the oxidation of CO adsorbed on Pt sites[47]. The role of this mechanism in the oxidation of small organic molecules was reviewed 30 years ago by Parsons and Van der Noot[48] and more recently for CO and methanol oxidation on Pt-Sn catalysts by Antolini and Gonzalez[49]. The structural characterisation data presented above indicates that a proportion of the Sn is present as SnO_2, with SnO_2 present as a separate phase for the air annealed catalyst. Adsorption of CO and the alcohols requires available Pt sites on the surface of the catalyst nanoparticles, whilst removal of CO and any partial oxidation products of the alcohols requires nearby Sn sites.

For CO oxidation, the lowest onset potential was obtained for the H_2 annealed sample, which has the greatest extent of alloying of the three. As discussed above and in agreement with Rizo *et al*.[3] this result suggests that the onset of the reaction is determined by the availability of Sn atoms at which

water is activated, i.e. those not present as a separate SnO_2 phase, adjacent to Pt atoms on which CO is adsorbed.

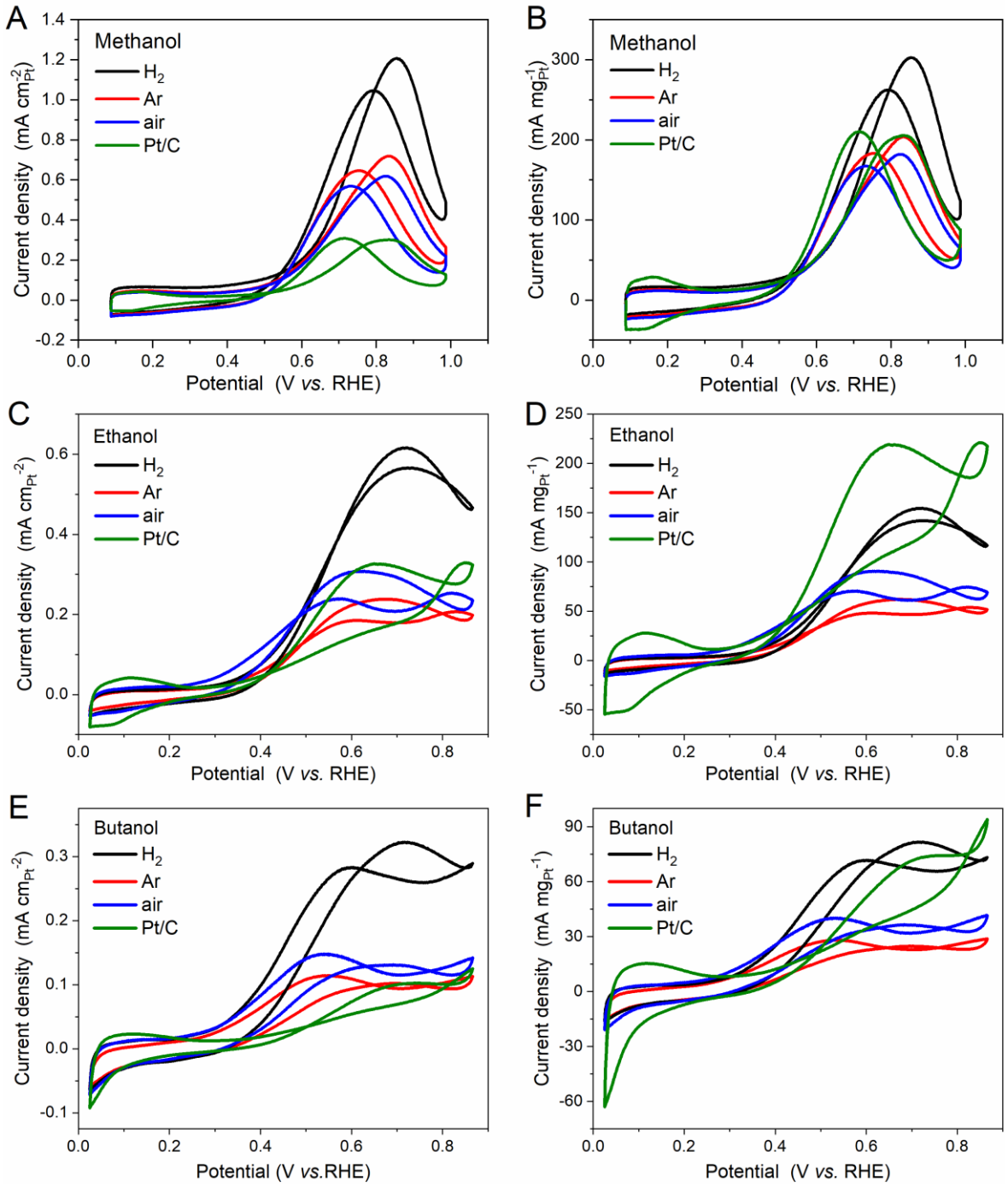

Figure 3-7 Cyclic voltammograms illustrating the specific activities (A, C, and E) and mass activities (B, D, and E) of the heat treated Pt_3Sn catalysts and the commercial Pt/C reference catalyst in 0.1 mol dm^{-3} H_2SO_4 and 0.1 mol dm^{-3} (A and B) methanol, (C and D) ethanol, and (E and F) 1-butanol at 25 °C with a scan rate of 50 mV s^{-1}.

For methanol oxidation, no variation in the onset potential was observed, although the H_2 annealed sample exhibited the largest specific activity. This result is in agreement with those of Haner and Ross[9] for methanol oxidation, who showed enhanced current density at $Pt_3Sn(111)$ compared to

Pt(111), but no shift in the onset or peak potentials, and in contrast to the conclusions of the review by Antolini and Gonzalez, who found that best methanol oxidation catalyst was a mixture of Pt and SnO_2, suggesting that the air annealed sample should have been best. The latter has been interpreted as the need to provide Pt sites for methanol adsorption, whilst minimising facilitating CO oxidation by the availability of active Sn sites. Our results suggest that the active Sn sites need to be associated with the Pt sites of the nanoparticles and are not easily accessible if present as a separate SnO_2 phase.

For ethanol oxidation, the air annealed catalyst exhibited the lowest onset potential, whilst the H_2 annealed sample exhibits the largest specific activity. These results are in good agreement with the previously reported work by Jiang *et al.*[50] who show that the less well alloyed Pt_3Sn catalyst is more active at low current densities or potentials and Godoi *et al.*[29] who show that the oxidation current increases with alloying. This suggests that, as in the case of methanol, a balance must be struck between availability of adsorption site, defining the onset potential, and electronic or bifunctional effects that are important to sustain higher current densities.

Finally, for 1-butanol oxidation, all of the Pt_3Sn catalysts exhibited similar lower onset potentials compared to the Pt/C reference catalyst, suggesting that the availability of either adjacent Sn sites at which water activation takes place or adsorbed OH on non-adjacent Sn sites facilitates the oxidation. The observation that only the H_2 annealed Pt_3Sn catalyst exhibits much increase in the specific activity, suggests that the former is more important in determining 1-butanol oxidation activity.

3.4 Conclusions

Annealing of carbon supported Pt_3Sn nanoparticles under air, Ar and H_2 atmospheres has provided a means of varying the extent of alloying without changing the overall composition of the catalyst. The structures of the nanoparticles were then then characterised using TEM, XRD, XPS, XANES, and EXAFS at both the Pt L_3 and Sn K edges. The extent of alloying was quantified using lattice parameters from XRD, oxidation states from XPS, LCF from XANES, $R_{Pt\text{-}Pt}$ from EXAFS and $J_{Pt\text{-}Sn}$ from EXAFS, and as shown in Table 3-3, the values obtained vary significantly. Oxidation states from XPS may be interfered by the extreme measurement condition (UHV) and the relatively arbitrary but necessary data deconvolution, and the Vegard's law, the empirical relationship between the extent of alloying and lattice parameter (XRD, or $R_{Pt\text{-}Pt}$ from EXAFS), is not applicable of Pt-Sn bimetallic materials. The LCF from XANES and $J_{Pt\text{-}Sn}$ from EXAFS produce similar values and contain less arbitrary parameters in data analysis, and XAS is a bulk technique conducted in the ambient condition. We believe that the extent of alloying from LCF and $J_{Pt\text{-}Sn}$ can better represent the actual value. It should be noted that the trend is the same for each of the methods with the extent of alloying increasing air < Ar < H_2 annealed, in agreement with previously published studies[28, 29, 50], although none of these previous studies of provide as detailed characterisation as reported in this study.

The activity enhancements, compared to the activity of the 20 wt% Pt/C reference catalyst, observed for CO, methanol, ethanol, and 1-butanol oxidation can be understood in terms of the relative effects of active Sn atoms that are close to (alloyed with) the Pt atoms on the surface of the catalyst nanoparticles and other Sn species such as SnO_2. For CO oxidation, the lowest onset potential was observed for the H_2 annealed catalyst, which is also the most well alloyed catalyst, with the smallest fraction of Sn present as SnO_2, supporting the view that water activation at Sn sites provides the enhancement. For methanol oxidation, no shift in onset potential was observed with variation in the extent of alloying, but the enhanced specific activity of the H_2 annealed catalyst once again suggests that the mechanism of enhancement is similar to that for CO oxidation. For ethanol oxidation, the onset potential was lowest for the air annealed catalyst, which has more Pt rich nanoparticles as more of the Sn is present as SnO_2, but the largest specific activity was obtained for the well-alloyed H_2 annealed sample. These conflicting results indicate that a balance must be struck between availability of Pt sites (onset) and active Sn atoms to assist in more complete oxidation. In contrast, for 1-butanol oxidation, the onset potentials of all the heat treated Pt_3Sn catalysts were similar, with only the H_2 annealed sample exhibiting any significant increase in specific activity. This result suggests that, whilst both types of Sn sites enhance activity, as observed for CO, methanol, and ethanol, water activation at Sn atoms adjacent to the Pt atoms on the surface of the catalyst nanoparticles is the dominant enhancement mechanism.

Whilst current results suggest that the activity enhancement of alcohol oxidation is affected by the extent of alloying of Pt-Sn electrocatalysts, it should be noted that alcohol oxidation is complex in terms of mechanism and the products. Even for methanol oxidation, the products can be soluble intermediates, HCHO and HCOOH, adsorbed intermediate CO and the final product CO_2 (direct from methanol or from the intermediates), and the activity represented by current may not means the generation of the desired CO_2. To better establish the structure-performance relationship, online product analysis and *in situ* spectroscopy, such as differential electrochemical mass spectrometer (DEMS) and infrared spectroscopy, are required. In addition, for electrocatalysis, the surface structure under *in situ*/*operando* condition play a more important and direct role in determining the catalytic properties than the general structure. In Chapter 6, the current XAS data will be further analysed and combined with those measured in H_2 to understand the bond length contraction on the Pt-Sn bimetallic surface, and in Chapter 5, an *in situ* and surface sensitive XAS study will be used to investigate the details of the bifunctional mechanism active for CO oxidation.

3.5 References

[1] W.-P. Zhou, W. An, D. Su, R. Palomino, P. Liu, M.G. White, R.R. Adzic, Electrooxidation of Methanol at SnO_x–Pt Interface: A Tunable Activity of Tin Oxide Nanoparticles, J. Phys. Chem. Lett., 3 (2012) 3286-3290.

[2] M.B. de Oliveira, L.P.R. Profeti, P. Olivi, Electrooxidation of methanol on PtM_yO_x (M=Sn, Mo, Os or W) electrodes, Electrochem. Commun., 7 (2005) 703-709.

[3] R. Rizo, E. Pastor, M.T.M. Koper, CO electrooxidation on Sn-modified Pt single crystals in acid media, J. Electroanal. Chem., 800 (2017) 32-38.

[4] B.E. Hayden, M.E. Rendall, O. South, The stability and electro-oxidation of carbon monoxide on model electrocatalysts: Pt(111) – Sn(2×2) and Pt(111) – Sn($\sqrt{3}\times\sqrt{3}$)R30°, J. Mol. Catal. A: Chem., 228 (2005) 55-65.

[5] K. Wang, H.A. Gasteiger, N.M. Markovic, P.N. Ross, On the reaction pathway for methanol and carbon monoxide electrooxidation on Pt-Sn alloy versus Pt-Ru alloy surfaces, Electrochim. Acta, 41 (1996) 2587-2593.

[6] B.E. Hayden, M.E. Rendall, O. South, Electro-oxidation of carbon monoxide on well-ordered Pt(111)/Sn surface alloys, J. Am. Chem. Soc., 125 (2003) 7738-7742.

[7] V.R. Stamenkovic, M. Arenz, C.A. Lucas, M.E. Gallagher, P.N. Ross, N.M. Markovic, Surface chemistry on bimetallic alloy surfaces: adsorption of anions and oxidation of CO on Pt_3Sn(111), J. Am. Chem. Soc., 125 (2003) 2736-2745.

[8] V. Stamenkovic, M. Arenz, B.B. Blizanac, K.J.J. Mayrhofer, P.N. Ross, N.M. Markovic, In situ CO oxidation on well characterized Pt_3Sn(hkl) surfaces: A selective review, Surf. Sci., 576 (2005) 145-157.

[9] A.N. Haner, P.N. Ross, Electrochemical Oxidation of Methanol on Tin-Modified Platinum Single-Crystal Surfaces, J. Phys. Chem., 95 (1991) 3740-3746.

[10] G. Stalnionis, L. Tamašauskaitė-Tamašiūnaitė, V. Pautienienė, Z. Jusys, Modification of a Pt surface by spontaneous Sn deposition for electrocatalytic applications. 2. Oxidation of CO, formaldehyde, formic acid, and methanol, J. Solid State Electrochem., 8 (2004) 900-907.

[11] X. Lu, Z. Deng, C. Guo, W. Wang, S. Wei, S.P. Ng, X. Chen, N. Ding, W. Guo, C.M. Wu, Methanol Oxidation on Pt_3Sn(111) for Direct Methanol Fuel Cells: Methanol Decomposition, ACS Appl. Mater. Interfaces, 8 (2016) 12194-12204.

[12] H. Wang, Z. Jusys, R.J. Behm, Ethanol electro-oxidation on carbon-supported Pt, PtRu and Pt_3Sn catalysts: A quantitative DEMS study, J. Power Sources, 154 (2006) 351-359.

[13] T. Herranz, M. Ibáñez, J.L. Gómez de la Fuente, F.J. Pérez-Alonso, M.A. Peña, A. Cabot, S. Rojas, In Situ Study of Ethanol Electrooxidation on Monodispersed Pt_3Sn Nanoparticles, ChemElectroChem, 1 (2014) 885-895.

[14] A. Velázquez-Palenzuela, F. Centellas, E. Brillas, J.A. Garrido, C. Arias, R.M. Rodríguez, P.-L. Cabot, Sn-modified carbon-supported Pt nanoparticles synthesized using spontaneous deposition as electrocatalysts for direct alcohol fuel cells, Int. J. Hydrogen Energy, 38 (2013) 16418-16426.

[15] L. Calvillo, L. Mendez De Leo, S.J. Thompson, S.W.T. Price, E.J. Calvo, A.E. Russell, In situ determination of the nanostructure effects on the activity, stability and selectivity of Pt-Sn ethanol oxidation catalysts, J. Electroanal. Chem., 819 (2018) 136-144.

[16] V.K. Puthiyapura, D.J. Brett, A.E. Russell, W.F. Lin, C. Hardacre, Biobutanol as Fuel for Direct Alcohol Fuel Cells-Investigation of Sn-Modified Pt Catalyst for Butanol Electro-oxidation, ACS Appl. Mater. Interfaces, 8 (2016) 12859-12870.

[17] K. Loza, M. Heggen, M. Epple, Synthesis, Structure, Properties, and Applications of Bimetallic Nanoparticles of Noble Metals, Adv. Funct. Mater., 30 (2020) 1909260.

[18] E. Antolini, E.R. Gonzalez, Effect of synthesis method and structural characteristics of Pt–Sn fuel cell catalysts on the electro-oxidation of CH_3OH and CH_3CH_2OH in acid medium, Catal. Today, 160 (2011) 28-38.

[19] R. Rizo, D. Sebastián, M.J. Lázaro, E. Pastor, On the design of Pt-Sn efficient catalyst for carbon monoxide and ethanol oxidation in acid and alkaline media, Appl. Catal., B, 200 (2017) 246-254.

[20] J.H. Kim, S.M. Choi, S.H. Nam, M.H. Seo, S.H. Choi, W.B. Kim, Influence of Sn content on PtSn/C catalysts for electrooxidation of C_1–C_3 alcohols: Synthesis, characterization, and electrocatalytic activity, Appl. Catal., B, 82 (2008) 89-102.

[21] J. Asgardi, J.C. Calderón, F. Alcaide, A. Querejeta, L. Calvillo, M.J. Lázaro, G. García, E. Pastor, Carbon monoxide and ethanol oxidation on PtSn supported catalysts: Effect of the nature of the carbon support and Pt:Sn composition, Appl. Catal., B, 168-169 (2015) 33-41.

[22] F. Colmati, E. Antolini, E.R. Gonzalez, Pt–Sn/C electrocatalysts for methanol oxidation synthesized by reduction with formic acid, Electrochim. Acta, 50 (2005) 5496-5503.

[23] Q. Chen, Y. Yang, Z. Cao, Q. Kuang, G. Du, Y. Jiang, Z. Xie, L. Zheng, Excavated Cubic Platinum-Tin Alloy Nanocrystals Constructed from Ultrathin Nanosheets with Enhanced Electrocatalytic Activity, Angew. Chem., Int. Ed., 55 (2016) 9021-9025.

[24] X.D. Wang, L. Altmann, J. Stover, V. Zielasek, M. Baumer, K. Al-Shamery, H. Borchert, J. Parisi, J. Kolny-Olesiak, Pt/Sn Intermetallic, Core/Shell and Alloy Nanoparticles: Colloidal Synthesis and Structural Control, Chem. Mater., 25 (2013) 1400-1407.

[25] D.Y. DeSario, F.J. DiSalvo, Ordered Intermetallic Pt–Sn Nanoparticles: Exploring Ordering Behavior across the Bulk Phase Diagram, Chem. Mater., 26 (2014) 2750-2757.

[26] M. Zhu, G. Sun, Q. Xin, Effect of alloying degree in PtSn catalyst on the catalytic behavior for ethanol electro-oxidation, Electrochim. Acta, 54 (2009) 1511-1518.

[27] W. Du, G. Yang, E. Wong, N.A. Deskins, A.I. Frenkel, D. Su, X. Teng, Platinum-tin oxide core-shell catalysts for efficient electro-oxidation of ethanol, J. Am. Chem. Soc., 136 (2014) 10862-10865.

[28] G. Wang, T. Takeguchi, T. Yamanaka, E.N. Muhamad, M. Mastuda, W. Ueda, Effect of preparation atmosphere of Pt–SnO_x/C catalysts on the catalytic activity for H_2/CO electro-oxidation, Appl. Catal., B, 98 (2010) 86-93.

[29] D.R.M. Godoi, J. Perez, H.M. Villullas, Alloys and oxides on carbon-supported Pt–Sn electrocatalysts for ethanol oxidation, J. Power Sources, 195 (2010) 3394-3401.

[30] D.-H. Lim, D.-H. Choi, W.-D. Lee, H.-I. Lee, A new synthesis of a highly dispersed and CO tolerant PtSn/C electrocatalyst for low-temperature fuel cell; its electrocatalytic activity and long-term durability, Appl. Catal., B, 89 (2009) 484-493.

[31] D.-H. Kwak, Y.-W. Lee, S.-B. Han, E.-T. Hwang, H.-C. Park, M.-C. Kim, K.-W. Park, Ultrasmall PtSn alloy catalyst for ethanol electro-oxidation reaction, J. Power Sources, 275 (2015) 557-562.

[32] L. Vegard, Die konstitution der mischkristalle und die raumfüllung der atome, Zeitschrift für Physik, 5 (1921) 17-26.

[33] L. Vegard, XV. Die Röntgenstrahlen im Dienste der Erforschung der Materie, Zeitschrift für Kristallographie-Crystalline Materials, 67 (1928) 239-259.

[34] B. Liu, Z.W. Chia, Z.Y. Lee, C.H. Cheng, J.Y. Lee, Z.L. Liu, A General Protocol for the Synthesis of Pt-Sn/C Catalysts for the Ethanol Electrooxidation Reaction, Fuel Cells, 12 (2012) 670-676.

[35] C. Bock, C. Paquet, M. Couillard, G.A. Botton, B.R. MacDougall, Size-selected synthesis of PtRu nano-catalysts: reaction and size control mechanism, J. Am. Chem. Soc., 126 (2004) 8028-8037.

[36] A.B.A.A. Nassr, I. Sinev, W. Grünert, M. Bron, PtNi supported on oxygen functionalized carbon nanotubes: In depth structural characterization and activity for methanol electrooxidation, Appl. Catal., B, 142-143 (2013) 849-860.

[37] D.A. Shirley, High-Resolution X-Ray Photoemission Spectrum of the Valence Bands of Gold, Phys. Rev. B, 5 (1972) 4709-4714.

[38] A. Neitzel, G. Kovács, Y. Lykhach, N. Tsud, S.M. Kozlov, T. Skála, M. Vorokhta, V. Matolín, K.M. Neyman, J. Libuda, Steering the formation of supported Pt–Sn nanoalloys by reactive metal–oxide interaction, RSC Adv., 6 (2016) 85688-85697.

[39] L.Y. Kraya, G.F. Liu, X. He, B.E. Koel, Structures and Reactivities of Tin Oxide on Pt(111) Studied by Ambient Pressure X-ray Photoelectron Spectroscopy (APXPS), Top. Catal., 59 (2016) 497-505.

[40] E.A. Owen, E.L. Yates, XLI.Precision measurements of crystal parameters, Philosophical Magazine, Serie 7, 15 (1933) 472-488.

[41] J.S. Charlton, M. Cordey-Hayes, I.R. Harris, A study of the 119Sn mössbauer isomer shifts in some platinum-tin and gold-tin alloys, J. Less-Common Met., 20 (1970) 105-112.

[42] J.T. Miller, A.J. Kropf, Y. Zha, J.R. Regalbuto, L. Delannoy, C. Louis, E. Bus, J.A. van Bokhoven, The effect of gold particle size on AuAu bond length and reactivity toward oxygen in supported catalysts, J. Catal., 240 (2006) 222-234.

[43] J.R. Gallagher, T. Li, H. Zhao, J. Liu, Y. Lei, X. Zhang, Y. Ren, J.W. Elam, R.J. Meyer, R.E. Winans, J.T. Miller, In situ diffraction of highly dispersed supported platinum nanoparticles, Catal. Sci. Technol., 4 (2014) 3053-3063.

[44] B.J. Hwang, L.S. Sarma, J.M. Chen, C.H. Chen, S.C. Shih, G.R. Wang, D.G. Liu, J.F. Lee, M.T. Tang, Structural models and atomic distribution of bimetallic nanoparticles as investigated by X-ray absorption spectroscopy, J. Am. Chem. Soc., 127 (2005) 11140-11145.

[45] Q.-S. Chen, J. Solla-Gullón, S.-G. Sun, J.M. Feliu, The potential of zero total charge of Pt nanoparticles and polycrystalline electrodes with different surface structure: The role of anion adsorption in fundamental electrocatalysis, Electrochim. Acta, 55 (2010) 7982-7994.

[46] J. Zheng, M. Busch, L. Artiglia, T. Skála, J. Rossmeisl, S. Agnoli, A DFT Structural Investigation of New Bimetallic $PtSn_x$ Surface Alloys Formed on the Pt(110) Surface and Their Interaction with Carbon Monoxide, J. Phys. Chem. C, 120 (2016) 25306-25316.

[47] M. Watanabe, M. Shibata, S. Motoo, Electrocatalysis by ad-atoms, J. Electroanal. Chem. Interfacial Electrochem., 187 (1985) 161-174.

[48] R. Parsons, T. Vandernoot, The Oxidation of Small Organic-Molecules - a Survey of Recent Fuel-Cell Related Research, J. Electroanal. Chem., 257 (1988) 9-45.

[49] E. Antolini, E.R. Gonzalez, The electro-oxidation of carbon monoxide, hydrogen/carbon monoxide and methanol in acid medium on Pt-Sn catalysts for low-temperature fuel cells: A comparative review of the effect of Pt-Sn structural characteristics, Electrochim. Acta, 56 (2010) 1-14.

[50] L. Jiang, Z. Zhou, W. Li, W. Zhou, S. Song, H. Li, G. Sun, Q. Xin, Effects of Treatment in Different Atmosphere on Pt_3Sn/C Electrocatalysts for Ethanol Electro-oxidation, Energy Fuels, 18 (2004) 866-871.

Chapter 4 The role of SnO_2 in the bifunctional mechanism of CO oxidation at Pt-SnO_2 electrocatalysts

4.1 Introduction

Carbon monoxide oxidation remains an important reaction in PEM fuel cells, as CO is present as an impurity from reformate gas[1, 2] and a main intermediate from the incomplete oxidation of small fuel molecules (methanol, ethanol, etc.)[3-6]. CO poisons Pt surfaces and thus severely retards the oxidation of fuel molecules[7]. The addition of oxophilic metals, such as Sn, Ru, Mo and W, has been the favoured approach to achieve CO tolerance via the bifunctional mechanism, through which the oxophilic sites provide the adsorbed hydroxide (OH_{ads}) reactant at much lower potential than at Pt[8]. Pt-Ru is the state-of-the-art electrocatalyst for methanol oxidation, as it can decrease the overpotentials required for both methanol oxidation and CO oxidation, ~200 mV compared to those on Pt. However, Pt-Ru still requires ~400 mV overpotential for methanol oxidation and ~500 mV for CO oxidation[9], and Ru is as scarce as Pt on the Earth's crust. It should be noted that it is not appropriate to attribute the promotion effects of Pt-Ru to the bifunctional effect (although many studies do), as the Ru sites and monometallic Ru can co-adsorb CO and oxygenated species that is necessary for CO oxidation [10, 11]. As a contrast, Mo and W promote CO oxidation on Pt via a typical bifunctional mechanism by only providing oxygenated species, with the overpotentials as low as ~200 mV. However, Pt-Mo/W can only oxidatively remove CO in the weakly adsorbed state (~10% out of the total adsorbed CO) [12-15], not improving the CO-tolerance of Pt to a large extent.

Pt-Sn bimetallic electrocatalysts, especially Pt-Sn alloys, stand out for the low overpotential for CO oxidation[16-19], which has been attributed to a combination of the bifunctional mechanism, the electronic/ligand mechanism, through which alloyed Sn atoms alter the electronic properties of Pt and thus weaken the Pt-CO interaction[19-21], and the ensemble mechanism, through which the binding site geometry of CO on Pt is altered because the Pt surface is diluted by CO-inert but hydrophilic Sn atoms[20, 21]. Nevertheless, for practical applications, the instability of the active Pt-Sn alloy surfaces and Sn dissolution narrow the useful upper limit of the potential window to 0.5~0.6 V *vs.* SHE[22-24]. Additionally, the presence of the inactive Sn inhibits C-H bond dissociation in methanol oxidation[25, 26] and lowers the CO_2 selectivity in ethanol oxidation[3, 25, 27, 28].

Pt modified SnO_2, Pt-SnO_2, in which the contributions from the ligand and ensemble effects no longer exist, has been shown to promote the oxidation of CO, and other site blocking intermediates, at low overpotentials via a bifunctional mechanism similar to that for the Pt-Sn alloy[17, 29-31]. Our group[32] reported a study of well characterized Pt-Sn nanoparticles, in which the SnO_2-to-alloyed

Sn ratio was changed by heat treatment in different atmospheres. We found that the onset potential of CO stripping, although increased subtly, is not proportional to the fraction of SnO_2 (~0.39 V for the sample with ~92 at % SnO_2 out of total Sn), implying that both SnO_2 and alloyed Sn may facilitate CO oxidation on Pt. Evidence of this relationship can also be found in other studies of Pt-Sn bimetallic catalysts[33, 34], and the similar activity for CO oxidation was also found on Sn modified Pt nanoparticles, in which Sn was found to exist as SnO_2, which was deposited on Pt using a surface organometallic chemistry method[35] or via borohydride reduction[28]. In addition, phase segregation of Pt-Sn alloys into Pt-Sn^{4+} or Pt-SnO_2 was observed during low temperature CO oxidation in both experimental [36, 37] and theoretical studies[38].

If a bifunctional mechanism is active for Pt-SnO_2 catalysts, a redox couple corresponding to the formation and dissociation of Sn-OH should exist, as Hayden *et al.*[8] found on Pt(111)/Sn surface alloys. Cathro[39] proposed that increased activity of a Pt-Sn catalyst, electrodeposited from a mixed solution of H_2PtCl_6 and $SnCl_4$ at 0.05 V vs. SHE, for C_1 fuel molecules oxidation could be ascribed to the $Sn(OH)_3^+/Sn^{2+}$ couple (0.142 V[40]). On the other hand, Rabis *et al.*[41] showed two irreversible redox couples on a SnO_2 thin film, the presence of which depends the (reducing or oxidizing) synthesis conditions; SnO_2 prepared under reducing conditions at ~0.1 V/~0.4 V and that prepared under oxidising conditions at ~-0.2 V/~-0.3 V. Lim *et al.*[42, 43] reported an irreversible redox couple at ~0.7 V/~0.5 V vs. SHE of partially alloyed PtSn and attributed this to the absorption and desorption of oxygen-containing species of SnO_2. Matsui *et al.z*[44] observed a similar redox couple on a SnO_x supported Pt catalyst.

Although bifunctional effects from SnO_2 are likely to exist and have comparable enhancement for CO oxidation to that of the alloys, the interference from the tiny amount of alloyed Sn may not be innocent and unambiguous evidence of the bifunctional effects is still lacking. Therefore, it is important to ascertain the contribution of the bifunctional mechanism from SnO_2 on an unalloyed Pt-SnO_2 to identify the origin of this mechanism.

To obtain an unalloyed Pt-SnO_2 catalyst, the choice of Sn precursors and reducing condition need to be taken into careful consideration to avoid the formation of the strong Pt-Sn intermetallic bond whilst increasing the intermixing of these two phases. First, the commonly used stannous chloride ($SnCl_2$) should be avoided, because the oxidation state of Sn is not the targeted one, and more importantly because $SnCl_2$ can form a Pt-$SnCl_3$ complex with Pt precursors[45, 46]. Secondly, the reducing agent should be of modest strength, so as to selectively reduce Pt only and should not contain organic residues that complicate the interpretation of results. Considering these two factors, sodium stannate (Na_2SnO_3) and stannic chloride ($SnCl_4$) could be good choices of the Sn precursor, and low temperature reduction in a H_2(g) atmosphere could reduce Pt (hydro)oxides (PtO_x) to metallic Pt leaving the SnO_2 unaltered, given the differences between the standard electrode potentials of Pt, Sn and H, in which the reducing potential of H_2/H^+ (0 V) is much lower than that of $Pt^{II}O$ /Pt or $Pt^{IV}O_2$/Pt (both ~1.0 V) but higher than that of SnO_2/Sn^0 (both ~-0.1 V) [40].

In this work, a Pt-SnO_2 nanoparticle catalyst supported on carbon (Pt-SnO_2/C) is synthesized based on the above considerations. The structure of Pt-SnO_2/C is studied by STEM and XRD, and the absence of alloyed Sn is interrogated by detailed XAS analysis. On Pt-SnO_2/C, CO oxidation at low overpotentials is promoted and capable of proceeding without being poisoned, supporting our hypothesis that bifunctional effects from SnO_2 are active in CO oxidation. Based on these results, it is suggested that the bifunctional mechanism involves Sn-OH species and a Sn^{IV}/Sn^{II} redox couple on the surface of SnO_2.

4.2 Experimental section

4.2.1 Sample preparation

Hexachloroplantic acid ($H_2PtCl_6 \cdot 6H_2O$, 99.999% metals basis) and tin(IV) oxide nanopowder (SnO_2, >99.9%, 8-10 nm) were purchased from Alfa Aesar. The XRD and TEM data of the SnO_2 nanopowder are shown in Figure S4-1. Sodium stannate trihydrate ($Na_2SnO_3 \cdot 3H_2O$, 95%), sodium hydroxide (NaOH, ≥98%) and Nafion perfluorinated resin solution (5 wt%) were purchased from Sigma Aldrich. Vulcan XC-72R carbon and commercial Pt/C (20 wt%) were supplied by Cabot and Johnson Matthey, respectively. High-purity N_2 (≥99.998%), H_2 (≥99.999%), and CO (≥99.9%) were supplied by BOC. All materials were used as received.

100 mg Vulcan XC-72R carbon was dispersed into 200 mL ultrapure water (18.2 MΩ) by sonication for 1 h. To the colloid solution, H_2PtCl_6 solution (~0.2 M), NaOH solution (~0.2 M) at 4 molar equivalent to H_2PtCl_6, and Na_2SnO_3 solution were introduced stepwise with an interval of 5 min sonication and 30 min stirring. The resultant solution was heated under reflux at 90 °C for 1 h, then allowed to settle overnight. The solid product was collected via centrifugation and washed three times with water before being dried under vacuum. The total metal loading (Pt + Sn) on the carbon was controlled to be 20 wt%. Using the same method, PtO_x-SnO_2/C catalysts with nominal Pt/Sn molar ratios of 3/1 and 1/3, as well as PtO_x/C, were synthesized.

PtO_x/C and PtO_x-SnO_2/C were reduced into Pt/C and Pt-SnO_2/C, respectively, by exposure to H_2 (g) at room temperature. The reduction was carried out in an air-tight cell fitted to a flow regulator and gas bubbler (Figure S4-2). N_2, H_2, and N_2 gases (40 mL min^{-1}) were purged through each sample consecutively for 20 min periods. The resultant samples were stored in air-tight vials. **Caution – the reduced sample in H_2 should not be directly exposed to air – fire risk.**

4.2.2 Characterisation

SEM-EDX (FEI XL30 ESEM equipped with an Ultradry detector and JOEL JSM5400 SEM equipped with an Oxford INCA x-sight 7418 EDS probe) and thermogravimetric analysis (Netzch TG209) under 40 mL min^{-1} O_2/Ar were carried out to determine the composition and metal loading

of the as-prepared samples. For our targeted sample Pt-SnO_2/C, the atomic ratio of Pt to Sn, and the loadings of Pt and SnO_2 are 2.62 ± 0.12, ~12.3 wt% and ~4.0 wt%, respectively. The morphology and the size of the deposited metal nanoparticles were imaged using a transmission electron microscope (TEM; FEI, Tecnai T12) at 80 kV. X-ray diffraction (XRD) patterns were obtained using a Bruker D2 Phaser diffractometer with Cu K_α radiation (λ = 1.5418 Å) and a LYNXEYE detector.

X-ray absorption spectra (XAS) were acquired in an airtight gas cell under H_2(g), unless otherwise indicated and for the oxide reference samples, which were measured in air. The multiple-shell EXAFS fitting was carried out on Pt L_3-edge data using a model based on the face-cubic structure of Pt. The same model was applied to a Pt foil spectrum to obtain the amplitude reduction factor of Pt, 0.837. Similarly, the amplitude reduction factor of Sn is 1.034, obtained by a two-shell fit of a SnO_2 reference sample. The Fourier transformation from EXAFS spectra in k-space to those in R-space was conducted over a k-range of 3.0–15.0 $Å^{-1}$ for the Pt L_3-edge and a k-range of 3.5–13.4 $Å^{-1}$ for the Sn K-edge. The spectra in R space, presented in the text, are not phase-corrected.

Electrochemical measurements were performed on a standard three-electrode cell connected to a PGSTAT12 potentiostat (Metrohm Autolab, with a SCANGEN module). A Pt gauze was used as the counter electrode, and a home-made reversible hydrogen electrode (RHE) equipped with a Luggin capillary as the reference electrode. The RHE consists of a Pt gauze electrode over which a slow yet continuous stream of H_2 (g) bubbles were passed, using the same electrolyte as the main cell compartment. The values of potentials in the text are referenced against this RHE, unless stated otherwise.

For powder catalysts, the working electrode was prepared by drop-casting 10 μL of a catalyst ink onto an inverted polished glassy carbon (GC) electrode (5 mm diameter, Pine) and drying at 700 rpm and under an IR lamp (250 W). The catalyst ink was prepared by dispersing 2 mg of each sample into 1 mL isopropanol alcohol (IPA) aqueous solution (20 vol% of IPA). The catalyst inks of Pt/C-SnO_2 physical mixtures were prepared by dispersing SnO_2 into a commercial Pt/C ink whilst maintaining the concentration of Pt/C as 2 mg mL^{-1}. Prior to measurements, the prepared working electrodes were conditioned in N_2-purged 0.1 M $HClO_4$ (Suprapur, Merck) by cycling between 50 mV and 800 mV for at least 10 cycles with a scan rate of 100 mV s^{-1}.

For the CO stripping voltammetry, CO was bubbled into degassed 0.1 M $HClO_4$ for 20 min whilst the potential of the prepared working electrode was held at 0.2 V. Subsequently, N_2 was purged for another 20 min to remove CO from the electrolyte and the potential was then swept to 0.05 V at a scan rate of 20 mV s^{-1} and then cycled between 0.05 V and 1 V for 3 cycles with the same scan rate.

Oxide modified Pt and GC electrodes were also used as working electrodes. Each metal oxide, SnO_2 (8–10 nm, Alfa Aesar), Al_2O_3 (0.05 μm, BUEHLER) or TiO_2 (P25), was loaded onto a Pt electrode (5 mm diameter, Pine) or a polished GC electrode (5mm diameter) using the drop-casting method as described above. Metal oxide suspensions were prepared by sonicating 5 mg of each metal oxide in

1 mL IPA aqueous solution (40 vol% of IPA). Each bare Pt electrode was polished and then conditioned by cycling between 0.05–1.40 V in N_2-purged 0.1 M $HClO_4$ with 200 mV s^{-1} for at least 40 cycles. Before electrochemical measurements, the modified Pt and GC electrodes were conditioned over a narrower potential windows (0.05–1.0 V). The CO stripping voltammetry on the Pt electrodes was carried out at a scan rate of 50 mV s^{-1}.

4.3 Results and discussion

4.3.1 Electron microscopy and microanalysis

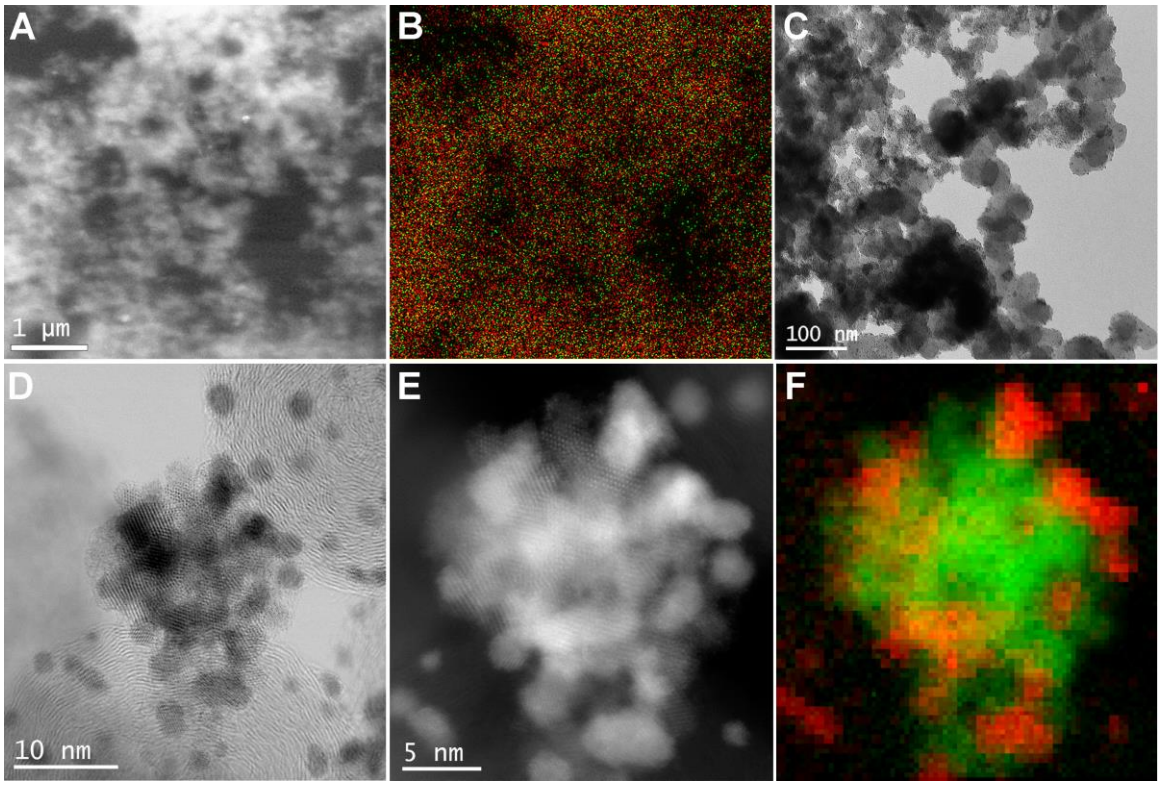

Figure 4-1. Elemental distribution and morphology of Pt-SnO_2/C. (A) A SEM image and (B) the corresponding EDS mapping image of Pt $M_{\alpha 1}$ (red) and Sn $L_{\alpha 1}$ (green). (C) An overview TEM image, (D) BF and (E) HAADF STEM images zooming at a Pt-SnO_2 mixed region, and (E) the corresponding STEM-EELS mapping image using Pt $M_{4,5}$ edge (red), and overlapped edges of Sn $M_{4,5}$ and O K (green). The SEM sample was dropcasted as a thin film on a carbon-coated Cu grid.

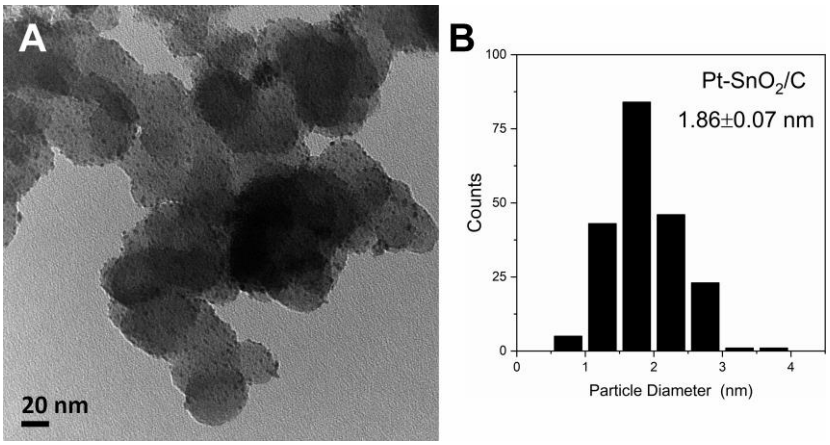

Figure 4-2 A representative TEM image of Pt-SnO_2/C at a low magnification, along with a histogram of particle size distribution.

Elemental distribution and morphology of the as-prepared samples were studied using electron microscopic techniques and the equipped spectroscopies. Figure 4-1A-B show SEM-EDS mapping images of Pt-SnO_2/C, which was deposited as a thin film on a carbon-coated Cu grid to minimize the sample stacking. At this large field of view Sn and Pt atoms are present at the same location, suggesting that on the whole the SnO_2 of Pt-SnO_2/C distributes evenly in the catalyst, rather than forming agglomerates that separate from Pt and carbon. Figure 4-1C-D show representative (S)TEM images of Pt-SnO_2/C with smaller fields of view. The overview TEM image shows that the nanoparticles are uniformly deposited on the carbon support in forms of isolated nanoparticles (~1.9 nm, Figure S4-3) and nanoparticle clusters (~10 nm). The well-dispersed and isolated nanoparticles are found to be pure Pt without detectable Sn and O by STEM-EELS measurements (Figure S4-4 and Figure S4-5), and these particles prevail in the as-prepared Pt/C (Figure S4-6). On nanoparticle clusters of Pt-SnO_2/C, the close-up BF and HAADF STEM images (Figure 4-1D-1E, Figure S4-8 for another region) reveal the nanoparticle clusters are assemblies of nanocrystals with different lattice fringes and contrasts, implying their different identities. With the help of STEM-EELS elemental mapping (Figure 4-1F) and EELS spectra on selected area (Figure S4-7), the nanoparticle clusters are revealed to consist of both Pt and tin oxide nanocrystals with comparable particle sizes and these two types of particles are in intimate contact.

4.3.2 XRD

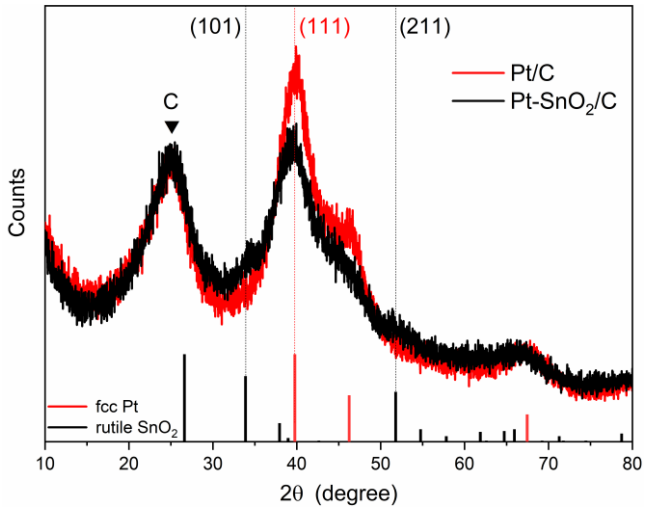

Figure 4-2. XRD patterns of Pt-SnO_2/C and Pt/C powder samples, along with the standard patterns of fcc Pt (JCPDS No. 04-0802) and rutile SnO_2 (JCPDS No. 41-1445). The peak ascribed to the carbon support is indicated. The Pt loading of Pt/C is ~12.6 wt%, and the Pt and SnO_2 loadings of Pt-SnO_2/C are ~12.3 wt% and 4.0 wt%, respectively.

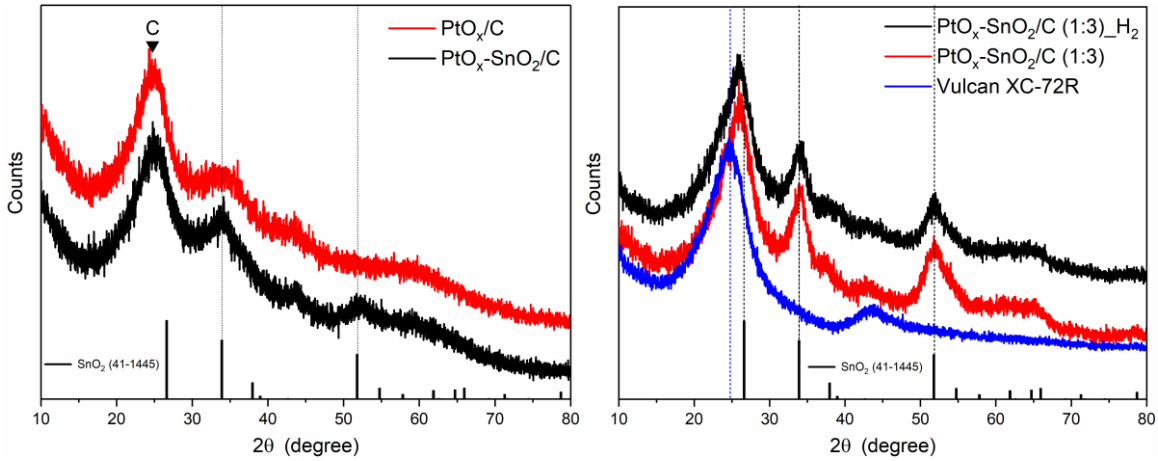

Figure 4-4. XRD patterns of (top) PtO_x/C and PtO_x-SnO_2/C with a nominal Pt-Sn molar ratio of 3:1 and (bottom) of 1:3, along with the standard peak positions of SnO_2 (JCPDS No. 41-1445) as vertical bars. The peaks ascribed to carbon support and SnO_2 is indicated by a blue line and three black dash lines, respectively.

Crystalline phases of the as-prepared samples were also identified using powder XRD. Figure 4-2 shows XRD patterns of Pt-SnO_2/C and Pt/C, along with standard peak positions of face-centred cubic (fcc) Pt and rutile SnO_2 as vertical bars in the diagram. Pt-SnO_2/C shares a largely similar pattern with Pt/C, with a broad diffraction peak (~25°) from Vulcan XC-72R carbon (Figure 4-4) and a set of peaks (~40°, 46° and ~67°) from fcc Pt. The only mismatches found are the weak yet discernible peaks at ~34° and ~52° of Pt-SnO_2/C, which can be indexed to SnO_2(101) and SnO_2(211), respectively. The SnO_2 diffraction peaks are also observed in the precursor of Pt-SnO_2/C before H_2 reduction (Figure 4-4 top), and they become more dominant and more defined when the SnO_2 loading

was increased (Figure 4-4 bottom). Thus, the weak signal of the SnO_2 phase in Pt-SnO_2/C is possibly due to the nanocrystalline nature of the SnO_2 and the low concentration of SnO_2 (~4 wt%), and the presence of crystallized Pt and SnO_2 is in good agreement with STEM microanalysis. Other than those from Pt, SnO_2 and carbon, no extra diffraction peak relating to crystalline Pt_3Sn phases or other Pt-Sn alloys are noticeable, indicating that the crystalline Sn of Pt-SnO_2/C is in the form of SnO_2 rather than alloyed Sn. In addition, from the width of Pt (111) diffraction, Pt crystallite sizes of Pt-SnO_2/C and Pt/C were estimated to be ~1.8 nm and ~2.1 nm, respectively, in good agreement with the particle size from the corresponding TEM images.

4.3.3 XAS analysis

Although no crystalline Pt-Sn alloy, but only SnO_2 is found by XRD, it is too early to assert that no Pt-Sn alloy phase is present. If there were alloyed Sn species, they might be re-oxidized after exposure to air, or their amount may be below the detection limit of XRD. Thus, the speciation of Sn in Pt-SnO_2/C was further characterised from aspects of local coordination environment and oxidation state, by combining XAS data obtained at the Pt L_3 and Sn K edges. For comparison, the spectrum of SnO_2 nanopowder (8–10 nm diameter) is presented, along with those of a Pt-Sn alloy/C from our recent work[32] and the as-prepared Pt/C. The spectra, except those of SnO_2 and foils, were collected in H_2(g) to minimise the contribution of surface oxides on Pt-based nanoparticles and to exclude the possible dealloying of Pt-Sn due to exposure to air.

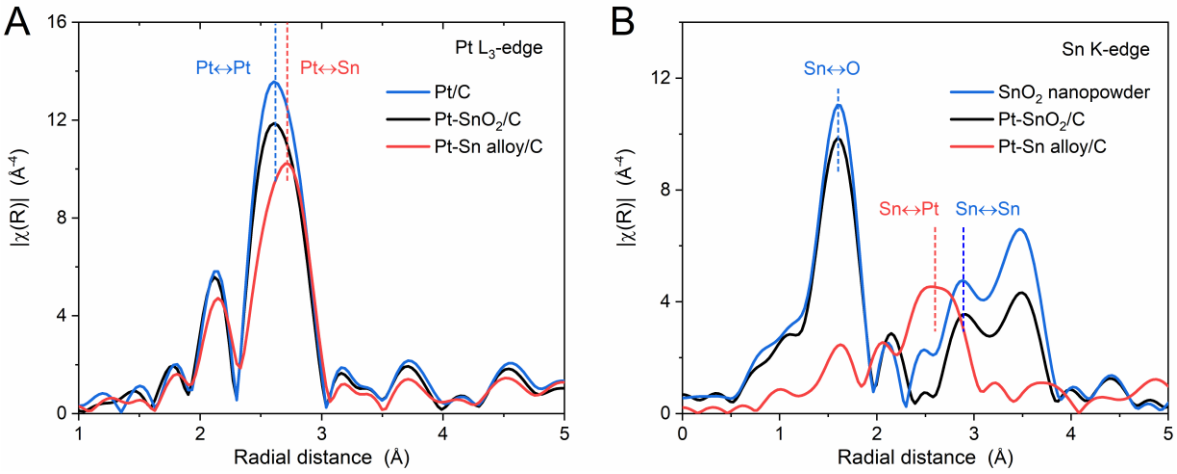

Figure 4-3. Fourier transforms without phase correction of k^3-weighted EXAFS spectra of BN pellets of Pt-SnO_2/C at (A) Pt L_3-edge and (B) Sn K-edge, compared to those of the reference samples, Pt/C at Pt L_3-edge, SnO_2 nanopowder at Sn K-edge and Pt-Sn alloy/C at both edges. The comparison is also shown in both k space and the real part of R space (Figure 4-4). The spectra are measured in H_2(g), except for the SnO_2 nanopowder, which was measured in air.

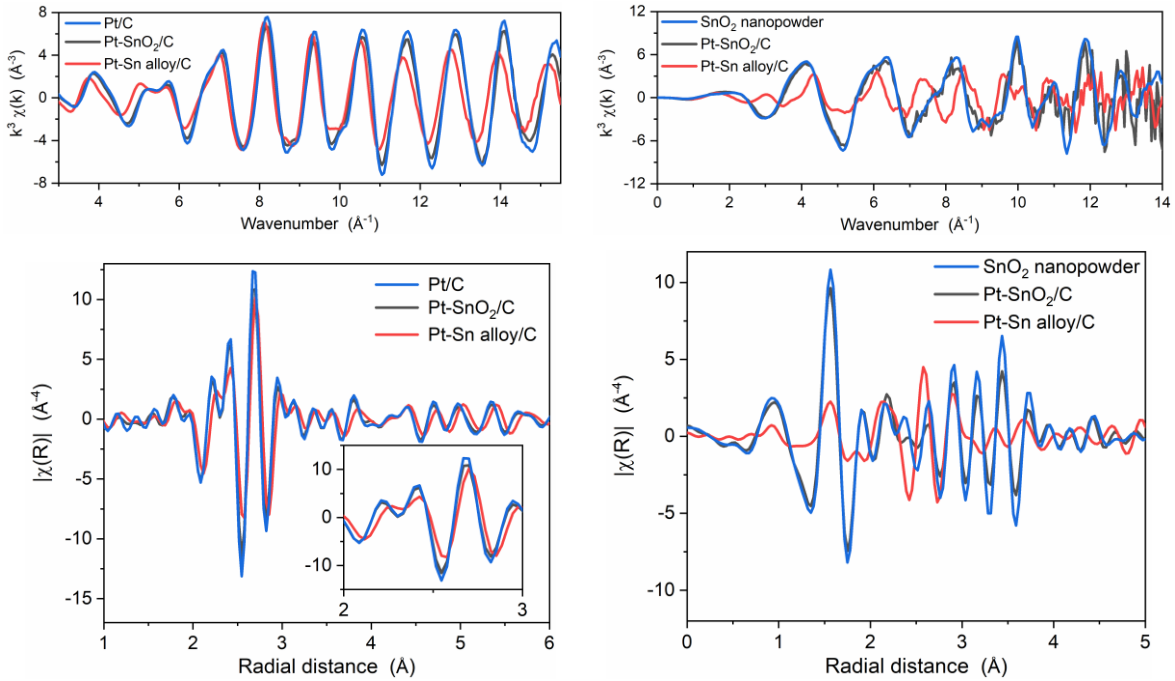

Figure 4-4. (left panels) Comparison of k^3-weighted Pt L_3 edge EXAFS spectra of Pt-SnO_2/C, Pt/C and Pt-Sn alloy/C, and (right panels) comparison of k^3-weighted Sn K edge EXAFS spectra of Pt-SnO_2/C, SnO_2 nanopowder and Pt-Sn alloy/C. The spectra are shown in (top panels) *k* space and (bottom panels) the real part of *R* space, and all spectra were measured in H_2 (g) except for SnO_2 nanopowder.

Figure 4-3A shows Fourier transforms (FTs) of the Pt L_3-edge EXAFS spectra, with the fits of Pt-SnO_2/C and Pt/C in Figure 4-5, and of Pt-Sn alloy/C in Figure 4-7. The structural parameters extracted from the fittings are listed in Table 4-1. The spectrum of the Pt-SnO_2/C follows that of Pt/C well, which is reflected in the k-space and the real part of the R-space plots (Figure 4-4), suggesting a similar Pt coordination environment. Further, quantitative results can be found from the corresponding data fitting. A constrained model that is based on the symmetry of fcc structure of pure Pt to minimises the number of variables in the multiple-shell fitting was used to fit the EXAFS of Pt-SnO_2/C and Pt/C. The fitting model yields good R-factors (<0.7%) and Pt↔Pt distances (R) that are the same within the error of fitting, e.g., 2.754(2) Å vs. 2.756(2) Å. As the fitted values for mean square relative displacement (σ^2) are also similar, the decrease in the magnitude for the Pt-SnO_2 may be attributed to the lower coordination number (CN) of the Pt↔Pt first-shell of the Pt-SnO_2/C (~8.8) compared to that of Pt/C (~9.3), which is consistent with the smaller Pt particle size of Pt-SnO_2/C indicated by the TEM and XRD results presented above. In contrast, for the Pt-Sn alloy/C data (Figure 4-3A), a scattering path with longer scattering distance than Pt↔Pt was found and suggested to be Pt↔Sn scattering by fitting. The CN of the Pt↔Sn (~2.79 Å) is 2.2(2). Due to lattice expansion from the alloying of the larger Sn atom[28, 32], the Pt↔Pt distance (~2.779 Å) is significantly larger than that of Pt/C (~2.756 Å).

The contrast in local coordination environments for Pt-SnO_2/C and Pt-Sn alloy/C is more readily distinguished at the Sn K-edge. Figure 4-3B shows Fourier transforms of the EXAFS spectra at the Sn K-edge, with the corresponding fits to the data for Pt-SnO_2/C in Figure 4-6, for Pt-Sn alloy/C in Figure 4-7 and for SnO_2 in Figure S4-10. The extracted structural parameters are combined with the Pt L_3-edge data are shown in Table 4-1. A unique Sn↔Pt scattering path (~2.79 Å) is dominant the EXAFS of the alloy sample, with a weak contribution of Sn↔O (CN = ~1), whilst Pt-SnO_2/C shares a similar profile to the SnO_2 nanopowder and no scattering path with R close to 2.8 Å can be found or fitted. This contrast suggests that the contribution of alloyed Sn is negligible in the Sn coordination of Pt-SnO_2/C.

Careful examination of the data and corresponding fits reveals that the magnitude of the Fourier transform of the spectrum of Pt-SnO_2/C is lower than that of SnO_2 in two regions, the Sn↔O region (1.0–2.0 Å) and the high R region (2.5–3.8 Å). The lower magnitude in the former region yields a CN of 5.6(3), which is slightly less than the theoretical value of SnO_2 (CN = 6). To ascertain the cause of this decreased CN(Sn↔O), the XAS of Pt-SnO_2/C was also measured in air (Figure S4-11) and found to match that of the SnO_2 reference sample in the first-shell R range, with the fit yielding a CN of 6.1(2), suggesting that the SnO_2 in the as-prepared Pt-SnO_2/C is fully oxidized with a Sn-O_6 first shell coordination, Thus, the above EXAFS results, in combination of the decreased whiteline intensity as compared to SnO_2 (Figure 4-8A), suggest that the lower magnitude of Pt-SnO_2/C is due to the subtle reduction of SnO_2 by H_2 measuring atmosphere.

The lower magnitude of Pt-SnO_2/C in the higher R region than that of SnO_2 is also discussed. This difference is not unique for this sample but can be also observed when the FTs of the two SnO_2 reference samples with different crystallite sizes are compared (Figure S4-11). That for the smaller size gives a smaller magnitude in the high R region but both of them have a first shell Sn↔O with ~6 CN. The inconsistency between Sn↔O region and the high R region then can be rationalized as follows. SnO_2 prepared via wet-chemical methods at low temperature has a surface saturated with hydroxyl and/or water, and the magnitude of Sn↔Sn scattering paths at higher shells are related to the particle size. Additionally, the small crystallite size of SnO_2 in Pt-SnO_2/C is consistent with the nanocrystalline nature observed by STEM (~3 nm). Thus, the mismatches between Pt-SnO_2/C and SnO_2 in the Sn K-edge spectra originate from a combination of the measurement atmosphere and the size of the SnO_2 particles and no evidence of the formation of Sn alloyed with Pt can be found in the as-prepared Pt-SnO_2/C.

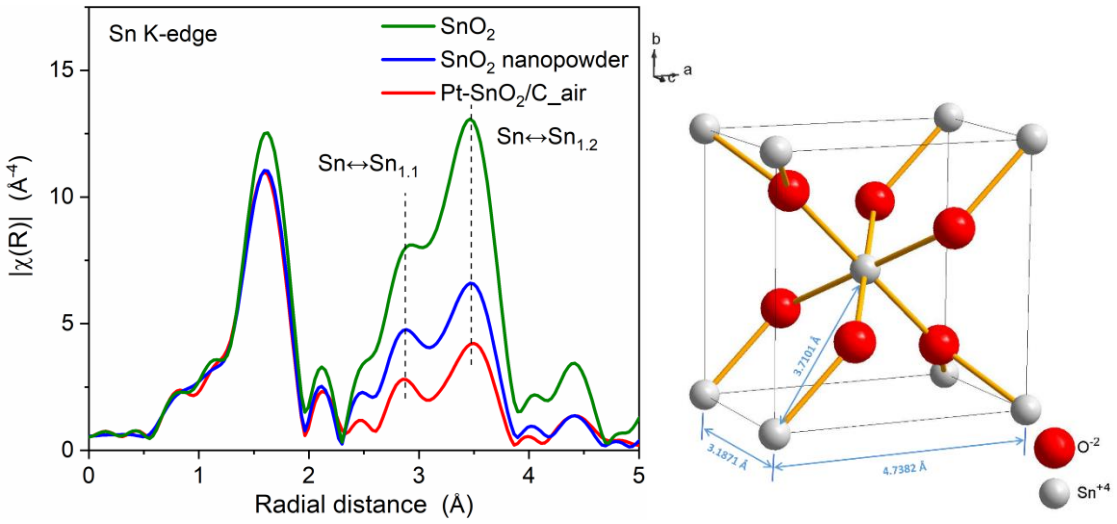

Figure 4-7. (Left) Fourier transforms of Sn K-edge EXAFS spectra of Pt-SnO_2/C (measured in air), SnO_2 nanopowder (8–10 nm, Alfa Aesar) and a SnO_2 reference sample, comparing the size effect of SnO_2 on the intensity of Sn↔$Sn_{1.1}$ (R = 3.1871 Å) and Sn↔$Sn_{1.2}$ single scattering paths (R = 3.7101 Å). (Right) The unit cell of rutile SnO_2 (ICSD No.647469), showing the corresponding Sn↔Sn scattering paths in the crystal structure.

To further confirm that alloyed Sn was not formed in H_2(g), the identity of the reduced SnO_2 of Pt-SnO_2/C is also discussed. Comparing the Fourier transforms of the spectra measured in H_2 and air (Figure S4-12), other than the slightly less intense Sn↔O, a mismatch only exists for R < 2.5 Å, which also does not correspond to any features from Sn↔Pt in the data for the Pt-Sn alloy. Such a mismatch is also present in the residual plot of the fit of Pt-SnO_2/C, in which the scattering paths are generated using rutile SnO_2 (ICSD No.647469) as the input file (Figure S4-13). Thus, the reduced SnO_2 is not likely to exist as alloyed Sn, even in H_2(g). A phase transformation from SnO_2 to SnO can be neglected, as the EXAFS spectra of SnO show significant differences in k space and R space compared to those of Pt-SnO_2/C and SnO_2 (Figure S4-14). We suggest that the reduced SnO_2 is from surface oxygen vacancies on SnO_2, in which oxygen containing ligands were partly depleted by H_2. This suggestion is consistent with the surface composition and structure of SnO_2, in which low index SnO_2 surfaces under reducing conditions tend to lose surface lattice oxygen and relax into Sn^{II} state termination[47]. One may notice that this surface Sn^{II} can be easily oxidized under ambient conditions, as shown in the EXAFS data obtained in air. This dual valency gives us the first indication that a redox couple may exist on the SnO_2 surface. The existence of this redox couple is also found in the electrochemical response described below, and is key to the bifunctional mechanism for CO oxidation on Pt.

Table 4-1. Structural parameters of Pt-SnO_2/C, Pt-SnO_2/C_air (Pt-SnO_2/C measured in air), Pt-Sn alloy/C, Pt/C, SnO_2 nanopowder and Pt foil, obtained from EXAFS fitting. A double dataset fitting was conducted on Pt-Sn alloy/C because a pair of scattering paths between Pt and Sn (Pt↔Sn and Sn↔Pt) were founded in each edge.

Sample	Edge [a]	Scattering path*	R (Å) [b]	N [c]	σ^2 (x10^3 Å^2)[d]	ΔE_0 (eV)	R factor (%)
Pt-SnO_2/C	Pt L_3	Pt↔Pt	2.754(2)	8.8(3)	6.5(2)	5.6(4)	0.68
	Sn K	Sn↔O	2.054(7)	5.6(3)	4.3(8)	5(1)	1.2
		Sn↔Sn	3.21(2)	2(1)	7(3)		
Pt-SnO_2/C_air	Sn K	Sn↔O	2.052(4)	6.1(2)	4.2(5)	4.2(6)	0.4
		Sn↔Sn	3.21(1)	1.6(7)	6(2)		
Pt-Sn alloy/C	Pt L_3	Pt↔Pt	2.779(1)	8.2(2)	6.9(1)	4.9(2)	0.88
		Pt↔Sn	2.788(5) [e]	2.2(2)	12(1) [e]		
	Sn K	Sn↔O	2.02(3)	1(1)	4(8)	3(1)	
		Sn↔Pt	2.788(5) [e]	9(2)	12(1) [e]		
Pt/C	Pt L_3	Pt↔Pt	2.756(2)	9.3(3)	6.2(2)	6.8(3)	0.57
SnO_2	Sn K	Sn↔O	2.055(4)	6.0(2)	4.0(5)	4.2(6)	0.33
		Sn↔Sn	3.201(7)	1.2(5)	2(2)		
Pt foil [f]	Pt L_3	Pt↔Pt	2.765(1)	12	4.9(1)	7.2(3)	1.6

[a] For the Pt L_3-edge data, only the first coordination shell is presented;

[b] R, the average distance of absorber↔backscatter pair scattering; [c] N, the coordination number of the scattering; [d] σ^2, the mean square relative displacement of the R.

[e] For Pt-Sn alloy/C data, Pt↔Sn and Pt↔Sn scatterings were constrained to have an equal R and σ^2;

[f] The coordination numbers of different shells were kept the same as the theoretical model (ICSD No. 52250).

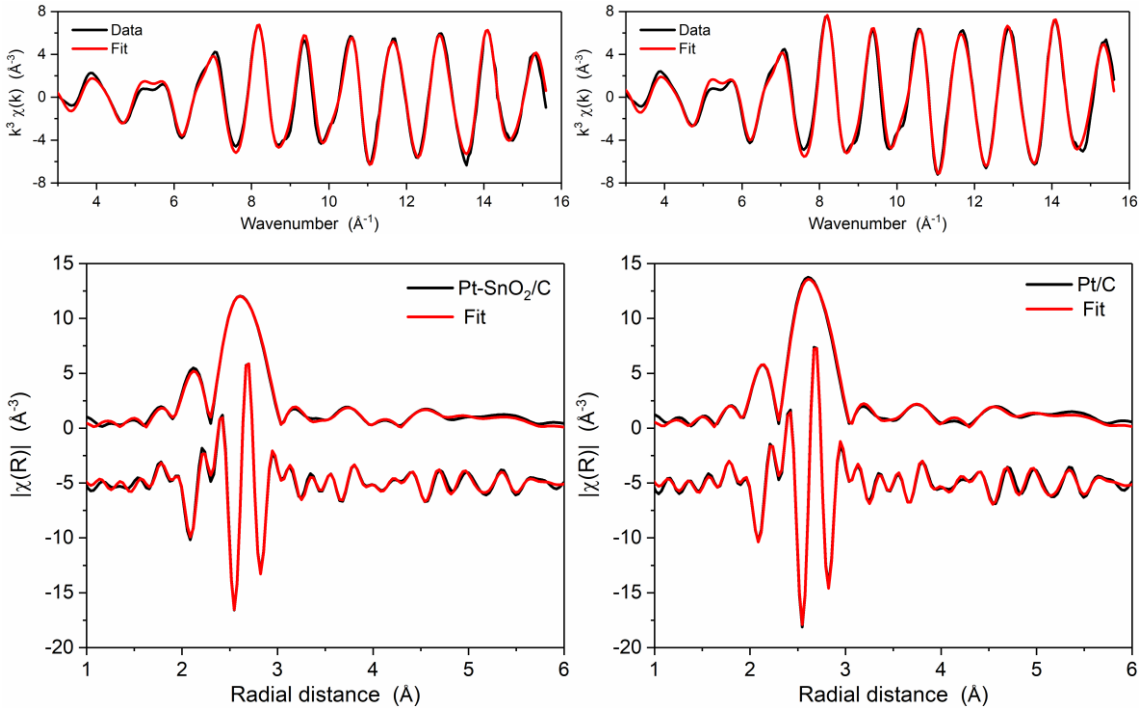

Figure 4-5. Fits of Pt L_3-edge EXAFS spectra (measured in H_2) of (left column) Pt-SnO_2/C and (right column) Pt/C, plotting as (top) k^3-weighting EXAFS spectra and (bottom) their Fourier transforms in magnitude and real part (offset by -5 $Å^{-4}$ for clarity). The fitting was carried out in a R-range of 1.5 Å to 5.5 Å, producing R-factors of ~0.7% for Pt-SnO_2/C and ~0.6% for Pt/C. The structural parameters obtained are listed in Table 4-1.

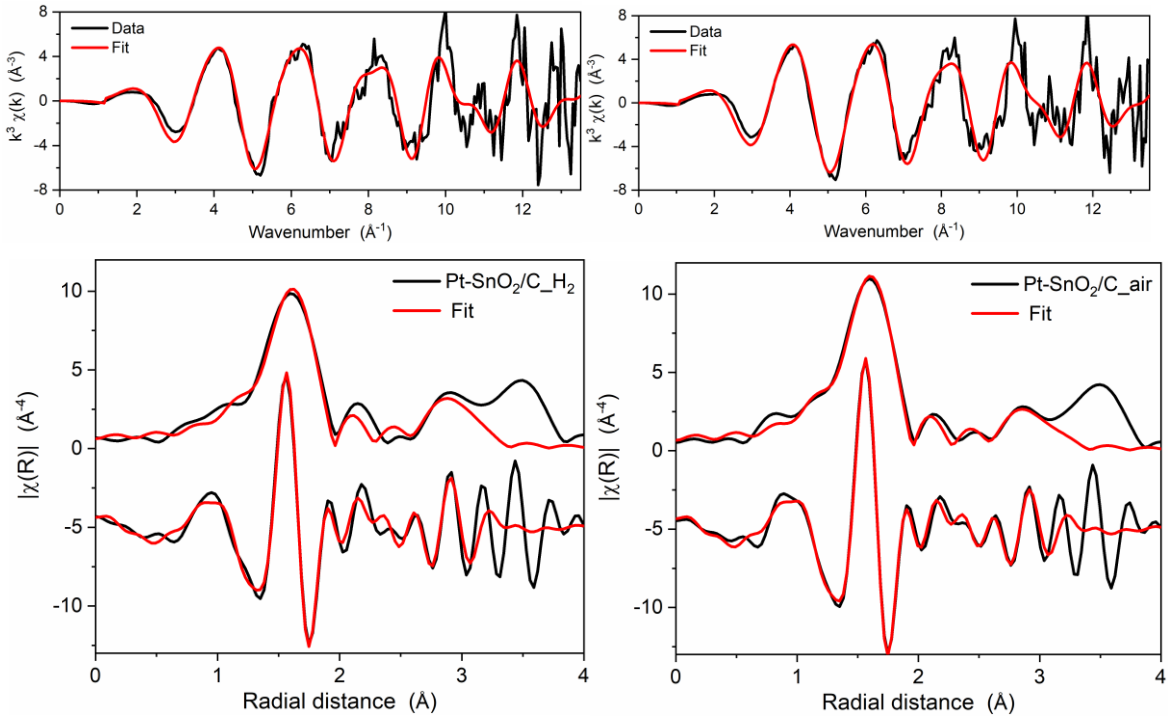

Figure 4-6. Fits of Sn K-edge EXAFS spectra of Pt-SnO_2/C measured in (left column) H_2 and (right column) air, plotting as (top) k^3-weighting EXAFS spectra and (bottom) their Fourier transforms in magnitude and real part (offset by -5 $Å^{-4}$ for clarity). The fitting was conducted in 1.0–3.0 Å, producing R-factors of ~1.2% for that measured in H_2 and 0.4% for that in air. The structural parameters obtained are listed in Table 4-1.

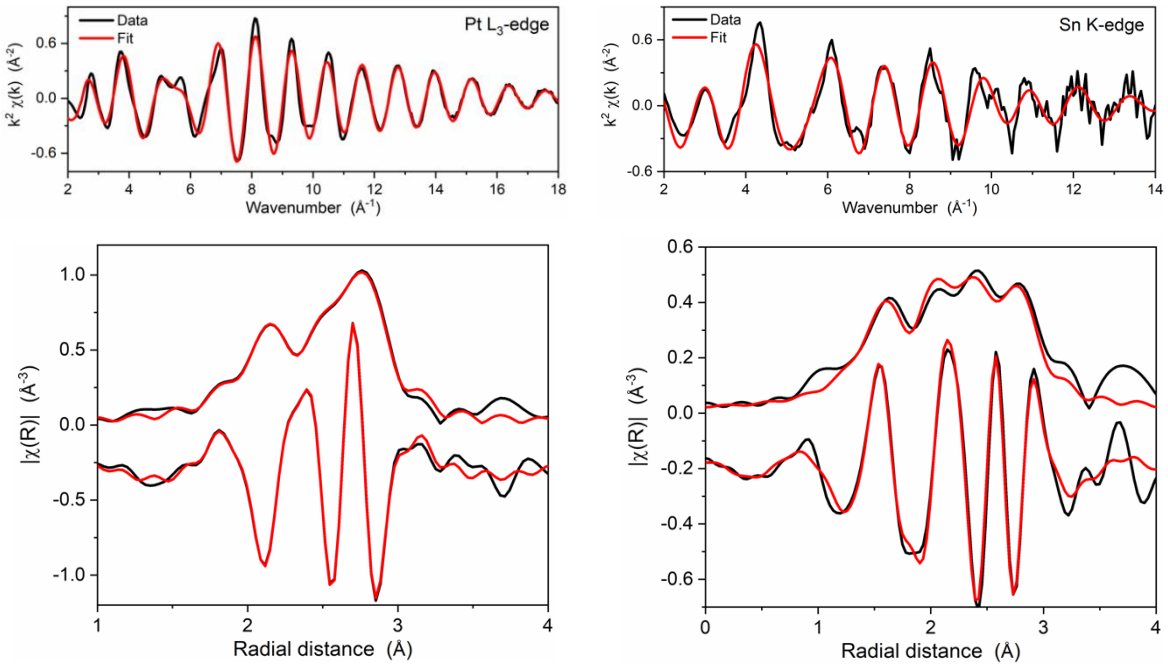

Figure 4-7. A first-shell fit of Pt-Sn alloy/C (measured in H_2) combining the data measured at (left column) Pt L_3-edge and Sn K-edge (right column). (top) k^2-weighting EXAFS spectra and (bottom) their Fourier transforms plotted as magnitude and real part (offset for clarity by -0.3 $Å^{-3}$ for Pt L_3-edge and -0.2 $Å^{-3}$ for Sn K-edge). The combined fitting was carried out in R-ranges of 1.35–3.0 Å for Pt L_3-edge and of 1.0–3.0 Å for Sn K-edge, and produced a fit with an R-factor of 0.9% and structural parameters listed in Table 4-1.

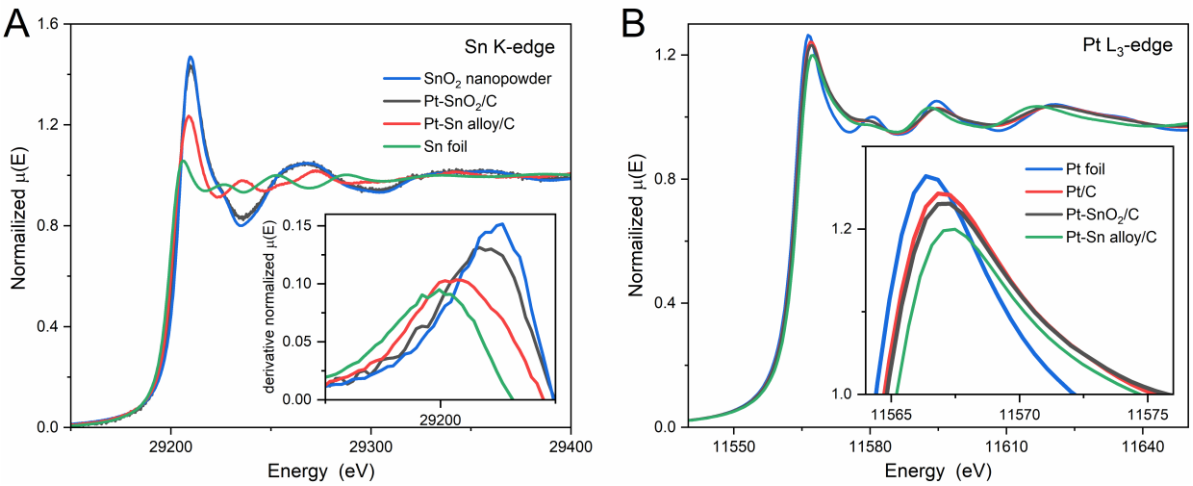

Figure 4-8. XANES spectra of Pt-SnO_2/C at (A) Sn K-edge and (B) Pt L_3-edge, compared those of the reference samples, Pt/C, Pt-Sn alloy/C and Pt foil at Pt L_3-edge, SnO_2 nanopowder, Pt-Sn alloy/C and Sn foil at Sn K-edge. The spectra of Pt-SnO_2/C, Pt/C and Pt-Sn alloy/C were collected in H_2(g). The inset of the left shows the first derivative of normalized XANES spectra around the Sn K-edge, and the inset of the right shows an enlargement in the whiteline region.

The speciation of Sn is corroborated by the X-ray absorption near-edge structure (XANES) as shown in Figure 4-8. Two features in these data are of interest, the post-edge whiteline intensity, the sharp feature at the top of the edge, describing the unfilled electronic states of Sn 5p, and the edge position, selected as the maximum of the first derivative (the inset of Figure 4-8A), representing the energy required to allow the K-edge transition. Because of the clear differences between SnO_2 and alloyed Sn in oxidation state and electron configuration (Sn^{IV}: $[Kr]5s^25p^2$; Sn^0: $[Kr]5s^05p^0$), the Sn K-edge XANES provides a means of differentiating these two Sn species.

Figure 4-8A compares Sn K-edge XANES of Pt-SnO_2/C with those of SnO_2, a Pt-Sn alloy/C, and Sn foil. The Pt-SnO_2/C data show nearly identical whiteline intensity and peak position to that for SnO_2, indicating that SnO_2 is the dominate Sn species in Pt-SnO_2/C. The negligibly small differences in the whiteline intensity and the edge position observed can be attributed to the surface oxygen vacancies of SnO_2 formed in H_2 (g), consistent with the discussion of the EXAFS data above. In contrast, a significant decrease in the whiteline intensity and a negative shift in the edge position are found in the Pt-Sn alloy/C data compared to the SnO_2 data. In addition, there is an excellent match in the other features in the XANES above the edge in Figure 4, between 29250 and 29400 eV, for the Sn K-edge data obtained for SnO_2 and Pt-SnO_2/C.

The characterization data presented above do not provide any evidence of the formation of alloyed Sn and, thus, the electronic/ligand effect from alloyed Sn can be excluded, meaning that the Pt d-band occupancy of Pt-SnO_2/C is expected to be unperturbed. Figure 4-8B compares Pt L_3-edge XANES of Pt-SnO_2/C with those of Pt/C, Pt-Sn alloy/C and Pt foil. Compared to the standard Pt foil, the sample spectra show whiteline features that are lower in intensity and broadened on the high energy side, with the data for Pt-SnO_2/C and Pt/C nearly overlapping. These results suggest that the electronic states of Pt of Pt-SnO_2 and Pt/C are different from those in the Pt foil, but those for Pt-SnO_2/C and Pt/C are similar. The deviation from the Pt foil data can be attributed to the charge transfer between Pt and other species, caused by chemically adsorbed hydrogen (H_{ads}) and/or by alloyed Sn. Under H_2(g), which is used to minimize the contribution of Pt surface oxides, H_2 is dissociated and the H_{ads} covers the Pt surface[48]. Assuming the size dependence of the coverage of H_{ads} is negligible, the distortion from H_{ads} in Pt L_3-edge data should be proportional to the surface-to-bulk ratio of Pt particles because the XAS data reflect the per-atom-average. Thus, the subtly smaller intensity in the whiteline of Pt-SnO_2/C compared that of Pt/C can be rationalized by the smaller Pt particle size in the former, which is in good agreement with the other structural characterizations presented above. For the Pt-Sn alloy, ~6 nm[32], the influence of H_{ads} should be diluted by Pt atoms in the core, and the significant decrease in the whilteline of Pt edge can be attributed to the alloyed Sn, in which the electrons from Sn are partly donated to the available Pt 5d states[49, 50].

Combined with the STEM results and the XAS analysis at both the Pt L_3 and Sn K edges, we confirm that a metal-metal oxide junction, Pt-SnO_2, is formed without any measurable Pt-Sn intermetallic

bonds, which would be indicative of alloy formation, in air and in the presence of H_2 (g). On such a catalyst, the classical bifunctional mechanism from alloyed Sn, as well as the ligand and ensemble effects, are no longer applicable.

4.3.4 CO oxidation voltammetry

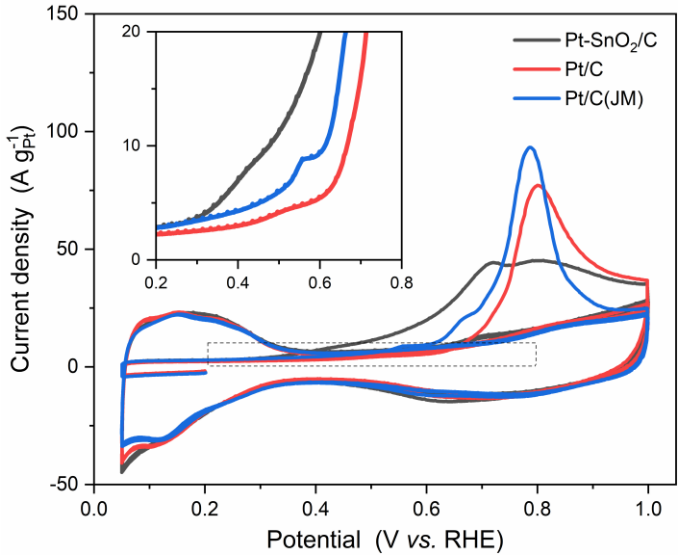

Figure 4-9. CO stripping voltammograms of Pt-SnO_2/C, Pt/C and Pt/C (JM) in N_2-saturated 0.1 M $HClO_4$ solution at a scan rate of 20 mV s^{-1}. A saturated CO adlayer was adsorbed by potential hold at 0.2 V for at least 15 min, followed by displacement of dissolved CO from the solution by N_2.

Figure 4-9 shows the CO-stripping voltammograms of the as-prepared samples, Pt-SnO_2/C and Pt/C, as well as a commercial Pt/C (20 wt%) from Johnson Matthey (JM). After a saturated CO adlayer was formed at 0.2 V in 0.1 M $HClO_4$, the potential was swept backwards to 0.05 V in CO-free electrolyte and cycled in 0.05–1.0 V for three cycles. As the Pt surface is completely blocked by CO, the hydrogen adsorption/desorption ($H_{ads/des}$) features from Pt (0.05–0.35 V) are absent in the first cycle as expected and appear after the adsorbed CO (CO_{ads}) is stripped off. The $H_{ads/des}$ pseudocapacitive current also appeared in the second cycle, with the Pt-SnO_2/C CV largely overlapping that for the Pt/C samples and that for the Pt-Sn alloy/C being considerably smaller (Figure S4-15). This similarity confirms the absence of the Pt-Sn alloy in the Pt-SnO_2/C catalyst, as the presence of either alloyed Sn[8, 20, 32] or irreversibly adsorbed Sn[23, 51] has been found to diminish the $H_{ads/des}$ features.

Interesting results are found for the CO stripping peaks. Whilst the Pt/C catalysts show a main peak at ~0.8 V and small pre-peaks between 0.4 V and 0.7 (the inset of Figure 4-9), Pt-SnO_2/C gives a broad peak, from 0.3 V to 1 V, with significantly more contribution from the pre-peaks and less from the main peak. Two features are noteworthy. The first is the low onset potential, as low as ~0.3 V, which is close to the reported value for Pt-Sn alloys[8, 20] and Sn-modified Pt[51, 52], indicating

that CO oxidation at the Pt-SnO_2 catalyst is indeed promoted. The second is the shape of the peak. At potentials below and above this peak the voltammogram resembles those of Pt-Sn alloys and that of Pt/C, respectively, suggesting that both highly active sites and less active sites (pure Pt sites) coexist on Pt-SnO_2/C. The multiplicity of active sites is consistent with the STEM results, which show that the Pt particles may or may not be in contact with SnO_2. The percentage of active sites is estimated by a CO pre-stripping voltammogram (Figure S4-16), in which ~36% CO_{ads} was removed by potential hold at 0.5 V prior to CO stripping.

These CO stripping voltammogram features of Pt-SnO_2/C are reproducible using sulfuric acid as the electrolyte (Figure S4-17), and repeatable on physical mixtures of the two commercial components, Pt/C(JM) and SnO_2 nanopowders (8–10 nm), prepared over a range of molar ratios of Pt to SnO_2 (3:1, 1:1 and 1:3, Figure 4-10A). A consistent trend is clearly obtained; the higher portion of the added SnO_2, the larger charge in the pre-peak region, although the extent of the promotional effect is less than that of Pt-SnO_2/C. In addition, by changing the random mixture configuration to layer-by-layer ones, that is, a SnO_2 layer on a Pt/C and the opposite, we found that the charge on the pre-peak region depends not simply on the content or presence of SnO_2, but also on the contact between Pt and SnO_2 (Figure 4-10B).

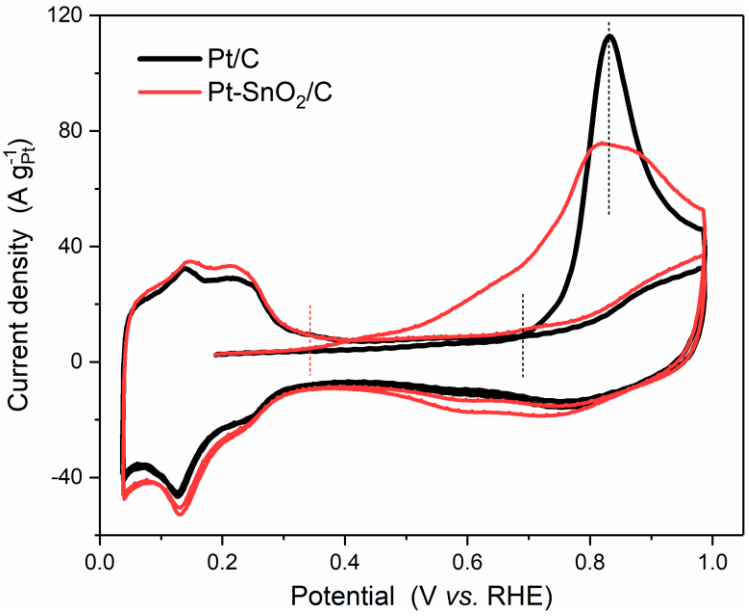

Figure 4-13. CO stripping voltammograms of Pt/C and Pt-SnO_2/C. The voltammograms were collected in N_2-saturated 0.1 M H_2SO_4 solution with a scan rate of 20 mV s^{-1}.

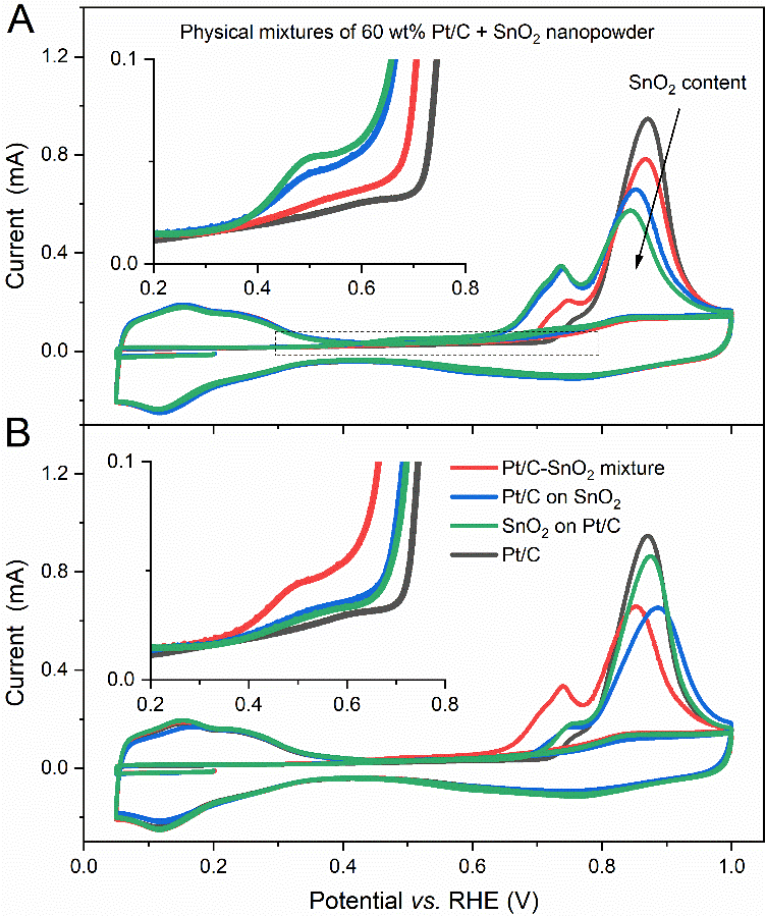

Figure 4-10. CO stripping voltammograms of electrodes modified by 60 wt% Pt/C (Johnson Matthey) and SnO_2 nanopowder with different (A) SnO_2 contents and (B) microstructures. (A) Physical mixtures of the Pt/C and the SnO_2 (Pt:Sn molar ratios of 3:1, 1:1 and 1:3), with a constant Pt loading on the electrodes (~61 μg_{Pt} cm^{-2}) and with the SnO_2 loadings of ~15 μg cm^{-2}, ~46 μg cm^{-2} and ~138 μg cm^{-2}, respectively. (B) Layer-on-layer structures formed via drop-casing sequences (a Pt/C layer on a SnO_2 layer, and *vice versa*), and the Pt and SnO_2 loading were constant, ~61 μg cm^{-2} and ~46 μg cm^{-2}, respectively. The voltammograms were conducted in N_2-saturated 0.1 M $HClO_4$ solution with a scan rate of 20 mV s^{-1}, and the insets magnify the first sweeps of the voltammograms at the onset of CO_{ads} oxidation.

Since SnO_2 itself is inert for CO oxidation (Figure S4-18), the CO stripping voltammograms of the Pt-SnO_2/C and the physical mixtures of Pt/C and SnO_2 clearly indicate that CO adlayer oxidation at the Pt surface is facilitated by $Sn^{IV}O_2$. The conventional bifunctional mechanism from alloyed Sn, in which water molecules are activated by the oxidation of the Sn sites[8, 20], fails to explain the promotional effect from SnO_2. One may argue that the mechanism is still applicable at SnO_2 by forming OH_{ads} adsorbed on SnO_2, as supposed by many previous studies[29-31, 42, 53], but we think otherwise, and that it is the OH species on the SnO_2 surface, (SnO_2)Sn-OH, that are the active species for the bifunctional mechanism from SnO_2. There are three reasons for our proposal. First, Sn^{IV} of SnO_2 is in the highest oxidation state of Sn and has a saturated first coordination shell, as we ascertained using XAS above. These two factors clearly do not allow the addition of OH coordination by further oxidation of Sn^{IV}. Second, the surface hydroxyl on SnO_2 has been verified[47, 54, 55],

which is formed by the dissociative adsorption of water. In this process, water molecules coordinate on an undercoordinated Sn^{IV} site (with net positive charge) and transfer one of the protons to an oxygen atom (with net negative charge), and the oxidation state of Sn remains unchanged. Third, in heterogeneous catalysis the surface hydroxyl on SnO_2 has been found to participate in CO oxidation on Pt at low temperature[56, 57]. Thus, based on the widely accepted Langmuir-Hinshelwood (L-H) type reaction on Pt[6, 16, 58], which is also supported by the Pt/C-SnO_2 physical mixture data, the bifunctional mechanism of SnO_2 can be tentatively written as

$$Pt\text{-}CO_{ads} + (SnO_2)Sn\text{-}OH + H_2O \rightarrow CO_2 + H_3O^+ + e^- + Pt + (SnO_2)Sn^* \quad \text{(eq. 1)}$$

where $(SnO_2)Sn^*$ is an oxygen vacancy site of SnO_2, possibly the same species as observed in the XAS under H_2(g). This reaction not only regenerates a Pt site available for another CO, but also gives a defect site of SnO_2, which may or may not form back to Sn-OH under the experimental conditions. If not, the Sn-OH would be consumed and the reaction would be discontinued.

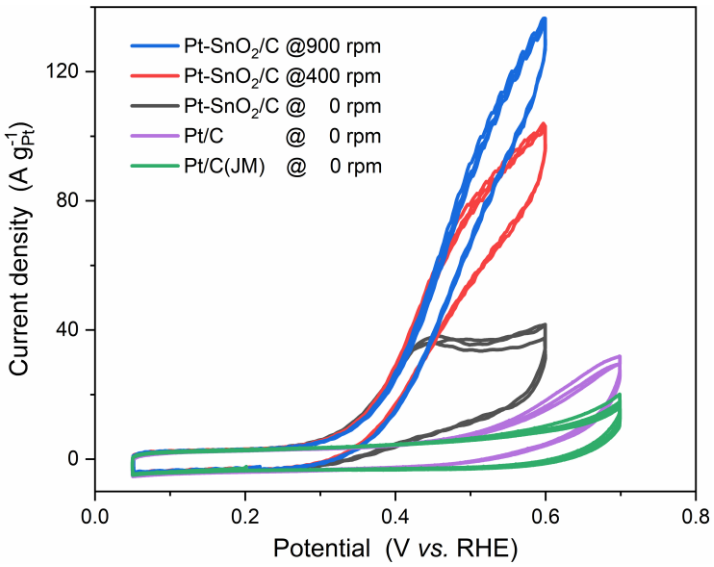

Figure 4-11. CO continuous (dissolved) oxidation voltammograms of Pt-SnO_2/C, Pt/C and Pt/C (JM) in CO-saturated 0.1 M $HClO_4$ solution with a scan rate of 20 mV s^{-1}. The rotation rates are indicated in the figure legend.

The bifunctional mechanism of SnO_2 for CO oxidation at low overpotential was then studied by continuous oxidation, in which cyclic voltammetry is carried out in a CO-saturated electrolyte and the mass transport of the dissolved CO is controlled by the rotating disc electrode (RDE) configuration. Figure 4-11 compares CO bulk oxidation voltammograms of the Pt-SnO_2/C, Pt/C and commercial Pt/C under stationary conditions. The upper limits of the potential windows were chosen to emphasize the pre-peak characteristic, i.e., 0.6 V for Pt-SnO_2/C and 0.7 V for the Pt/C catalysts. Pt/C catalysts were also tested to higher potential upper limits to obtain comparable rate of CO oxidation to that observed for Pt-SnO_2/C (Figure S4-19 and Figure S4-20). In CO-saturated

electrolyte, free Pt surface sites are continuously blocked by CO molecules, and thus the voltammograms show no hydrogen adsorption/desorption features in all three cycles.

Under continuous supply of CO at 0 rpm, the samples show much enhanced current for CO oxidation, but the extent of enhancement and the stability depends on the catalyst composition (Figure 4-11 and Figure S4-21). For continuous CO oxidation the prepared Pt/C yields a higher current than the commercial sample, which is attributed to the higher fraction of defective sites on smaller Pt nanoparticles (~ 2 nm for the prepared and ~3 nm for the commercial samples), which facilitate the formation of Pt-OH_{ads} at lower potentials[59, 60]. The current is much larger at Pt-SnO_2/C than the Pt/C samples, especially at the onset of CO oxidation, and the current becomes dependent on rotation rate, which is not observed on Pt/C catalysts even when being cycled to 0.9 V (Figure S4-19 and Figure S4-20). The rotation rate dependent current indicates that the CO oxidation kinetics on Pt-SnO_2/C are so fast that the diffusion of dissolved CO become the rate-determining step when the potential is ≥ 0.4 V. Such fast kinetics at such a low potential have rarely been reported. Gasteiger et al.[1] showed similar rotation rate dependent CO oxidation current on a well-characterised Pt_3Sn electrode but over a narrower potential windows (< 0.5 V) to avoid Sn dissolution.

From the kinetically controlled portion of the voltammogram, a constant Tafel slope of ~134 mV dec^{-1} was obtained for the low potential CO oxidation (Figure 4-12). This value is similar to both that reported for the pre-peak CO oxidation on Pt(111) in alkaline electrolyte (130 mV dec^{-1})[58] and that simulated on Pt in acidic electrolyte when OH coverage is constant and not dependent on the potential (120 mV dec^{-1})[61]. Both cases consider that the L-H reaction between Pt-CO_{ads} and OH_{ads} to be the rate-determining step of CO oxidation.

Returning to the CO continuous oxidation voltammograms, the CO oxidation current at Pt-SnO_2/C is repeatable within cycles at different rotation rates. In contrast, Pt/C catalysts show a gradual decrease in the current and a positive shift during cycling (Figure S4-19 and Figure S4-20). The deactivation has been attributed to the reconstruction of surface defects[60, 62, 63]. Stable CO oxidation at Pt-SnO_2/C was also tested by chronoamperometry. At 0.4 V, where pure Pt is inactive, Pt-SnO_2/C delivers a steady current for 0.5 h (Figure 4-13). If the Sn-OH is not regenerated during the CO oxidation at this potential, the current should decay to zero. Thus, the opposite is valid, and the results indicate that the (SnO_2)Sn-OH and (SnO_2)Sn* are interconvertible at potentials below or around the onset of the L-H reaction.

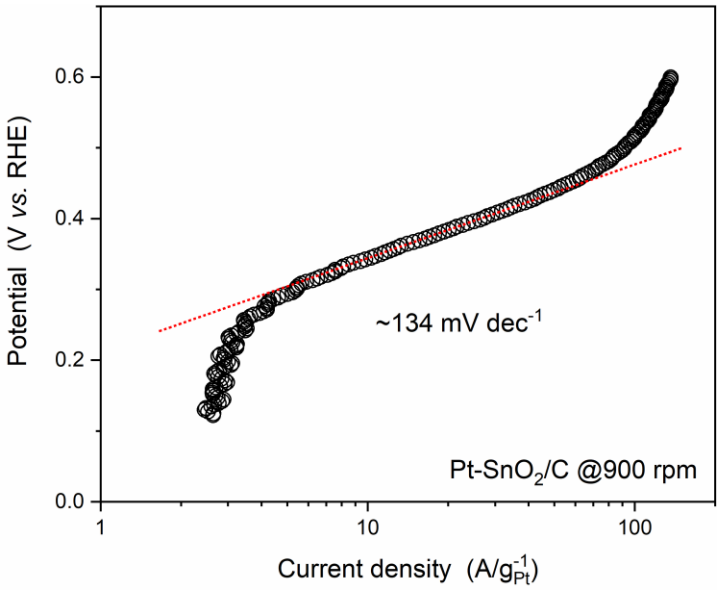

Figure 4-12. A Tafel plot of CO oxidation on Pt-SnO_2/C with 20 mV s^{-1} scan rate and 900 rpm rotation rate in CO-saturated 0.1 M $HClO_4$. The plot is not IR-corrected.

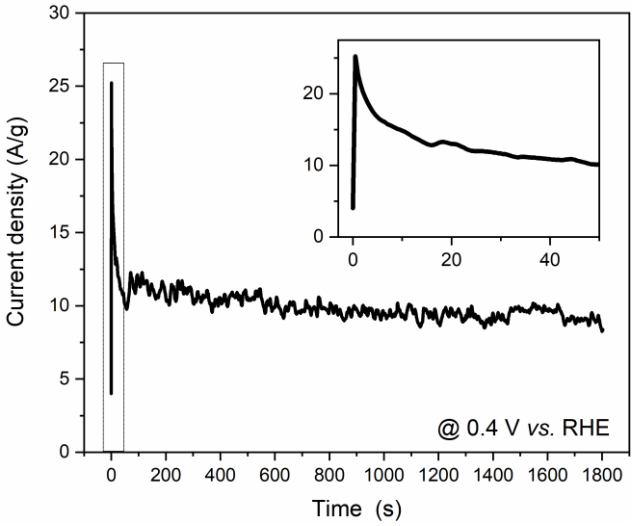

Figure 4-13. A 0.5 h chronoamperommogram of Pt-SnO_2/C for CO oxidation under an applied potential of 0.4 V *vs.* RHE and a rotation rate of 0 rpm in CO-bubbling 0.1 M $HClO_4$. The sharp decrease at the start is due to the contribution of capacitance current.

4.3.5 Voltammetry of SnO_2 nanoparticles

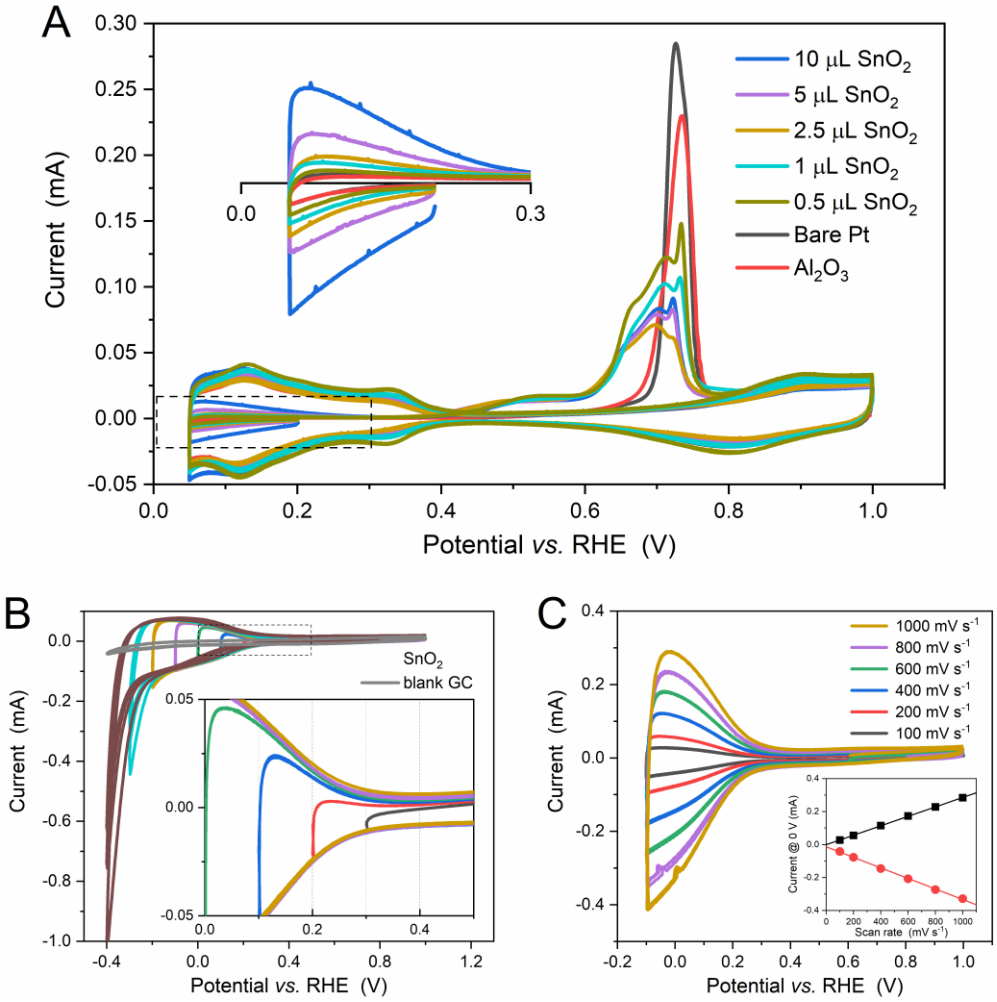

Figure 4-14. (A) CO stripping voltammograms of SnO_2 nanopowder on a polycrystalline Pt disc electrode (5 mm diameter) with a scan rate of 50 mV s^{-1} and with the SnO_2 loading varied by adding different volume of 5 mg mL^{-1} SnO_2 suspension. The inset magnifies the $H_{ads/des}$ region on the first cycles of the voltammograms. The voltammogram of Al_2O_3 on Pt is also present for comparison. (B) The window-opening and (C) scan-rate-dependent cyclic voltammograms of SnO_2 nanopowder on a glassy carbon electrode (GC, 5 mm diameter), with the inset showing the linear relationship between the current at 0 V and the corresponding scan rate. In the window-opening experiment, the scan rate is 200 mV s^{-1} and the blank (GC) data is also present as a reference.

Although we confirm that there is a redox reaction happening on the surface of SnO_2 at low potential, neither Pt-SnO_2/C nor the physical mixtures between SnO_2 and Pt/C show any features relating to SnO_2 in the voltammograms. The double layer charging from carbon support may obscure these results. Thus, commercial SnO_2 nanoparticles were directly loaded on Pt and glassy carbon (GC) electrodes.

Figure 4-14A shows CO stripping voltammograms of SnO_2 deposited on a Pt disc electrode with different SnO_2 loadings. On the whole, a similar promotional effect as observed for carbon supported

Pt-SnO_2 catalysts was found on these directly modified electrodes (unaffected $H_{ads/des}$ peak in shape, low onset potential for CO adlayer oxidation, and the SnO_2-coverage-depedent decrease in the CO stripping main peak). These results indicate that the commercial SnO_2 nanoparticles have qualitatively the same effect on the CO oxidation on Pt as that of Pt-SnO_2/C. Closer examination of the hydrogen region of the first scan, in which Pt electrochemistry is completely blocked by CO_{ads}, reveals an unconventional pseudo-capacitance, in which the charge increases proportional to the loading of SnO_2. This suggests that the pseudo-capacitance is not from Pt but from SnO_2.

The electrochemistry of SnO_2 was then studied on a SnO_2-modified GC electrode. Figure 4-14B and 7C shows window-opening and scan-rate dependent voltammograms. The pseudo-capacitance of SnO_2 is repeatable on GC in the same potential region, and found to be related to a highly reversible and surface-bounded redox couple. The redox couple is observed between -0.2–0.3 V, and its kinetics allows a symmetric peak shape to be maintained at sweep rates up to 1 V s^{-1}. When the potential limit is extended below -0.2 V a further irreversible reduction is observed. According to the well-accepted dual valency of Sn in tin oxide chemistry[47, 54] and the standard electrode potential data of Sn[40], the redox couple found on SnO_2 is attributed to the reversible interconversion between Sn^{IV} and Sn^{II} on a fraction of the surface of SnO_2, in good agreement with the reduced SnO_2 in H_2(g) as the XAS results suggested. Thus, the regeneration of Sn-OH, following the L-H reaction of CO oxidation, can tentatively be written as

$$(SnO_2)Sn^{IV}(OH)_2 + 2\ H^+ + 2e^- \rightleftharpoons (SnO_2)Sn^{II} + 2\ H_2O \qquad \text{(eq.2)}$$

We should highlight that the exact coordination structure of this Sn^{IV}/Sn^{II} is not yet known and that the double coordinated OH in $Sn^{IV}(OH)_2$ is used for balancing the change of the Sn oxidation state. Further reduction drives the irreversible transformation from Sn^{IV} to Sn^{II}, or even Sn^{II} to Sn^0

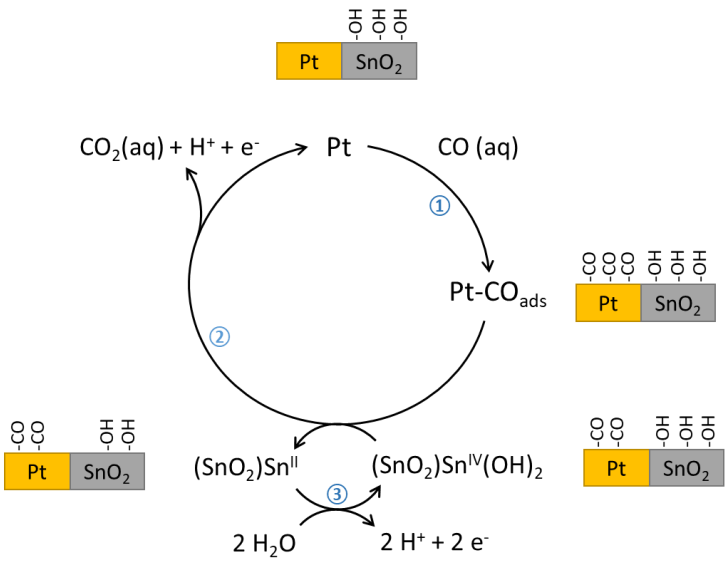

Figure 4-15. Catalysis cycle of CO oxidation on Pt with the co-catalyst SnO_2.

From above voltammetry studies, SnO_2 is confirmed to enable CO oxidation at Pt at a low overpotential possibly by providing Sn-OH, and the bifunctional mechanism on Pt-SnO_2 is attributed to the co-catalysis of SnO_2, in which the Sn-OH is constantly supplied by a reversible redox couple located on the surface of SnO_2. By such a mechanism, the catalysis cycle of CO oxidation, which is disconnected on Pt due to unfavourable formation of Pt-OH_{ads} at low potential[6, 16], but is completed on Pt-SnO_2 (Figure 4-15). Dissolved CO molecules chemisorb on active Pt sites, forming Pt-CO_{ads} (step ①), and then the CO_{ads} reacts with Sn-OH species (step ②), releasing CO_2, a free Pt site and a Sn^{II} that can be oxidized and regenerated Sn-OH species at the potential of step ② (step ③).

Both the L-H type reaction and the reversible reaction of SnO_2 involve the redox couple of Sn^{IV}/Sn^{II} as well as the formation/cleavage of Sn^{IV}-OH. The appropriate Sn^{IV}-OH energetics may be responsible for the unique property of SnO_2 for CO oxidation at low overpotential. The effects of two other metal oxide nanoparticles, Al_2O_3 (Figure 4-14A) and TiO_2 (P25, Figure S4-22) on CO oxidation at Pt, were then explored. They showed no improvement for CO oxidation but instead blockage of the Pt sites was found. For TiO_2, we found a similar reversible redox couple relating to Ti^{IV}/Ti^{III} [64, 65] to that for SnO_2, but it begins at a more negative potential (<-0.1 V, Figure S4-23), suggesting stronger driving force is needed to dissociate the Ti^{IV}-OH bond. As the opposite, CeO_2, which has a redox couple of Ce^{IV}/Ce^{III} > 1 V[66, 67], also shows no promotional effects when loaded on Pt[68]. Recently, Olu *et al*. reported enhanced CO oxidation activity on a Pt electrode modified by RuO_2 nanosheets[69] or WO_3 nanoparticles[15], but they found different mechanisms; the RuO_2 formed 'Ru metal-like' sites that provide ligand effects to Pt and additional sites for CO absorption, and the WO_3, the hydroxyl formation of which is less reversible than that of SnO_2, can only assist in the removal of the weakly adsorbed CO.

4.4 Conclusions

A Pt-SnO_2/C catalyst, without Pt-Sn intermetallic bonding, was designed to isolate the bifunctional effects from SnO_2 for CO electro-oxidation. The structure of Pt-SnO_2/C was confirmed by STEM, XRD and detailed XAS analysis. CO oxidation is strongly promoted on Pt-SnO_2 surfaces, which are constructed from the Pt-SnO_2/C, mixtures of Pt/C and SnO_2 nanoparticles, or a SnO_2-modified Pt electrode, with the onset potential of ~0.3 V. CO oxidation on Pt-SnO_2 is continuous at low overpotentials, and with fast kinetics such that the diffusion of dissolved CO becomes the rate-determining-step beyond ~0.4 V. By finding a revesible Sn^{IV}/Sn^{II} redox couple on the surface of SnO_2 that provides necessary OH species for CO oxidation at low potentials, and combining the evidence above, we propose that the bifunctional mechanism of Pt-SnO_2 originates from a co-catalysis of SnO_2, in which Sn-OH is consumed in reacting Pt-CO_{ads} at the interface and regenerated by dissociating water. The unique promotional effect of SnO_2 is then discussed in relation to the appropriate energetics of metal-oxide bond. It should be mentioned that this chapter is unable to

provide direct evidence proving the direct involvement of the Sn-OH and information regarding the location of the active Sn-OH of Pt-SnO_2 (the whole SnO_2 particles, or only the Pt-SnO_2 the interface). To validate the former, additional differential electrochemical mass spectrometer (DEMS) experiments using isotope-label SnO_2 can provide evidence to some extent, but the exchange rate of O between the SnO_2 surface and water might be critical. For the latter, SnO_2 islands with controllable size on Pt single crystals can be used as the model system, as the Pt-SnO_2 interface increases with decreasing the size of the SnO_2 island, and the location of the active Sn-OH can be studied using scanning electrochemical cell microscopy during CO oxidation.

4.5 References

[1] H.A. Gasteiger, N.M. Markovic, P.N. Ross, Electrooxidation of CO and H_2/CO Mixtures on a Well-Characterized Pt_3Sn Electrode Surface, J. Phys. Chem., 99 (1995) 8945-8949.

[2] H.A. Gasteiger, N.M. Marković, P.N. Ross, Structural effects in electrocatalysis: electrooxidation of carbon monoxide on Pt_3Sn single-crystal alloy surfaces, Catal. Lett., 36 (1996) 1-8.

[3] Q. Wang, G.Q. Sun, L.H. Jiang, Q. Xin, S.G. Sun, Y.X. Jiang, S.P. Chen, Z. Jusys, R.J. Behm, Adsorption and oxidation of ethanol on colloid-based Pt/C, PtRu/C and Pt_3Sn/C catalysts: in situ FTIR spectroscopy and on-line DEMS studies, Phys. Chem. Chem. Phys., 9 (2007) 2686-2696.

[4] S.X. Liu, L.W. Liao, Q. Tao, Y.X. Chen, S. Ye, The kinetics of CO pathway in methanol oxidation at Pt electrodes, a quantitative study by ATR-FTIR spectroscopy, Phys. Chem. Chem. Phys., 13 (2011) 9725-9735.

[5] M. Heinen, Z. Jusys, R. J. Behm, Reaction pathway analysis and reaction intermediate detection via simultaneous differential electrochemical mass spectrometry (DEMS) and attenuated total reflection fourier transform infrared spectroscopy (ATR‐FTIRS), Handbook of Fuel Cells2010.

[6] M.T.M. Koper, S.C.S. Lai, E. Herrero, Mechanisms of the Oxidation of Carbon Monoxide and Small Organic Molecules at Metal Electrodes, Fuel Cell Catalysis2009, pp. 159-207.

[7] G. Garcia, M.T. Koper, Carbon monoxide oxidation on Pt single crystal electrodes: understanding the catalysis for low temperature fuel cells, ChemPhysChem, 12 (2011) 2064-2072.

[8] B.E. Hayden, M.E. Rendall, O. South, Electro-oxidation of carbon monoxide on well-ordered Pt(111)/Sn surface alloys, J. Am. Chem. Soc., 125 (2003) 7738-7742.

[9] E.M. Crabb, M.K. Ravikumar, D. Thompsett, M. Hurford, A. Rose, A.E. Russell, Effect of Ru surface composition on the CO tolerance of Ru modified carbon supported Pt catalysts, Phys. Chem. Chem. Phys., 6 (2004).

[10] A. Rose, R. Bilsborrow, C.R. King, M.K. Ravikumar, Y. Qian, R.J.K. Wiltshire, E.M. Crabb, A.E. Russell, In situ Ru K-edge EXAFS of CO adsorption on a Ru modified Pt/C fuel cell catalyst, Electrochim. Acta, 54 (2009) 5262-5266.

[11] C.J. Pelliccione, E.V. Timofeeva, J.P. Katsoudas, C.U. Segre, In situ Ru K-edge X-ray absorption spectroscopy study of methanol oxidation mechanisms on model submonolayer ru on Pt nanoparticle electrocatalyst, J. Phys. Chem. C, 117 (2013) 18904-18912.

[12] Y. Dai, Y. Liu, S. Chen, Pt–W bimetallic alloys as CO-tolerant PEMFC anode catalysts, Electrochim. Acta, 89 (2013) 744-748.

[13] Z. Liu, J.E. Hu, Q. Wang, K. Gaskell, A.I. Frenkel, G.S. Jackson, B. Eichhorn, PtMo alloy and MoO(x)@Pt core-shell nanoparticles as highly CO-tolerant electrocatalysts, J. Am. Chem. Soc., 131 (2009) 6924-6925.

[14] G. Samjeske, H.S. Wang, T. Loffler, H. Baltruschat, CO and methanol oxidation at Pt-electrodes modified by Mo, Electrochim. Acta, 47 (2002) 3681-3692.

[15] P.-Y. Olu, T. Ohnishi, Y. Ayato, D. Mochizuki, W. Sugimoto, Insights into the enhanced tolerance to carbon monoxide on model tungsten trioxide-decorated polycrystalline platinum electrode, Electrochem. Commun., 71 (2016) 69-72.

[16] N. Markovic, Surface science studies of model fuel cell electrocatalysts, Surf. Sci. Rep., 45 (2002) 117-229.

[17] E. Antolini, E.R. Gonzalez, The electro-oxidation of carbon monoxide, hydrogen/carbon monoxide and methanol in acid medium on Pt-Sn catalysts for low-temperature fuel cells: A comparative review of the effect of Pt-Sn structural characteristics, Electrochim. Acta, 56 (2010) 1-14.

[18] Y. Liu, D. Li, V.R. Stamenkovic, S. Soled, J.D. Henao, S. Sun, Synthesis of Pt_3Sn Alloy Nanoparticles and Their Catalysis for Electro-Oxidation of CO and Methanol, ACS Catal., 1 (2011) 1719-1723.

[19] Z. Liu, G.S. Jackson, B.W. Eichhorn, PtSn intermetallic, core-shell, and alloy nanoparticles as CO-tolerant electrocatalysts for H_2 oxidation, Angew. Chem., Int. Ed., 49 (2010) 3173-3176.

[20] V.R. Stamenkovic, M. Arenz, C.A. Lucas, M.E. Gallagher, P.N. Ross, N.M. Markovic, Surface chemistry on bimetallic alloy surfaces: adsorption of anions and oxidation of CO on $Pt_3Sn(111)$, J. Am. Chem. Soc., 125 (2003) 2736-2745.

[21] V. Stamenkovic, M. Arenz, B.B. Blizanac, K.J.J. Mayrhofer, P.N. Ross, N.M. Markovic, In situ CO oxidation on well characterized $Pt_3Sn(hkl)$ surfaces: A selective review, Surf. Sci., 576 (2005) 145-157.

[22] B.E. Hayden, M.E. Rendall, O. South, The stability and electro-oxidation of carbon monoxide on model electrocatalysts: Pt(111) – Sn(2×2) and Pt(111) – Sn($\sqrt{3}\times\sqrt{3}$)R30°, J. Mol. Catal. A: Chem., 228 (2005) 55-65.

[23] A.N. Haner, P.N. Ross, Electrochemical oxidation of methanol on tin-modified platinum single-crystal surfaces, J. Phys. Chem., 95 (1991) 3740-3746.

[24] G. Stalnionis, L. Tamašauskaitė-Tamašiūnaitė, V. Pautienienė, A. Sudavičius, Z. Jusys, Modification of a Pt surface by spontaneous Sn deposition for electrocatalytic applications, J. Solid State Electrochem., 8 (2004) 892-899.

[25] E. Antolini, E.R. Gonzalez, Effect of synthesis method and structural characteristics of Pt–Sn fuel cell catalysts on the electro-oxidation of CH_3OH and CH_3CH_2OH in acid medium, Catal. Today, 160 (2011) 28-38.

[26] X. Lu, Z. Deng, C. Guo, W. Wang, S. Wei, S.P. Ng, X. Chen, N. Ding, W. Guo, C.M. Wu, Methanol Oxidation on $Pt_3Sn(111)$ for Direct Methanol Fuel Cells: Methanol Decomposition, ACS Appl. Mater. Interfaces, 8 (2016) 12194-12204.

[27] J.M. Jin, T. Sheng, X. Lin, R. Kavanagh, P. Hamer, P. Hu, C. Hardacre, A. Martinez-Bonastre, J. Sharman, D. Thompsett, W.F. Lin, The origin of high activity but low CO_2 selectivity on binary PtSn in the direct ethanol fuel cell, Phys. Chem. Chem. Phys., 16 (2014) 9432-9440.

[28] L. Calvillo, L. Mendez De Leo, S.J. Thompson, S.W.T. Price, E.J. Calvo, A.E. Russell, In situ determination of the nanostructure effects on the activity, stability and selectivity of Pt-Sn ethanol oxidation catalysts, J. Electroanal. Chem., 819 (2018) 136-144.

[29] Y. Lin, S. Zhang, S. Yan, G. Liu, The effect of Sn content in Pt–SnO_2/CNTs for methanol electro-oxidation, Electrochim. Acta, 66 (2012) 1-6.

[30] M. Arenz, V. Stamenkovic, B. Blizanac, K. Mayrhofer, N. Markovic, P. Ross, Carbon-supported Pt–Sn electrocatalysts for the anodic oxidation of H_2, CO, and H_2/CO mixtures.Part II: The structure–activity relationship, J. Catal., 232 (2005) 402-410.

[31] F. Ye, J. Li, T. Wang, Y. Liu, H. Wei, J. Li, X. Wang, Electrocatalytic Properties of Platinum Catalysts Prepared by Pulse Electrodeposition Method Using SnO_2 as an Assisting Reagent, J. Phys. Chem. C, 112 (2008) 12894-12898.

[32] H. Huang, A. Nassr, V. Celorrio, S.F.R. Taylor, V.K. Puthiyapura, C. Hardacre, D.J.L. Brett, A.E. Russell, Effects of heat treatment atmosphere on the structure and activity of Pt_3Sn nanoparticle electrocatalysts: a characterisation case study, Faraday Discuss., 208 (2018) 555-573.

[33] G. Wang, T. Takeguchi, T. Yamanaka, E.N. Muhamad, M. Mastuda, W. Ueda, Effect of preparation atmosphere of Pt–SnO_x/C catalysts on the catalytic activity for H_2/CO electro-oxidation, Appl. Catal., B, 98 (2010) 86-93.

[34] D.R.M. Godoi, J. Perez, H.M. Villullas, Alloys and oxides on carbon-supported Pt–Sn electrocatalysts for ethanol oxidation, J. Power Sources, 195 (2010) 3394-3401.

[35] E.M. Crabb, R. Marshall, D. Thompsett, Carbon Monoxide Electro-oxidation Properties of Carbon-Supported PtSn Catalysts Prepared Using Surface Organometallic Chemistry, J. Electrochem. Soc., 147 (2000) 4440-4447.

[36] W.D. Michalak, J.M. Krier, S. Alayoglu, J.-Y. Shin, K. An, K. Komvopoulos, Z. Liu, G.A. Somorjai, CO oxidation on PtSn nanoparticle catalysts occurs at the interface of Pt and Sn oxide domains formed under reaction conditions, J. Catal., 312 (2014) 17-25.

[37] J.L. Margitfalvi, I. Borbáth, M. Hegedűs, E. Tfirst, S. Gőbölös, K. Lázár, Low-Temperature CO Oxidation over New Types of Sn–Pt/SiO_2 Catalysts, J. Catal., 196 (2000) 200-204.

[38] M. Vandichel, A. Moscu, H. Grönbeck, Catalysis at the Rim: A Mechanism for Low Temperature CO Oxidation over Pt_3Sn, ACS Catal., 7 (2017) 7431-7441.

[39] K.J. Cathro, The Oxidation of Water-Soluble Organic Fuels Using Platinum-Tin Catalysts, J. Electrochem. Soc., 116 (1969) 1608-1611.

[40] P. Vanysek, Electrochemical series, CRC handbook of chemistry and physics1998.

[41] A. Rabis, D. Kramer, E. Fabbri, M. Worsdale, R. Kötz, T.J. Schmidt, Catalyzed SnO_2 Thin Films: Theoretical and Experimental Insights into Fabrication and Electrocatalytic Properties, J. Phys. Chem. C, 118 (2014) 11292-11302.

[42] D.-H. Lim, D.-H. Choi, W.-D. Lee, H.-I. Lee, A new synthesis of a highly dispersed and CO tolerant PtSn/C electrocatalyst for low-temperature fuel cell; its electrocatalytic activity and long-term durability, Appl. Catal., B, 89 (2009) 484-493.

[43] D.-H. Lim, D.-H. Choi, W.-D. Lee, D.-R. Park, H.-I. Lee, The Effect of Sn Addition on a Pt ∕ C Electrocatalyst Synthesized by Borohydride Reduction and Hydrothermal Treatment for a Low-Temperature Fuel Cell, Electrochem. Solid-State Lett., 10 (2007) B87-B90.

[44] T. Matsui, K. Fujiwara, T. Okanishi, R. Kikuchi, T. Takeguchi, K. Eguchi, Electrochemical oxidation of CO over tin oxide supported platinum catalysts, J. Power Sources, 155 (2006) 152-156.

[45] M.S. Holt, W.L. Wilson, J.H. Nelson, Transition metal-tin chemistry, Chem. Rev., 89 (1989) 11-49.

[46] O.I. Milner, G.F. Shipman, Colorimetric Determination of Platinum with Stannous Chloride, Anal. Chem., 27 (1955) 1476-1478.

[47] M. Batzill, U. Diebold, The surface and materials science of tin oxide, Prog. Surf. Sci., 79 (2005) 47-154.

[48] M.K. Oudenhuijzen, J.H. Bitter, D.C. Koningsberger, The Nature of the Pt−H Bonding for Strongly and Weakly Bonded Hydrogen on Platinum. A XAFS Spectroscopy Study of the Pt−H Antibonding Shaperesonance and Pt−H EXAFS, J. Phys. Chem. B, 105 (2001) 4616-4622.

[49] S. Mukerjee, J. McBreen, An In Situ X‐Ray Absorption Spectroscopy Investigation of the Effect of Sn Additions to Carbon‐Supported Pt Electrocatalysts: Part I, J. Electrochem. Soc., 146 (1999) 600-606.

[50] Y. Uemura, Y. Inada, K.K. Bando, T. Sasaki, N. Kamiuchi, K. Eguchi, A. Yagishita, M. Nomura, M. Tada, Y. Iwasawa, Core−Shell Phase Separation and Structural Transformation of Pt_3Sn Alloy Nanoparticles Supported on γ-Al_2O_3 in the Reduction and Oxidation Processes Characterized by In Situ Time-Resolved XAFS, J. Phys. Chem. C, 115 (2011) 5823-5833.

[51] R. Rizo, E. Pastor, M.T.M. Koper, CO electrooxidation on Sn-modified Pt single crystals in acid media, J. Electroanal. Chem., 800 (2017) 32-38.

[52] M.J.S. Farias, W. Cheuquepán, A.A. Tanaka, J.M. Feliu, Nonuniform Synergistic Effect of Sn and Ru in Site-Specific Catalytic Activity of Pt at Bimetallic Surfaces toward CO Electro-oxidation, ACS Catal., 7 (2017) 3434-3445.

[53] T. Takeguchi, A. Kunifuji, N. Narischat, M. Ito, H. Noguchi, K. Uosaki, S.R. Mukai, Ligand effect of SnO_2 on a Pt–Ru catalyst and the relationship between bond strength and CO tolerance, Catal. Sci. Technol., 6 (2016) 3214-3219.

[54] S. Das, V. Jayaraman, SnO_2: A comprehensive review on structures and gas sensors, Prog. Mater. Sci., 66 (2014) 112-255.

[55] H. Tamura, K. Mita, A. Tanaka, M. Ito, Mechanism of Hydroxylation of Metal Oxide Surfaces, J. Colloid Interface Sci., 243 (2001) 202-207.

[56] D.R. Schryer, B.T. Upchurch, B.D. Sidney, K.G. Brown, G.B. Hoflund, R.K. Herz, A proposed mechanism for Pt/SnO_x-catalyzed CO oxidation, J. Catal., 130 (1991) 314-317.

[57] D.R. Schryer, B.T. Upchurch, J.D. Van Norman, K.G. Brown, J. Schryer, Effects of pretreatment conditions on a Pt/SnO_2 catalyst for the oxidation of CO in CO_2 lasers, J. Catal., 122 (1990) 193-197.

[58] J.S. Spendelow, J.D. Goodpaster, P.J. Kenis, A. Wieckowski, Mechanism of CO oxidation on Pt(111) in alkaline media, J. Phys. Chem. B, 110 (2006) 9545-9555.

[59] M. Arenz, K.J. Mayrhofer, V. Stamenkovic, B.B. Blizanac, T. Tomoyuki, P.N. Ross, N.M. Markovic, The effect of the particle size on the kinetics of CO electrooxidation on high surface area Pt catalysts, J. Am. Chem. Soc., 127 (2005) 6819-6829.

[60] D.S. Strmcnik, D.V. Tripkovic, D. van der Vliet, K.C. Chang, V. Komanicky, H. You, G. Karapetrov, J.P. Greeley, V.R. Stamenkovic, N.M. Markovic, Unique activity of platinum adislands in the CO electrooxidation reaction, J. Am. Chem. Soc., 130 (2008) 15332-15339.

[61] C.A. Angelucci, E. Herrero, J.M. Feliu, Modeling CO Oxidation on Pt(111) Electrodes, J. Phys. Chem. C, 114 (2010) 14154-14163.

[62] J. Inukai, D.A. Tryk, T. Abe, M. Wakisaka, H. Uchida, M. Watanabe, Direct STM elucidation of the effects of atomic-level structure on Pt(111) electrodes for dissolved CO oxidation, J. Am. Chem. Soc., 135 (2013) 1476-1490.

[63] A.V. Rudnev, A. Kuzume, Y. Fu, T. Wandlowski, CO Oxidation on Pt(100): New Insights based on Combined Voltammetric, Microscopic and Spectroscopic Experiments, Electrochim. Acta, 133 (2014) 132-145.

[64] L.A. Lyon, J.T. Hupp, Energetics of the Nanocrystalline Titanium Dioxide/Aqueous Solution Interface: Approximate Conduction Band Edge Variations between H_0= −10 and H_-= +26, J. Phys. Chem. B, 103 (1999) 4623-4628.

[65] K.R. Reyes-Gil, Z.D. Stephens, V. Stavila, D.B. Robinson, Composite WO_3/TiO_2 nanostructures for high electrochromic activity, ACS Appl. Mater. Interfaces, 7 (2015) 2202-2213.

[66] S.A. Hayes, P. Yu, T.J. O'Keefe, M.J. O'Keefe, J.O. Stoffer, The Phase Stability of Cerium Species in Aqueous Systems, J. Electrochem. Soc., 149 (2002) C623-C630.

[67] N. Padmanathan, S. Selladurai, Electrochemical capacitance of porous NiO–CeO_2 binary oxide synthesized via sol–gel technique for supercapacitor, Ionics, 20 (2014) 409-420.

[68] Y. Katayama, T. Okanishi, H. Muroyama, T. Matsui, K. Eguchi, Enhanced Supply of Hydroxyl Species in CeO_2-Modified Platinum Catalyst Studied by in Situ ATR-FTIR Spectroscopy, ACS Catal., 6 (2016) 2026-2034.

[69] P.-Y. Olu, T. Ohnishi, D. Mochizuki, W. Sugimoto, Uncovering the real active sites of ruthenium oxide for the carbon monoxide electro-oxidation reaction on platinum: The catalyst acts as a co-catalyst, J. Electroanal. Chem., 810 (2018) 109-118.

Chapter 5 Use of Sn ad-atom modified Pt/C to explore details of the bifunctional mechanism of CO oxidation

5.1 Introduction

The addition of a second, or even third, metal component to form bi-/tri-metallic electrocatalysts offers a means of enhancing electrocatalytic activity through promotional effects and/or improving the atom-economy for precious metal-based electrocatalysts. The promotional effects of the second component (which may or may not be active) on the catalytic activity of the active host metal are usually attributed to the ligand mechanism, the strain mechanism, the ensemble mechanism, the bifunctional mechanism, or a combination of them. Among these mechanism, the bifunctional mechanism, where a second component provides a necessary intermediate at low overpotentials, has been considered as the major promotional mechanism in sluggish anodic reactions on Pt, such as CO and methanol oxidation in acidic solution[1-7] and H_2 oxidation in alkaline solution[8, 9]. For these anodic reactions, an oxophilic second component is often chosen so that oxygenated species are able to nucleate from water dissociation at potentials more negative than that on pure Pt, hence allowing the adsorbed species (Pt-CO_{ad}/H_{ad}) to be oxidatively removed at a much lower overpotential. The bifunctional mechanism was proposed in 1975 by Watanabe and Motoo [10, 11] to explain the promoted activity for methanol oxidation on Pt-Ru alloy and why the activity reaches the maximum on the Pt_1Ru_1 surface, although the following *in situ* studies demonstrated that Pt-Ru is not a typical bifunctional electrocatalyst as Ru can also adsorb CO under the same condition[12, 13]. Pt-Sn, Pt-Mo and Pt-W are typical bifunctional electrocatalysts for CO and methanol oxidation[5].

Although the bifunctional mechanism is well-acknowledged, debates are ongoing regarding the nature and electrochemistry of the second component, in particular determining at which potential the oxygenated species are present as well as their form. Take the well-studied Pt-Sn system for CO oxidation as an example, where the Sn can be multivalent, and the oxygenated species can be different in nature (adsorbed OH, H_2O, or the formation of a distinct oxide phase) and coverage. On practical Pt-Sn nanoparticle catalysts, the presence of Sn in any form (whether alloyed[14], as SnO_2[15, 16], or as mixtures of these[17-19]) is found to negatively shift the onset potential by a common value; ~0.4 V relative to the standard Pt/C. The details of the active oxygenated species and the formation of these species from water dissociation on the Sn sites are thus unclear. Hayden *et al*.[20] suggested this was Sn/Sn-OH in a study of Pt(111)/Sn surface alloys. They observed a redox couple at 0.28 V_{RHE}/0.15 V_{RHE} and associated it with the adsorption/desorption of hydroxide on the Sn sites, respectively. This redox couple assignment was supported by the observation that the

potential coincides with CO oxidation and by ex-situ photoelectron spectroscopy, which indicated the oxidation of alloyed Sn (0.1 V_{RHE}) to Sn^{II} (0.4 V_{RHE}). However, such a redox couple was not found on a $Pt_3Sn(111)$ alloy surface[7, 21], the surface of which had the same atomic arrangement as one of the Pt(111)/Sn surface alloys. In addition, an *in situ* infrared spectroscopy study on $Pt_3Sn(111)$ suggested that continuous oxidative removal of CO_{ad} begins at ~0.1 V_{RHE}[21], which is lower than the reduction peak of the proposed redox couple.

The oxidation state of Sn on a Pt surface can be also assessed by monitoring the underpotential deposition (upd) process of Sn. Sobkowski *et al*.[22] measured the surface coverage of upd Sn using an *in situ* radiotracer method, and by correlating the surface coverage with its effects on the voltammetric features they proposed the upd Sn is mainly Sn^{II}. Bittins-Cattaneo *et al*.[23] measured the charge required for Sn upd as a function of adsorption potential. By combining these results with the data from Sobkowski *et al*., the number of electrons required for the formation of an adsorbed Sn atom at each potential was obtained, suggesting that the oxidation state of the upd Sn gradually increases from Sn^0 (<0.25 V_{RHE}) to Sn^{II} and then to Sn^{IV}. Interestingly, from their cyclic voltammograms, no other extra redox peak can be associated with the Sn^0/Sn^{II} transition, apart from a characteristic redox couple at ~0.7 V_{RHE} commonly attributed to Sn^{II}/Sn^{IV}.

To probe the chemical nature of the each component of a bimetallic material, X-ray absorption spectroscopy (XAS) has unique advantages over other techniques, because it provides both electronic structure and local coordination specific to the element of interest, and it can be carried out *in situ* under electrochemical conditions[24, 25]. However, it also should be acknowledged that XAS is a bulk-averaging technique, unable to provide information exclusive to electrode surface unless the experiment is properly designed[25, 26]. Such *in situ* XAS measurements of the Pt-Sn system were first carried out by Mukerjee *et al*.[27] using upd Sn on Pt/C as a surface-sensitive probe. The oxidation state of Sn was found to increase with applied potential, but without the accompanying change in the number of oxygen neighbours. No Sn-Pt interaction was detected at potentials less than 0.25 V, which disagreed with Bittins-Cattaneo *et al*.'s finding described above. Recently, Seo *et al*.[28] performed a similar measurement but with Sn^{2+} dissolved in the acidic electrolyte. Compared with Mukerjee's study, they found that both the oxidation state of Sn and the number of oxygen nearest neighbours consistently increase with potential, and that the Sn-Pt interaction exists at potentials ≤ 0.25 V_{RHE}. A mismatch between the spectroscopy and electrochemistry can be revealed in Seo's work, by correlating the changes of the oxidation state and coordination with the dominant Sn^{II}/Sn^{IV} redox peak in the voltammogram; the former occurs at a much lower potential than the latter (-0.05–0.45 V_{RHE} *vs.* 0.5–0.9 V_{RHE}). This possibly arose from further Sn deposition (> 1 monolayer) after long polarisation in the Sn^{2+}-containing solution at potentials < 0.2 V_{RHE} [29], which can be also inferred from the presence of Sn-Sn interaction.

A consistent picture correlating structure, electrochemistry and *in situ* XAS is needed in order to truly understand how the Sn behaves on Pt under potential control and the nature/role of adsorbed

oxygenated species (Sn-OH) of the bifunctional mechanism. To do so a model catalyst exclusively with surface Sn ad-atoms on Pt is required, which maximises the portion of the bifunctional mechanism attributed to promotional effects and enables the quantitative study of the effect of Sn on the voltammetry and *in situ* XAS. To prepare this model catalyst, a surface organometallic chemistry (SOMC) approach, well-established for surface modification for metals and oxides[30-33], is chosen, via which naked and isolated Sn ad-atoms are able to be obtained by complete hydrogenolysis of an organotin complex by hydrogen chemisorbed hydrogen on a Pt surface. The Sn coverage on Pt can be straightforwardly controlled by the amount of the organotin precursor, and these Sn ad-atoms without oxygenated ligands are a good starting point for the current study.

In this study, such a model catalyst, Sn ad-atoms on Pt/C, was prepared, and the proposed structure confirmed by powder X-ray diffraction (XRD), scanning transmission electron microscopy-electron energy loss spectroscopy (STEM-EELS) microanalysis, and XAS. The effects of the Sn ad-atoms on CO oxidation were studied by CO stripping voltammograms as a function of Sn coverage. The oxidation state and local coordination of the Sn ad-atoms as a function of potential were assessed by *in situ* XAS. The combined analysis of the voltammetry, ex situ XAS, and *in situ* XAS results reveals the Sn species responsible for the bifunctional mechanism and the identity of the redox couple that generates this Sn species.

5.2 Experimental

5.2.1 Preparation of Sn_{ad}-Pt/C

Sn_{ad}-Pt/C was prepared by depositing Sn ad-atoms on the commercial Pt/C (60 wt%, Johnson Matthey, ~3 nm in diameter for the Pt particle size, Figure S5-1) using the surface organometallic chemistry (SOMC) approach[31, 34]. The synthesis was carried out in a gas-tight Schlenk tube equipped with a gas-inlet, a gas-outlet (connected to an oil-bubbler) and a septum. The atmosphere of the tube was controlled to be either N_2 or H_2 using a three-way valve, and the gas flow of both gases was regulated to be 40 ml min^{-1}. Into the reaction tube 120 mg of the Pt/C was loaded, and the air inside the tube was replaced by flowing N_2 for 20 min. Then, the gas was switched to H_2 **(FIRE RISK, never let Pt nanoparticles meet H_2 and air at the same time)** and maintained in constant H_2 flow for 20 min to reduce surface oxides of the Pt nanoparticles. To remove the resulting water vapour, the residual H_2 was first replaced by N_2 for 20 min at room temperature, and then the tube was heated to ~100 °C and maintained at the temperature for 30 min under N_2 flow. The reduced and dried Pt/C was cooled down under N_2 flow. Then, 2 ml anhydrous heptane solution containing the calculated amount of tetrabutyltin ($SnBu_4$, 96%, ACROS Organics) was added into the reaction tube using a syringe. The suspension was stirred for 10 min at room temperature in N_2. The atmosphere was then switched to H_2, followed by 30 min stirring at room temperature, 30 min at 50 °C and 2 hours at 90 °C. After the reaction the solid product was allowed to cool down to room temperature.

The residual H_2 inside the reaction tube was replaced by 20 min N_2 flow, and the gas out-let of the reaction tube was open to ambient atmosphere overnight, to passivate the synthesized catalyst by a small amount of air leaking into the reaction vessel (**FIRE RISK, never expose the freshly reduced sample to air directly**). The sample was stored in a gas-tight vial.

The Sn_{ad}-Pt/C samples with Sn coverage from 0.0033 ML to 0.2 ML were synthesized by varying the volume of the $Sn(Bu)_4$ heptane solution. The Sn coverage was relative to a saturated layer of adsorbed H on the Pt/C (assumed to be 1 ML) measured by cyclic voltammetry (yielding a charge density of ~120 C/g_{Pt}). The amount of $Sn(Bu)_4$ required for each coverage can be calculated using Faraday's law. The structural characterizations shown below were obtained using the sample with 0.2 ML Sn coverage, unless stated otherwise.

5.2.2 *In situ* XAS measurements

Sn_{ad}-Pt/C electrodes for the *in situ* XAS measurements were prepared so as to balance the needs of the electrochemistry and the spectroscopy and to avoid structural changes of the Sn ad-atoms. A catalyst paste (50 mg mL^{-1} in H_2O) was applied on one side of a carbon paper (TGP-H-60, Toray, with a microporous carbon layer), and then smoothened and dried mostly by sandwiching the electrode between a clean Kapton film (catalyst side) and a paper towel (carbon paper side) . A few drops of Nafion solution (1 wt% in 25 vol% IPA aqueous solution) were dropcast on top of the catalyst layer, and then dried mostly under an IR lamp. The electrode was pressed at 60°C to obtain a smooth layer, and then completely dried in a vacuum desiccator. The catalyst loading was calculated by subtracting the mass of the electrode with and without the catalyst layer. The catalyst loading of the electrode present in the text is ~5.8 mg cm^{-2} and the corresponding Sn loading is ~108 μg cm^{-2}, unless stated specifically.

The above preparation procedure and the catalyst loading were tested electrochemically using Pt/C to make sure that all Pt nanoparticles are electrically connected to carbon paper and accessible to electrolyte during the *in situ* XAS measurement. Pt/C test electrodes with a catalyst loading < 6.4 mg cm^{-2} were found to produce similar electrochemical surface areas in the *in situ* cell (see below) as that obtained for thin film-modified glassy carbon electrodes in a conventional electrochemical cell (Figure S5-2). This suggests that the catalyst is fully utilized in the *in situ* XAS measurements.

XAS spectra as a function of applied potentials were collected using a customized spectro-electrochemistry cell[35]. A flattened Au wire was used as a contact to the catalyst electrode, and a Pt coil as the counter electrode and a commercial RHE electrode (HydroFlex, Gaskatel GmbH) as the reference electrode. Before being loaded in the cell, each *in situ* electrode was flooded by water in a vacuum desiccator. The N_2-purged 1 M $HClO_4$ (TraceSELECT, Honeywell) was circulated through the cell using a peristaltic pump. The CV of the Sn_{ad}-Pt/C was reproduced in the spectro-electrochemistry cell (Figure S5-3).

The XAS spectra were measured under potential control. The potential was stepped from 0 V to 0.8 V in 0.2 V steps. The XAS spectra were collected after each step reached a plateau (Figure S5-3). Whilst both fluorescence and transmission spectra were collected at the Sn K edge, only fluorescence data will be presented as these had better signal-to-noise ratio. The effect of self-adsorption in the fluorescence spectra were confirmed to be insignificant in our data by comparing the spectra for: (i) a pellet sample that had 2 times higher Sn loading than the current *in situ* electrode, where we found that the transmission and fluorescence spectra overlapped (Figure S5-4, ~0.02 *vs.* ~0.01 in the edge step of transmission) and (ii) another electrode with decreased Sn loading, which produced identical but noisier spectra (Figure S5-5). The spectrum from a Sn foil placed in the reference channel was obtained simultaneously to allow energy calibration.

5.3 Results and discussion

5.3.1 XRD, TEM and aberration-corrected STEM-EELS microanalysis

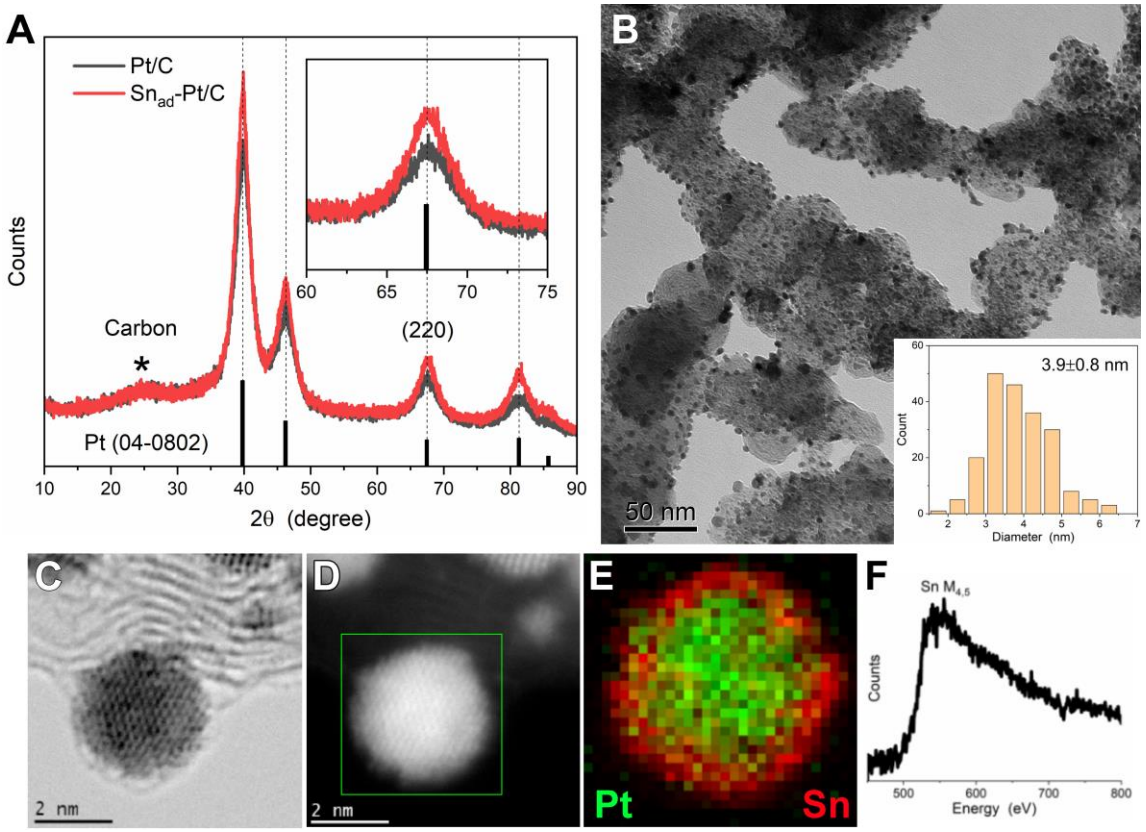

Figure 5-1 Structural characterisations of Sn_{ad}-Pt/C (0.2 ML). (A) XRD patterns of the Pt/C and the Sn_{ad}-Pt/C, along with the standard pattern of Pt (No. 04-0802, JCPDS database). The diffraction peak from carbon supports is highlighted by a star, and the patterns in 60°–75° are magnified in the inset. (B) A representative TEM image, along with (inset) the size distribution of the nanoparticles. (C) A BF-STEM image, (D) the corresponding HAADF-STEM image and (E) a STEM-EELS mapping image of Pt and Sn for a selected area (the green square in D, corrected by spatial drift). (F) a representative EELS at Sn $M_{4,5}$ edge at the edge of the particle in E (see Figure S5-7 for other EELS spectra and the corresponding areas). A similar distribution of Pt and Sn can be found from other regions as shown in Figure S5-8 and Figure S5-9.

Sn ad-atoms were deposited on a commercial Pt/C catalyst (60 wt%, JM), where 3~4 nm Pt nanoparticles are distributed evenly distributed on the Ketjen black carbon support with a small amount of agglomeration (Figure S5-1). Figure 5-1A compares XRD patterns of Sn_{ad}-Pt/C and Pt/C, along with the standard peak positions of face-centred-cubic (fcc) Pt. Sn_{ad}-Pt/C shows a nearly identical pattern as the starting material Pt/C, with a weak and broad peak of graphitized carbon at ~25° and a set of well-defined diffraction peaks assigned to the fcc Pt. The similarity in XRD pattern suggests that the long-range order of the Pt nanoparticles are unaltered after Sn deposition, and that the Sn species of Sn_{ad}-Pt/C are unlikely to exist as crystallized SnO_2 or alloyed Sn, which are the two main forms of Sn reported in Pt-Sn bimetallic nanoparticles[17, 36, 37]. Also, no obvious change in morphology is discernible in the TEM images before and after Sn deposition (Figure S5-1 and Figure 5-1B). From the width of the (220) peak, the crystallite size of Pt is estimated as ~3.2 nm for both Pt/C and Sn_{ad}-Pt/C, which is within the error of the particle size obtained from analysis of the TEM images (Figure S5-1and Figure 5-1B).

The presence and location of Sn in Sn_{ad}-Pt/C were studied using aberration-corrected STEM microanalysis. Figure 5-1C and Figure 5-1D show a nanoparticle on the edge of the carbon support. On this nanoparticle a Pt-core and Sn-shell configuration is clearly shown (Figure 5-1E and Figure S5-6), with an even shell of sub-nanometer thickness. A similar configuration was consistently obtained in the data for two other regions (Figure S5-8 and Figure S5-9). The nature of the surface Sn atoms was estimated by EELS. Figure 5-1F shows a typical Sn $M_{4,5}$ edge EELS spectrum of a selected area on the edge of the particles, and same spectra can be found along the edge (Figure S5-7). The spectra show features comparable to the Sn thin film reference (Figure S5-7), without the characteristic sharp peaks from O K-edge (~550 eV). The atomic thin Sn layer on the Pt nanoparticles and the absence of oxygen with Sn (at least under the electron microscopic conditions) are consistent with the mostly unaffected XRD patterns and TEM images before and after Sn deposition, providing direct evidence of the formation of Sn ad-atoms on Pt nanoparticles.

5.3.2 *Ex situ* XAS

After the general structure of Sn_{ad}-Pt/C was revealed, the detailed nature (speciation, oxidation state and coordination) of the Sn ad-atoms was further studied from the perspective of Sn using XAS. The XAS measurements were carried out at the Sn K-edge in air and in H_2(g). H_2(g) is used to reduce the surface oxides of the metallic nanoparticles and to mimic the environment used in the Sn deposition. Sn_{ad}-Pt/C samples with Sn coverage of 0.033 ML, 0.1 ML and 0.2 ML were studied by XAS, and their spectra were found to be largely similar (Figure S5-10 and Figure S5-11).

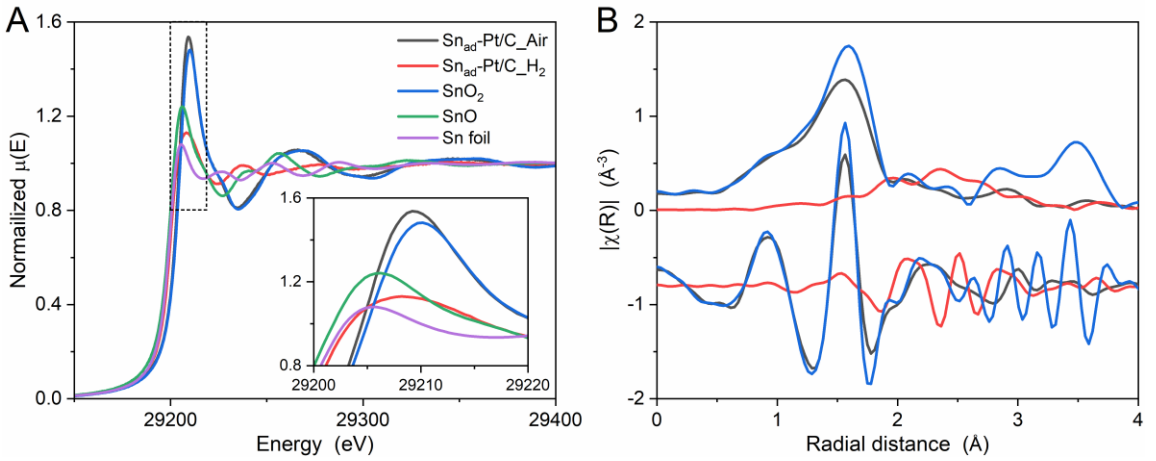

Figure 5-2 (A) XANES spectra and (B) Fourier transforms of k^2-weighted EXAFS spectra (the amplitude and the real part) of Sn_{ad}-Pt/C, measured in air and in H_2(g), along with those for the Sn references. The whiteline region is magnified in the inset. The Fourier transformation was carried out over a k range of 3.4–14.0 $Å^{-1}$, and the real part plots of Fourier transforms are shifted -0.6 $Å^{-3}$ for clarity. The comparison of the EXAFS of the samples with two other Sn references can be found in Figure S5-12. The Fourier transforms are not phase-corrected.

The XAS spectra of Sn_{ad}-Pt/C are extremely sensitive to the measurement atmosphere. Figure 5-2 shows the effects of air and H_2 in the XANES and EXAFS regions. The spectra measured in air are similar to those of SnO_2 in both XANES and EXAFS, but show much less intensity in the high *k* (>9 $Å^{-1}$) and high *R* regions (>2.2 Å). The fully oxidized Sn species of Sn-modified Pt/C in air was also reported using XPS[15]. Since the components of SnO_2 in these two regions can be mainly ascribed to two Sn–Sn scattering paths, as shown in the unit cell of rutile SnO_2 (Figure S5-13), the simple oscillation of the air data indicates that the Sn adatoms, although oxidised in air, lack long-range order, which is consistent with the XRD result. The coordination of Sn was quantitatively analysed by EXAFS fitting (Figure 5-3 and Table 5-1, Table S5-3 for samples with other Sn coverage). The Sn is saturated with ~6 oxygen neighbours in the first coordination shell as for rutile SnO_2, hence denoted as $[Sn^{IV}O_6]$. A disordered Sn–Sn scattering path with a slightly longer R than that of SnO_2 was also found, 3.27(1) Å *vs.* 3.200(9) Å. The CN of the Sn–Sn increased with Sn coverage (~0.8 for 0.033 ML, ~1.3 for 0.1 ML and ~1.6 for 0.2 ML), which indicates that the $[Sn^{IV}O_6]$ species are relatively isolated on Pt, with little connectivity to each other.

When in H_2, the $[Sn^{IV}O_6]$ is reduced and transformed completely (Figure 5-2). The XANES shows a sharp decrease in whiteline intensity and a negative shift in edge position, which indicates a significant decrease in the oxidation state of Sn, and a unique spectrum is found with comparable whiteline intensity and edge position as those of SnO and Sn foil, respectively. In the EXAFS, the dominant Sn–O measured in air diminishes, and a new scattering path becomes dominant at ~2.5 Å, which is attributed to Sn–Pt with CN = ~4.5 and *R* = ~2.69 Å (Figure 5-3 and Table 5-1). Sn neighbours in the first shell are completely absent because the formation of strong intermetallic bonds between Pt and Sn is favourable[38, 39], as also found in other Pt-Sn nanoparticles with low Sn

content[17, 18, 30, 40]. Thus, the fully oxidized [$Sn^{IV}O_6$] in air is completely reduced into Sn^0(Pt) in H_2(g). This starkly contrasting response in air and H_2(g) provides a strong evidence that all the Sn atoms of Sn_{ad}-Pt/C are reducible by H atoms formed by reaction of H_2 with the Pt surface, and thus are located on the Pt surface. These two extreme cases can thus be used as intrinsic references for the *in situ* XAS studies described below. The location of the Sn is also supported by the low CN of Sn–Pt (~4.5) relative to that of Pt_3Sn (12).

Further inspection of the structural parameters reveals that the CN of Sn–Pt decreases monotonously with the Sn coverage, 5.7(9) for 0.033 ML, 4.8(4) for 0.1 ML and 4.5(4) for 0.2 ML (Table S5-3). These values are closed to each other, and data from lower coverage samples and with better quality are required to fully understand the coverage-dependent CN(Sn–Pt). However, the current trend provides preliminary results inferring that the Sn was preferentially deposited on surface sites that maximise the coordination with Pt. From a structural model of Pt nanoparticles determined by atomic resolution STEM[41], the preferential order for Sn deposition could start from vacancy sites (CN=7~9) and step sites (CN = 5~6), followed by (111)/(100) terrace sites (CN=3~4). Similar site-preferential deposition can also be found in studies of the electrodeposition of Sn[42, 43] (and other p-block metals[44]) on stepped Pt surfaces.

Table 5-1 Structural parameters of Sn_{ad}-Pt/C (measured in air and in H_2), obtained from EXAFS fitting[a]. Plots of the data and the corresponding fits are shown in Figure 5-3.

Sample	Scattering path	R (Å)	N	σ^2 (x10^3 Å^2)	ΔE_0 (eV)	R factor (%)
Sn_{ad}-Pt/C_Air	Sn–O	2.051(3)	6.4(2)	6.6(4)	2.2(4)	0.26
	Sn–Sn	3.272(9)	1.6(4)	9(2)		
Sn_{ad}-Pt/C _H_2	Sn–Pt	2.690(7)	4.5(4)	8.8(6)	-3(1)	1.17
SnO_2	Sn–O	2.053(5)	6.1(4)	4.0(7)	4.0(8)	0.79
	Sn–Sn_1	3.200(9)	1.2(5)	3(2)		
	Sn–Sn_2	3.725(7)	2.2(8)	2(2)		
Pt_3Sn[b]	Sn–Pt	2.829	12	N.A.	N.A.	N.A.

[a] R is the distance between the absorber–scatterer pair, N is the coordination number, σ^2 is the Debye-Waller (disorder) factor, ΔE_0 is the shift in the edge energy, and R factor is a measure of the goodness of fit.
[b] calculated from Pt_3Sn crystal (ICSD 105796) using Feff6.

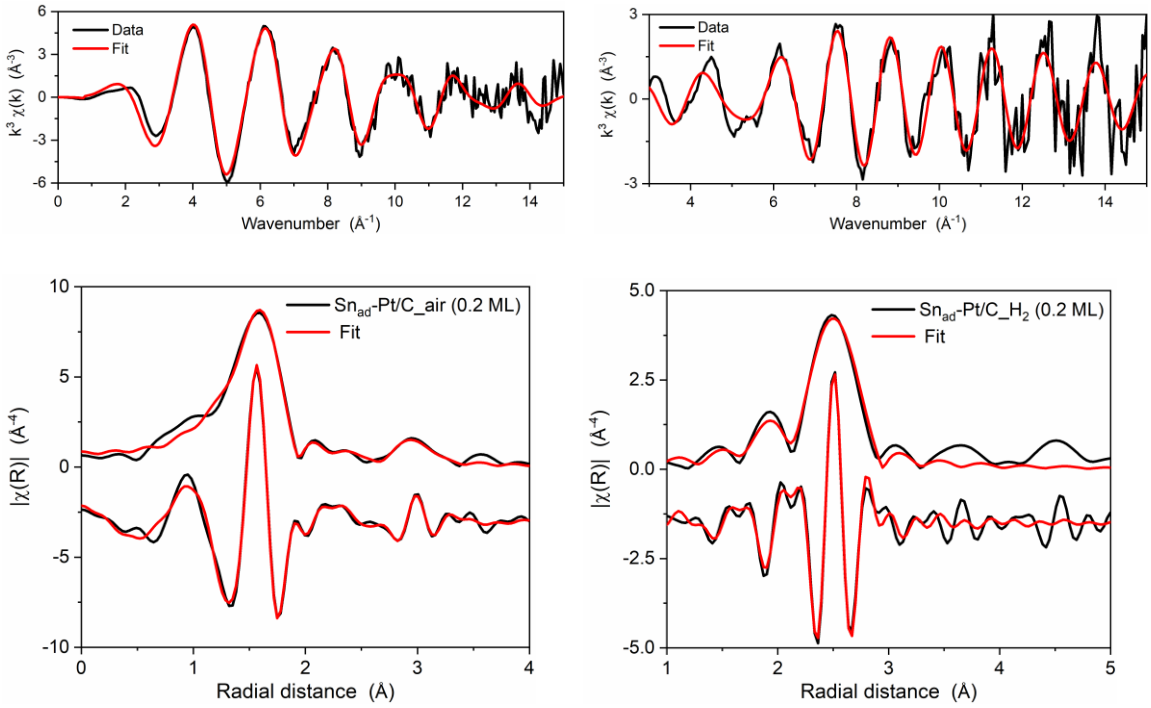

Figure 5-3 Fits for Sn K-edge EXAFS spectra of the Sn_{ad}-Pt/C sample (0.2 ML Sn coverage), showing as k^3-weighted (top panels) k space and (bottom panels) the magnitude and the real part of R space. Both the spectra measured in (left panels) air and (right panels) H_2(g) are shown. For the air data, The Fourier transformation was performed in a k range of 3.4–14.0 Å^{-1}, and the fitting was carried in a R-range of 1.0–3.2 Å, and for the H_2 data, the Fourier transformation was performed in a k range of 5.8–14.0 Å^{-1}, and the fitting was carried in a R-range of 1.2–3.2 Å.

5.3.3 CO stripping

The promotional role of these potentially redox-active Sn ad-atoms for the CO oxidation was then studied using CO stripping voltammetry. On each catalyst-modified electrode a saturated CO adlayer was adsorbed at 0.1 V, and then oxidatively removed by sweeping to 0.9 V in N_2-saturated 0.1 M $HClO_4$ solution. The completeness of the stripping was assessed by monitoring successive CV cycles. On all samples, the desorption of underpotential deposited H is completely suppressed by adsorbed CO (CO_{ad}) in the 1st sweep (Figure 5-4A) and re-emerges in the successive cycles (Figure 5-4B, Figure S5-17). The parent Pt/C catalyst shares a typical CO stripping voltammogram with polycrystalline Pt, showing negligible Faradaic current before ~0.65 V and a single but composite peak at ~0.8 V with a shoulder at ~0.72 V. The shoulder can be attributed to the slight aggregation of Pt nanoparticles due to the high Pt loading (60 wt%)[45-47] as shown in the TEM image.

With the addition of Sn ad-atoms, the CO adlayer oxidation on Pt is highly promoted and becomes more complicated. Generally, the onset potential is shifted to ~0.25 V (Figure 5-4 inset), which is 0.4 V lower than that of Pt/C, and instead of a single sharp peak the voltammograms become a doublet or even a triplet stretching over a potential range of ~0.6 V. At high Sn coverage (≥0.1 ML), the voltammetric profiles are in line with those of Pt-Sn alloy nanoparticles[14, 18, 48], with the

main peak of CO oxidation being shifted to 0.7 V and an additional shoulder at ~0.5 V. Decreasing the Sn coverage, although producing few and subtle changes on the main peak at 0.7 V, has obvious effects on the wave at ~0.5 V and the Pt peak at ~0.8 V. Whilst the decreased charge of the Pt peak can be easily understood by the decreased number of pure Pt ensembles as the Sn coverage increases, the coverage-dependence of the wave in terms of charge and onset potential indicates the direct involvement of the Sn ad-atoms in CO oxidation at low potential, probably via the bifunctional mechanism. Note that the origin of the features at ~0.7 V is complex and may include decreased CO coverage due to the wave at lower potential, and the presence of oxygenated species, the formation of which are promoted by the neighboring Sn atoms. However, this aspect is not the focus of the study described herein.

The surface electrochemistry of Sn_{ad}-Pt/C without CO_{ad} was also studied by the successive cycles of CO stripping voltammograms (Figure 5-4B). The voltammogram of Pt/C shows a typical profile of polycrystalline Pt in $HClO_4$ solution, which can be divided into three regions, a pseudocapacitance in 0.05–0.4 V for reversible adsorption and desorption of underpotential deposited H on Pt (denoted as H_{upd} region), a redox couple at ~0.8 V for irreversible Pt oxide formation and reduction (denoted as oxide region) and double layer charging current in between (~0.5 V, denoted as DL region).

All these potential regions are altered by the presence of Sn ad-atoms, and the extent depends on the Sn coverage. Starting with the oxide region, a new irreversible redox peak develops with increasing the Sn coverage in terms of charge and potential, at ~0.72 V in the forward sweep and ~0.66 V in the backward sweep for low Sn coverages (<0.1 ML), and a ~0.7 V/~0.55 V pair for high Sn coverages (≥0.1 ML), which is characteristic of Sn-modified Pt surfaces[22, 29, 49-51] and of Pt_3Sn alloys[14, 52, 53]. Opposite to this trend, the charge of the pristine Pt oxide formation at ~0.85 V decreases with Sn coverage.

For the DL region, the increased charge with Sn coverage becomes obvious when the coverage is higher than 0.01 ML. Compared with the previous CO stripping sweeps, the DL capacitance shown in 0.05–0.2 V remains constant with Sn coverage. In addition, from the above structural characterisation no discernible change of general structure was found after Pt/C modified by Sn. Thus, the increased charge at ~0.5 V is probably not due to double layer charging, but instead to the Faradaic current relating to the oxidation of the Sn ad-atoms. This electrochemically activity of the Sn ad-atoms in the DL region may also be inferred from literature in studies of the stepwise stripping of Sn ad-atoms[23, 49, 50]. However, the early Sn oxidation and the onset potential, which could be crucial to understand the bifunctional mechanism of CO oxidation at low potential, have not previously been discussed in detail.

In contrast to the oxide region and the DL region, the pseudocapacitance of the H_{upd} region decreases with Sn coverage, which is as expected because Sn ad-atoms block the H adsorption sites of Pt and weaken the H adsorption of Pt atoms adjacent to the Sn[54]. Further inspection reveals that the extent

of the decrease is more pronounced at the peak related to (110) sites (~0.12 V) [55], supporting the preferential deposition of Sn ad-atoms found from the EXAFS fitting.

It is well-established that CO oxidation on Pt follows a Langmuir–Hinshelwood (L-H) mechanism (eq. 1)[2-6], via which adsorbed CO on a Pt site (Pt-CO_{ads}) reacts with the adjacent hydroxide species on metal sites (M-OH_{ads}), yielding a free Pt site and a free metal sites (M*), and the CO_{ads} and OH_{ads} may or may not form at the same site, even on pure Pt surfaces[3, 56].

$$Pt\text{-}CO_{ads} + M\text{-}OH_{ads} + H_2O \rightarrow Pt + M^* + CO_2(aq) + H_3O^+ + e^- \quad \text{(eq. 1)}$$

With the modification of Sn ad-atoms, the situation gets even more complex, as shown in the CO stripping voltammograms. The active M-OH species on the Pt-Sn surface could be Sn-OH from the water dissociation on the Sn ad-atoms (i.e. the bifunctional mechanism)[20] or Pt-OH, the formation of which could be promoted by the neighboring Sn that lowers the local work function of Pt atoms[7, 36, 57](i.e. the ligand mechanism, also see examples of other p-block metals on Pt surface[44, 58, 59]). These two cases, although both possible, operate in different potential ranges and the CO oxidation at low potential (0.2–0.5 V) is mainly attributed to the bifunctional mechanism of Sn-OH. If, however, the Pt-OH participates at such low potentials, then Pt-OH would co-exist with Pt-H at the terrace sites. In contrast participation of Pt-OH at the step/defect sites is unlikely as these are occupied by Sn ad-atoms at high Sn coverage as shown in blank CV and ex-situ EXAFS fitting. Also, DFT calculations on Pt_3Sn (111) suggest that OH interacts preferentially with the Sn over the Pt[57, 60]. Thus, the main operative route for CO oxidation at low potential is via the bifunctional mechanism with Sn-OH species.

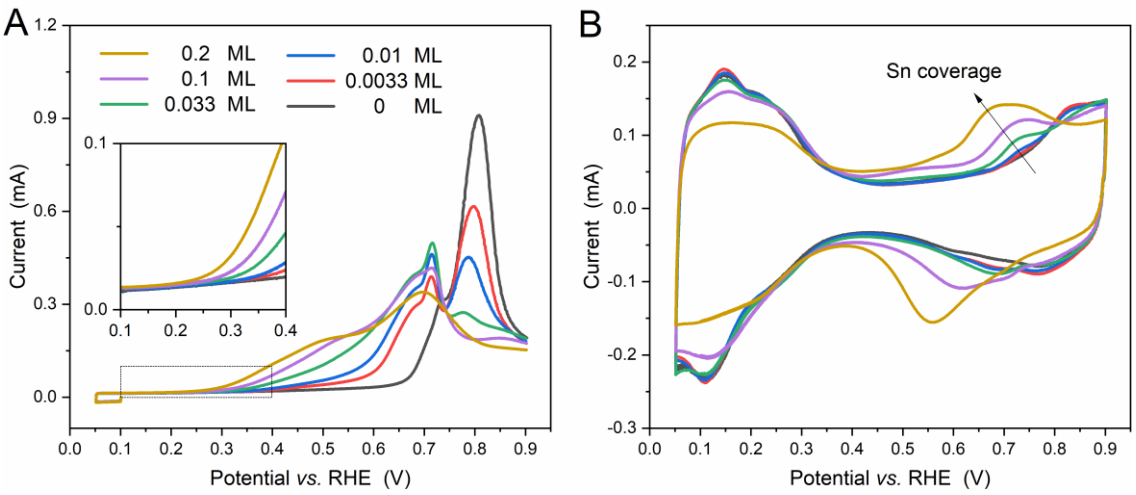

Figure 5-4 CO stripping voltammograms of Sn_{ad}-Pt/C samples (Sn coverage from 0 ML to 0.2 ML). (A) 1st forward sweeps and (B) 2nd CV voltammograms of Sn_{ad}-Pt/C in N_2-saturated 0.1 M $HClO_4$ solution with a scan rate of 20 mV s^{-1}. The saturated CO adlayer was adsorbed by potential hold at 0.1 V, followed by displacement of dissolved CO from the solution by at least 30 min N_2 purge.

5.3.4 *In situ* XAS

Considering the contrasting coordination the Sn ad-atoms measured in air and in H_2, the Sn ad-atoms may or may not have direct interaction with Pt, and the number of oxygen containing ligands may vary with potential. The identity and electrochemistry of the Sn-OH are now questions of interest, especially at low potential when the Sn-OH is the sole active species. Examining the CO stripping voltammograms of Sn_{ad}-Pt/C (Figure 5-4), the onset potential of CO_{ad} oxidation is ~0.4 V lower than that of the characteristic redox peaks for surface Sn (0.6–0.7 V), indicating that the commonly believed redox couple cannot be attributed to the CO oxidation at low potential. Alternatively, a Faradaic process happening in the DL region may be responsible for providing Sn-OH species. Due to the overlap of the pseduocapacitance of H_{upd}, the process may start in the H_{upd} region or even lower.

To ascertain the nature of the electrochemically active Sn ad-atoms, *in situ* XAS measurements were carried out in N_2-saturated 1 M $HClO_4$ under potential control from 0 V to 0.8 V with a 0.2 V interval (Figure S5-3). In both XANES and EXAFS regions the spectra measured under potential control fall in-between the spectra measured in H_2 and in air (Figure 5-5 and Figure S5-20), indicating that the Sn ad-atoms in the potential range are neither fully reduced nor fully oxidized.

A potential dependence is clearly observed in the *in situ* XAS data. In the XANES, the whiteline intensity changes little between 0 V and 0.2 V (~1.17), increases gradually from 0.2 V to 0.6 V (~1.26), and jumps to the maximum at 0.8 V (~1.43), consistent with the positive shift of the edge position (Figure 5-5A inset). Assuming the oxidation states of the Sn ad-atoms are proportional to the whiteline intensity regardless of coordination, the average Sn oxidation states under potential control can be estimated using the ex situ data as the references for 0 and +4 oxidation state, gradually increasing from 0.2 to 3.1 for the Sn from 0 to 0.8 V as shown in Figure 5-6A. The oxidation of the Sn ad-atoms was also quantified electrochemically for the same electrode. From the voltammograms the number of electrons lost per Sn atom (N_{eL}) is estimated using eq. 2:

$$N_{eL} = C/(C_0 \times \theta_{Sn}) \quad \text{(eq. 2)}$$

Where the C is the charge difference between Sn_{ad}-Pt/C and Pt/C in a given potential range, C_0 is the charge corresponding to the transfer of one electron per Pt atom on the surface, obtained from the H_{upd} desorption (assumed to be 1 ML), and θ_{Sn} is the Sn coverage. N_{eL} was found to be ~ 0.7 over the potential range of 0.4–0.6 V and ~2.0 between 0.6–0.8 V, in good agreement with the difference of the average oxidation state in the same potential range (Figure 5-6A) and with Bittins-Cattaneo *et al.*'s work on the upd process of Sn^{4+} on Pt[23].

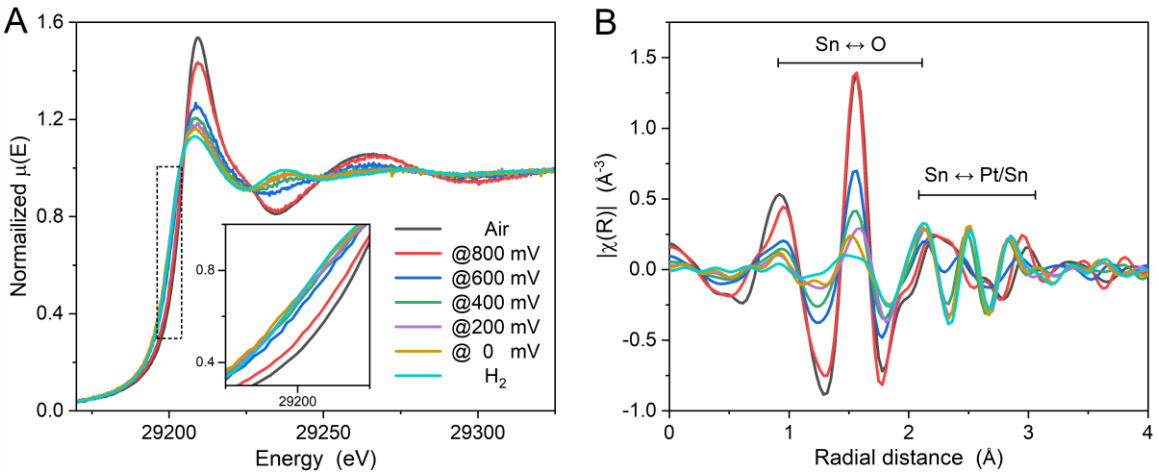

Figure 5-5 (A) In situ XANES spectra and (B) Fourier transforms of k_2-weighted EXAFS spectra (the real part) of a Sn_{ad}-Pt/C (0.2 ML) painted electrode under potential control in N_2-satureated 1 M $HClO_4$ solution, along with Sn_{ad}-Pt/C pellet samples measured in air and in H_2(g). The applied potentials are against a reversible hydrogen electrode. The Sn loading on the electrode is ~108 $\mu g_{Sn}/cm^2$. The Fourier transformation was carried out over a k-range of 3.4–12.2 $Å^{-1}$.

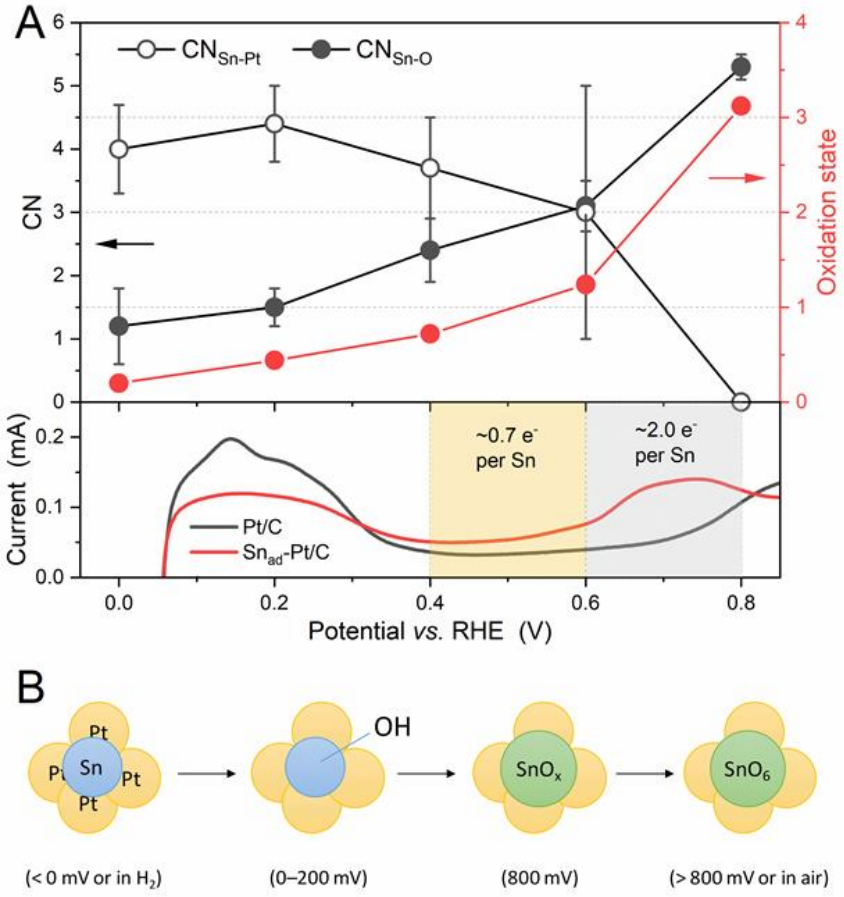

Figure 5-6 Potential-dependence of Sn_{ad}-Pt/C. (A) CN(Sn–O), CN(Sn–Pt), oxidation state and current as a function of applied potentials. The voltammograms was also present for comparison, and the voltammograms were collected using RDE measurements in N_2-saturated 0.1 M $HClO_4$ solution with a scan rate of 20 mV s^{-1}. (B) Schematic illustration of the speciation of the Sn ad-atoms as a function of applied potentials.

In the EXAFS (Figure 5-5B), whilst the Sn–O oscillation (1–2 Å in the real part of the Fourier transform) increases with potential in terms of amplitude, the Sn–Pt oscillation (2–3 Å) is largely unaffected from 0 V to 0.4 V and is distorted at 0.6 V. Further examination of the Fourier transform shows that the Sn-Pt contribution is replaced by Sn–Sn at 0.8 V. When the potential is stepped from 0.8 V back to 0 V, the spectral features of the 0 V data can be reproduced (Figure S5-18 and Figure S5-19).

From the potential dependence in both XANES and EXAFS, some puzzles from the voltammetric studies can be answered. From 0.05–0.2 V no observable electrochemical reaction occurs on Sn, whilst in the DL region the additional charge is shown to correspond to the partial oxidation and oxygenation of Sn ad-atoms. The oxidation peak at ~0.7 V then corresponds to the further oxidation of the Sn ad-atoms, which is accompanied by loss of the Sn-Pt interaction.

The speciation of the Sn ad-atoms under potential control was further identified using EXAFS fitting. The fits are shown from Figure 5-7 to Figure 5-9 with the structural parameters obtained listed in Table 5-2. The discussion of the data below is divided into three potential regions, 0–0.2 V, 0.4–0.6 V and 0.8 V. Because of the similarity at 0 V and 0.2 V, only spectra at 0.2 V are described.

At 0/0.2 V, the Sn ad-atoms share a similar local coordination environment with that in H_2, with the same number of Pt neighbors (~4.5), but also have ~1.5 oxygen neighbors. Both the Sn-Pt and Sn-O bonds are weakened as evidenced by the increase in R(Sn–Pt) is ~2.73 Å, 0.04 Å longer than that of Sn^0(Pt), and R(Sn–O) is ~2.08 Å, 0.03 Å longer than that of the [$Sn^{IV}O_6$]. These differences in bond distance suggest that the Sn species at 0/0.2 V is not a simple physical mixture of [$Sn^{IV}O_6$] and Sn^0(Pt). The identity of the oxygenated ligand can be inferred from R(Sn–O), which could be either Sn-OH or Sn-(H_2O). Whilst the bond distance between water and metal ions/metal surface is generally 0.1~0.2 Å longer than that with OH[61, 62], only an increase of 0.01~0.02 Å was found in R(Sn–O) of the intermediates compared to $Na_2Sn(OH)_6$ (2.08~2.09 Å *vs.* 2.071 Å). Thus, the oxygenated ligand is likely to be Sn-OH rather than Sn-(H_2O). To summarise, the intermediates at 0/0.2 V can be estimated to have an averaged composition as $Pt_{4.5}$Sn-$(OH)_{1.5}$ (henceforth denoted as Pt-Sn-OH for simplicity). Transferring this speciation to the electrochemistry indicates that this Pt-Sn-OH, the only oxygenated species available around the onset of CO oxidation, is responsible for the bifunctional mechanism in this low potential region (eq. 3).

$$Pt\text{-}CO_{ads} + Pt\text{-}Sn\text{-}OH \rightarrow Pt + Pt\text{-}Sn^* + CO_2(aq) + H_3O^+ + e^- \quad \text{(eq. 3)}$$

When the potential increases to 0.4 V and 0.6 V, the Pt-Sn-OH is further oxidized, with an increase of CN(Sn–O) at the expense of CN(Sn–Pt). The Pt-Sn part of the intermediate becomes distorted at 0.6 V, suggested by increase of the bond length and Debye Waller (disorder) factor of the Sn-Pt.

Further increasing potential to 0.8 V transforms Sn-Pt into Sn-O. However, the oxidation to [$Sn^{IV}O_6$] is not complete, with only ~4.7 oxygen neighbors found. Based on the similarity with the Sn-O and

Sn-Sn scattering paths of the ex situ air data, the Sn species at 0.8 V can be considered as $SnO_{4.7}$, a partly reduced form of $[Sn^{IV}O_6]$ with an unsaturated oxygen shell and decreased oxidation state (henceforth denoted as SnO_x for simplicity). Since the Pt-Sn bonds, a direct interaction between Sn and Pt are not observed at this potential, the SnO_x species may or may not stay on the Pt surface, which could cause Sn dissolution as reported on Pt-Sn catalysts at similar potentials[19, 43, 49]. However, on our Sn_{ad}-Pt/C the loss of Sn signal is indiscernible during the spectra collection at 0.8 V (~20 min, Figure 5-10), and the $Pt|SnO_x$ can be transformed back to the Pt-Sn-OH configuration when the potential is applied back to 0 V (Figure 5-9 and Table 5-2). This suggests that the SnO_x largely remains its original location at 0.8 V and that oxygen-bridges are likely to exist between the Sn ad-atoms and the substrate Pt even after the destruction of Sn-Pt bonds, forming $Pt|SnO_x$.

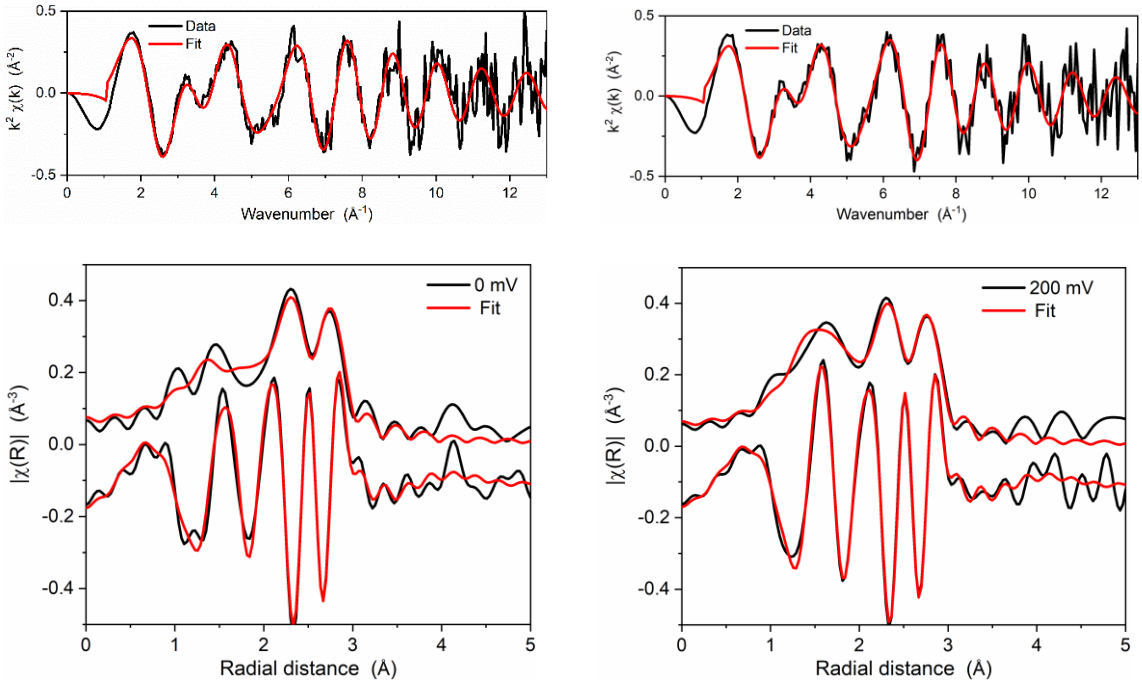

Figure 5-7 Fits for Sn K-edge EXAFS spectra of Sn_{ad}-Pt/C samples, measured under potential control of 0 V (left panels) and 0.2 V (right panels), showing as k^2-weighted (top panels) k space and (bottom panels) the magnitude and the real part of R space. The Fourier transformation was performed in a k range of 2.3–12.2 $Å^{-1}$, and the fitting was carried in a R-range of 1.0–3.2 Å.

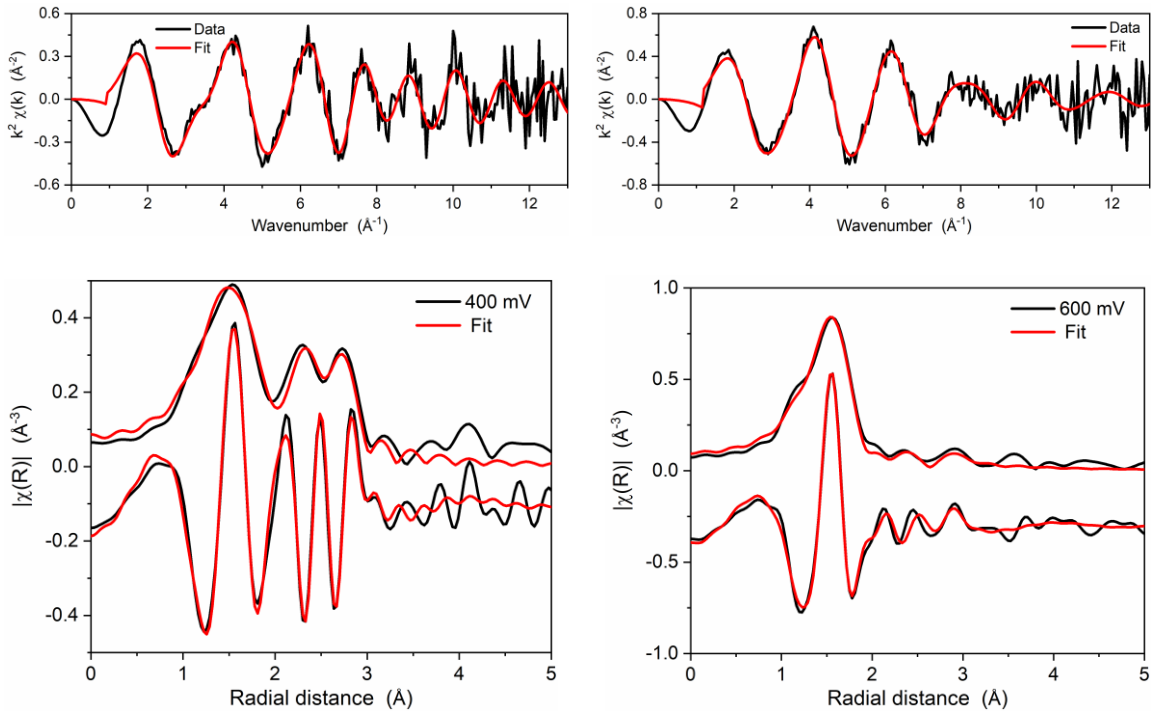

Figure S5-8 Same as Figure 5-7 but for the Sn_{ad}-Pt/C samples, measured (left) at 0.4 V and (right) at 0.6 V.

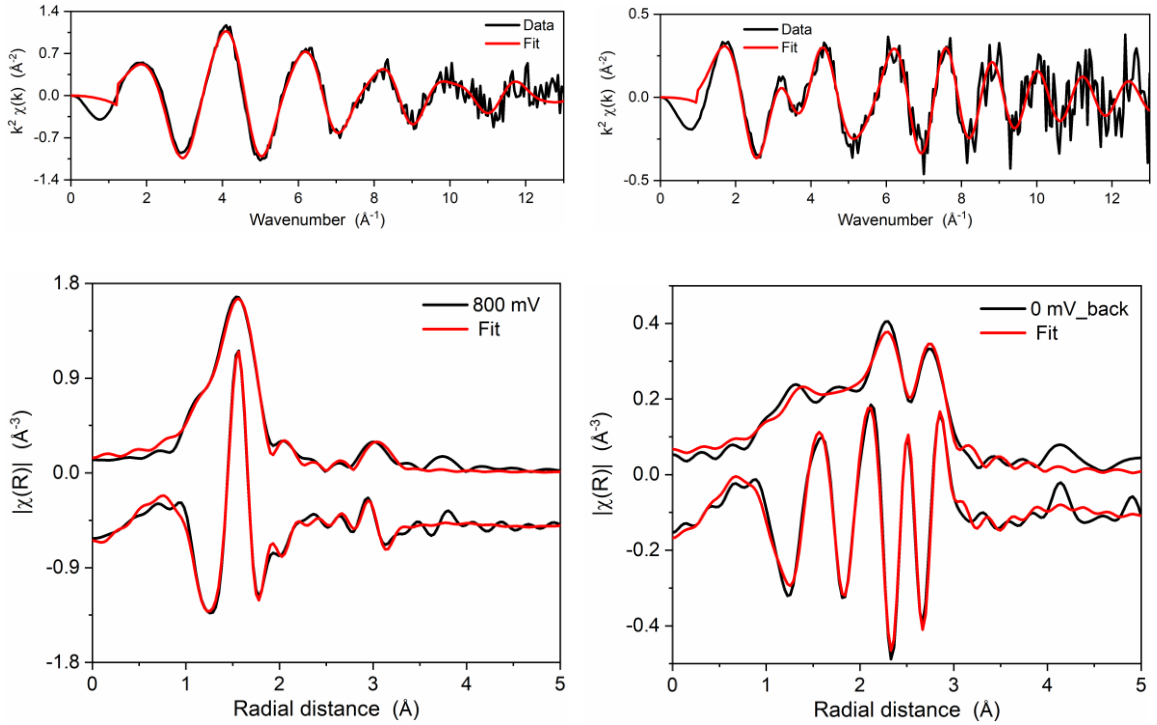

Figure 5-9 Same as Figure 5-7 but for the Sn_{ad}-Pt/C samples, measured (left) at 0.8 V and (right) at 0 mV_back.

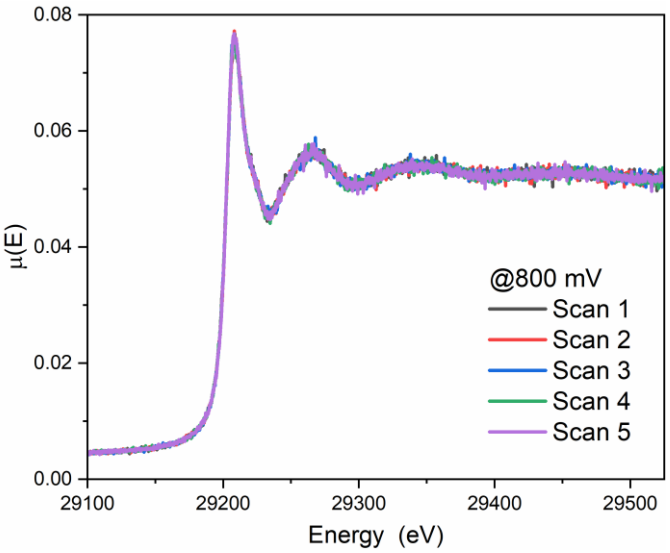

Figure 5-10 Raw *in situ* XAS spectra of Sn_{ad}-Pt/C at 0.8 V, showing that no significant loss of the fluorescence signal was observed during the measurements (20 min in total)

Table 5-2 Structural parameters of Sn_{ad}-Pt/C (0.2 ML) under potential control from 0 V to 0.8 V, obtained from EXAFS fitting. The fitting k-range is 2.3–12.2 $Å^{-1}$ unless specified. Plots of the data and the corresponding fits are shown in figures from Figure 5-7 to Figure 5-9

Sample	Scattering path	*R* (Å)	*N*	σ^2 (x10^3 $Å^2$)	ΔE_0 (eV)	R factor (%)
0 V	Sn – O	2.09(1)	2.1(7)	22(8)	4.2(7)	2.9
	Sn – Pt	2.718(7)	4.5(4)	9.1(9)		
0.2 V	Sn – O	2.083(6)	1.6(2)	9(2)	4.5(4)	1.0
	Sn – Pt	2.728(4)	4.4(3)	9.0(6)		
0.4 V	Sn – O	2.048(8)	2.2(3)	9(2)	3.3(9)	1.8
	Sn – Pt	2.703(8)	3.1(4)	8(1)		
0.6 V	Sn – O	2.051(9)	2.6(2)	5(1)	5.4(9)	2.1
	Sn – Pt	2.75(2)	2.3(9)	15(6)		
0.8 V	Sn – O	2.056(6)	4.7(2)	3.6(8)	5.5(6)	0.93
	Sn – Sn	3.27(2)	2(1)	9(4)		
0 V_back	Sn – O	2.084(9)	1.8(4)	18(5)	3.7(5)	1.4
	Sn – Pt	2.720(5)	4.7(3)	10.0(7)		

5.3.5 CO bulk oxidation

As shown above, the Sn atoms for Sn_{ad}-Pt/C are oxygenated throughout 0–0.8 V but the extent of oxygenation is stepwise and potential-dependent, starting from Pt-Sn-(OH) in 0–0.2 V and being oxidized to Pt|SnO_x at 0.8 V (Figure 5-6B). If the Sn species in 0.4–0.6 V is considered as a part of reaction from the Pt-Sn-OH to Pt|SnO_x, the electrochemistry of the Sn ad-atoms can be written as two redox couples, Pt-Sn*/Pt-Sn-OH and Pt-Sn-OH/Pt|SnO_x. Whilst the latter represents an irreversible redox couple in the DL and oxide regions, as identified by the above *in situ* XAS spectra, the former that generates one of the reactants of the bifunctional mechanism (Pt-Sn-OH) is not confirmed, i.e. once consumed via eq.1, Pt-Sn-OH may or may not be regenerated, as the *in situ* XAS sample is reduced from the fully oxidized Sn_{ad}-Pt/C by potential hold at 0 V.

If the bifunctional mechanism from Pt-Sn/Pt-Sn-OH is able to operate in a continuous fashion at low overpotential (eq.3), the two reactants have to be supplied from the corresponding channels, from the Pt-Sn/Pt-Sn-OH redox couple generating hydroxide species and from the regeneration of Pt-CO_{ads}, which includes mass-transport of dissolved CO to the electrode surface (eq. 4) and the subsequent adsorption of the CO on the available Pt sites (eq. 5).

$$CO(aq) \rightleftharpoons CO_{surface} \quad \text{(eq. 4)}$$

$$CO_{surface} + Pt \rightarrow Pt\text{-}CO_{ads} \quad \text{(eq. 5)}$$

To probe the Pt-Sn/Pt-Sn-OH redox couple, the CO channel needs to be saturated. Figure 5-11A shows CO bulk oxidation voltammograms of the Sn_{ad}-Pt/C in a rotating disc experiment in CO-saturated 0.1 M $HClO_4$ solution, along with that for Pt/C (Figure S5-22 for each sample). With constant supply of CO(aq), the Sn_{ad}-Pt/C samples show stable currents over many cycles and produce rotation-rate-dependent currents at high overpotentials, indicating that the Pt-Sn-OH is not depleted by CO oxidation but can be regenerated from the proposed Pt-Sn/Pt-Sn-OH redox couple by water dissociation (eq.6).

$$Pt\text{-}Sn^* + 2H_2O \rightarrow Pt\text{-}Sn\text{-}OH + H_3^+O + e^- \quad \text{(eq. 6)}$$

Compared to CO adlayer oxidation, where the CO coverage decreases with potential sweeping, the bulk CO oxidation current is highly promoted with constant supply of CO in a potential window of 0.05–0.6 V (Figure S5-22). This positive reaction order of CO coverage indicates that the rate-determining step of charge transfer is not Pt-Sn-OH formation (eq. 4) but the L-H reaction (eq.1). If the opposite holds true, then the CO bulk oxidation current would not increase by increasing the mass transport of CO by increasing the rotation rate (Figure S5-22).

Comparison of the CO oxidation data from the Sn ad-atoms with those from Pt-SnO_2 studied in Chapter 4 reveals similar bifunctional mechanism, but the origin was proposed differently, $(SnO_2)Sn^{IV}(OH)_2/(SnO_2)Sn^{II}$ for the Pt-SnO_2 and Pt-Sn*-OH/Pt-Sn^0 for the Sn ad-atoms on Pt. First,

whilst the Pt-Sn*-OH can be confirmed by in situ XAS as the active species for CO oxidation at low potentials, the active Sn-OH of Pt-SnO_2 is still unclear, which requires further *in situ* experiments. However, from the current *ex situ* results, I think that the active Sn-OH of Pt-SnO_2 is unlikely to be the same as the Pt-Sn*-OH of the Sn ad-atoms for two reasons. One is that XAS data measured in H_2 (a strong reducing condition relative to the measured potential range for CO oxidation) does not suggest the formation of Sn-Pt bonds; another one is that the similar CO oxidation activity can be found on two controlled samples, physical mixture of commercial SnO_2 nanoparticles and Pt/C and commercial SnO_2 nanoparticles on Pt disk electrodes, which unlikely contains surface alloyed Sn during the preparation.

Second, the redox couples generating OH species are different, $(SnO_2)Sn^{IV}(OH)_2/(SnO_2)Sn^{II}$ for SnO_2 surface (~-0.1 V, obtained using voltammetry) and Pt-Sn*-OH/Pt-Sn^0 for the Sn ad-atoms (<0 V, estimated using *in situ* XAS), and the relative close redox potential can be inferred from the standard electrode potentials of $SnO_2/Sn(OH)^+$ and Sn^{2+}/Sn, which are also close (-0.194 V vs. -0.1375 V). Third, as discussed in Chapter 4, a viable redox couple that provides OH requires appropriate redox potential, not too high (less than the Pt) and not too low (too strong for the metal-OH bond, such as TiO_2 shown in Chapter 4), and thus the similar redox potential of the Sn ad-atoms and SnO_2 surface enable comparable kinetics of OH formation (unknown, but faster than the L-H reaction). Thus, although the active redox couples from SnO_2 surface and Sn ad-atoms act similar in providing OH in the bifunctional mechanism, they are different in nature.

Further inspection reveals that CO bulk oxidation voltammograms are highly dependent on the Sn coverage in terms of the rotation-rate-dependent current, the potential shift and Tafel slope (Figure 5-11B and Figure 5-12). The increased current can be attributed to the increased number of Sn-OH with Sn coverage as per the rate-determined L-H step. The decreased Tafel slope at low Sn coverage (0.01 ML and 0.0033 ML) then presumably results from the coverage-dependent coordination environments of Sn suggested by the EXAFS fitting, which changes the geometry of the Pt-CO_{ad} + Pt-Sn-OH active sites[21, 50]. However, the negative shift of voltammetric profiles with Sn coverage cannot be simply rationalized by the Sn-OH part of the L-H reaction, but probably due to the Pt-CO part. Considering the Sn ad-atoms at low potential interact with both Pt and OH, the Pt-CO bond can be weakened by a combination of ligand effects from strong Sn-Pt intermetallic bonds[57, 63, 64] and intermolecular repulsion between the co-adsorbed Pt-CO and Sn-OH[7]. Such a negative shift of onset potential for CO oxidation can also be found on Sn-modified Pt(110)[50] and Pt stepped surfaces[42, 43].

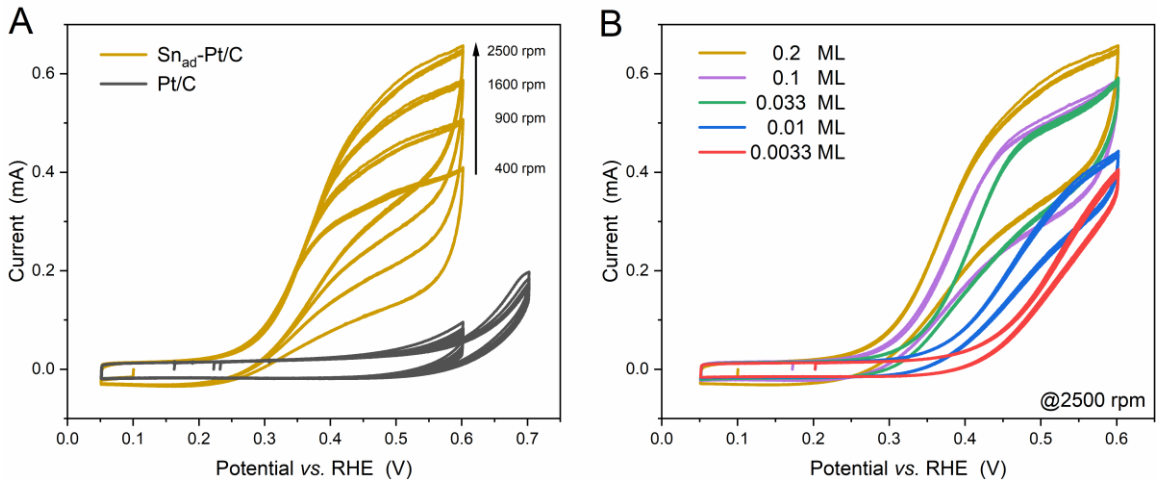

Figure 5-11 (A) CO continuous oxidation voltammograms of Sn_{ad}-Pt/C (0.2 ML) with the rotation rates from 400 rpm to 2500 rpm, and (B) the voltammograms of Sn_{ad}-Pt/C with Sn coverage from 0.0033 ML to 0.2 ML at 2500 rpm. The measurements were carried out in CO-saturated 0.1 M $HClO_4$ solution with a scan rate of 20 mV s^{-1} in all cases three cycles are shown. The Pt/C shows current independent on the rotation rate.

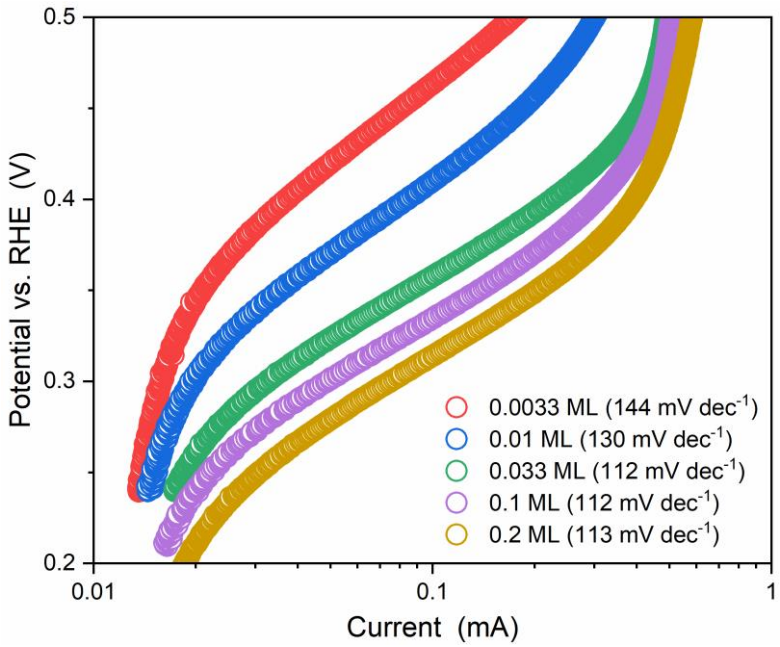

Figure 5-12 Tafel plots of CO bulk oxidation on Sn_{ad}-Pt/C samples with different Sn coverages. The CO bulk oxidation was carried out with a scan rate of 20 mV s^{-1}, and the corresponding Tafel slopes are listed in the figure legend, showing a transition of Tafel slope when the Sn coverage reaches 0.033 ML.

5.4 Conclusion

A consistent picture correlating structure, electrochemistry and *in situ* XAS is presented in order to understand how Sn ad-atoms behave on Pt under potential control and the nature and role of the adsorbed oxygenated species on Sn in the bifunctional mechanism. A model catalyst, where Sn ad-atoms are exclusively on the surface of Pt nanoparticles (Sn_{ad}-Pt/C), was prepared using the SOMC approach and characterized unambiguously using STEM-EELS microanalysis and XAS. The measurement atmosphere of XAS shows impacts on the Sn ad-atoms in terms of oxidation state and local coordination, with the fully oxidized [$Sn^{IV}O_6$] in air and fully reduced Sn^0(Pt) in H_2(g). These redox active Sn ad-atoms were found to highly promote the CO adlayer oxidation on Pt, with the onset potential shifted to ~0.25 V, in agreement with the reported Pt-Sn electrocatalysts. Sn-coverage-dependent CO stripping voltammograms suggest that the Sn ad-atoms are directly involved in the onset wave of CO oxidation (<0.5 V) and are electrochemically active in the DL region.

In situ XAS measurements at Sn K-edge show potential dependence in both XANES and EXAFS. Using the ex situ XAS data as the internal references, the oxidation of the Sn ad-atoms is quantified as 0.2, 0.4, 0.7, 1.2 and 3.1 for the Sn at 0, 0.2, 0.4, 0.6 and 0.8 V, respectively, in agreement with the additional charge in the corresponding potential range obtained from voltammetry. The speciation of the Sn ad-atoms under potential control was revealed using EXAFS fitting. The Sn ad-atoms are oxygenated throughout 0–0.8 V but the extent of oxygenation is stepwise and potential-dependent, starting from Pt-Sn-(OH) coordinated with both Pt and O in 0–0.2 V and being oxidized to Pt|SnO_x with the destruction of Sn-Pt interaction at 0.8 V. The electrochemistry of the Sn ad-atoms on Pt is proposed to consist of two redox couples, Pt-Sn*/Pt-Sn-OH and Pt-Sn-OH/Pt|SnO_x. That the former generates one of the reactants of the bifunctional mechanism at low potential (Pt-Sn-OH) was ascertained by CO bulk oxidation, where the CO_{ads} coverage is constant. From the Sn coverage dependence of CO bulk oxidation, CO oxidation at low potential is also promoted by weakening Pt-CO via a combination of ligand effects from strong Sn-Pt intermetallic bonds and intermolecular repulsion between the co-adsorbed Pt-CO and Sn-OH.

5.5 References

[1] C. Lu, C. Rice, R.I. Masel, P.K. Babu, P. Waszczuk, H.S. Kim, E. Oldfield, A. Wieckowski, UHV, Electrochemical NMR, and Electrochemical Studies of Platinum/Ruthenium Fuel Cell Catalysts, J. Phys. Chem. B, 106 (2002) 9581-9589.

[2] Mechanistic aspects of carbon monoxide oxidation, Handbook of Fuel Cells2010.

[3] H. Wang, Z. Jusys, R.J. Behm, H.D. Abruña, New Insights into the Mechanism and Kinetics of Adsorbed CO Electrooxidation on Platinum: Online Mass Spectrometry and Kinetic Monte Carlo Simulation Studies, J. Phys. Chem. C, 116 (2012) 11040-11053.

[4] M.T.M. Koper, S.C.S. Lai, E. Herrero, Mechanisms of the Oxidation of Carbon Monoxide and Small Organic Molecules at Metal Electrodes, Fuel Cell Catalysis2009, pp. 159-207.

[5] N. Markovic, Surface science studies of model fuel cell electrocatalysts, Surf. Sci. Rep., 45 (2002) 117-229.

[6] S. Gilman, The Mechanism of Electrochemical Oxidation of Carbon Monoxide and Methanol on Platinum. II. The "Reactant-Pair" Mechanism for Electrochemical Oxidation of Carbon Monoxide and Methanol, J. Phys. Chem., 68 (1964) 70-80.

[7] V.R. Stamenkovic, M. Arenz, C.A. Lucas, M.E. Gallagher, P.N. Ross, N.M. Markovic, Surface chemistry on bimetallic alloy surfaces: adsorption of anions and oxidation of CO on Pt_3Sn(111), J. Am. Chem. Soc., 125 (2003) 2736-2745.

[8] D. Strmcnik, M. Uchimura, C. Wang, R. Subbaraman, N. Danilovic, D. van der Vliet, A.P. Paulikas, V.R. Stamenkovic, N.M. Markovic, Improving the hydrogen oxidation reaction rate by promotion of hydroxyl adsorption, Nat. Chem., 5 (2013) 300-306.

[9] J. Li, S. Ghoshal, M.K. Bates, T.E. Miller, V. Davies, E. Stavitski, K. Attenkofer, S. Mukerjee, Z.F. Ma, Q. Jia, Experimental proof of the bifunctional mechanism for the hydrogen oxidation in alkaline media, Angew. Chem., Int. Ed., 56 (2017) 15594-15598.

[10] M. Watanabe, S. Motoo, Electrocatalysis by ad-atoms, J. Electroanal. Chem. Interfacial Electrochem., 60 (1975) 275-283.

[11] M. Watanabe, S. Motoo, Electrocatalysis by ad-atoms, J. Electroanal. Chem. Interfacial Electrochem., 60 (1975) 267-273.

[12] A. Rose, R. Bilsborrow, C.R. King, M.K. Ravikumar, Y. Qian, R.J.K. Wiltshire, E.M. Crabb, A.E. Russell, In situ Ru K-edge EXAFS of CO adsorption on a Ru modified Pt/C fuel cell catalyst, Electrochim. Acta, 54 (2009) 5262-5266.

[13] C.J. Pelliccione, E.V. Timofeeva, J.P. Katsoudas, C.U. Segre, In situ Ru K-edge X-ray absorption spectroscopy study of methanol oxidation mechanisms on model submonolayer ru on Pt nanoparticle electrocatalyst, J. Phys. Chem. C, 117 (2013) 18904-18912.

[14] Y. Liu, D. Li, V.R. Stamenkovic, S. Soled, J.D. Henao, S. Sun, Synthesis of Pt_3Sn Alloy Nanoparticles and Their Catalysis for Electro-Oxidation of CO and Methanol, ACS Catal., 1 (2011) 1719-1723.

[15] E.M. Crabb, R. Marshall, D. Thompsett, Carbon Monoxide Electro-oxidation Properties of Carbon-Supported PtSn Catalysts Prepared Using Surface Organometallic Chemistry, J. Electrochem. Soc., 147 (2000) 4440-4447.

[16] T. Matsui, K. Fujiwara, T. Okanishi, R. Kikuchi, T. Takeguchi, K. Eguchi, Electrochemical oxidation of CO over tin oxide supported platinum catalysts, J. Power Sources, 155 (2006) 152-156.

[17] H. Huang, A. Nassr, V. Celorrio, S.F.R. Taylor, V.K. Puthiyapura, C. Hardacre, D.J.L. Brett, A.E. Russell, Effects of heat treatment atmosphere on the structure and activity of Pt_3Sn nanoparticle electrocatalysts: a characterisation case study, Faraday Discuss., 208 (2018) 555-573.

[18] L. Calvillo, L. Mendez De Leo, S.J. Thompson, S.W.T. Price, E.J. Calvo, A.E. Russell, In situ determination of the nanostructure effects on the activity, stability and selectivity of Pt-Sn ethanol oxidation catalysts, J. Electroanal. Chem., 819 (2018) 136-144.

[19] S. Stevanović, D. Tripković, V. Tripković, D. Minić, A. Gavrilović, A. Tripković, V.M. Jovanović, Insight into the Effect of Sn on CO and Formic Acid Oxidation at PtSn Catalysts, J. Phys. Chem. C, 118 (2014) 278-289.

[20] B.E. Hayden, M.E. Rendall, O. South, Electro-oxidation of carbon monoxide on well-ordered Pt(111)/Sn surface alloys, J. Am. Chem. Soc., 125 (2003) 7738-7742.

[21] V. Stamenkovic, M. Arenz, B.B. Blizanac, K.J.J. Mayrhofer, P.N. Ross, N.M. Markovic, In situ CO oxidation on well characterized Pt_3Sn(hkl) surfaces: A selective review, Surf. Sci., 576 (2005) 145-157.

[22] J. Sobkowski, K. Franaszczuk, A. Piasecki, Influence of tin on the oxidation of methanol on a platinum electrode, J. Electroanal. Chem. Interfacial Electrochem., 196 (1985) 145-156.

[23] B. Bittins-Cattaneo, T. Iwasita, Electrocatalysis of methanol oxidation by adsorbed tin on platinum, J. Electroanal. Chem. Interfacial Electrochem., 238 (1987) 151-161.

[24] A.I. Frenkel, Applications of extended X-ray absorption fine-structure spectroscopy to studies of bimetallic nanoparticle catalysts, Chem. Soc. Rev., 41 (2012) 8163-8178.

[25] A.E. Russell, A. Rose, X-ray absorption spectroscopy of low temperature fuel cell catalysts, Chem. Rev., 104 (2004) 4613-4636.

[26] R.R. Adžić, J.X. Wang, B.M. Ocko, J. McBreen, EXAFS, XANES, SXS, Handbook of Fuel Cells2010.

[27] S. Mukerjee, J. McBreen, An In Situ X-Ray Absorption Spectroscopy Investigation of the Effect of Sn Additions to Carbon-Supported Pt Electrocatalysts: Part I, J. Electrochem. Soc., 146 (1999) 600-606.

[28] M. Seo, H. Habazaki, M. Inaba, M. Yokomizo, T. Nakayama, In situ X-ray absorption spectroscopy of Sn species adsorbed on platinized platinum electrode in perchloric acid solution containing stannous ions, J. Solid State Electrochem., 23 (2019) 2261-2275.

[29] M.M. Stefenel, T. Chierchie, C. Mayer, On the Underpotential Deposition of Tin on Platinum in Acid Solution, Zeitschrift für Physikalische Chemie, 135 (1983) 251-257.

[30] F. Humblot, F. Lepeltier, J.P. Candy, J. Corker, O. Clause, F. Bayard, J.M. Basset, Surface Organometallic Chemistry on Metals: Formation of a Stable ⋮Sn(n-C_4H_9) Fragment as a Precursor of Surface Alloy Obtained by Stepwise Hydrogenolysis of $Sn(n\text{-}C_4H_9)_4$ on a Platinum Particle Supported on Silica, J. Am. Chem. Soc., 120 (1998) 137-146.

[31] G.F. Santori, M.L. Casella, G.J. Siri, H.R. Adúriz, O.A. Ferretti, Hydrogenation of crotonaldehyde on Pt/SiO_2 catalysts modified with tin added via surface organometallic chemistry on metals techniques, Appl. Catal., A, 197 (2000) 141-149.

[32] J.-M. Basset, R. Psaro, D. Roberto, R. Ugo, Modern surface organometallic chemistry, John Wiley & Sons2009.

[33] K. Pelzer, J.-P. Candy, G. Godard, J.-M. Basset, Surface Organometallic Chemistry on Metal: Synthesis, Characterization and Application in Catalysis, Nanoparticles and Catalysis2007, pp. 553-620.

[34] Controlled Preparation of Heterogeneous Catalysts for Chemo- and Enantioselective Hydrogenation Reactions, Modern Surface Organometallic Chemistry, pp. 239-291.

[35] A.M. Wise, P.W. Richardson, S.W.T. Price, G. Chouchelamane, L. Calvillo, P.J. Hendra, M.F. Toney, A.E. Russell, Inhibitive effect of Pt on Pd-hydride formation of Pd@Pt core-shell electrocatalysts: An in situ EXAFS and XRD study, Electrochim. Acta, 262 (2018) 27-38.

[36] E. Antolini, E.R. Gonzalez, The electro-oxidation of carbon monoxide, hydrogen/carbon monoxide and methanol in acid medium on Pt-Sn catalysts for low-temperature fuel cells: A comparative review of the effect of Pt-Sn structural characteristics, Electrochim. Acta, 56 (2010) 1-14.

[37] D.R.M. Godoi, J. Perez, H.M. Villullas, Alloys and oxides on carbon-supported Pt–Sn electrocatalysts for ethanol oxidation, J. Power Sources, 195 (2010) 3394-3401.

[38] M. Galeotti, A. Atrei, U. Bardi, G. Rovida, M. Torrini, Surface alloying at the Sn-Pt(111) interface: a study by X-ray photoelectron diffraction, Surf. Sci., 313 (1994) 349-354.

[39] W.M.H. Sachtler, Ensemble and Ligand Effects in Metal Catalysis, Handbook of Heterogeneous Catalysis2008, pp. 1585-1593.

[40] W. Du, G. Yang, E. Wong, N.A. Deskins, A.I. Frenkel, D. Su, X. Teng, Platinum-tin oxide core-shell catalysts for efficient electro-oxidation of ethanol, J. Am. Chem. Soc., 136 (2014) 10862-10865.

[41] J. Aarons, L. Jones, A. Varambhia, K.E. MacArthur, D. Ozkaya, M. Sarwar, C.K. Skylaris, P.D. Nellist, Predicting the Oxygen-Binding Properties of Platinum Nanoparticle Ensembles by Combining High-Precision Electron Microscopy and Density Functional Theory, Nano Lett., 17 (2017) 4003-4012.

[42] M.J.S. Farias, W. Cheuquepán, A.A. Tanaka, J.M. Feliu, Nonuniform Synergistic Effect of Sn and Ru in Site-Specific Catalytic Activity of Pt at Bimetallic Surfaces toward CO Electro-oxidation, ACS Catal., 7 (2017) 3434-3445.

[43] P. Berenz, S. Tillmann, H. Massong, H. Baltruschat, Decoration of steps at Pt single crystal electrodes and its electrocatalytic effect, Electrochim. Acta, 43 (1998) 3035-3043.

[44] V. Climent, N. Garca-Arez, J.M. Feliu, Clues for the Molecular-Level Understanding of Electrocatalysis on Single-Crystal Platinum Surfaces Modified by p-Block Adatoms, Fuel Cell Catalysis2009, pp. 209-244.

[45] A. López-Cudero, J. Solla-Gullón, E. Herrero, A. Aldaz, J.M. Feliu, CO electrooxidation on carbon supported platinum nanoparticles: Effect of aggregation, J. Electroanal. Chem., 644 (2010) 117-126.

[46] E.G. Ciapina, S.F. Santos, E.R. Gonzalez, Electrochemical CO stripping on nanosized Pt surfaces in acid media: A review on the issue of peak multiplicity, J. Electroanal. Chem., 815 (2018) 47-60.

[47] R.M. Arán-Ais, F.J. Vidal-Iglesias, M.J.S. Farias, J. Solla-Gullón, V. Montiel, E. Herrero, J.M. Feliu, Understanding CO oxidation reaction on platinum nanoparticles, J. Electroanal. Chem., 793 (2017) 126-136.

[48] G. Wang, T. Takeguchi, T. Yamanaka, E.N. Muhamad, M. Mastuda, W. Ueda, Effect of preparation atmosphere of Pt–SnO_x/C catalysts on the catalytic activity for H_2/CO electro-oxidation, Appl. Catal., B, 98 (2010) 86-93.

[49] G. Stalnionis, L. Tamašauskaitė-Tamašiūnaitė, V. Pautienienė, A. Sudavičius, Z. Jusys, Modification of a Pt surface by spontaneous Sn deposition for electrocatalytic applications, J. Solid State Electrochem., 8 (2004) 892-899.

[50] R. Rizo, E. Pastor, M.T.M. Koper, CO electrooxidation on Sn-modified Pt single crystals in acid media, J. Electroanal. Chem., 800 (2017) 32-38.

[51] S.A. Campbell, R. Parsons, Effect of Bi and Sn adatoms on formic acid and methanol oxidation at well defined platinum surfaces, J. Chem. Soc., Faraday Trans., 88 (1992) 833-841.

[52] S. García-Rodríguez, F. Somodi, I. Borbáth, J.L. Margitfalvi, M.A. Peña, J.L.G. Fierro, S. Rojas, Controlled synthesis of Pt-Sn/C fuel cell catalysts with exclusive Sn–Pt interaction, Appl. Catal., B, 91 (2009) 83-91.

[53] T. Herranz, S. García, M.V. Martínez-Huerta, M.A. Peña, J.L.G. Fierro, F. Somodi, I. Borbáth, K. Majrik, A. Tompos, S. Rojas, Electrooxidation of CO and methanol on well-characterized carbon supported Pt_xSn electrodes. Effect of crystal structure, Int. J. Hydrogen Energy, 37 (2012) 7109-7118.

[54] B.E. Koel, Structure, Characterization and Reactivity of Pt–Sn Surface Alloys, in: R. Rioux (Ed.) Model Systems in Catalysis, Springer New York, New York, NY, 2010, pp. 29-50.

[55] J. Solla-Gullon, P. Rodriguez, E. Herrero, A. Aldaz, J.M. Feliu, Surface characterization of platinum electrodes, Phys. Chem. Chem. Phys., 10 (2008) 1359-1373.

[56] N.P. Lebedeva, M.T.M. Koper, E. Herrero, J.M. Feliu, R.A. van Santen, CO oxidation on stepped Pt[n(111)×(111)] electrodes, J. Electroanal. Chem., 487 (2000) 37-44.

[57] P. Liu, A. Logadottir, J.K. Nørskov, Modeling the electro-oxidation of CO and H_2/CO on Pt, Ru, PtRu and Pt_3Sn, Electrochim. Acta, 48 (2003) 3731-3742.

[58] T.J. Schmidt, B.N. Grgur, R.J. Behm, N.M. Markovic, J.P.N. Ross, Bi adsorption on Pt(111) in perchloric acid solution: A rotating ring–disk electrode and XPS study, Phys. Chem. Chem. Phys., 2 (2000) 4379-4386.

[59] N. Garcia-Araez, V. Climent, J.M. Feliu, Evidence of water reorientation on model electrocatalytic surfaces from nanosecond-laser-pulsed experiments, J. Am. Chem. Soc., 130 (2008) 3824-3833.

[60] T.E. Shubina, M.T.M. Koper, Quantum-chemical calculations of CO and OH interacting with bimetallic surfaces, Electrochim. Acta, 47 (2002) 3621-3628.

[61] E. Magnusson, N.W. Moriarty, Binding Patterns in Single-Ligand Complexes of NH_3, H_2O, OH^-, and F^- with First Series Transition Metals, Inorg. Chem., 35 (1996) 5711-5719.

[62] T. Schiros, L.Å. Näslund, K. Andersson, J. Gyllenpalm, G.S. Karlberg, M. Odelius, H. Ogasawara, L.G.M. Pettersson, A. Nilsson, Structure and Bonding of the Water−Hydroxyl Mixed Phase on Pt(111), J. Phys. Chem. C, 111 (2007) 15003-15012.

[63] I. Pašti, S. Mentus, Electronic properties of the Pt_xMe_{1-x}/Pt(111) (Me=Au, Bi, In, Pb, Pd, Sn and Cu) surface alloys: DFT study, Materials Chemistry and Physics, 116 (2009) 94-101.

[64] Š. Pick, On the electronic structure of surface Pt–Sn alloys, Surf. Sci., 436 (1999) 220-226.

Chapter 6 Contrasting the EXAFS obtained under air and H_2 environments to reveal details of the surface structure of Pt-Sn nanoparticles

6.1 Introduction

Bimetallic nanoparticle catalysts are of research interest as they offer routes to obtain catalysts with improved activity, stability and selectivity, as compared to their monometallic counterparts[1-3]. Studies of bimetallic nanoparticles mainly focus on the ratio[4, 5] and the mixing patterns (alloy, core-/multi-shell or aggregate mixtures)[6-8] of the two constituent metals, and the effects of lattice strain of the de-alloyed shell in the core-shell structure[9-11]. Less attention has been paid to the structure of bimetallic surfaces, which is crucial in assessing the role of the second metal in determining the behaviour of the catalyst. In particular, there is a question regarding the validity of assuming that the atomic arrangement on the surface to be the same as that measured for the bulk. For example, it is established that clean solid surfaces usually contract due to unsaturated surface bonding[12, 13], and on monometallic single crystals, the extent of contraction is found to increase with lowering the atomic packing and density of the surface[13, 14]. Surface contractions have been also found on monometallic nanoparticles and assessed by several means. The size-dependent lattice contraction of clean nanoparticles has been ascertained by bulk analytic techniques, such as X-ray absorption spectroscopy (XAS)[15, 16], X-ray diffraction[17] and electron diffraction[18, 19]. Coherent diffraction and modelling studies showed that the lattice contraction was found to originate from the outermost layers and correlate to the coordination number[20]. The recent development of atomic resolution electronic tomography has enabled visualization of the surface displacement of each atom[21, 22].

Ascertaining the extent of surface contraction of bimetallic nanoparticles remains a challenge. The element distribution of bimetallic nanoparticles can be easily acquired using STEM-EELS/EDX, and more detailed information regarding surface composition can be achieved directly using XPS and AES and Tof-SIMS or indirectly using XAS and infrared spectroscopies using surface stimuli, such as, surface adsorbed CO and electrochemical events. For examples, Gibson et al.[23] used DRIFTS to monitor surface adsorbates on AuPd nanoparticles during CO oxidation at elevated temperatures, and the surface reconstruction from AuPd alloy surface to a Pd skin was confirmed by the disappearance of a band assigned to CO adsorbed on Au^0. Similarly, using CO as the probe molecule, the dominance of Ru on the surface of Pt nanoparticles can also be ascertained by a ~200 mV negative peak shift in CO stripping voltammograms[24]. Also, Price et al.[25] used *in situ* XAS under applied potentials to discriminate Au-Pd shells on Au core, with or without Pd islands/clusters, as an increased Pd-Pd

distance was observed on the shell with Pd islands/clusters at low potentials due to the absorption of H into the Pd lattice.

Although the aforementioned techniques are able to provide elemental distribution and detailed surface composition of bimetallic nanoparticles, they currently fail to obtain the more detailed structural information the bimetallic surface, such as the surface bond length, which is the object of interest in this chapter. Some understanding of the surface contraction of bimetallic nanoparticles can be obtained from XAS studies, but the results must be interpreted with caution as the environment in which the XAS data were acquired can have a significant effect. The well-studied Pt-Sn nanoparticles (Pt as the host metal and Sn as the guest one) may be used as an example. Decreases in the Sn-Pt bond length of between 0.03~0.15 Å have been reported compared to that of the Pt_3Sn structure[4, 26-29]. In some cases, the surface was oxidized, which changes the surface structure[4, 26]; whilst in other cases, harsh reduction conditions were used, which induces excessive Sn atom to diffuse into the interior[27-29]. Although the varying results from such XAS results seem discouraging and XAS is not a surface-sensitive technique, we will show in the study described herein that XAS stands out as a means of revealing the surface contraction for such bimetallic nanoparticles. This is because XAS not only provides structural information regarding coordination environments, but also can extract the information of the guest metal independently from that of the host metal. With these two advantages, as well as a wide choice of the measuring conditions, experiments can be better designed to let XAS 'see' the surface, with the key being to produce a clean, bimetallic surface on a nanoparticle without interference or with separable interference from the bulk.

In this study, H_2 at room temperature was selected as an appropriate environment during XAS measurements to produce such surfaces on dealloyed Pt-Sn nanoparticles (the air sample in Chapter 3), as this condition is capable of reducing the Pt surface oxides and, as will be demonstrated below, the oxidised surface Sn atoms of the Pt-Sn nanoparticles, whilst not resulting in diffusion of Sn. XAS data were first collected in air at room temperature to understand the Sn speciation and the surface-to-bulk Sn ratio, and the following measurements in H_2 at room temperature were allowed to assess the effects of freshly formed Pt-Sn surface on the average Pt-Sn bond length. Pt-Sn nanoparticle samples with different surface-to-bulk Sn ratios (the Ar sample and the H_2 sample in Chapter 3) are analysed using the same approach. The Pt-Sn bond length and the corresponding coordination number (CN), related specifically to the surface, were extracted using an improved fitting model combining the data measured in air and in H_2. These two parameters were also obtained from two control samples, in which the Sn was only present on the surface, and a correlation between bond length and coordination number is summarised and discussed.

6.2 Experimental

Preparation of dealloyed Pt-Sn: Three Pt-Sn samples, all with the same Pt:Sn ratio and total metal loading, were prepared as described previously in Chapter 3, by annealing a common parent Pt-Sn/C catalyst in different atmospheres. The parent Pt-Sn/C with a metal loading of 20 wt% was synthesized by a conventional polyol method. Briefly, 200 mg of the Vulcan XC-72R carbon black and 200 mg of NaOH were dispersed into 50 ml of ethylene glycol/H_2O (3:1 v/v) solution. Into this suspension, 100 mg of $H_2PtCl_6 \cdot 6H_2O$ and 16 mg of $SnCl_2 \cdot 2H_2O$ were dissolved. After being stirred for 1 hour and then sonicated for 15 min, the suspension was heated to 160 °C and maintained at this temperature for 2 hours. The product was collected using a centrifuge, washed with a 50% ethanol aqueous solution and dried under vacuum at 80 °C. The parent Pt-Sn/C was annealed at 250 °C in either air, Ar or H_2 (5%, balanced by N_2), yielding dealloyed Pt-Sn (the air sample in Chapter 3), partly alloyed Pt-Sn (the Ar sample in Chapter 3), and alloyed Pt-Sn (the H_2 sample in Chapter 3), respectively.

Preparation of SnO_2-Pt/C: SnO_2-Pt/C was synthesized by hydrolysing SnO_3^{2-} in a suspension of a commercial (Johnson Matthey) Pt/C (60 wt%, ~3 nm diameter Pt particles determined via TEM). 150 mg of the Pt/C was dispersed in 75 ml of H_2O by sonication. To the suspension, 412 μl of 100 mg/ml $Na_2SnO_3 \cdot 3H_2O$ aqueous solution was added, followed by 30 min stirring and 5 min sonication. The suspension was then heated to 90 °C and maintained at this temperature for 1 hour. The sample was collected by centrifugation, washed with water for at least 3 times and dried under vacuum.

6.3 Results and discussion

6.3.1 Surface contraction of Pt-Sn nanoparticles

As studied in Chapter 3, the surface-to-bulk Sn ratio (or the extent of alloying) of the Pt-Sn bimetallic particles can be varied by the atmosphere in which the parent Pt-Sn sample is annealed. Annealing in H_2(g) results in well-alloyed nanoparticles, partially alloyed nanoparticles in Ar(g), and dealloyed nanoparticles in air, in which the Sn is segregated to the surface. In the study reported, herein, the detailed structure and the configuration of Sn species of the dealloyed Pt-Sn sample were further analysed using XANES and EXAFS.

The local coordination of the oxidized Sn species was then studied by EXAFS in *k*-space and *R*-space (Figure 6-2). Compared to SnO_2, the Sn of the dealloyed Pt-Sn shows similar oscillation in the low *k* (3–9 $Å^{-1}$) and low *R* regions (1–2 Å) with lower intensity, but loses fine structures in the high *k* (>9 $Å^{-1}$) and high *R* regions (3–4 Å). Since the features at high *k* and high *R* mainly correspond to two Sn-Sn scattering paths in the SnO_2 rutile structure (Figure S6-2), the Sn species, although coordinated to oxygen atoms, lack long-range order.

To further identify the coordination environment of the Sn atoms in the dealloyed Pt-Sn sample, a double-dataset EXAFS fit was carried out; combining the data of the Sn K-edge and the Pt L_3-edge by setting the R and σ^2 of interatomic scattering paths as equal, that is, R(Sn–Pt) = R(Pt–Sn) and σ^2(Sn–Pt) = σ^2(Pt–Sn). The fitting results are shown in Figure 6-4 and Figure S6-3 and the corresponding structural parameters listed in Table 6-1. At both edges, oxygen neighbours are found in the first shell, 0.8 ± 0.1 for Pt and 5.0 ± 0.7 for Sn, consistent with the oxidized surface of the dealloyed Pt-Sn. In addition to the oxygen neighbours, Pt neighbours are also found with R = 2.82 ± 0.02 Å at the Sn edge, which is similar to that of bulk Pt_3Sn (2.829 Å, ICSD 105796). Since intermediate Sn species coordinating with both Pt and O are unlikely to exist on samples annealed in air (Figure 6-3), the presence of Sn–O and Sn–Pt in the first coordination shell suggests that the Sn species are a mixture of alloyed Sn^0 inside Pt lattice and fully oxidized Sn (denoted as $[Sn^{IV}O_6]$ due to lack of long-range order). This Sn speciation explains both the decreased whiteline intensity and the unsaturated oxygen shell of Sn (6 oxygen neighbours for Sn^{IV} in SnO_2) compared to SnO_2. The phase segregation of the Sn species is attributed to the dealloying process of heat treatment, in which the oxophilic Sn atoms migrate to the surface of Pt-Sn nanoparticles and get oxidized by O_2, forming $[Sn^{IV}O_6]$ species. The similar model for phase segregation and Sn oxidation of supported Pt_3Sn nanoparticles was also suggested by in-situ time-resolved XAFS[27, 30]. The presence of alloyed Sn in the current study is probably due to the relatively low temperature (250 °C) used in heat treatment, which limits the extent of phase segregation. Therefore, the Sn species of the dealloyed Pt-Sn are spatially separated, with a Pt and Sn oxide surface layer and a metallic Pt core (with a minute amount of alloyed Sn).

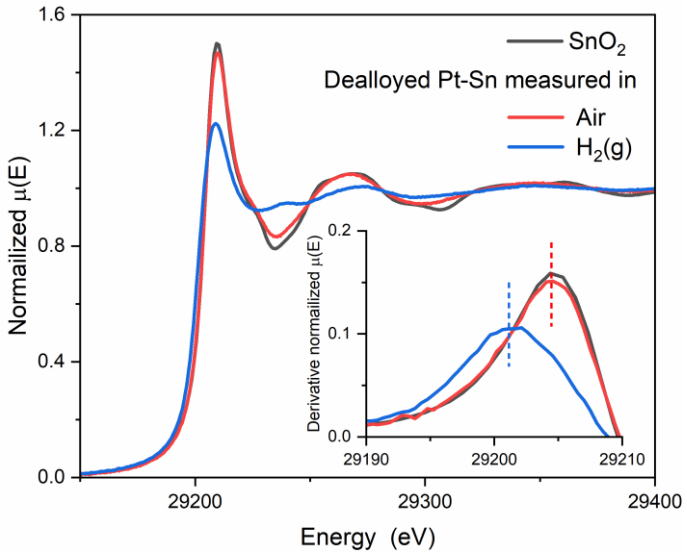

Figure 6-1 Sn K-edge XANES spectra of the dealloyed Pt-Sn samples measured in air and in H_2(g), along with their 1st derivative at the rising edge. The comparison shows a decreased whiteline intensity and a shift of edge position (vertical dash lines) towards low energy when the dealloyed sample was exposed to H_2(g), indicating the reduction of Sn^{IV}.

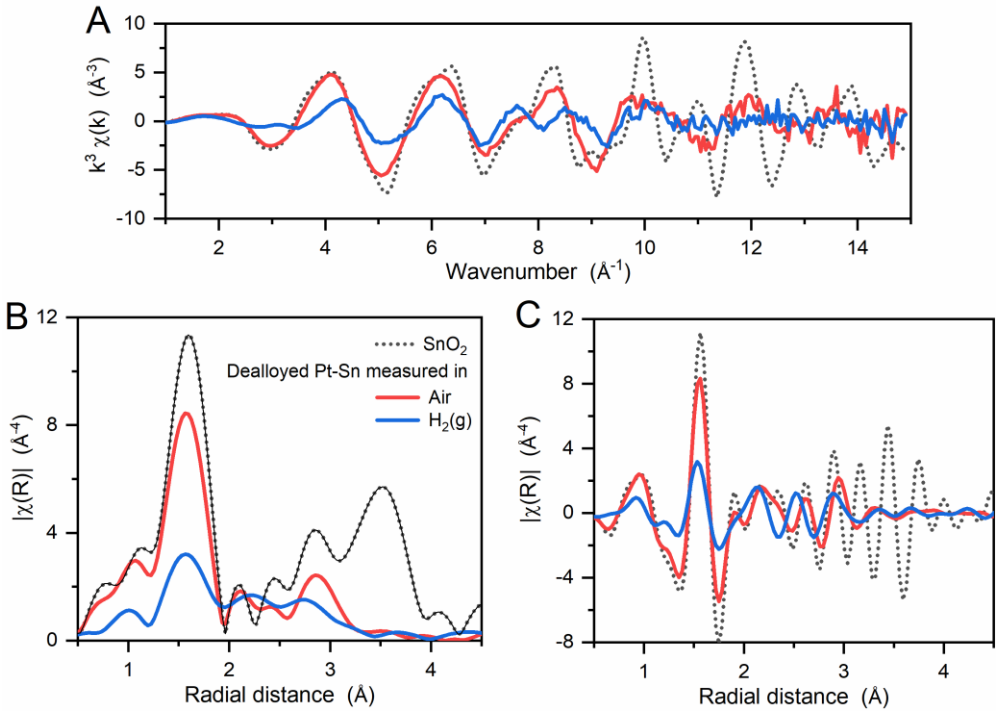

Figure 6-2 (A) k^3-weighted EXAFS spectra of the dealloyed Pt-Sn samples and that of the SnO_2 reference sample, and (B) the amplitude and (C) the real part of the corresponding Fourier transforms. The Fourier transformation was carried out in a k-range of 3.6–12.4 Å^{-1}. This figure shows the effects of the atmosphere in which the XAS measurement was conducted on the coordination of Sn, with a decrease intensity in an R-range of 1–2 Å and a shift in an R-range of 2–3 Å towards shorter radial distance when the samples are measured in H_2(g).

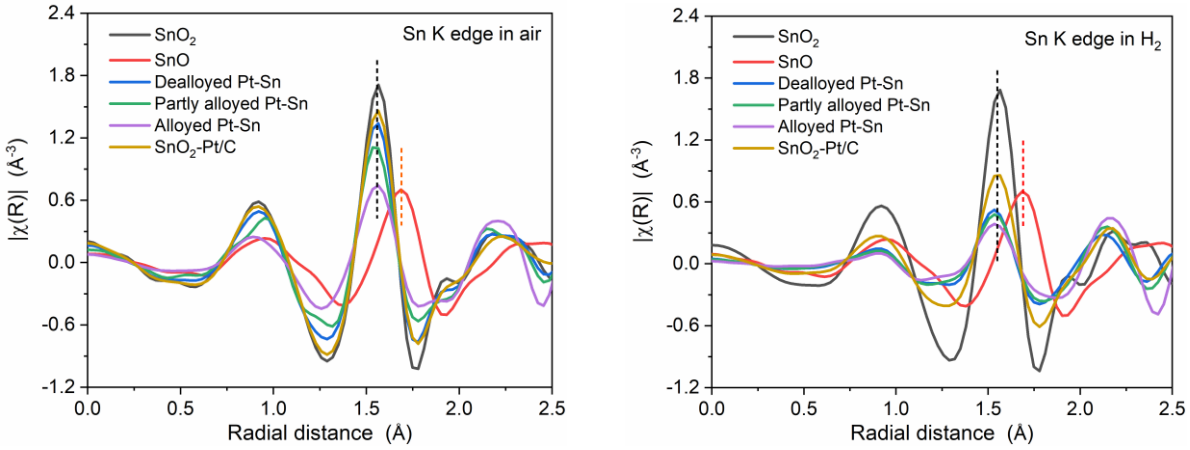

Figure 6-3 Fourier-transforms (the real part) of EXAFS spectra of the SnO_2 samples measured (left) in air and (right) in H_2, along with SnO_2 and SnO references (measured in air). The Fourier transformation was carried out in a k-range of 3.4–13.2 Å^{-1}. These two figures compare the Sn–O oscillation of Pt-Sn samples presented herein, showing the position of Sn–O aligns with that of SnO_2 regardless of samples and measurement atmospheres, and is significantly smaller than that of SnO. This suggests that Sn^{II}-O are unlikely to present in our samples.

Table 6-1 Structural parameters obtained from individual double-dataset fits of the dealloyed Pt-Sn data collected in air and in H_2. The fits use 18 variables out of ~27 independent points for the data collected in air, 17 out ~27 for the improved fit and 15 out of ~27 for the data collected in H_2(g). The first element in the scattering path indicates the absorption edge Pt (L_3) or Sn (K). Plots of the data and fits are shown in Figure 6-4 and Figure 6-5.

Samples	Scattering path	N [a]	R (Å) [b]	σ^2 ($\times 10^3$ Å^2) [c]	ΔE_0 (eV) [d]	R-factor (%) [e]
Dealloyed Pt-Sn (air)	Pt – O	0.8(1)	1.997(6)	5(1)		0.27
	Pt – Pt	7.5(2)	2.757(2)	7.6(2)	7.3(4)	
	Pt – Sn	0.6(3)	2.82(2) [f]	14(6) [f]		
	Sn – O	5.0(6) [g]	2.04(1)	5(1)		
	Sn – Pt	2(1) [g]	2.82(2) [f]	14(6) [f]	3(2)	
	Sn – Sn	2(2)	3.25(3)	8(6)		
Dealloyed Pt-Sn (H_2)	Pt – Pt	8.2(2)	2.760(1)	6.0(1)	5.2(3)	0.22
	Pt – Sn	0.9(2)	2.743(8) [f]	13(2) [f]		
	Sn – O	1.8(2)	2.035(8)	5(1)		
	Sn – Pt	5(1)	2.743(8) [f]	13(2) [f]	4(1)	
	Sn – Sn	0.6(5)	3.27(3)	10(6)		
SnO_2	Sn – O	6 [h]	2.056(4)	3.9(5)	4.7(7)	0.39
Pt_3Sn [i]	Sn – Pt	12	2.829	N.A.	N.A.	N.A.

[a] N, the degeneracy of the absorber – backscatterer scattering pair; [b] R, the average distance of the pair; [c] σ^2, the mean square relative replacement of the R; [d] ΔE_0, the difference with the assigned E_0; [e] R factor, a measure of the goodness of fit;

[f] Pt – Sn and Sn – Pt scattering paths are set to have the same value in R and σ^2;

[g] N(Sn–Pt) was fit as 12*[1-N(Sn–O)/6], assuming the CN of Sn-O is 6, and the CN of Sn-Pt is 12. The fit without such a constraint is plotted in Figure S6-3 listed in Table S6-, producing approximate structural values but with large uncertainty in the N(Sn–Pt) value, 4(5);

[h] not allowed to vary;

[i] obtained from Feff calculation of the crystal structure of Pt_3Sn (ICSD 105796).

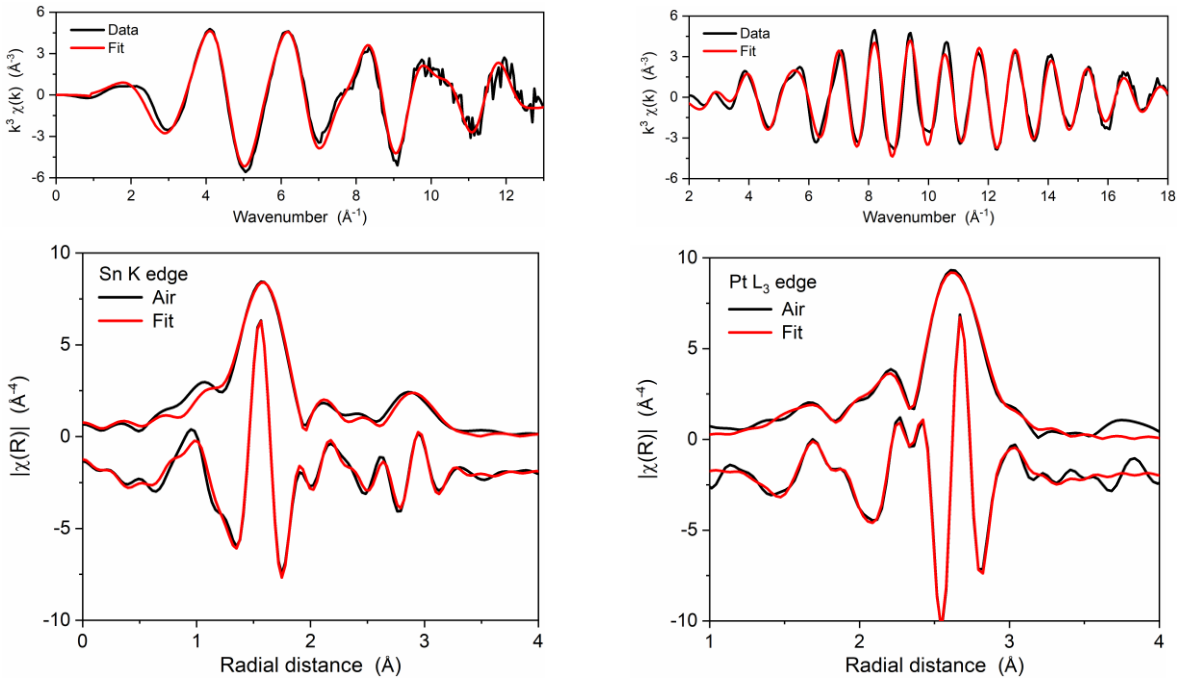

Figure 6-4 A double-dataset fit for the dealloyed Pt-Sn data measured in air, combining the EXAFS spectra collected at (left column) Sn K edge and (right column) Pt L_3 edge. The fit is shown in both (top) k^3-weighted EXAFS spectra and (bottom) their Fourier transforms plotted as the magnitude and the real part (offset toward lower magnitude for clarity), and the Fourier transformation was carried out in k-ranges of 3.6–12.4 Å^{-1} for the Sn K-edge and of 3.5–18.0 Å^{-1} for the Pt L_3 edge. The fit was performed in R ranges of 1.2–3.2 Å for the Sn K-edge and of 1.2–3.0 Å for the Pt L_3 edge, yielding an R-factor of 0.27% and the obtained structural parameters listed in Table 6-1.

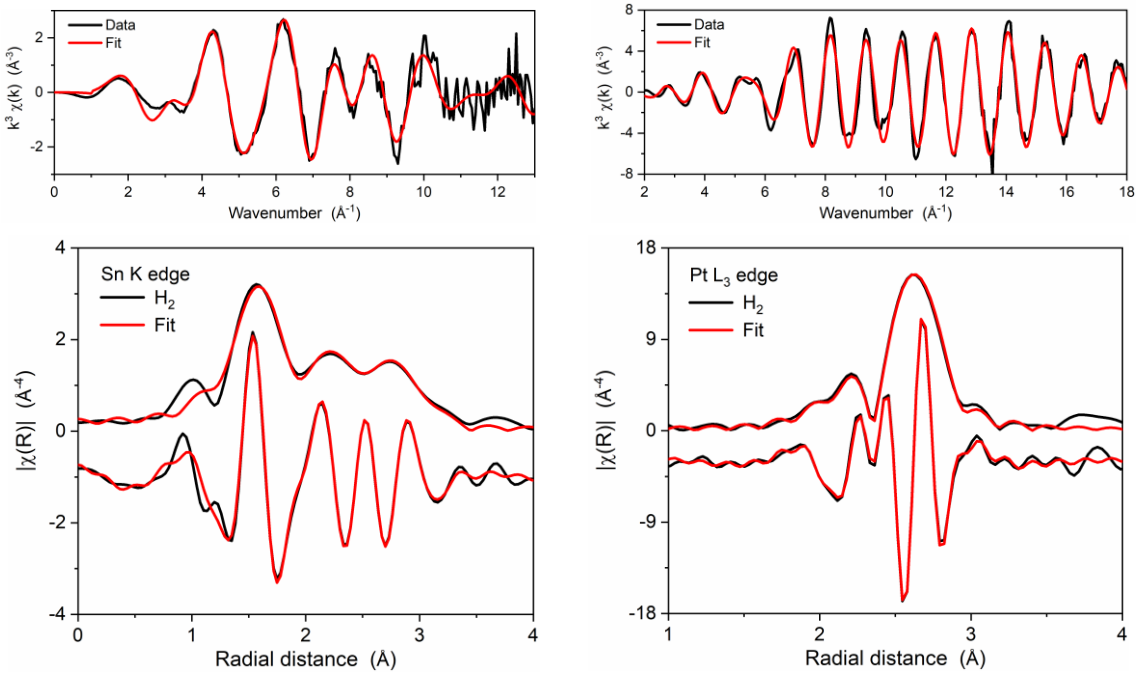

Figure 6-5 Same as Figure 6-4 but for the data measured in H_2 (g) and with an R-factor of 0.22%.

The XAS data were also collected under an atmosphere of H_2(g). The XANES spectrum at the Sn K-edge shows a sharp decrease of whiteline intensity from ~1.46 to ~1.22 and a negative shift of the edge position (defined as the first maxim of the derivative around the rising edge) by ~3 eV (Figure 6-1), indicating that the oxidation state of the Sn decreased significantly under H_2(g). The reduction of Sn is also supported by the decreased amplitude of the Sn–O component in EXAFS spectra (Figure 6-2). For the Pt edge data, the intensity of the whiteline decrease significantly, even lower than that of Pt foil, suggesting the complete reduction of the Pt surface oxide and that alloying with Sn in the core of the particles, which results in a downshift of the d-band center of Pt[31, 32].

The reduction product was further studied by fitting the EXAFS data using the same fitting model as that used for the data acquired under air. The fitting results are shown in Figure 6-5, with the obtained structural parameters listed in Table 6-1. The CN of Sn–O decreases to 1.8 ± 0.2 and that of Sn–Pt increases to 5 ± 1, with no Sn neighbours found in the first shell of Sn, suggesting that the reduction of [$Sn^{IV}O_6$] coincides with the formation of Sn-Pt bonds. Since the common oxidation states of Sn are 0, +2 and +4, the Sn-Pt bonds may come from alloyed Sn (Sn^0-Pt), intermediate Sn (Pt-Sn^{II}-O_x), or both. The presence of the intermediate Sn is negligible, as no significant change in the Sn–O distance was observed (Table 6-1 and Figure 6-3), which should be seen if Pt-Sn^{II}-O_x or $Sn^{II}O$ is present. Thus, the formation of Sn-Pt bonds is attributed to Sn^0 alloyed with Pt.

The selective conversion of [$Sn^{IV}O_6$] to Sn^0 alloyed with Pt suggests that the reduction of [$Sn^{IV}O_6$] is facilitated by the Pt surface[27, 28, 33-35]. The promotional role of Pt is ascertained by H_2 temperature-programmed reduction (Figure 6-6), showing that the dealloyed Pt-Sn sample requires ~60 °C lower temperature for the reduction than SnO_2/C. However, the reduction of [$Sn^{IV}O_6$] is not complete in the room temperature experiments reported herein. The residual contribution of Sn–O is attributed to excess clusters of [$Sn^{IV}O_6$] on Pt particles, where the Sn:Pt ratio exceeds capacity of the topmost layer to reduce all the Sn atoms (see below), and/or to [$Sn^{IV}O_6$] species located on the carbon support.

The Sn^0 atoms arising from the Pt facilitated reduction in H_2 are expected to stay on the nanoparticle surface rather than migrate into the Pt lattice. Although the formation enthalpy of Pt-Sn intermetallic compounds is highly negative, -55.3 kJ mol^{-1} for Pt_3Sn[36], Sn^0 diffusion into bulk Pt crystal is unfavourable and limited to the topmost layers[37], presumably due to the significant lattice expansion accompanying the transition from Pt (3.92 Å, ffc) to Pt_3Sn (4.00 Å, ffc). As previously reported, even for the formation of Pt-Sn surface alloys (single layer and multiple layers, dependent on the Sn coverage) heat treatment is required to incorporate deposited excessive Sn layers into Pt crystals[37-40]. This is also supported by the configuration of Sn ad-atoms on Pt deposited under electrochemical controls[41, 42] and other mild conditions[28, 33, 43].

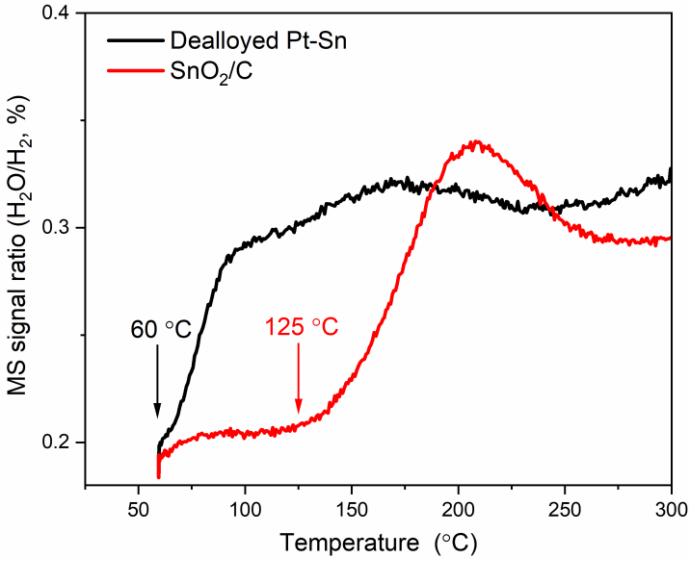

Figure 6-6 H_2 temperature-programmed reduction (TPR) of the dealloyed Pt-Sn and a SnO_2/C reference sample in a flowing H_2/He mixed gas (4 ml min^{-1} H_2 and 30 ml min^{-1} He). The H_2-TPR profile shows that the onset temperature of tin oxide reduction on SnO_2/C is much higher than that on the dealloyed Pt-Sn, suggesting that the involvement of Pt facilitate the reduction of SnO_2, and implying the reduction of H_2 is likely to be unfavourable at low temperature if Pt is not involved. The H_2-TPR was performed on CATLAB (RCaH), a microreactor system integrating with a mass spectrometer and a precise gas flow control. The samples were dried at 120 °C in 30 ml min^{-1} He for 20 min and allowed to cool down naturally to 60 °C. The gas was then switched the mixed H_2/He gas and the temperature was stabilized for 10 min, to reduce Pt surface oxide before temperature program started. After that, the temperature was increased to 400 °C with a ramping rate of 5 °C min^{-1}. This mass spectrometer signals of H_2 and H_2O were started to collect after the temperature stabilization started.

The Sn species of the dealloyed Pt-Sn in H_2(g) can therefore be considered a mixture of Sn inside the Pt lattice (alloyed) and Sn coordinated to Pt at the surface of the particles as a Pt rich core/Sn rich shell structure, with some residual [$Sn^{IV}O_6$]. The averaged structural parameters of Sn–Pt from the EXAFS analysis arising from these two Sn alloy environments yield a significantly shortened bond length, R = 2.743 ± 0.008 Å, which is shorter than that measured in air (2.82 ± 0.02 Å) and that of bulk Pt_3Sn (~2.829 Å). Such a decrease was found in a Al_2O_3-supported Pt-Sn nanoparticle catalyst[44], the R(Pt-Sn) of which decreased from ~2.82 Å to 2.73~2.74 Å on after cycles of reaction, regeneration (in O_2) and re-activation (in H_2), and the regeneration is analogous to the dealloying process carried out on the dealloyed Pt-Sn sample.

The same XAS analysis in air and H_2(g) was conducted for the alloyed Pt-Sn and partly alloyed Pt-Sn, prepared by heat-treating the parent Pt-Sn catalyst in H_2(g) and the Ar(g), respectively, as shown in Chapter 3, with the expectation that as the extent of alloying increased the effects of the mild H_2 reduction would decrease owing to the lower fraction of Sn atoms at or near the surface of the particles. The XANES data are shown in Figure 6-7 and EXAFS and the fitting results in Figure S6-4–Figure S6-7 and Table S6-2. Comparison of the XANES in air and H_2(g) shows that the [$Sn^{IV}O_6$] species of both samples were also reduced by H_2, but the extent of reduction as assessed by the decrease in the Sn

K-edge whiteline, is less than that for dealloyed Pt-Sn, as expected. The accompanying decrease in the Sn–O CN obtained by fitting the EXAFS data is shown in Figure 6-8A and follows the same trend. Finally, the effects of the extent of alloying on the Sn–Pt distance obtained from the EXAFS fitting are shown in Figure 6-8B, with both the shortest Sn–Pt distance after H_2 reduction and largest effect of that reduction found for the dealloyed catalysts, which further suggests contraction of the Sn-Pt bond for Sn atoms located at the surface of the particles.

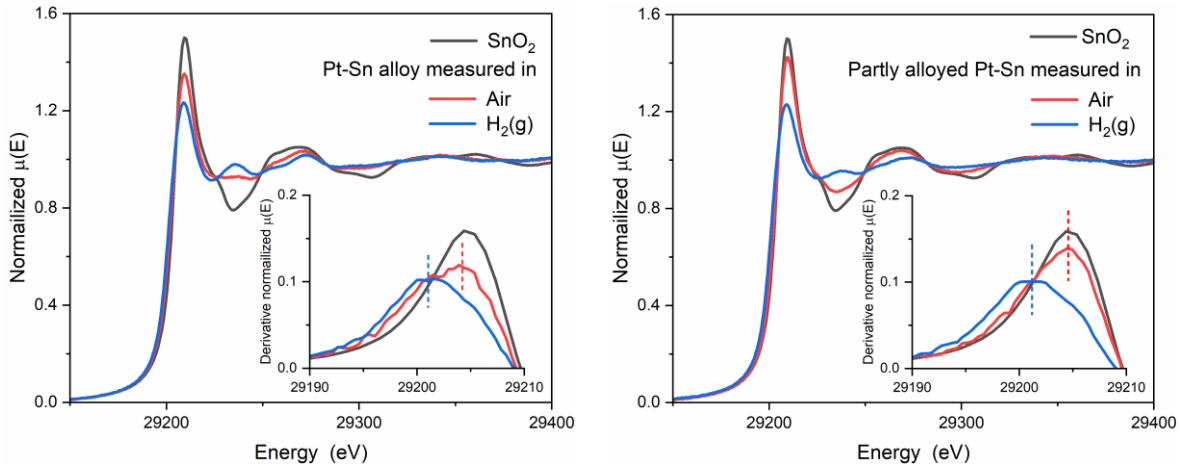

Figure 6-7 XANES spectra of (left) Pt-Sn alloy and (right) partly alloyed Pt-Sn samples, measured in air and in H_2, along with (inset) their 1st derivative at the rising edge. For the data measured in air, the extent of alloying is indicated by the decrease of the whiteline intensity and the lower-energy shoulder of the 1st derivative. The extents of decrease in whiteline intensity and of negative shift in edge position are less than those of the dealloyed one, indicating that less Sn^{IV} is reduced.

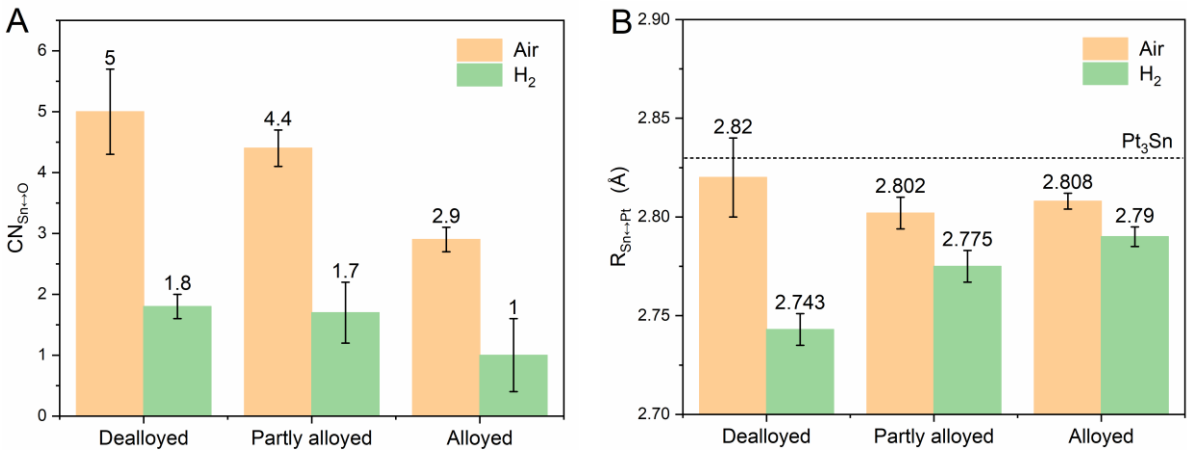

Figure 6-8 Comparison of the dealloyed Pt-Sn, the partly alloyed Pt-Sn and the alloyed Pt-Sn in terms of the decrease of (A) CN(Sn–O) and (B) R(Sn–Pt) when being exposed to H_2. The average CN(Sn–O) and R(Sn–Pt) values are labelled on the top of columns, along with the one calculated from Pt_3Sn crystal (ICSD 105796) using Feff6.

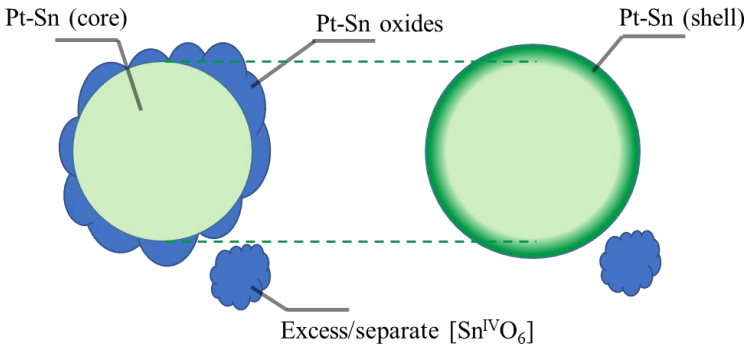

Figure 6-9 Schematic illusion of the structural model of the dealloyed Pt-Sn

6.3.2 *Extracting* surface structural parameters

These results suggest that *R*(Sn–Pt) is related to the fraction of Sn at the surface (shell) of the Pt-Sn particles. The Sn–Pt CN is also a measure of this fraction, as only Sn atoms located in the core have a full Pt coordination shell corresponding to the Pt_3Sn structure. The relationship between these two measures was further explored by the use of an improved fitting model (Table S6-3). In this model, the added surface metal atoms and any structural changes due to the reduction of the [Sn^{IV}O$_6$] shell are assumed independent from the metallic core (mainly Pt with alloyed Sn). Thus, parameters obtained from the metallic core of the air data can be transferred to the H_2 data as an unaffected 'core', and the contribution of the reduced Pt and Sn atoms to the structural parameters are described as the 'shell' (Figure 6-9). The *R* and σ^2 values of Sn–O and Sn–Sn are also assumed to be transferrable between data measured in the two atmospheres. As the fitting result shown in Figure 6-10 and the obtained structural parameters listed in Table 6-2, the improved fitting model yields a good fit that only uses 28 variables out of ~54 independent points and produces an *R*-factor of 0.38% and improved accuracy in the obtained structural parameters.

Using the improved fitting model, structural parameters specifically of the surface Sn atoms were obtained. Compared with the conventional fitting model above, an even shorter bond length for the "shell" Sn–Pt was found, 2.72 ± 0.02 Å, which is expected because a small amount of Sn–Pt from the core (with longer *R*) was separated in the fitting model. Assuming the Sn atoms of tin oxide species are saturated with 6 oxygen atoms (unreduced SnO_2) in both atmospheres, the amount of the freshly formed surface Sn atoms ($Sn^0_{surface}$%) is equal to $[N(Sn–O)_{air} – N(Sn–O)_{H2}]/6$, and the CN of the shell Sn–Pt is equal to $N(Sn–Pt)shell/Sn^0_{surface}$%, 5.4 ± 3.3.

Table 6-2 Structural parameters obtained from the 4 dataset fit of the dealloyed Pt-Sn samples. The fit uses 28 variables out of ~54 independent points. Plots of the data and fits are shown in Figure 6-10

Data set	Scattering path	*N*	*R* (Å)	σ^2 ($\times 10^3$ Å^2)	Δ*E* (eV)	*R*-factor (%)
Pt L_3 in air	Pt – O	0.84(8)	1.998(4)	5(1)	7.3(2)	0.38
	Pt – Pt	7.4(2)*	2.757(1)*	7.5(1)*		
	Pt – Sn	0.6(2)*	2.82(1)*,***	14(4)*,***		
Sn K in air	Sn – O	5.0(4)	2.043(7)**	4.6(9)**	5(2)	
	Sn – Pt	2.1(8)*	2.82(1)*,***	14(4)*,***		
	Sn – Sn (2^{nd} shell)	1.9±1.1	3.25(2)**	9(4)**		
Pt L_3 in H_2	Pt – Pt (core)	7.4(2)*	2.757(1)*	7.5(1)*	4.9(4)	
	Pt – Sn (core)	0.6(2)*	2.82(1)*	14(4)*		
	Pt – Pt (shell)	1.5(3)	2.761(5)	3.5(6)		
	Pt – Sn (shell)	0.39±0.28	2.72(2)***	11(4)***		
Sn K in H_2	Sn – O	1.7(2)	2.043(7)**	4.6(9)**	3(1)	
	Sn – Pt (core)	2.1(8)*	2.82(1)*	14(4)*		
	Sn – Pt (shell)	3.0±1.8	2.72(2)***	11(4)***		
	Sn – Sn (2^{nd} shell)	0.5±0.6	3.25(2)**	9(4)**		

*Pt – Pt (core), Pt – Sn (core) and Sn – Pt (core) of the H_2 data and the corresponding ones of the air data are set to be equal in values of *N*, Δ*R* and σ^2;

** Sn – O and Sn – Sn (2^{nd} shell) are set to be equal in values of *R* and σ^2;

*** For data measured in the same atmosphere and probing the core or the shell, Pt – Sn and Sn – Pt are set to be equal in values of *R* and σ^2.

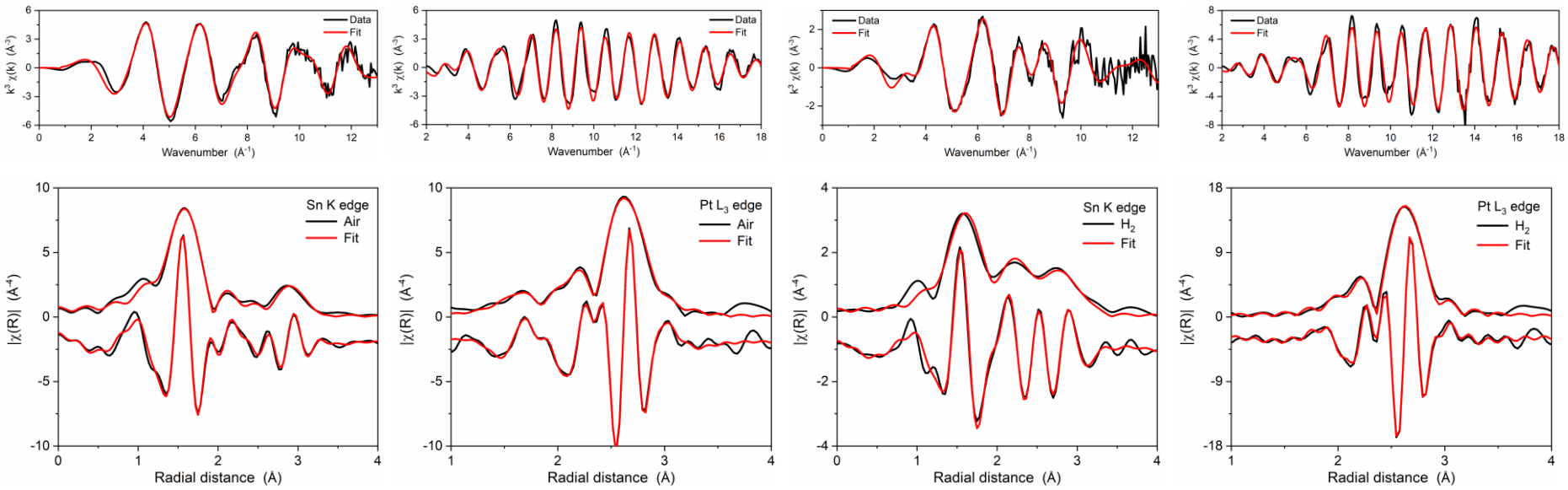

Figure 6-10 A 4-dataset fit for all EXAFS data of the dealloyed Pt-Sn, combining the data collected (1st and 2nd columns) in air and (3rd and 4th columns) in H2 (g), (1st and 3rd columns) at Sn K edge and (2nd and 4th columns) at Pt L3 edge. The fit is shown in both (top) k3-weighted EXAFS spectra and (bottom) their Fourier transforms plotted as the magnitude and the real part (offset toward lower magnitude for clarity). The Fourier transformation was carried out in k-ranges of 3.6–12.4 Å-1 for the Sn K-edge and of 3.5–18.0 Å-1 for the Pt L3 edge, and the fit was performed in R ranges of 1.2–3.2 Å for the Sn K-edge and of 1.2–3.0 Å for the Pt L3 edge, using a fitting model with guess parameters listed in Table S6-3. The fit yields an R-factor of 0.38% and the obtained structural parameters listed in Table 6-2.

To further explore the relationship between the CN and *R* for the surface Sn atoms, two control samples were prepared, in which the tin oxide phases were deposited on to a commercial Pt/C rather than mixing Pt and Sn precursors at the beginning of the synthesis; (i) SnO_2-Pt/C, in which disordered [SnO_6] was deposited on a commercial Pt/C catalyst (with naturally formed surface oxide layers) by hydrolysis of SnO_3^{2-}, and (ii) Sn_{ad}-Pt/C, in which Sn ad-atoms were deposited on the same Pt/C catalyst using a surface organometallic chemistry (SOMC) method where the Sn atoms are selectively deposited on freshly reduced Pt surface. XAS analysis in air and in H_2 was conducted on SnO_2-Pt/C like the dealloyed Pt-Sn sample (Supplementary note 1), whilst the Sn_{ad}-Pt/C data can be found in Chapter 5. Only Sn K edge data were collected for these two samples, because the Pt-Sn signal from the Pt edge data would be diluted by the dominant Pt atoms in the interior.

Shortened *R*(Sn-Pt) values were found for both control samples; 2.768 ± 0.007 Å for SnO_2-Pt./C and 2.690 ± 0.007 Å for Sn_{ad}-Pt/C, and the corresponding CN values are 8.8 ± 1.7 and 4.5 ± 0.4, respectively. Such a shortened Sn-Pt bond distance can also be found on Sn/Pt(111)[40, 45] and Sn/Pt(100)[46] surface alloys, where the Sn-Pt CN is 9 and 8, respectively. The surface Sn atoms of both surface alloys were found to protrude ~0.2 Å above the surface using scattering techniques, corresponding to a *R*(Sn-Pt) of ~2.78 Å[47, 48]. Comparison of these two surface alloys with SnO_2-Pt/C reveals that they share approximate values of *R* and CN, supporting data obtained by EXAFS fitting and suggesting that the *R*(Sn-Pt) is coordination-dependent regardless of single crystals or nanoparticles.

To summarise, the *R*(Sn-Pt) of the surface Sn are plotted as a function of CN(Sn-Pt) in Figure 6-11, which includes the dealloyed Pt-Sn, Sn_{ad}-Pt/C and SnO_2-Pt/C, Sn/Pt(111)[47, 48] and Sn/Pt(100)[47], and a reference Pt_3Sn crystal (CN = 12, R=2.829 Å). The correlation is almost linear. For bulk metals, the Goldschmidt correction was used to convert atomic radii of the metals to the value that they would have with 12-fold coordination, and as per the correction, atomic radii contract by 3%, 4% and 12% if the CN is reduced from 12 to 8, 6 and 4, respectively.[49] Sun[50, 51] formulates the correction into a CN-dependent bond-contraction coefficient,

$$C(z) = R(z)/R(12) = 2\{1+\exp[(12-z)/(8z)]\}^{-1}$$

where *z* is the CN. The equation was also found to agree with experimental data for Au nanoparticles[50, 52]. For the present Sn-on-Pt system, the data points fall on the function only when the CN is higher than 8, but the *R* with CN = 4~6 are clearly higher than those predicted by the function. This mismatch is mainly due to the nature of the Sn-Pt bond. Sn is a p-block metal and the orbitals involved in forming Sn-Pt bond should be different from Pt with other transition metals. Unlike other Pt-based alloys forming solid solution alloys, Pt_3Sn is an intermetallic compound with highly ordered atomic arrangement in which the Pt atoms in the corner-sites of ffc structure are substituted by Sn. Sn 5p orbitals are found to hybridize with Pt 5d orbitals and participate in forming bulk Pt_3Sn[53] and Pt-Sn surface alloys[32, 54], rather than s-orbitals mainly involved in Pt[55, 56].

Thus, the directionality of 5p orbitals may cause poor overlapping with the available orbitals of the Pt surface and lead to weaker bond strength than they would use s-orbital in transition metals is expected. The extent of overlapping decreases with lowering CN, consistent with the trend of the difference between the data collected and the theory.

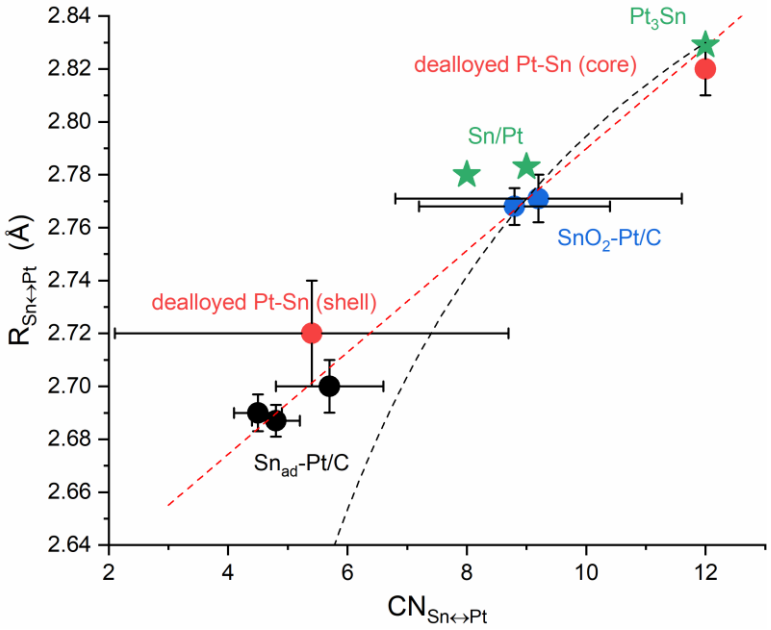

Figure 6-11 R(Sn-Pt) from different Pt-Sn systems plotted as a function of CN (Sn-Pt), showing a linear relationship. The Pt-Sn systems include the present data in this study, dealloyed Pt-Sn (core and shell), SnO_2-Pt/C from two batches and Sn_{ad}-Pt/C with different Sn coverages, and two reference data, Sn/Pt surface alloys on Pt(100) and on Pt(111)[47, 48] and Pt_3Sn crystal structure (ICSD 105796).

6.4 Conclusions

XAS measurements under H_2 at room temperature were carried out to ascertain the bond length contraction on the surface of Pt-Sn bimetallic nanoparticles. The measurement conditions produced clean Pt-Sn surfaces on nanoparticles without oxide layers and Sn diffusion into the interior. Dealloyed Pt-Sn nanoparticles, where most Sn atoms are segregated to the surface, show a ~0.09 Å shorter bond length of Sn-Pt than the bulk value on the whole, and the comparison study on Pt-Sn samples with lower surface-to-bulk Sn ratio show the contraction is less significant, supporting the contribution of surface contraction on the average bond length. To extract the structural information specifically of the surface from the average EXAFS results, an improved dataset fitting model combining the data measured in H_2 and in air was devised, yielding a good fit with R(Sn-Pt) = 2.72±0.02 Å and CN(Sn-Pt) = 5.4±3.3. Two control samples without Sn in the bulk were also studies in the same fashion, and the results support the surface contraction and produce data points for coordination-dependent bond length contraction. Combining the measured R and the

corresponding CN values, *R* is found to be proportional to the CN in bimetallic system, which is different from the established theory in monometallic system when the CN is low. The origin of the mismatch is attributed to the directionality of Sn 5p orbitals, which causes the poor overlapping with the available orbital on the Pt surface.

6.5 References

[1] K. Loza, M. Heggen, M. Epple, Synthesis, Structure, Properties, and Applications of Bimetallic Nanoparticles of Noble Metals, Adv. Funct. Mater., 30 (2020) 1909260.

[2] M. Sankar, N. Dimitratos, P.J. Miedziak, P.P. Wells, C.J. Kiely, G.J. Hutchings, Designing bimetallic catalysts for a green and sustainable future, Chem. Soc. Rev., 41 (2012) 8099-8139.

[3] W. Yu, M.D. Porosoff, J.G. Chen, Review of Pt-based bimetallic catalysis: from model surfaces to supported catalysts, Chem. Rev., 112 (2012) 5780-5817.

[4] J.H. Kim, S.M. Choi, S.H. Nam, M.H. Seo, S.H. Choi, W.B. Kim, Influence of Sn content on PtSn/C catalysts for electrooxidation of C_1–C_3 alcohols: Synthesis, characterization, and electrocatalytic activity, Appl. Catal., B, 82 (2008) 89-102.

[5] S.I. Choi, S. Xie, M. Shao, N. Lu, S. Guerrero, J.H. Odell, J. Park, J. Wang, M.J. Kim, Y. Xia, Controlling the size and composition of nanosized Pt-Ni octahedra to optimize their catalytic activities toward the oxygen reduction reaction, ChemSusChem, 7 (2014) 1476-1483.

[6] S. Alayoglu, P. Zavalij, B. Eichhorn, Q. Wang, A.I. Frenkel, P. Chupas, Structural and architectural evaluation of bimetallic nanoparticles: a case study of Pt-Ru core-shell and alloy nanoparticles, ACS Nano, 3 (2009) 3127-3137.

[7] R. Ferrando, J. Jellinek, R.L. Johnston, Nanoalloys: from theory to applications of alloy clusters and nanoparticles, Chem. Rev., 108 (2008) 845-910.

[8] L. Calvillo, L. Mendez De Leo, S.J. Thompson, S.W.T. Price, E.J. Calvo, A.E. Russell, In situ determination of the nanostructure effects on the activity, stability and selectivity of Pt-Sn ethanol oxidation catalysts, J. Electroanal. Chem., 819 (2018) 136-144.

[9] P. Strasser, S. Koh, T. Anniyev, J. Greeley, K. More, C. Yu, Z. Liu, S. Kaya, D. Nordlund, H. Ogasawara, M.F. Toney, A. Nilsson, Lattice-strain control of the activity in dealloyed core-shell fuel cell catalysts, Nat. Chem., 2 (2010) 454-460.

[10] B.T. Sneed, A.P. Young, C.K. Tsung, Building up strain in colloidal metal nanoparticle catalysts, Nanoscale, 7 (2015) 12248-12265.

[11] M. Escudero-Escribano, P. Malacrida, M.H. Hansen, U.G. Vej-Hansen, A. Velazquez-Palenzuela, V. Tripkovic, J. Schiotz, J. Rossmeisl, I.E. Stephens, I. Chorkendorff, Tuning the activity of Pt alloy electrocatalysts by means of the lanthanide contraction, Science, 352 (2016) 73-76.

[12] K. Oura, V. Lifshits, A. Saranin, A. Zotov, M. Katayama, Surface science: an introduction, Springer Science & Business Media2013.

[13] G.A. Somorjai, Y. Li, Introduction to surface chemistry and catalysis, John Wiley & Sons2010.

[14] F. Jona, P. Marcus, Surface Structures from LEED: Metal Surfaces and Metastable Phases, The structure of Surfaces II, Springer1988, pp. 90-99.

[15] J.T. Miller, A.J. Kropf, Y. Zha, J.R. Regalbuto, L. Delannoy, C. Louis, E. Bus, J.A. van Bokhoven, The effect of gold particle size on Au-Au bond length and reactivity toward oxygen in supported catalysts, J. Catal., 240 (2006) 222-234.

[16] G. Apai, J.F. Hamilton, J. Stohr, A. Thompson, Extended X-Ray Absorption Fine Structure of Small Cu and Ni Clusters: Binding-Energy and Bond-Length Changes with Cluster Size, Phys. Rev. Lett., 43 (1979) 165-169.

[17] J.R. Gallagher, T. Li, H. Zhao, J. Liu, Y. Lei, X. Zhang, Y. Ren, J.W. Elam, R.J. Meyer, R.E. Winans, J.T. Miller, In situ diffraction of highly dispersed supported platinum nanoparticles, Catal. Sci. Technol., 4 (2014) 3053-3063.

[18] R. Lamber, S. Wetjen, N.I. Jaeger, Size dependence of the lattice parameter of small palladium particles, Phys. Rev. B, 51 (1995) 10968-10971.

[19] C. Solliard, M. Flueli, Surface stress and size effect on the lattice parameter in small particles of gold and platinum, Surf. Sci., 156 (1985) 487-494.

[20] W.J. Huang, R. Sun, J. Tao, L.D. Menard, R.G. Nuzzo, J.M. Zuo, Coordination-dependent surface atomic contraction in nanocrystals revealed by coherent diffraction, Nat. Mater., 7 (2008) 308-313.

[21] R. Xu, C.C. Chen, L. Wu, M.C. Scott, W. Theis, C. Ophus, M. Bartels, Y. Yang, H. Ramezani-Dakhel, M.R. Sawaya, H. Heinz, L.D. Marks, P. Ercius, J. Miao, Three-dimensional coordinates of individual atoms in materials revealed by electron tomography, Nat. Mater., 14 (2015) 1099-1103.

[22] J. Miao, P. Ercius, S.J. Billinge, Atomic electron tomography: 3D structures without crystals, Science, 353 (2016) aaf2157.

[23] E.K. Gibson, A.M. Beale, C.R.A. Catlow, A. Chutia, D. Gianolio, A. Gould, A. Kroner, K.M.H. Mohammed, M. Perdjon, S.M. Rogers, P.P. Wells, Restructuring of AuPd Nanoparticles Studied by a Combined XAFS/DRIFTS Approach, Chem. Mater., 27 (2015) 3714-3720.

[24] A. Rose, R. Bilsborrow, C.R. King, M.K. Ravikumar, Y. Qian, R.J.K. Wiltshire, E.M. Crabb, A.E. Russell, In situ Ru K-edge EXAFS of CO adsorption on a Ru modified Pt/C fuel cell catalyst, Electrochim. Acta, 54 (2009) 5262-5266.

[25] S.W.T. Price, J.M. Rhodes, L. Calvillo, A.E. Russell, Revealing the Details of the Surface Composition of Electrochemically Prepared Au@Pd Core@Shell Nanoparticles with in Situ EXAFS, J. Phys. Chem. C, 117 (2013) 24858-24865.

[26] W. Du, G. Yang, E. Wong, N.A. Deskins, A.I. Frenkel, D. Su, X. Teng, Platinum-tin oxide core-shell catalysts for efficient electro-oxidation of ethanol, J. Am. Chem. Soc., 136 (2014) 10862-10865.

[27] Y. Uemura, Y. Inada, K.K. Bando, T. Sasaki, N. Kamiuchi, K. Eguchi, A. Yagishita, M. Nomura, M. Tada, Y. Iwasawa, Core−Shell Phase Separation and Structural Transformation of Pt_3Sn Alloy Nanoparticles Supported on γ-Al_2O_3 in the Reduction and Oxidation Processes Characterized by In Situ Time-Resolved XAFS, J. Phys. Chem. C, 115 (2011) 5823-5833.

[28] F. Humblot, F. Lepeltier, J.P. Candy, J. Corker, O. Clause, F. Bayard, J.M. Basset, Surface Organometallic Chemistry on Metals: Formation of a Stable ⋮Sn(n-C_4H_9) Fragment as a Precursor of Surface Alloy Obtained by Stepwise Hydrogenolysis of $Sn(n\text{-}C_4H_9)_4$ on a Platinum Particle Supported on Silica, J. Am. Chem. Soc., 120 (1998) 137-146.

[29] J.M. Ramallo-López, G.F. Santori, L. Giovanetti, M.L. Casella, O.A. Ferretti, F.G. Requejo, XPS and XAFS Pt $L_{2,3}$-Edge Studies of Dispersed Metallic Pt and PtSn Clusters on SiO_2 Obtained by Organometallic Synthesis: Structural and Electronic Characteristics, J. Phys. Chem. B, 107 (2003) 11441-11451.

[30] Y. Uemura, Y. Inada, K.K. Bando, T. Sasaki, N. Kamiuchi, K. Eguchi, A. Yagishita, M. Nomura, M. Tada, Y. Iwasawa, In situ time-resolved XAFS study on the structural transformation and phase separation of Pt_3Sn and PtSn alloy nanoparticles on carbon in the oxidation process, Phys. Chem. Chem. Phys., 13 (2011) 15833-15844.

[31] M.-L. Yang, Y.-A. Zhu, X.-G. Zhou, Z.-J. Sui, D. Chen, First-Principles Calculations of Propane Dehydrogenation over PtSn Catalysts, ACS Catal., 2 (2012) 1247-1258.

[32] Š. Pick, On the electronic structure of surface Pt–Sn alloys, Surf. Sci., 436 (1999) 220-226.

[33] K. Pelzer, J.-P. Candy, G. Godard, J.-M. Basset, Surface Organometallic Chemistry on Metal: Synthesis, Characterization and Application in Catalysis, Nanoparticles and Catalysis2007, pp. 553-620.

[34] J.M. Basset, A. Baudouin, F. Bayard, J.P. Candy, C. Copéret, A. De Mallmann, G. Godard, E. Kuntz, F. Lefebvre, C. Lucas, Preparation of Single Site Catalysts on Oxides and Metals Prepared via Surface Organometallic Chemistry, Modern Surface Organometallic Chemistry, Wiley Online Library2009, pp. 23-73.

[35] M. Chen, Y. Han, T.W. Goh, R. Sun, R.V. Maligal-Ganesh, Y. Pei, C.K. Tsung, J.W. Evans, W. Huang, Kinetics, energetics, and size dependence of the transformation from Pt to ordered PtSn intermetallic nanoparticles, Nanoscale, 11 (2019) 5336-5345.

[36] P. Anres, M. Gaune-Escard, J.P. Bros, E. Hayer, Enthalpy of formation of the (Pt–Sn) system, J. Alloys Compd., 280 (1998) 158-167.

[37] M. Galeotti, A. Atrei, U. Bardi, G. Rovida, M. Torrini, Surface alloying at the Sn-Pt(111) interface: a study by x-ray photoelectron diffraction, Surf. Sci., 313 (1994) 349-354.

[38] B.E. Hayden, M.E. Rendall, O. South, Electro-oxidation of carbon monoxide on well-ordered Pt(111)/Sn surface alloys, J. Am. Chem. Soc., 125 (2003) 7738-7742.

[39] S. Speller, U. Bardi, Chapter 6 - Surface alloys and alloy surfaces: the platinum-tin system, in: D.P. Woodruff (Ed.) The Chemical Physics of Solid Surfaces, Elsevier2002, pp. 184-224.

[40] M. Nakamura, R. Imai, N. Otsuka, N. Hoshi, O. Sakata, Ethanol Oxidation on Well-Ordered PtSn Surface Alloy on Pt(111) Electrode, J. Phys. Chem. C, 117 (2013) 18139-18143.

[41] S. Tillmann, G. Samjeské, K.A. Friedrich, H. Baltruschat, The adsorption of Sn on Pt(111) and its influence on CO adsorption as studied by XPS and FTIR, Electrochim. Acta, 49 (2003) 73-83.

[42] H. Massong, S. Tillmann, T. Langkau, E.A. Abd El Meguid, H. Baltruschat, On the influence of tin and bismuth UPD on Pt(111) and Pt(332) on the oxidation of CO, Electrochim. Acta, 44 (1998) 1379-1388.

[43] G. Stalnionis, L. Tamašauskaitė-Tamašiūnaitė, V. Pautienienė, A. Sudavičius, Z. Jusys, Modification of a Pt surface by spontaneous Sn deposition for electrocatalytic applications, J. Solid State Electrochem., 8 (2004) 892-899.

[44] A. Iglesias-Juez, A.M. Beale, K. Maaijen, T.C. Weng, P. Glatzel, B.M. Weckhuysen, A combined in situ time-resolved UV–Vis, Raman and high-energy resolution X-ray absorption spectroscopy

study on the deactivation behavior of Pt and PtSn propane dehydrogenation catalysts under industrial reaction conditions, J. Catal., 276 (2010) 268-279.

[45] S.H. Overbury, D.R. Mullins, M.T. Paffett, B.E. Koel, Surface structure determination of Sn deposited on Pt(111) by low energy alkali ion scattering, Surf. Sci., 254 (1991) 45-57.

[46] Y. Li, B.E. Koel, Structural studies of surfaces: conditions for alloy formation, Surf. Sci., 330 (1995) 193-206.

[47] D.P. Woodruff, J. Robinson, Some structural issues in surface alloys and alloy surfaces: rumpling, stacking faults and disorder, Appl. Surf. Sci., 219 (2003) 1-10.

[48] S.H. Overbury, Y. Ku, Formation of stable, two-dimensional alloy-surface phases: Sn on Cu(111), Ni(111), and Pt(111), Phys. Rev. B, 46 (1992) 7868-7872.

[49] M. Weller, T. Overton, J. Rourke, F. Armstrong, Inorganic Chemistry, OUP Oxford2014.

[50] C. Sun, The BOLS-NEP theory reconciling the attributes of undercoordinated adatoms, defects, surfaces and nanostructures, Nano Materials Science, 2 (2019) 333-345.

[51] C.Q. Sun, Relaxation of the chemical bond, 2014.

[52] W. Qi, B. Huang, M. Wang, Bond-Length and -Energy Variation of Small Gold Nanoparticles, J. Comput. Theor. Nanosci., 6 (2009) 635-639.

[53] H.L. Skriver, Electronic structure of the intermetallic compound Pt_3Sn, Phys. Rev. B, 14 (1976) 5187-5197.

[54] I. Pašti, S. Mentus, Electronic properties of the Pt_xMe_{1-x}/Pt(111) (Me=Au, Bi, In, Pb, Pd, Sn and Cu) surface alloys: DFT study, Materials Chemistry and Physics, 116 (2009) 94-101.

[55] A. Kokalj, M. Causà, Periodic density functional theory study of Pt(111): surface features of slabs of different thicknesses, J. Phys.: Condens. Matter, 11 (1999) 7463-7480.

[56] C. Elsasser, N. Takeuchi, K.M. Ho, C.T. Chan, P. Braun, M. Fahnle, Relativistic effects on ground state properties of 4d and 5d transition metals, J. Phys.: Condens. Matter, 2 (1990) 4371-4394.

Chapter 7 Conclusions

This thesis demonstrated the use of XAS for characterising the speciation, extent of alloying and surface structure of Pt-Sn bimetallic electrocatalysts, providing evidence that both SnO_2 and surface alloyed Sn/Sn ad-atoms are active for the bifunctional mechanism for CO oxidation and offering understanding regarding the surface contraction of Pt-Sn bimetallic nanoparticles. Using a combination of XAS and electrochemical measurements, this thesis probed the electrochemistry of Sn ad-atoms and obtained the active species for CO oxidation and proposed catalysis cycles for the bifunctional mechanism of SnO_2 surface and Sn ad-atoms.

In **Chapter 3**, the phase and extent of alloying of Pt_3Sn NPs were controlled by the annealing atmosphere and characterised using a number of techniques (TEM, XRD, XPS, XANES and EXAFS). Whilst the obtained extents of alloying vary with methods due to the intrinsic defects and relatively arbitrary data processing, the trend air < Ar < H_2 annealed samples was consistently found. CO stripping voltammograms showed that the extent of alloying had little effect on CO oxidation activity, which suggested that the other component of the Pt_3Sn NPs (mainly SnO_2) might be also active in promoting CO oxidation on Pt. To ascertain this, **Chapter 4** studied a Pt-SnO_2 catalyst without the presence Pt-Sn intermetallic bonds and catalysts comprising a SnO_2-modified Pt surface using CO oxidation voltammograms and results of all these samples suggested a bifunctional mechanism was indeed operative at such Pt-SnO_2 electrocatalysts for stable CO oxidation at low overpotentials. In addition, a surface hydroxide species generated from a Sn^{II}/Sn^{IV} reversible redox couple (-0.2–0.3 V_{RHE}) was found on the surface of SnO_2 and attributed to the co-catalysis role of SnO_2 during CO oxidation.

Likewise, a redox couple providing surface hydroxide species was also expected at surface alloyed Sn sites, which have been long considered as electrochemically active, but without detailed proof. In **Chapter 5** carefully designed Sn_{ad}-Pt/C samples, where Sn atoms were selectively deposited on the surface of Pt NPs, were studied using detailed voltammetric measurements and *in situ* XAS experiments. Sn-coverage-dependent CO stripping voltammograms suggested that the Sn ad-atoms were directly involved in the onset wave of CO oxidation (<0.5 V), and in situ XAS identified two redox couples, Pt-Sn*/Pt-Sn-OH (< 0 V_{RHE}) and Pt-Sn-OH/Pt|SnO_x (0.4–0.8 V_{RHE}), with the former generating one of the reactants of the bifunctional mechanism at low potential. The similarities of the active redox couples found on SnO_2 surface (in Chapter 4) and Sn ad-atoms (in Chapter 5) were discussed and considered as different in nature but similar in providing OH species.

Inspired by a ~0.14 Å surface contraction found from EXAFS fitting of the Sn_{ad}-Pt/C, in **Chapter 6** the Sn–Pt bond length of Pt-Sn NPs was inspected and found to be shorter than that of bulk Pt_3Sn. Freshly formed Pt-Sn surface alloys were designed on the basis of the XAS measurements of the Pt_3Sn NPs (from **Chapter 3)** in H_2 at room temperature. A multiple dataset fitting model combining

the data measured in H_2 and in air was devised to extract the Pt–Sn distances (*R*) and coordination number (CN) values specifically of the surface. Combined with the *R*~CN relationship from **Chapter 5** and from a control sample**,** *R* was found to be proportional to the CN in Pt-Sn bimetallic system.

Overall the work presented in this thesis illustrates how XAS measurements conducted as a function of the sample environment can provide an exceptional level of detail in terms of understanding the catalyst structure and thus provide new insights regarding the activity and mechanisms of the electrocatalytic reactions, even for well-established bimetallic catalysts, such as Pt-Sn.

Appendix A Supporting information of Chapter 4

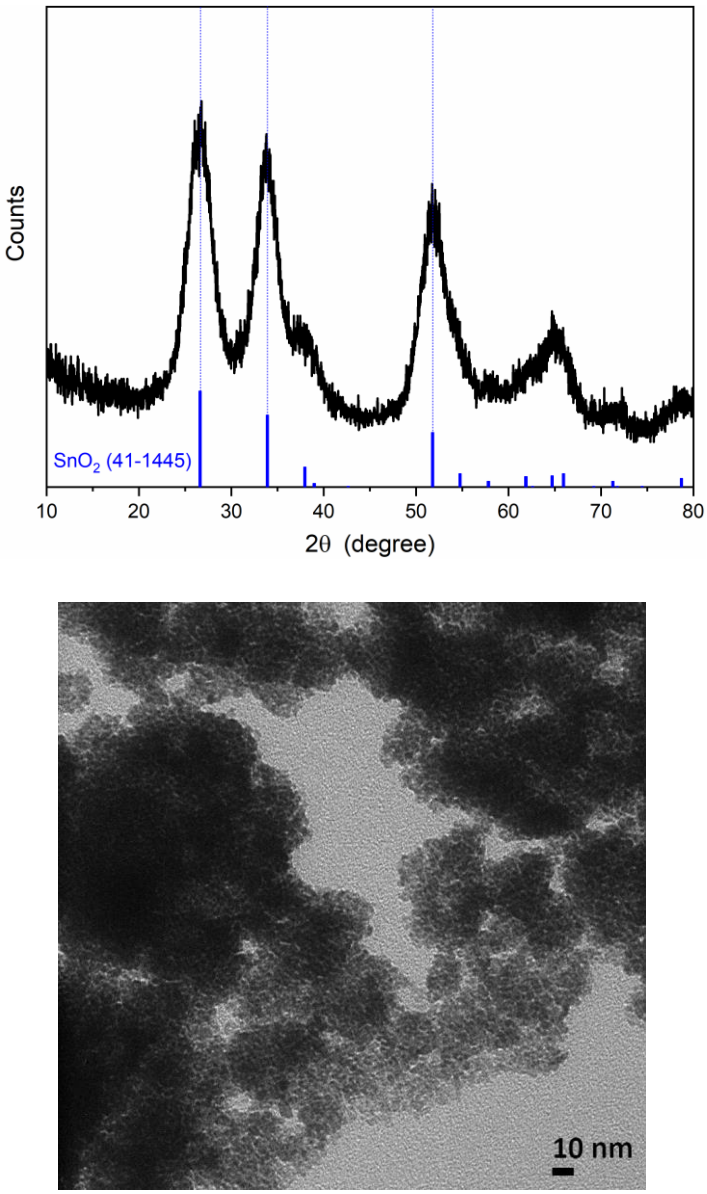

Figure S4-1 (top) XRD pattern and (bottom) a typical TEM image of SnO_2 nanopowder (8–10 nm, Alfa Aesar), showing that the actual particles size is largely consistent with the provided, and that the SnO_2 nanoparticles tend to aggregate. The standard pattern of rutile SnO_2 (41-1445) was obtained from the JCPDS database.

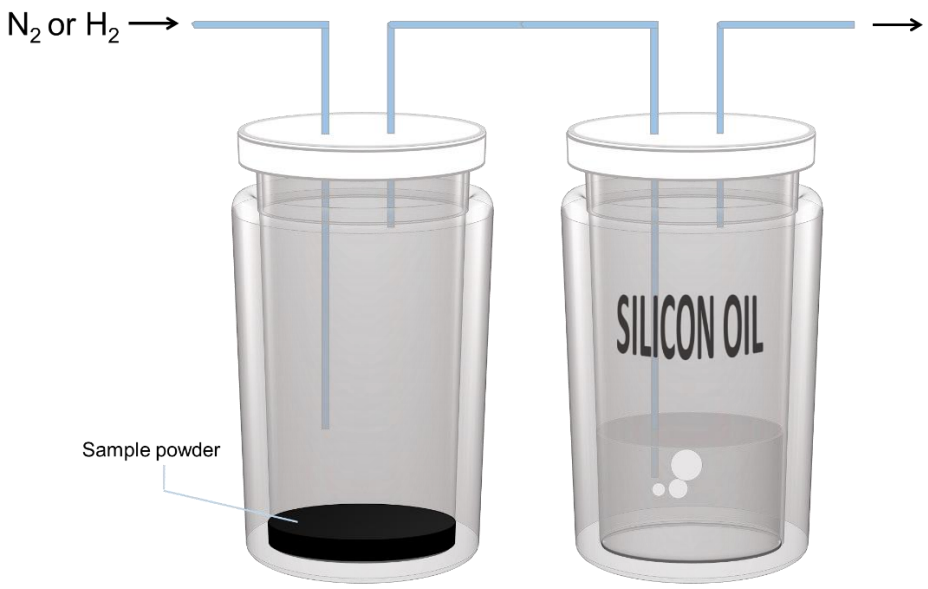

Figure S4-2 A schematic illustration of the setup for H_2(g) reduction at room temperature. Sample powder was placed in an air-tight vial (left) fitted to a flowmeter and a gas bubbler (right). N_2, H_2 and N_2 gases were purged consecutively for 20 min periods.

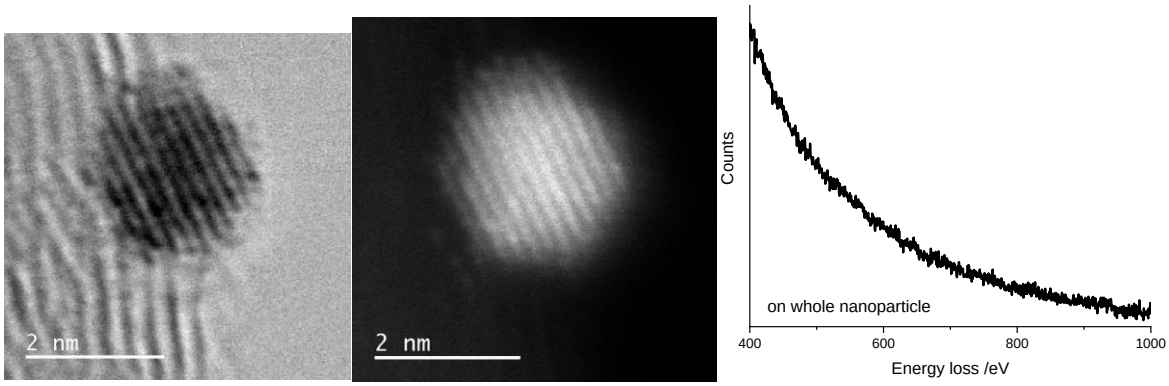

Figure S4-4. (left) representative STEM-BF and (middle) STEM-HADDF images on an isolated particle of Pt-SnO_2/C, and (right) a EELS spectrum (without background subtraction) on the whole particle, showing that no signal for Sn and O edges can be found.

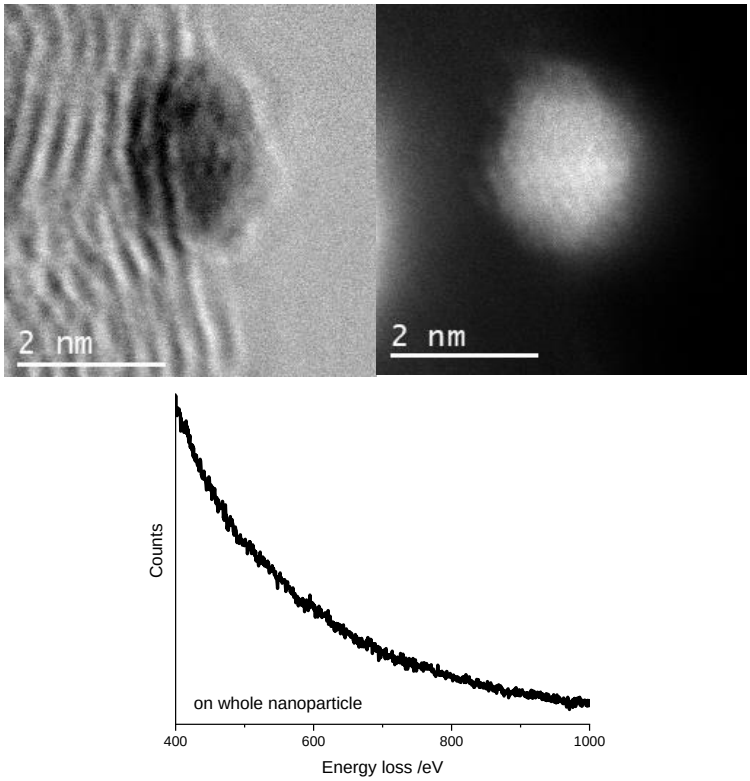

Figure S4-5. Same as Figure S4-4 but on a different region.

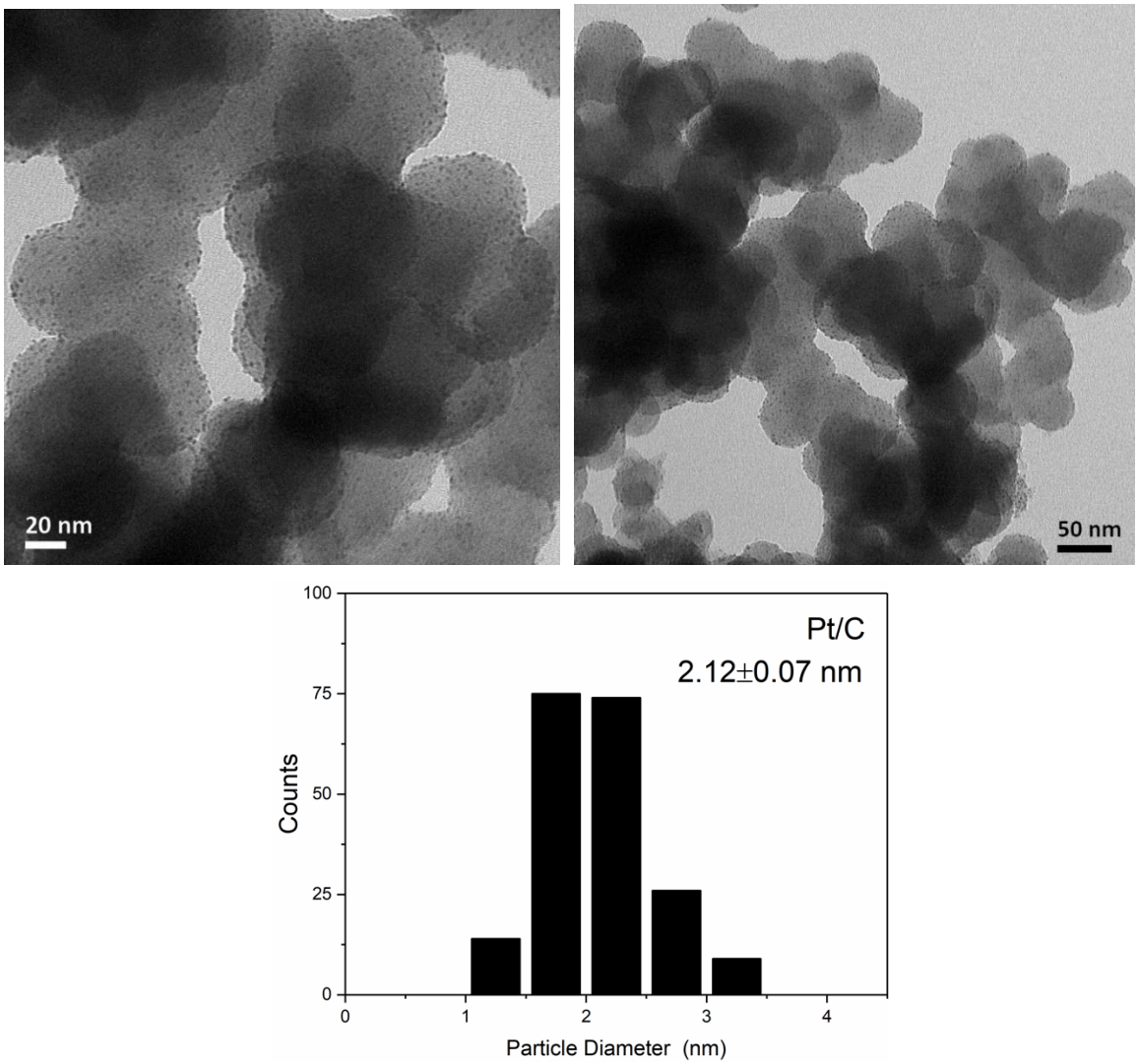

Figure S4-6. (top) TEM images of the as-prepared Pt/C at two magnifications, and (bottom) the corresponding particle size distribution with at least 200 nanoparticles measured. The Pt/C was synthesized using the same method as the Pt-SnO_2/C.

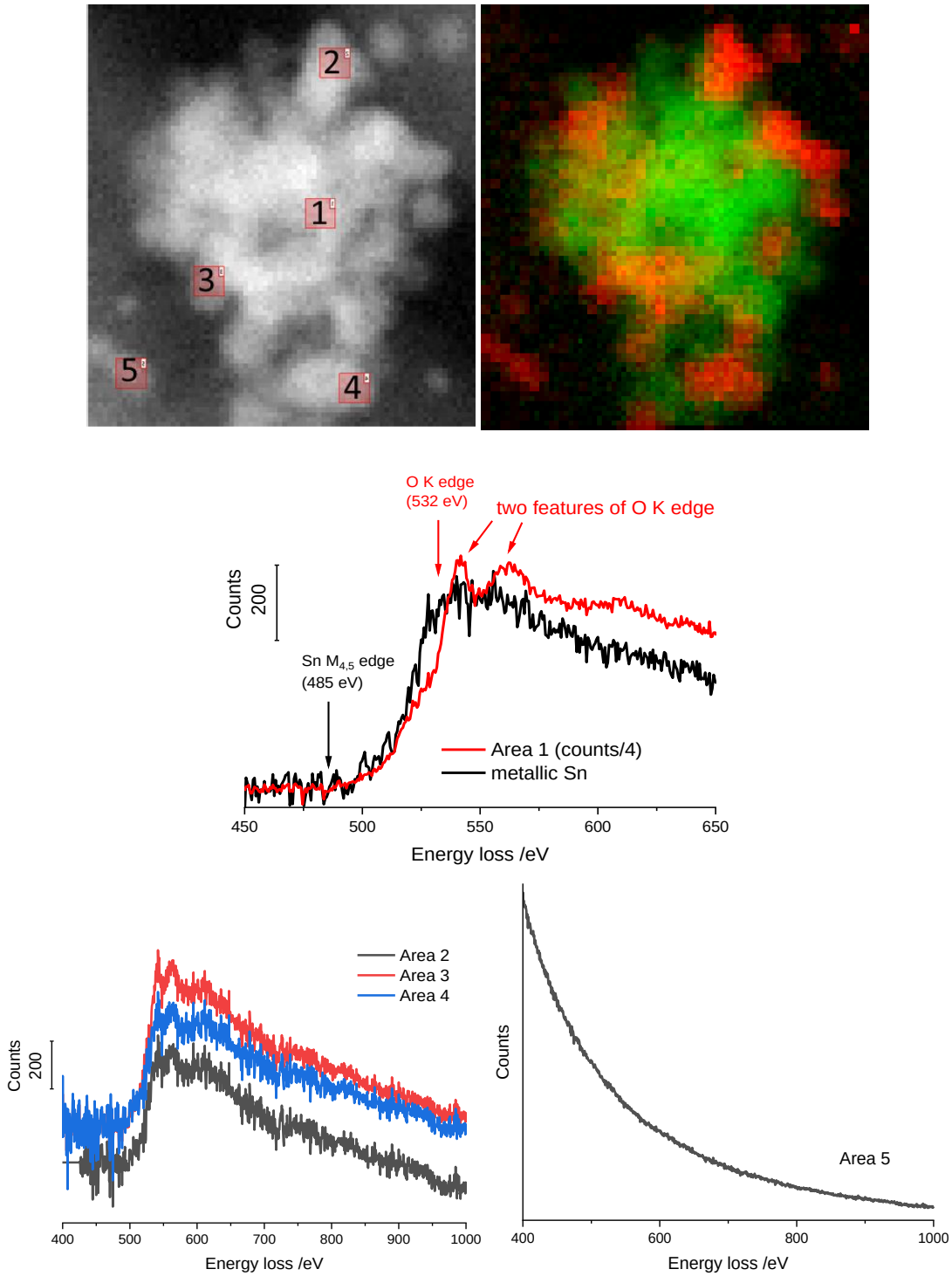

Figure S4-7. (top) The STEM-EELS mapping image as shown in Figure 4-1, and (middle and bottom) the corresponding EELS spectra of the selected areas, ranging from tin oxide-rich region to Pt-rich region. The spectrum on area 5 was not background-subtracted.

STEM-EELS spectra of Pt-SnO_2/C

Figure S4-7 show EELS spectra on selected areas of Pt-SnO_2/C from tin oxide-rich region to Pt-rich region. The spectra in the middle compare spectral features on the SnO_2-rich region of Pt-SnO_2/C and on a metallic Sn sample. Signals from the Sn $M_{4,5}$ edge (485 eV) and the O K edge (532 eV) are largely overlapped, resulting in a shoulder on the rising part of the O edge when both Sn and O are present. The existence of O can be easily identified by two sharp peaks at around 550 eV. On Pt-dominant regions (area 5 in Figure S4-7 and the single particles in Figure S4-4 and Figure S4-5) both Sn and O edge are absent, suggesting that on this sample oxygen atoms co-exist with Sn and not with Pt particles and carbon support. In addition, even on regions that Pt, Sn and O co-exist, the features of O edge are still clearly shown and no obvious spectral differences can be found on these mixed regions compared to that on the tin oxide-rich region. This feature is representative, which can also be found in another field of view (Figure S4-8). The co-location of Sn and O allow us to map the elemental distribution of Sn and O together.

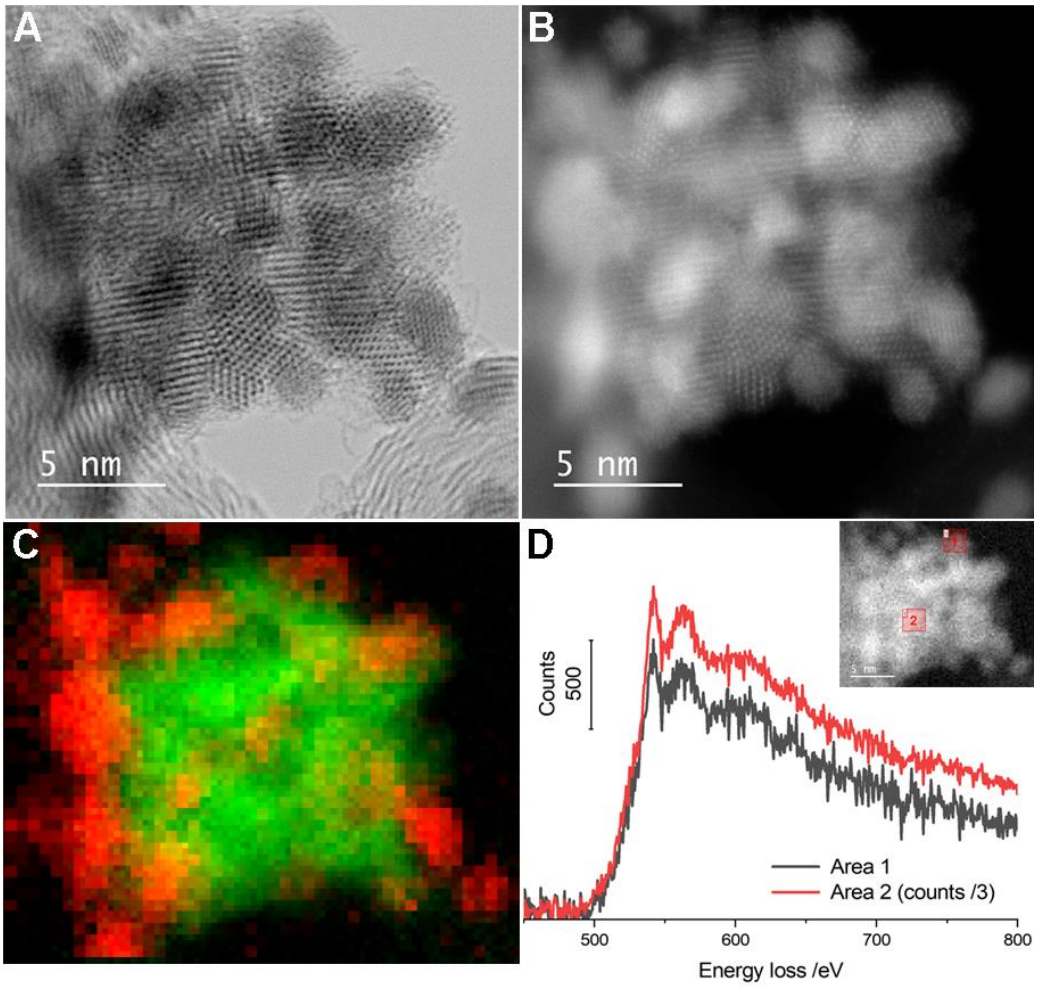

Figure S4-8. (A) STEM-BF and (B) STEM-HAADF images of a nanoparticle cluster region of Pt-SnO_2/C. (C) EELS mapping image of Pt $M_{4,5}$ edge (red), and of Sn $M_{4,5}$ edge and O K edge (green). (D) EELS spectra on the selected areas. The data here show the consistent result as Figure 4-1.

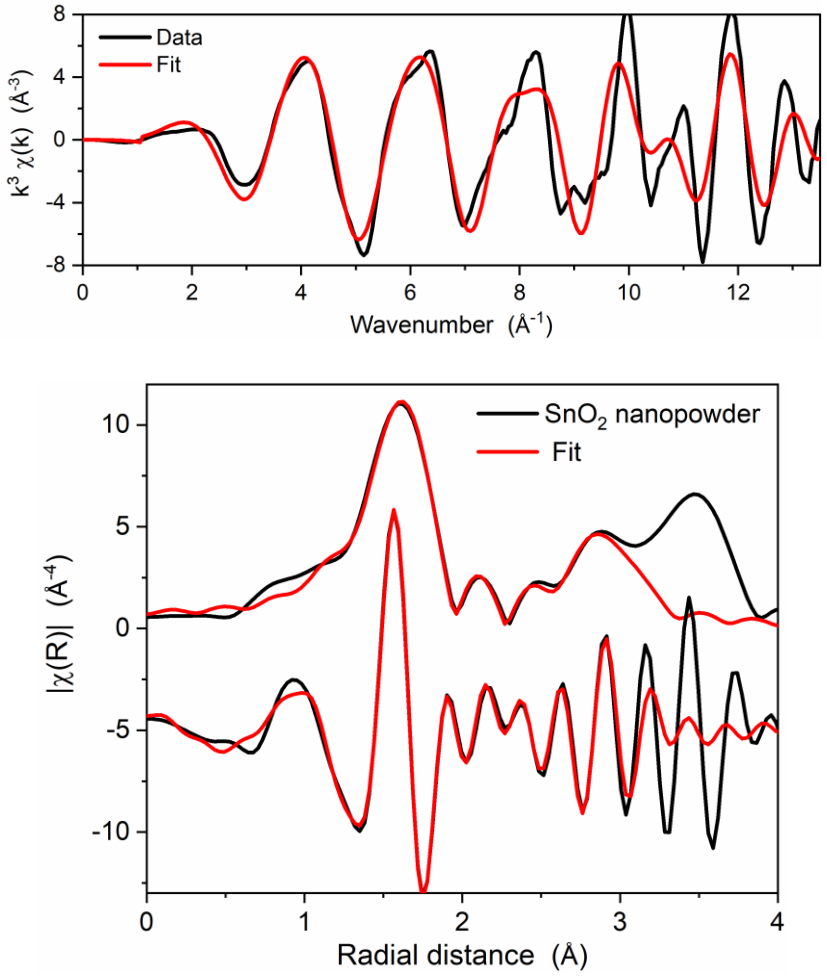

Figure S4-10. A fit of SnO_2 nanopowder (8–10 nm, Alfa Aesar) at Sn K-edge, plotting as (top) k^3-weighting EXAFS spectra and (bottom) their Fourier transforms in magnitude and real part (offset by -5 Å^{-4} for clarity). The fitting was conducted in 1.0–3.0 Å, producing a R-factor of ~1.2%. The structural parameters obtained are listed in Table 4-1.

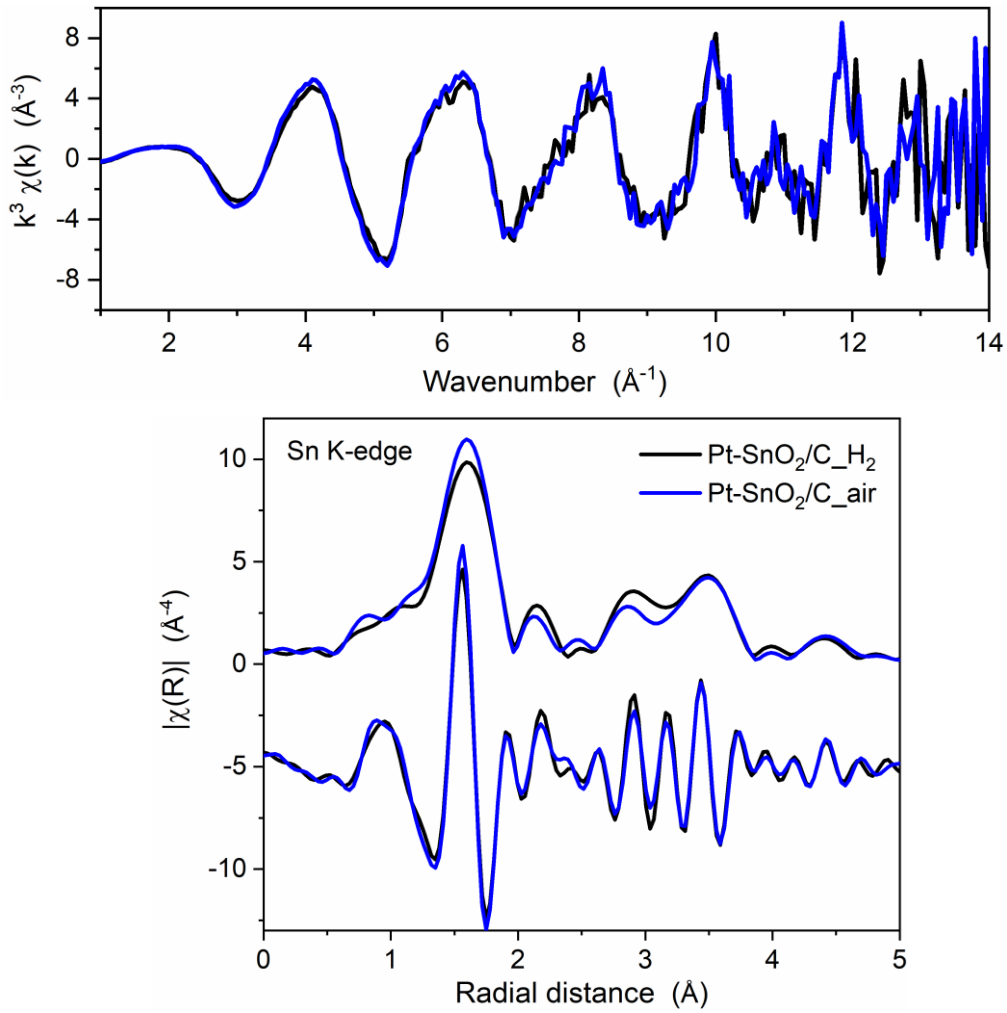

Figure S4-12. Comparison of the effect of measuring atmospheres (H_2 or air) on Pt-SnO_2/C in (top) k^3-weighted Sn K-edge EXAFS spectra and (bottom) their Fourier transforms in the magnitude and the real part.

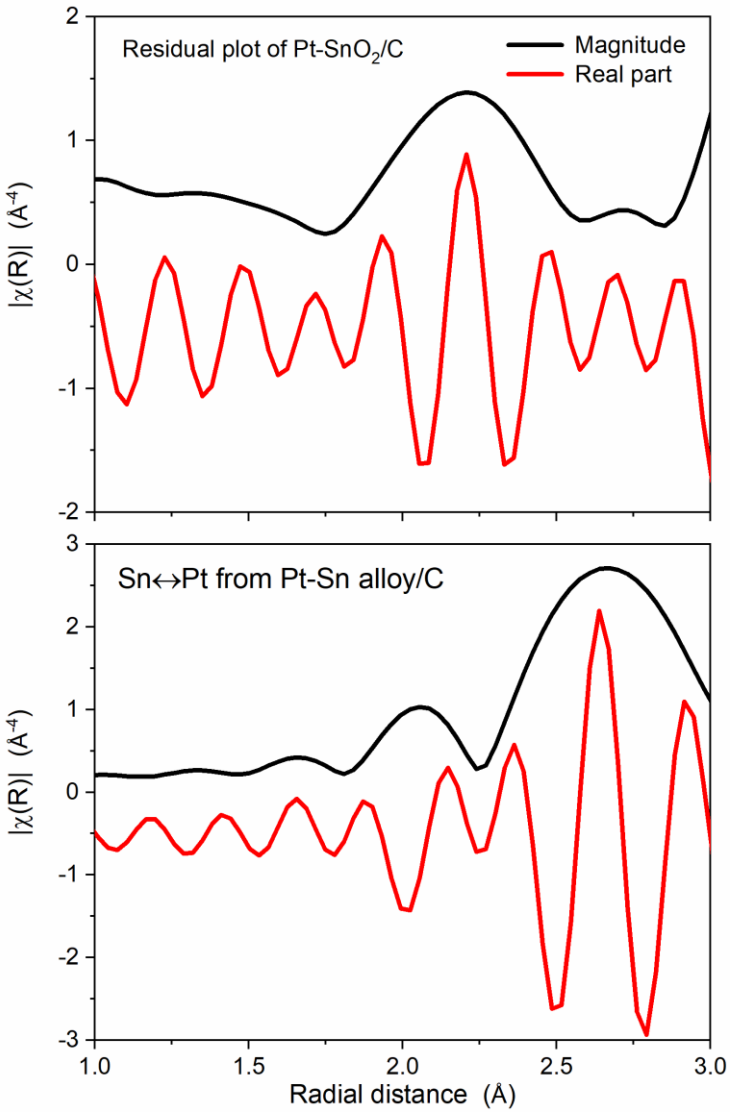

Figure S4-13. Comparison of (top) the residual plot from the fit of Pt-SnO_2/C (Figure 4-6) and (bottom) the Sn↔Pt from the fit of Pt-Sn alloy/C (Figure 4-7) in the magnitude and the real part at Sn K-edge, showing that the mismatch between the Sn K-edge data of Pt-SnO_2/C and SnO_2 structural model is not in a close phase/position as the Sn↔Pt of Pt-Sn alloy.

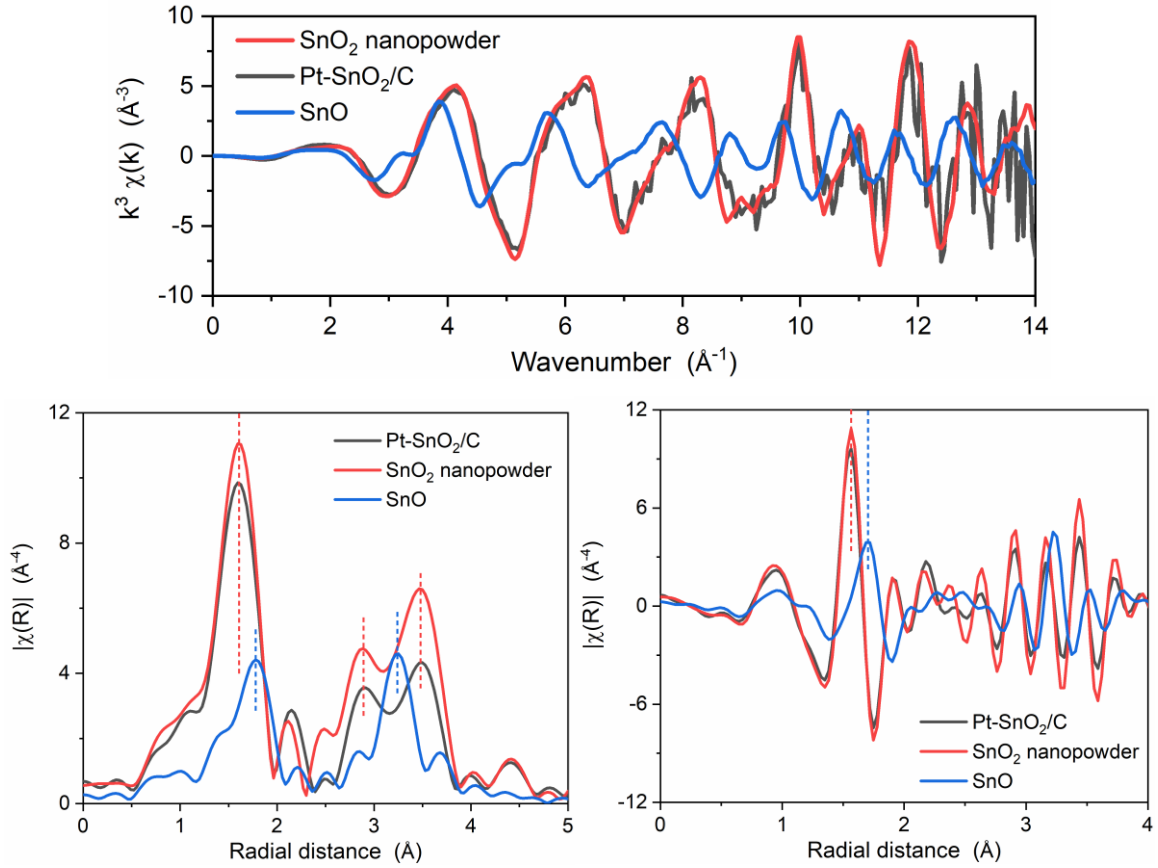

Figure S4-14. Comparison of the Sn K edge spectra of Pt-SnO_2/C, SnO_2 nanopowder and SnO in (top) k space, (bottom left) the magnitude of R space and (bottom right) the real part of R space, showing that the spectral features of Pt-SnO_2/C largely resemble those of SnO_2 nanopowder but are significantly different from those of SnO.

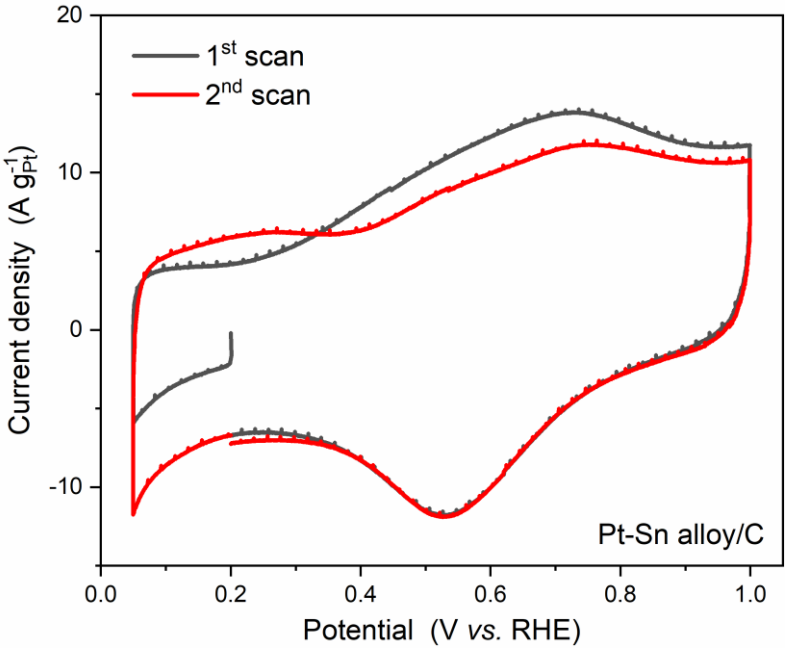

Figure S4-15. CO stripping voltammogram of Pt_3Sn alloy on carbon (20 wt% metal loading), with a scan rate of 20 mV s^{-1}.

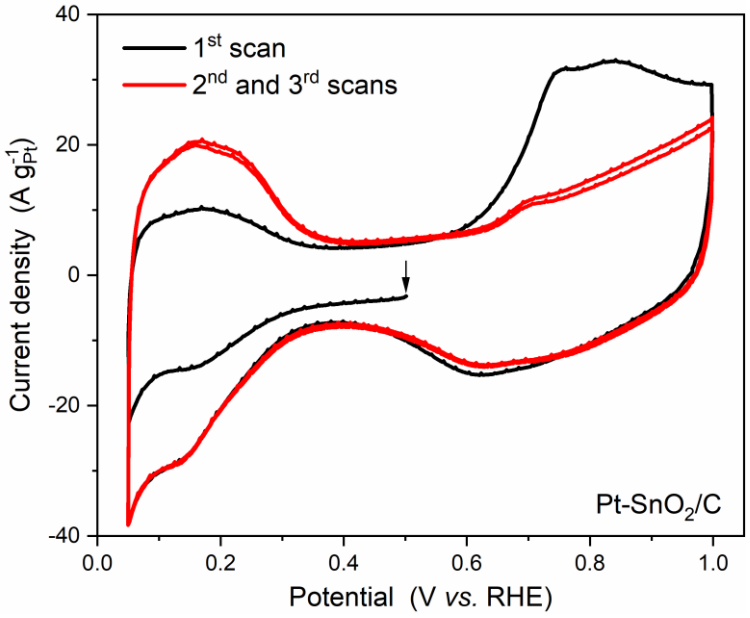

Figure S4-16. CO pre-stripping voltammogram on Pt-SnO_2/C in N_2-saturated 0.1 M $HClO_4$ with a scan rate of 20 mV s^{-1}. Before the voltammogram was measured, the saturated CO adlayer was partly stripped by potential hold at 0.5 V for 13 min in the solution. ~36% CO_{ads} was removed on the basis of the charge difference in the H_{des} waves between the 1st scan and the 2nd scan.

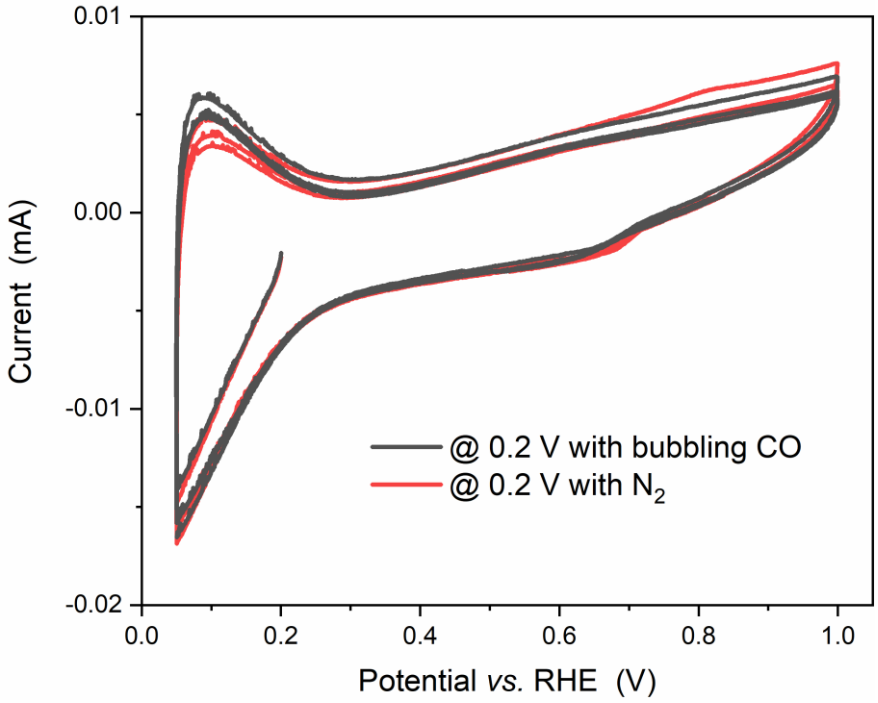

Figure S4-18. CO stripping voltammograms of SnO_2 nanopowders on a GC electrode, prior to which the electrodes were held at 0.2 V vs. RHE for 20 min with bubbling CO or with N_2, showing that SnO_2 is inert to CO absorption and oxidation. The scan rate was 20 mV s^{-1}.

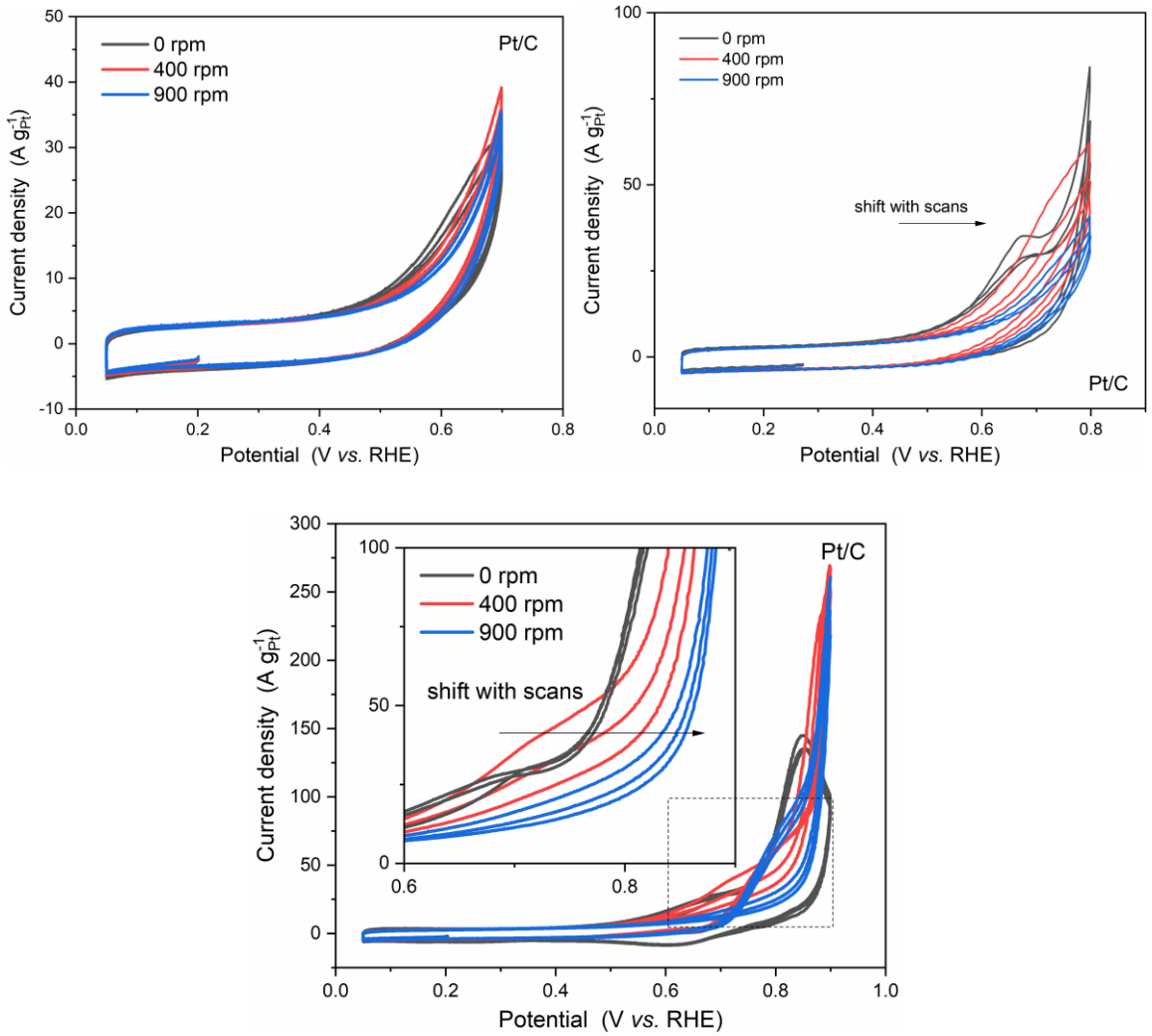

Figure S4-19. CO oxidation voltammograms of Pt/C in CO-saturated 0.1 M $HClO_4$ solution with upper potential limits of (top left) 0.7 V, (top right) 0.8 V and (bottom) 0.9 V. The rotation rates are indicated in the figure legends, and the inset of the right present only the forward scans of the magnified area, showing the oxidation waves shift positive with scans under convective-diffusion condition. The scan rates were 20 mV s^{-1}.

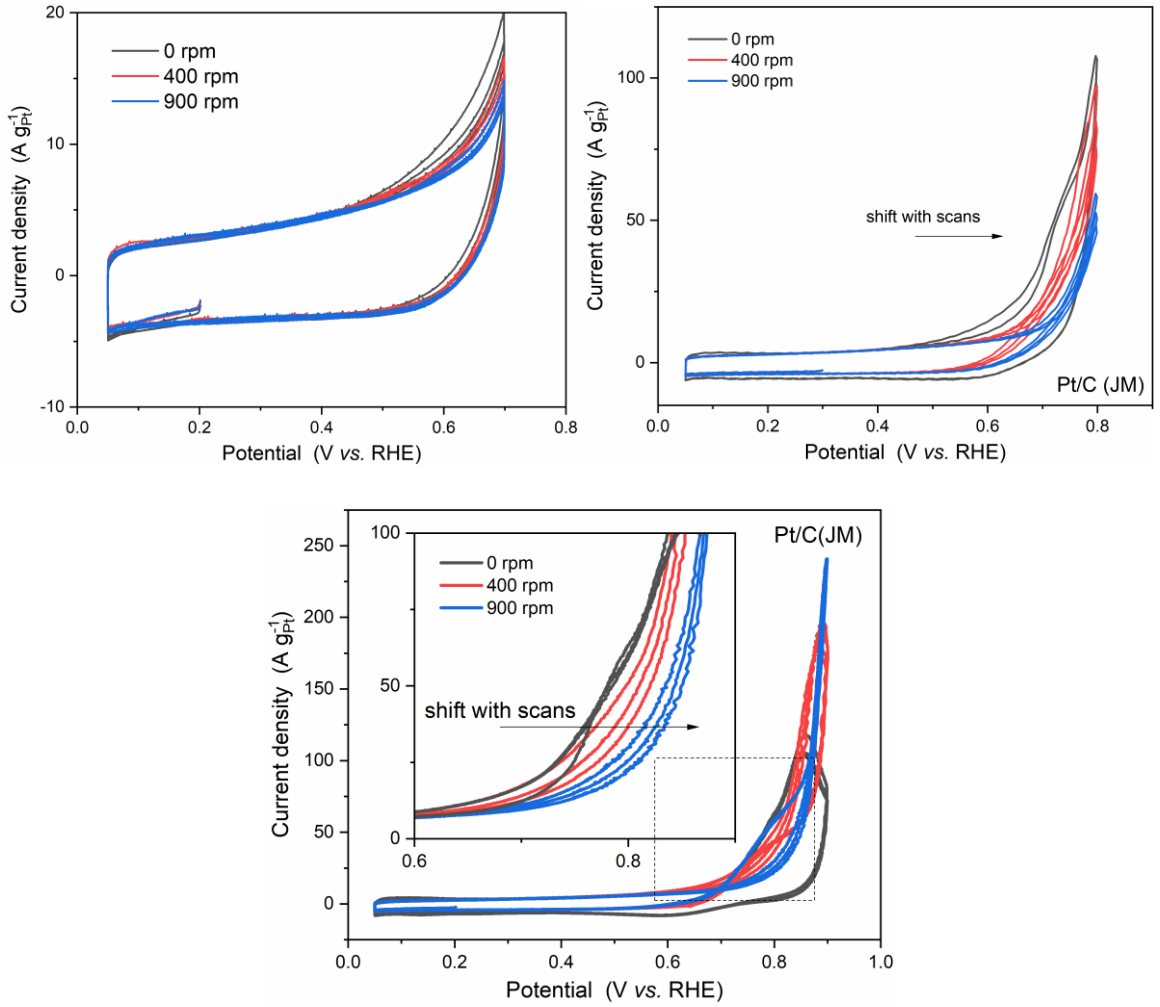

Figure S4-20. CO oxidation voltammograms of Pt/C (JM) in CO-saturated 0.1 M $HClO_4$ solution with upper potential limits of (top left) 0.7 V, (top right) 0.8 V and (bottom) 0.9 V. The rotation rates are indicated in the figure legend, and the inset of the right present only the forward scans of the magnified area, showing the oxidation waves shift positive with scans under convective-diffusion condition. The scan rates were 20 mV s^{-1}.

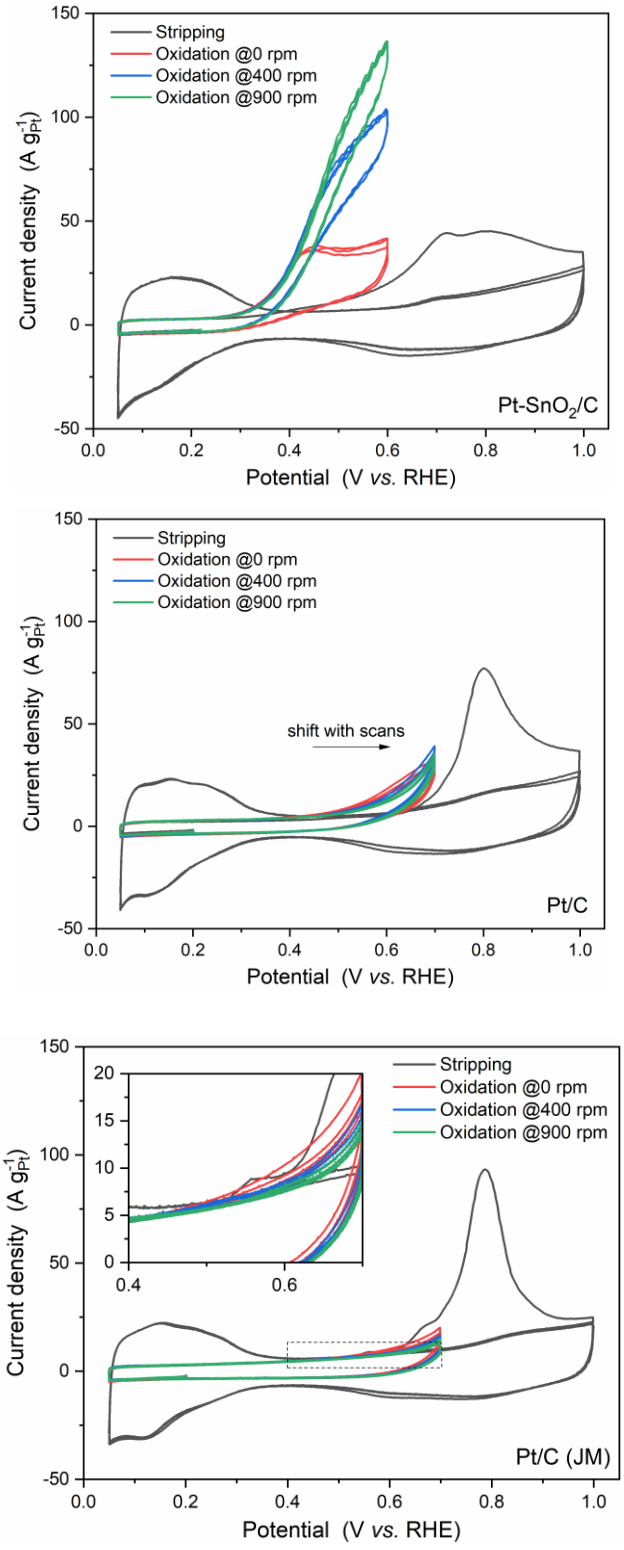

Figure S4-21. CO stripping and CO oxidation voltammograms of (top left) Pt-SnO_2/C, (top right) Pt/C and (bottom) Pt/C(JM) in 0.1 M $HClO_4$ with a scan rate of 20 mV s^{-1}. The cyclic voltammetry for CO oxidation was conducted in CO-saturated solution with different rotation rates (0 rpm, 400 rpm and 900 rpm in sequence), each of which was measured three scans.

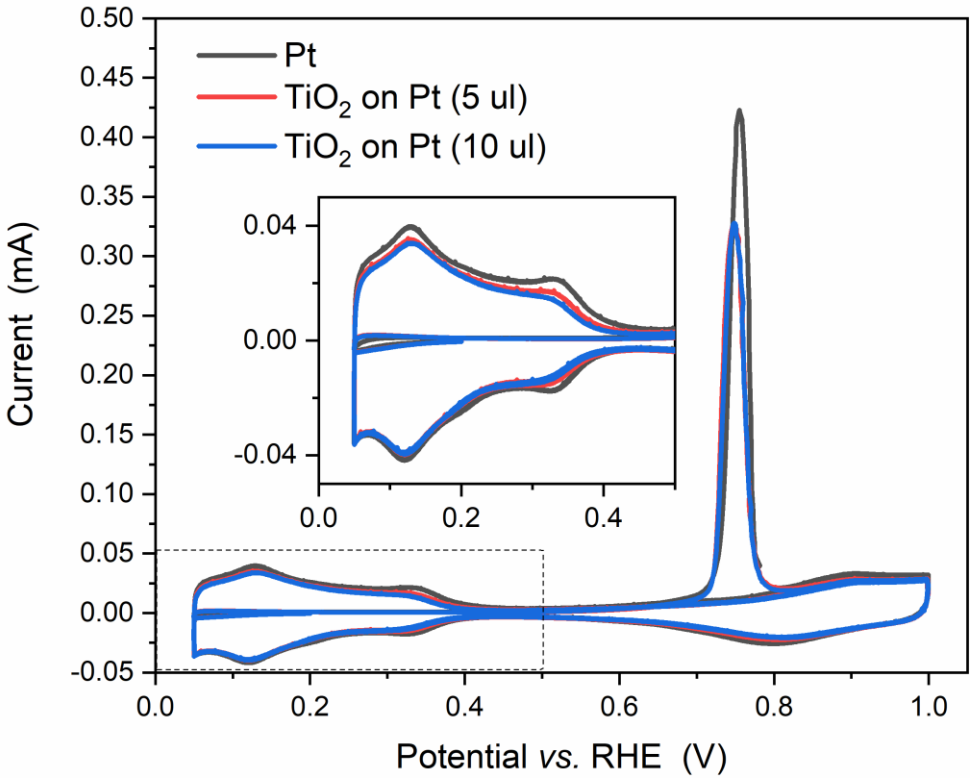

Figure S4-22. CO-stripping voltammograms of TiO_2-modified Pt electrode with three different loadings, 0, 5 and 10 ul 5 mg mL^{-1} TiO_2 suspension (H_2O-isopropanol solution with a water volume fraction of 60%) on a Pt electrode (5 mm diameter). The hydrogen region is magnified in the inset.

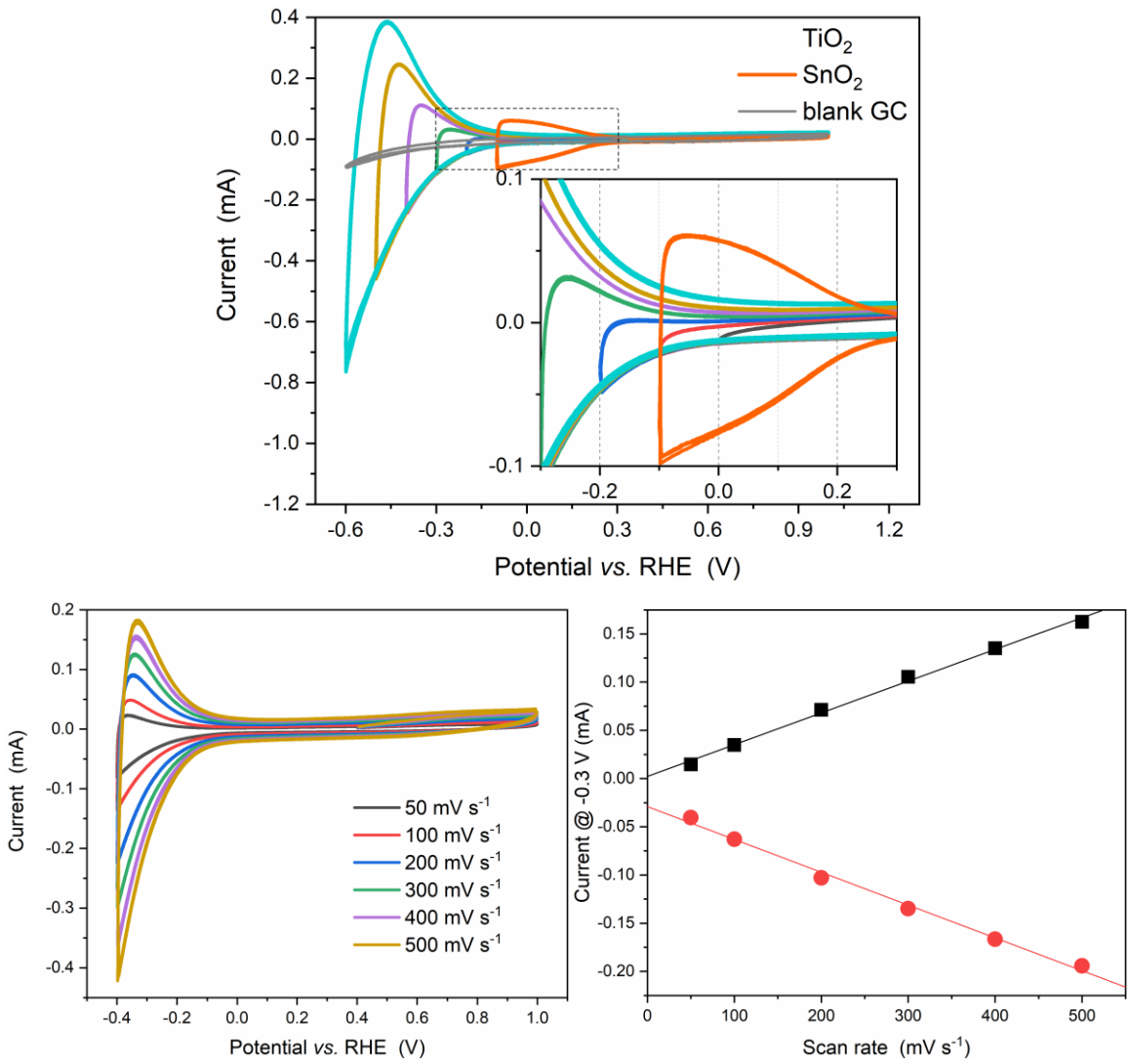

Figure S4-23. Cyclic voltammograms of TiO_2(P25) on a polished glassy carbon electrode (5 mm diameter) with (top) different potential lower limits (-0.6–0.0 V with interval of 0.1 V) and (bottom left) different scan rates. (bottom right) The currents at -0.3 V were plotted against the scan rates, showing linear relationships between the anodic/cathodic currents and scan rates. In the window-opening experiment, the scan rate was 200 mV s^{-1}, and the SnO_2 data and the blank glassy carbon (GC) data with the same scan rate were compared.

Appendix B Supporting information of Chapter 5

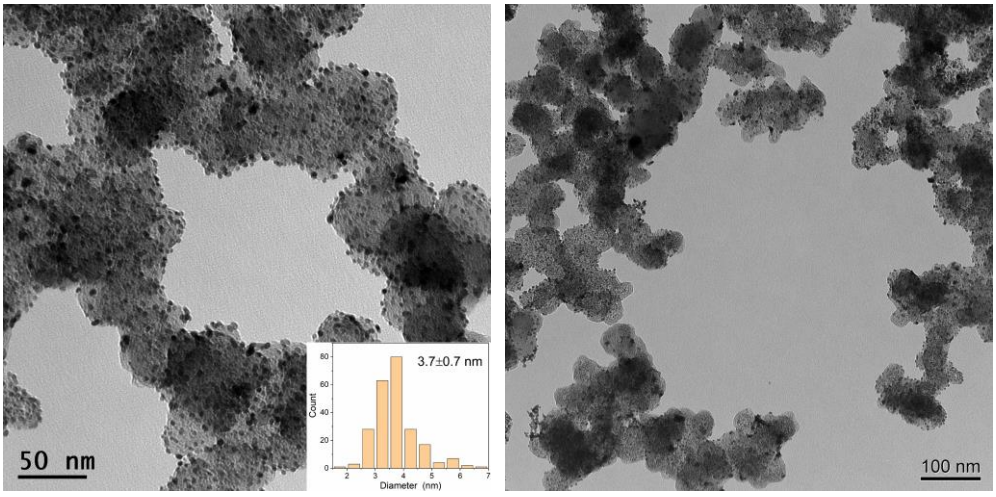

Figure S5-1 Representative TEM images of the commercial Pt/C (60 wt%) in two different fields of view, showing the size and dispersion of Pt nanoparticles. The inset (left) shows the size distribution of Pt nanoparticles (3.7±0.7 nm).

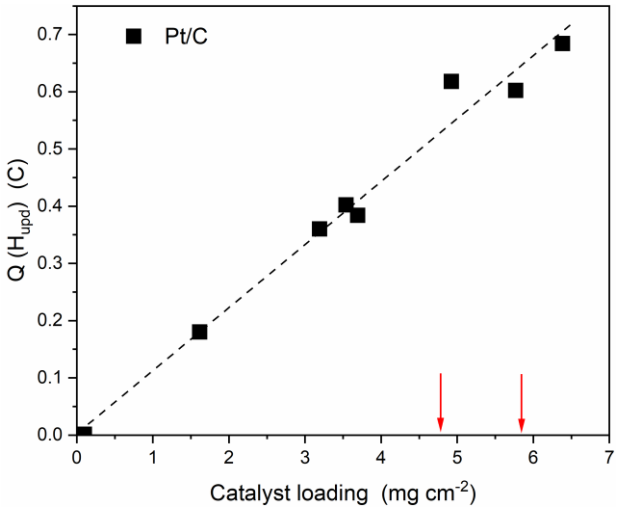

Figure S5-2 Electrochemistry testing for in situ XAS electrode preparation using Pt/C as the reference. Charge of H_{upd} of electrodes plotted as a function of catalyst loading, showing a linear relationship within ~6.4 mg cm^{-2}. The catalyst loadings of the two in situ electrodes of Sn_{ad}-Pt/C in this study (indicated by red arrows) are within the range.

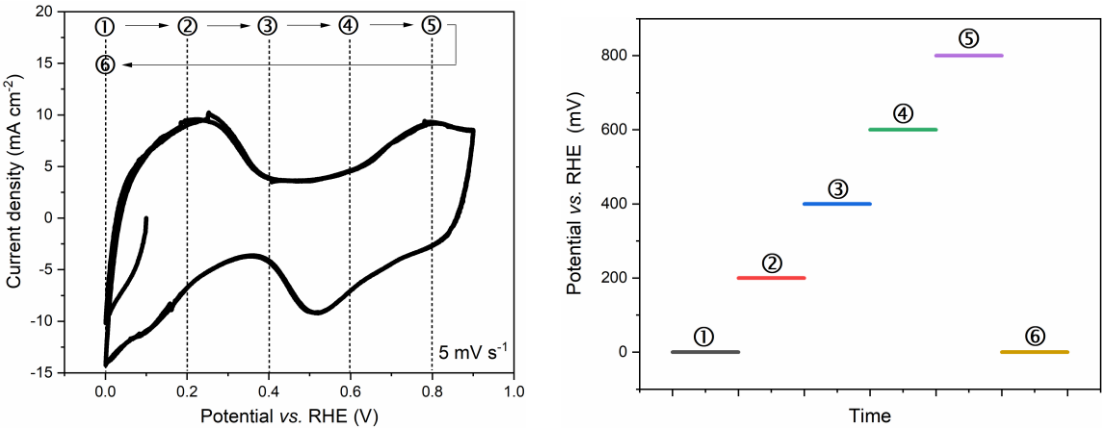

Figure S5-3 (left) a CV of a Sn_{ad}-Pt/C painted electrode carried out in N_2-saturated 1 M $HClO_4$ solution in the in situ XAS electrochemical cell, showing that the similar CV can be produced from a painted electrode in the in situ cell. The scan rate is 5 mV s^{-1}. The order of the applied potential during in situ XAS measurements is highlighted and shown.

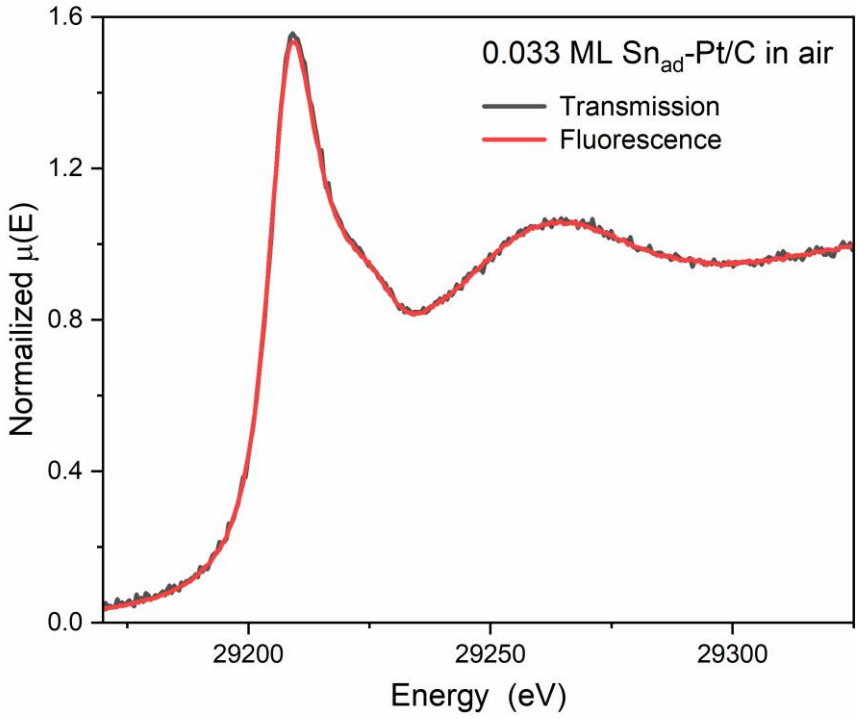

Figure S5-4 XANES spectra of a Sn_{ad}-Pt/C (0.033 ML) measured in transmission (~0.02 in edge step) and in fluorescence, showing that effects of self-adsorption from fluorescence data are negligible, as well as the in situ data, the edge step of which is half of that of 0.033 ML data.

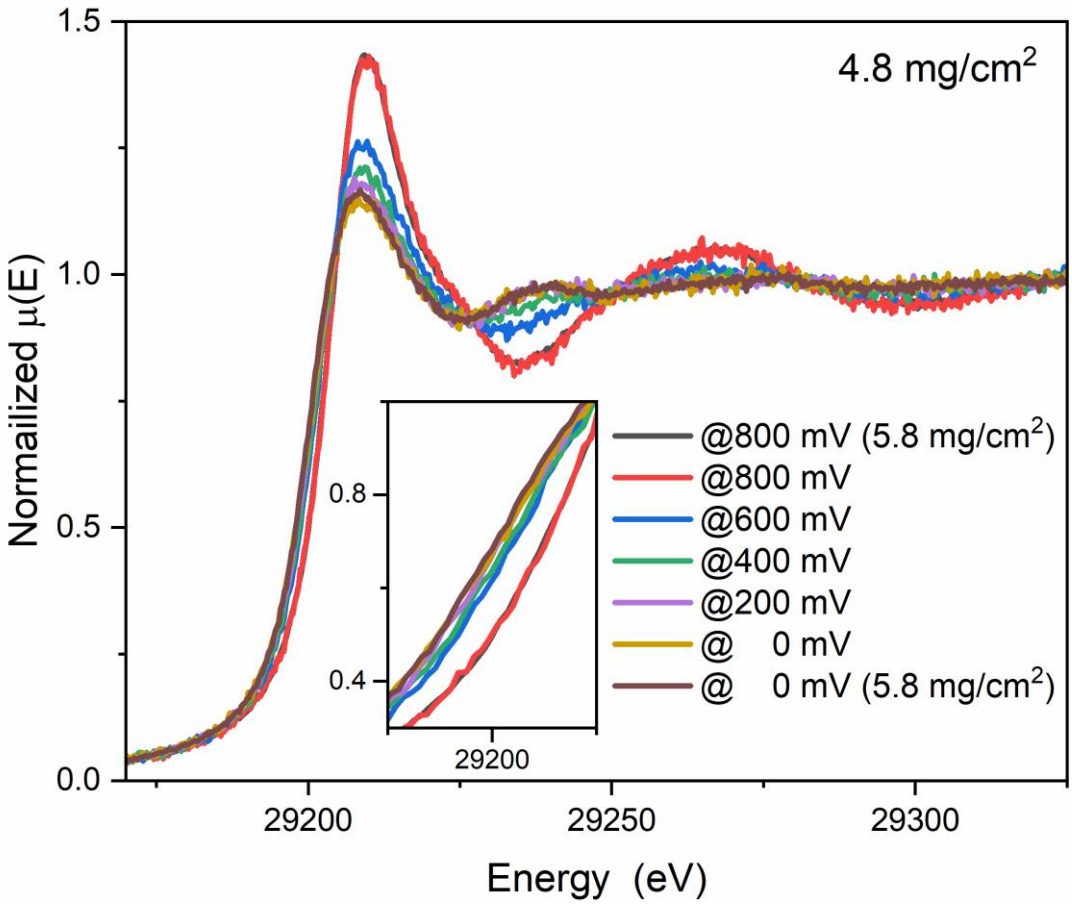

Figure S5-5 *In situ* XANES spectra of a Sn_{ad}-Pt/C painted electrode under potential control with less Sn loading (~89 $\mu g_{Sn}/cm^2$) on the electrode, showing the potential-dependent behaviour of Sn_{ad}-Pt/C is reproducible, and the self-adsorption effect of fluorescence is negligible. The edge steps of the 5.8 mg/cm^2 electrode and the 4.8 mg/cm^2 electrode in transmission are ~0.01 and ~0.003, respectively.

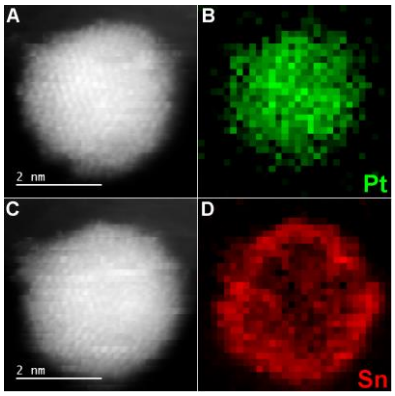

Figure S5-6 Uncorrected STEM-EELS images of Figure 5-1E. (A) The HAADF image during (B) EELS mapping for Pt, and (C) the HAADF image during (D) EELS mapping for Sn. Since these two mapping images were not collected simultaneously and the sample drifted slightly with time, there are two subtle differences in A and C, the shape and the position of the particle. The spatial drift was calibrated in Figure 5-1E by aligned the pixels of these two HAADF image, but the shape is unable to be corrected. Nevertheless, the extent of differences are subtle, which doesn't affect the data interpretation.

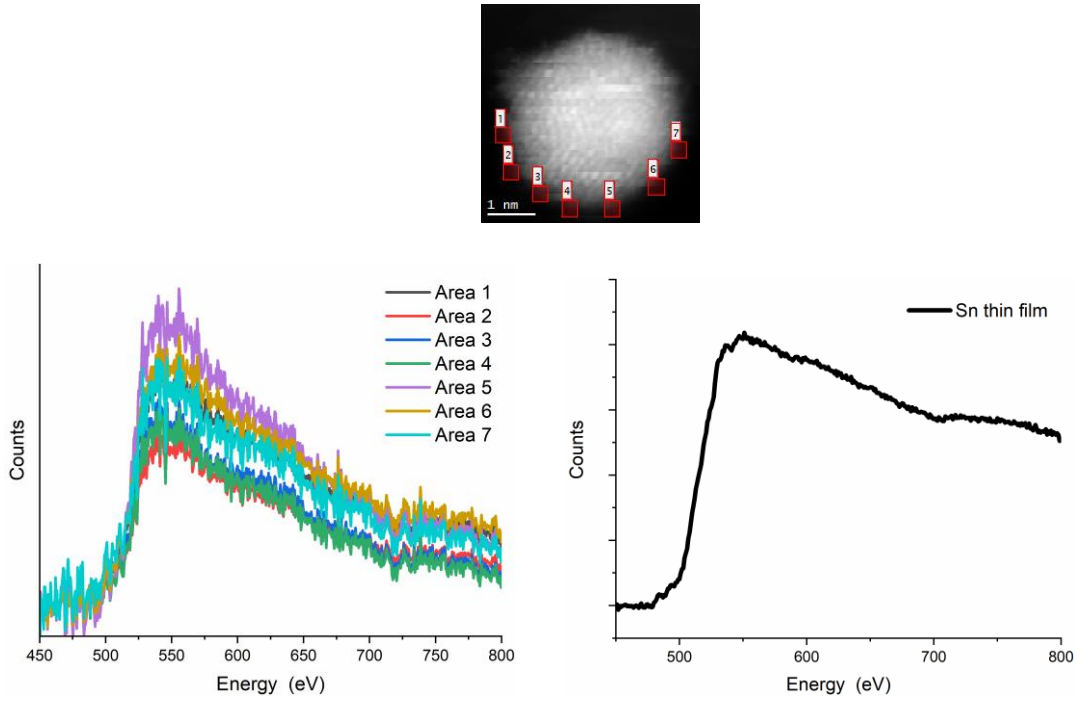

Figure S5-7 (left) EELS spectra of Sn_{ad}-Pt/C at Sn $M_{4,5}$ edge on selected areas as indicated by red squares in (top) a HADDF-STEM image. The spectra along the edge of the particle are consistent. As O K edge is at 532 eV and has well defined feature at ~550 eV, the absence of these feature suggest that the Sn ad-atoms are metallic and not coordinated with O. (right) A EELS spectrum of Sn thin film obtained from EELS altas database.

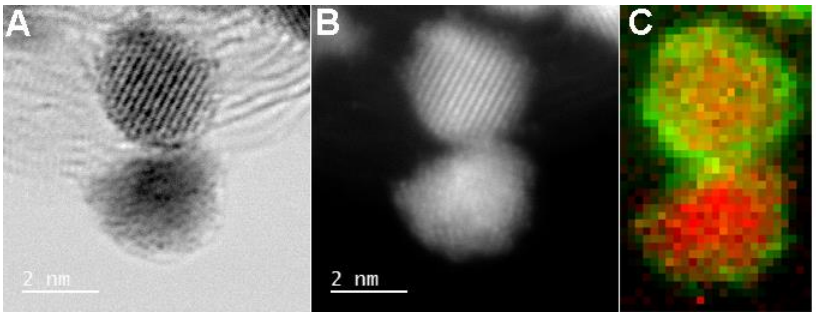

Figure S5-8 Same as Figure S5-6 but on a different region. Sn and Pt are shown in green and red, respectively.

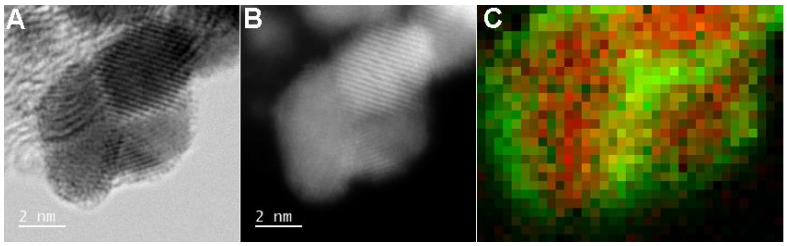

Figure S5-9 Same as Figure S5-6 but on a different region. Sn and Pt are shown in green and red, respectively.

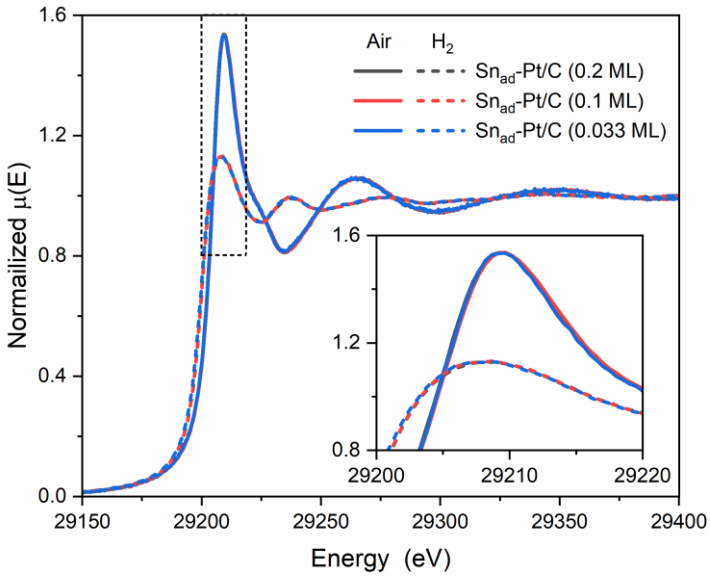

Figure S5-10 XANES spectra and (inset) their whiteline of Sn_{ad}-Pt/C with Sn coverage (on Pt) of 0.033–0.2 ML, measured in Air and in H_2 (g), showing that the XANES spectra of Sn_{ad}-Pt/C are consistent by varying the Sn coverage. The XAS data here and below were measure in transmission mode, apart from Sn_{ad}-Pt/C (0.033 ML) in fluorescence mode

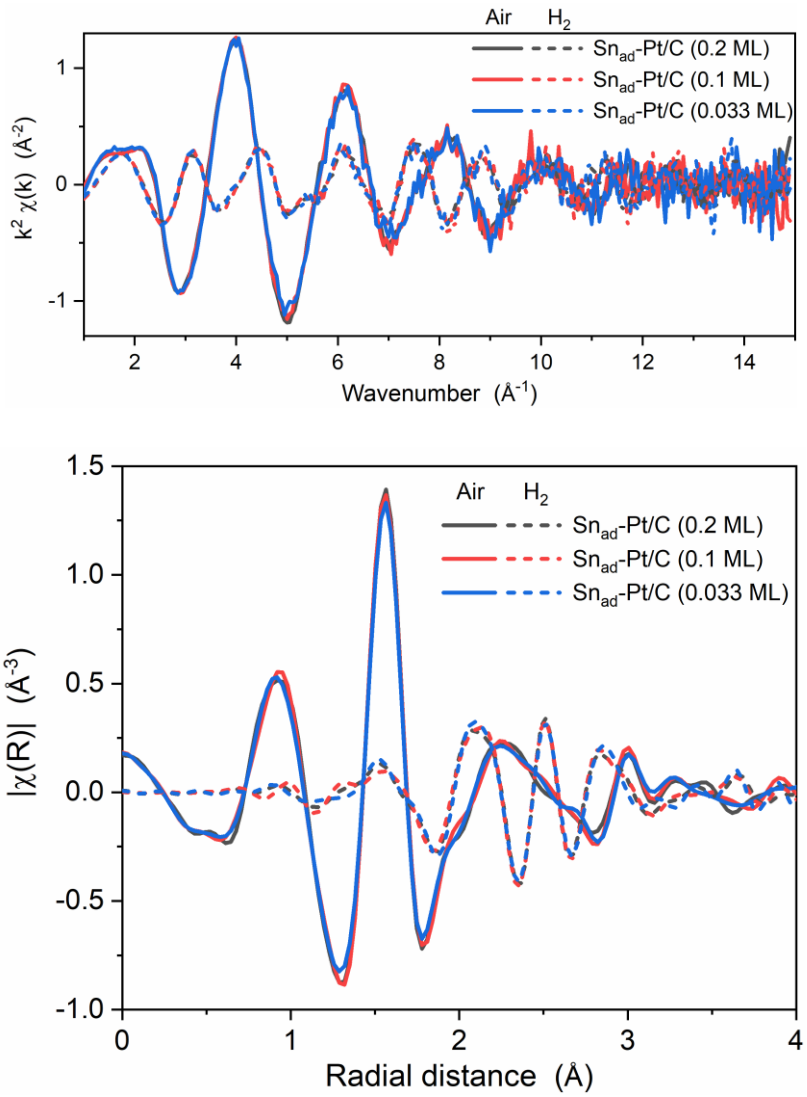

Figure S5-11 (top) k^2-weighted EXAFS spectra and (bottom) their Fourier transforms (real space) of Sn_{ad}-Pt/C with Sn coverage (on Pt) of 0.033–0.2 ML, measured in Air and in H_2 (g), showing that the EXAFS spectra of Sn_{ad}-Pt/C are consistent by varying the Sn coverage. The Fourier transformation was carried out in a k range of 3.4–14.0 $Å^{-1}$.

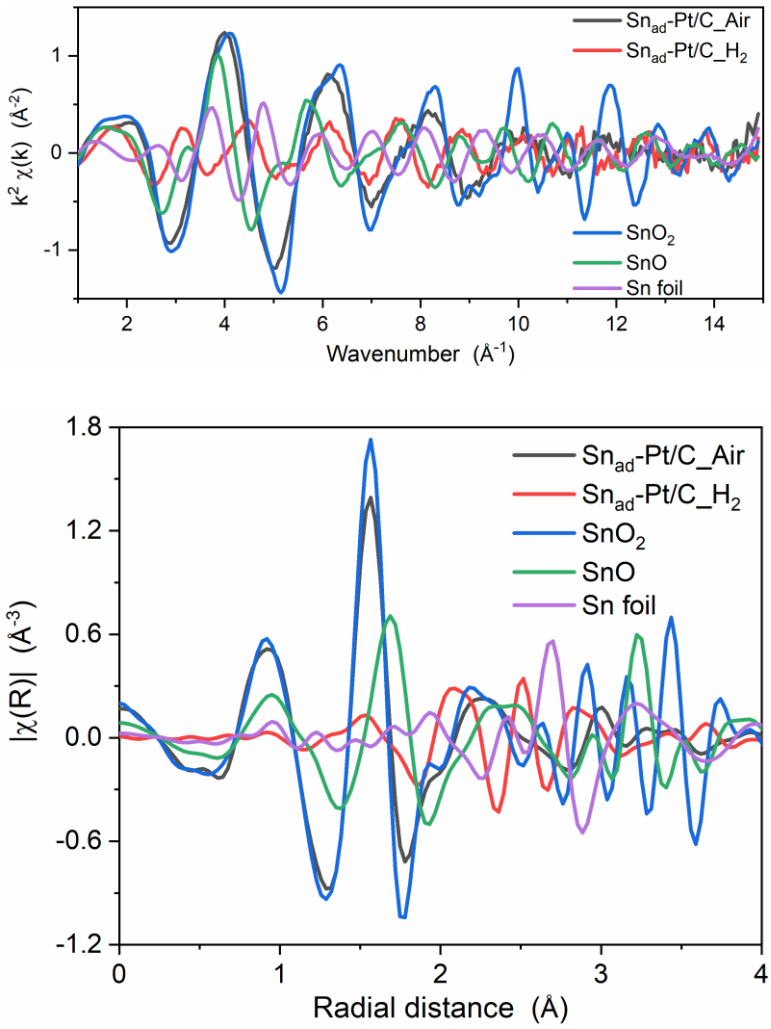

Figure S5-12 (top) k^2-weighted EXAFS spectra and (bottom) their Fourier transforms (real space) of Sn_{ad}-Pt/C, measured in air and in H_2 (g), along with Sn references (SnO_2, SnO and Sn foil).

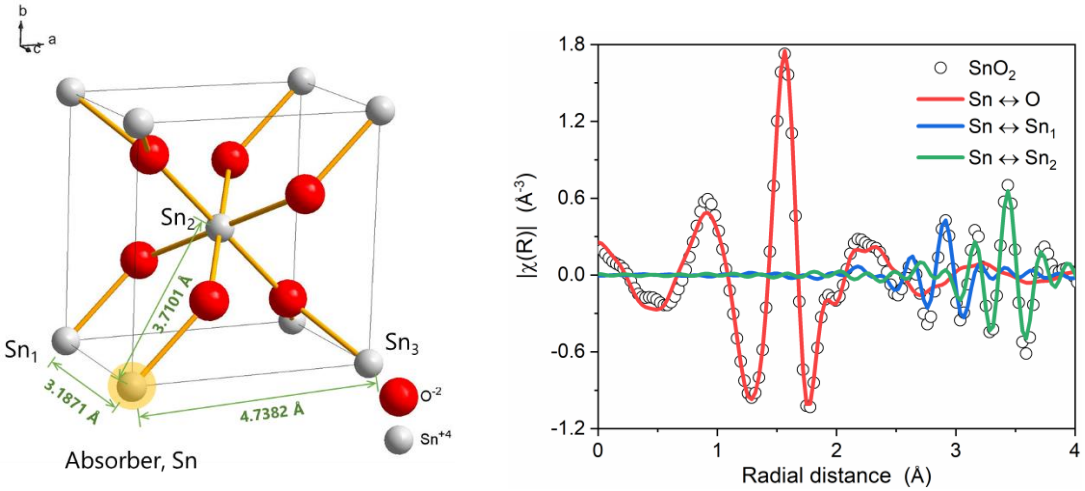

Figure S5-13 (Left)The unit cell of SnO_2 (ICSD No.647469) and (Right) the Fourier transform of a SnO_2 EXAFS spectrum in the real part, along with scattering paths used in the fit, showing a [SnO_6] in the first coordination shell of the Sn absorber and two Sn–Sn scattering paths from the higher shells.

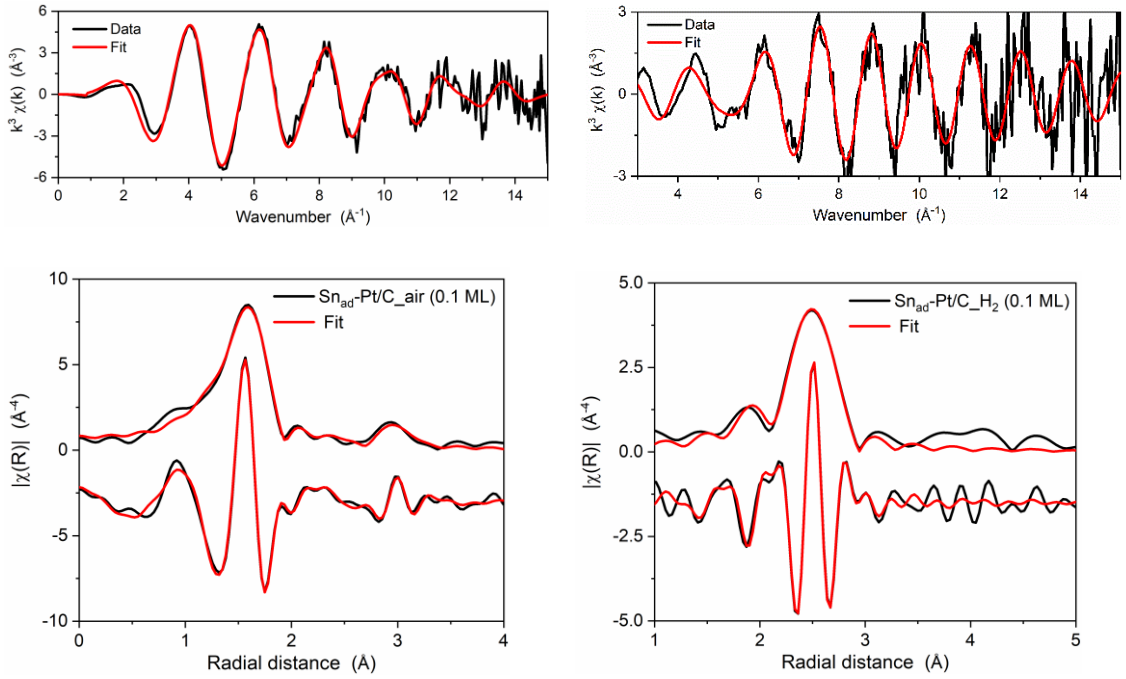

Figure S5-14 Same as Figure 5-3 but for a Sn_{ad}-Pt/C sample with a Sn coverage of 0.1 ML.

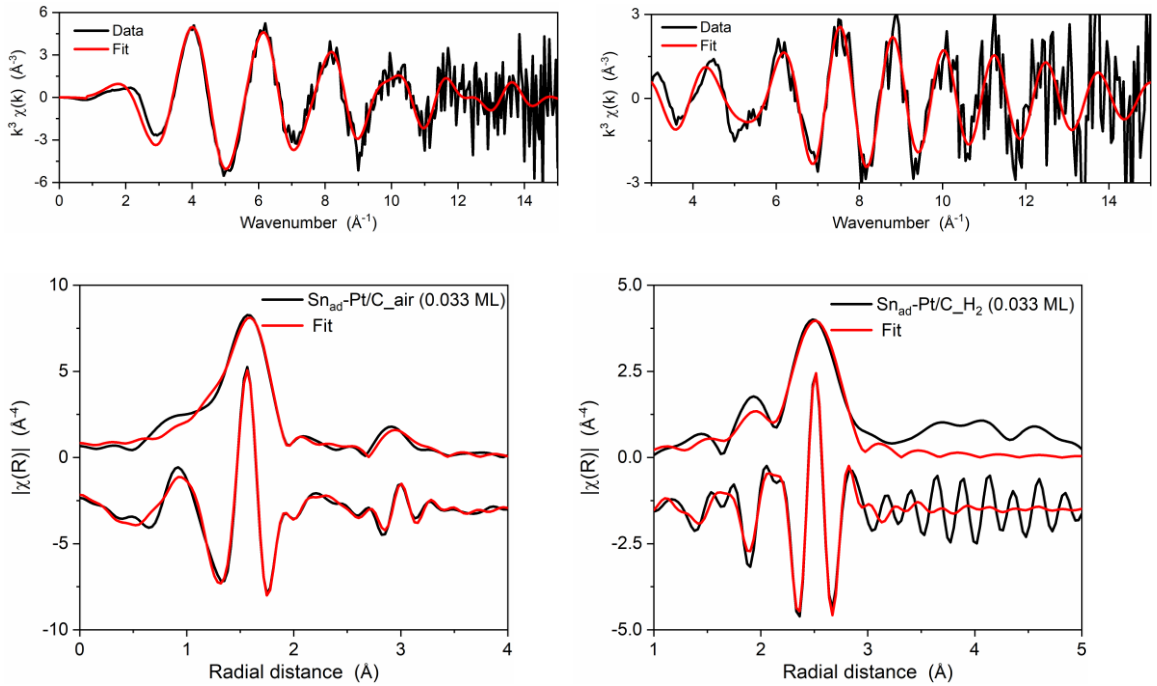

Figure S5-15 Same as Figure 5-3 but for a Sn_{ad}-Pt/C sample with a Sn coverage of 0.033 ML.

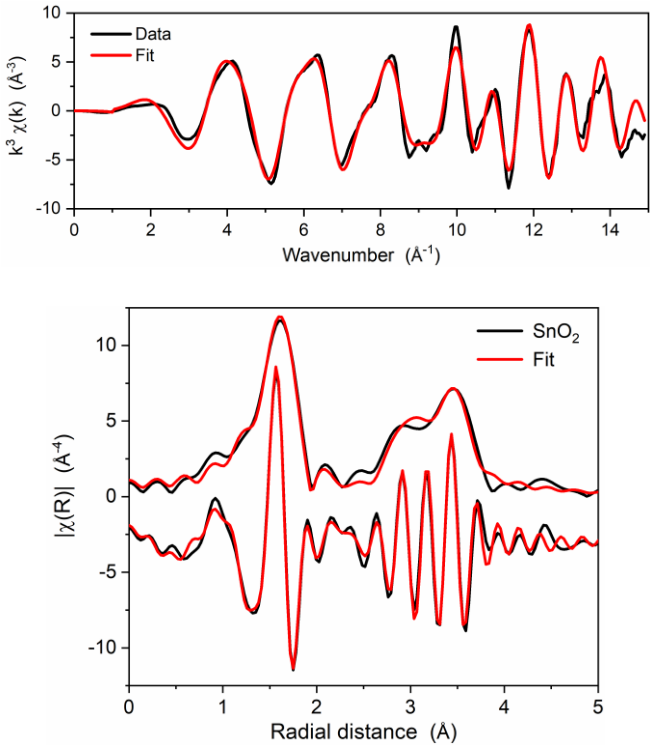

Figure S5-16 Fits for Sn K-edge EXAFS spectra of the SnO2 reference, showing as k^3-weighted (top panels) k space and (bottom panels) the magnitude and the real part of R space. The Fourier transformation was performed in a k range of 3.4–14.0 Å^{-1}, and the fitting was carried in a R-range of 1.0–3.7 Å.

Table S5-3 Structural parameters of Sn_{ad}-Pt/C (Sn coverage from 0.2 ML to 0.033 ML), obtained from EXAFS fitting. Plots of the data and the corresponding fits are shown in figures from Figure 5-3 to Figure S5-16.

Sample	Scattering path	*R* (Å)	*N*	σ^2 (x10^3 Å^2)	ΔE_0 (eV)	R factor (%)
0.2 ML_Air[a]	Sn – O	2.051(3)	6.4(2)	6.6(4)	2.2(4)	0.26
	Sn – Sn	3.272(9)	1.6(4)	9(2)		
0.1 ML_Air	Sn – O	2.051(6)	6.5(3)	7.1(8)	2.1(8)	1.1
	Sn – Sn	3.28(2)	1.3(7)	7(3)		
0.033 ML_Air[b]	Sn – O	2.052(4)	6.3(2)	7.1(5)	2.6(6)	0.42
	Sn – Sn	3.28(1)	0.8(4)	6(3)		
0.2 ML_H_2[a]	Sn – Pt	2.690(7)	4.5(4)	8.8(6)	-3(1)	1.17
0.1 ML_H_2	Sn – Pt	2.687(6)	4.8(4)	9.1(5)	-4(1)	0.86
0.033 ML_H_2[b]	Sn – Pt	2.70(1)	5.7(9)	10(1)	-2(2)	2.71
SnO_2	Sn – O	2.053(5)	6.1(4)	4.0(7)	4.0(8)	0.79
	Sn – Sn_1	3.200(9)	1.2(5)	3(2)		
	Sn – Sn_2	3.725(7)	2.2(8)	2(2)		
Pt_3Sn (theory)[c]	Sn – Pt	2.829	12	N.A.	N.A.	N.A.

[a] shown in the main text as the representative of Sn_{ad}-Pt/C sample.

[b] Fluorescence data were used for increasing signal-to-noise level, and no obvious self-adsorption was found in these data.

[c] calculated from Pt_3Sn crystal (ICSD 105796) using Feff6.

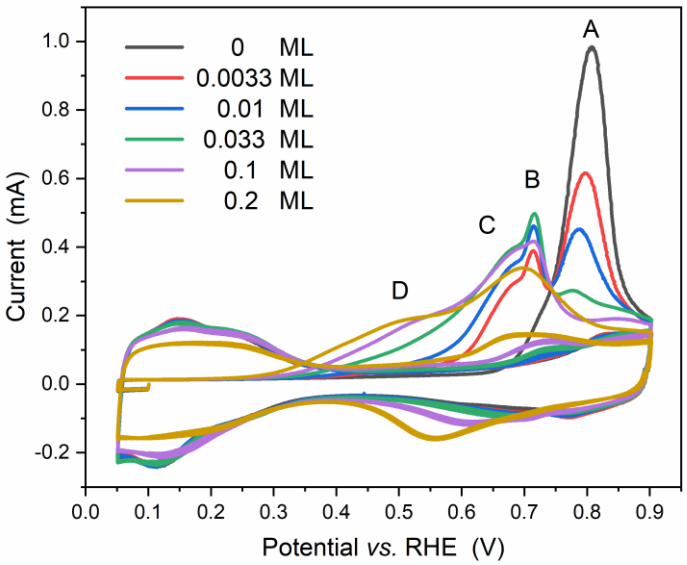

Figure S5-17 CO_{ad} stripping voltammograms of Sn_{ad}-Pt/C (Sn coverage from 0 ML to 0.2 ML) in N_2-saturated 0.1 M $HClO_4$ solution with a scan rate of 20 mV s^{-1}. The saturated CO adlayer was adsorbed by potential hold at 0.1 V, followed by displacement of dissolved CO from the solution by at least 30 min N_2 purge.

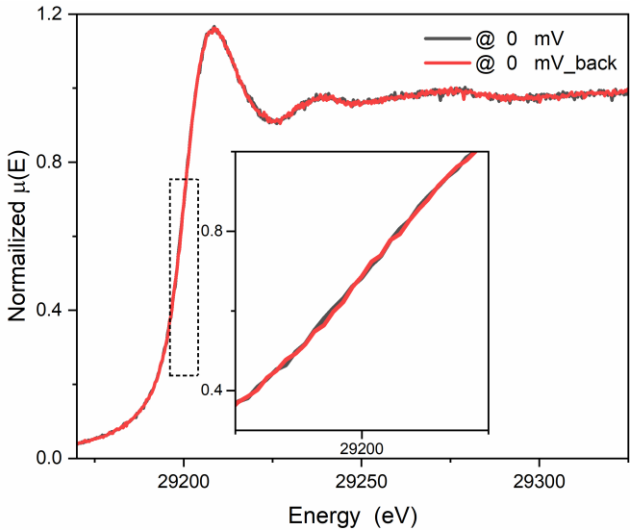

Figure S5-18 In situ XANES spectra of Sn_{ad}-Pt/C under 0 V from stepping back from 0.8 V and the one measured at 0 V, showing that the oxidized Sn at high potential and the metallic Sn under low potential are interconvertible.

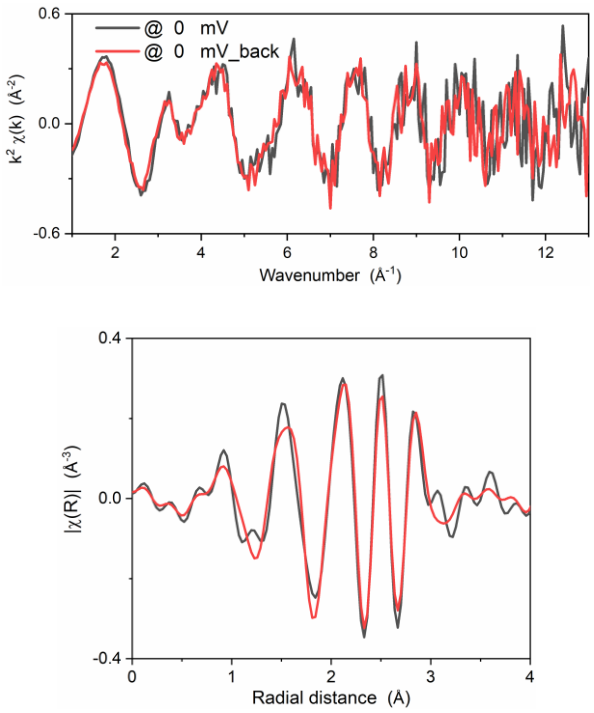

Figure S5-19 (top) k^2-weighted EXAFS spectra of Sn_{ad}-Pt/C under 0 V from stepping back from 0.8 V and the one measured at 0 V, along with (bottom) the real-space Fourier transforms.

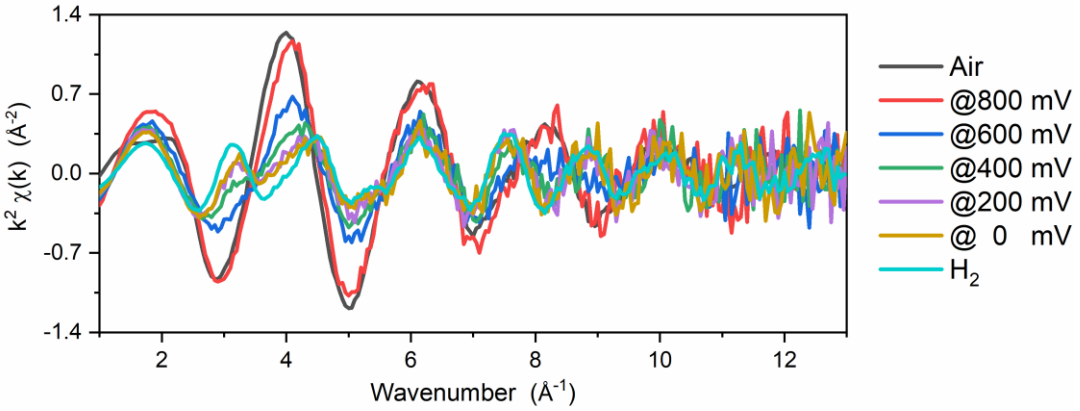

Figure S5-20 k^2-weighted EXAFS spectra of a Sn_{ad}-Pt/C painted electrode under potential control in N_2-saturated 1 M $HClO_4$ solution, along with Sn_{ad}-Pt/C pellet samples measured in air and in H_2(g), showing the potential dependence and isosbestic points in EXAFS k-space.

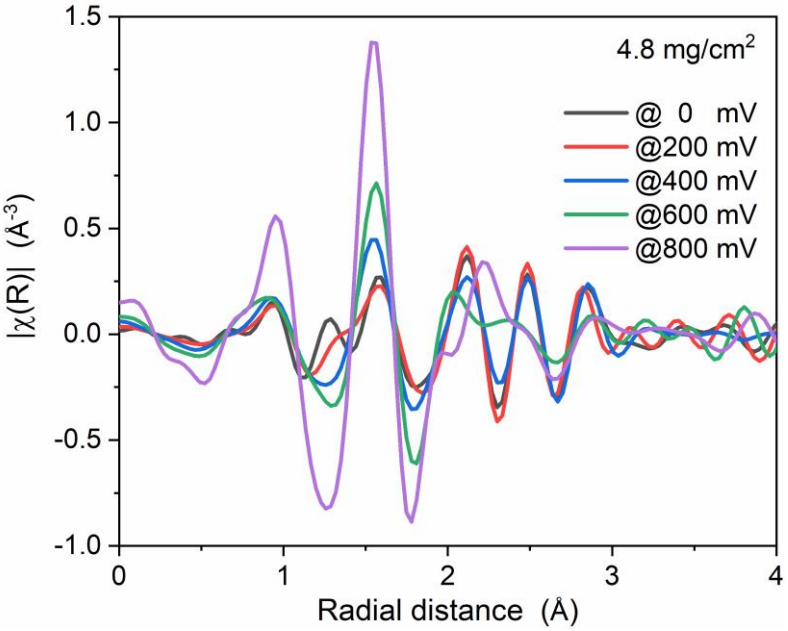

Figure S5-21 Fourier transforms (real part) of k^2-weighted EXAFS spectra of a Sn_{ad}-Pt/C painted electrode under potential control with less Sn loading (~89 $\mu g_{Sn}/cm^2$), showing that a positive shift of Sn–O scattering path when the applied potentials were 0 V and 0.2 V. The Fourier transformation was carried out in a k-range of 3.4–11.2 $Å^{-1}$.

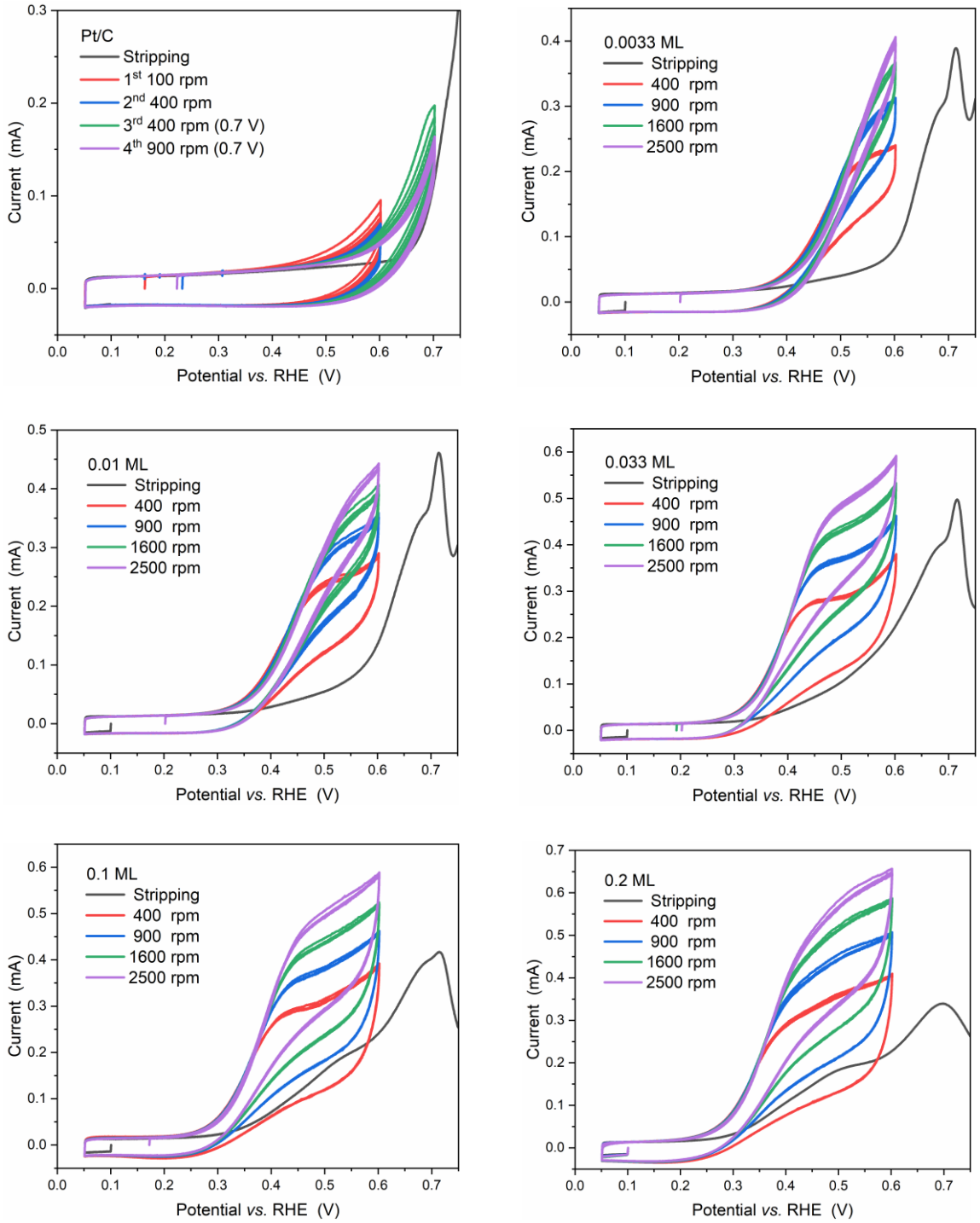

Figure S5-22 CO continuous oxidation voltammograms of Sn_{ad}-Pt/C, with Sn coverage from 0 ML to 0.2 ML. The measurements were conducted in CO-saturated 0.1 M $HClO_4$ solution with a scan rate of 20 mV s^{-1}, and the rotation rates are indicated in the figure legends.

Appendix C Supporting information of Chapter 6

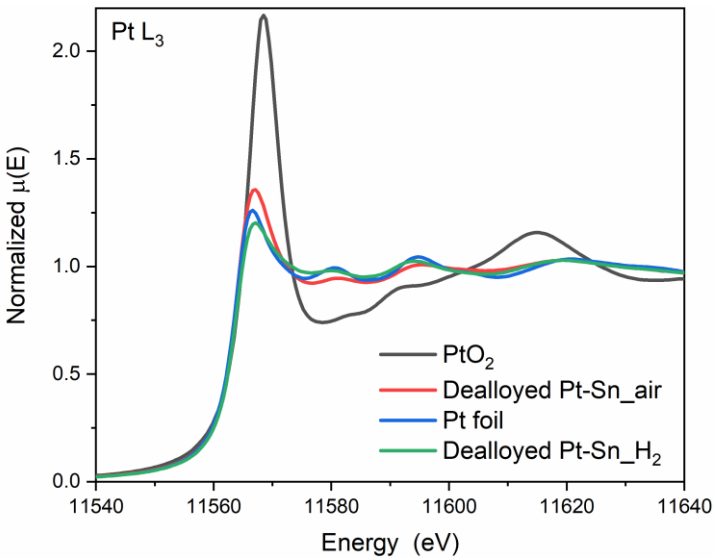

Figure S6-1 XANES of the dealloyed Pt-Sn sample at Pt L_3-edge, along with Pt foil and PtO_2 references.

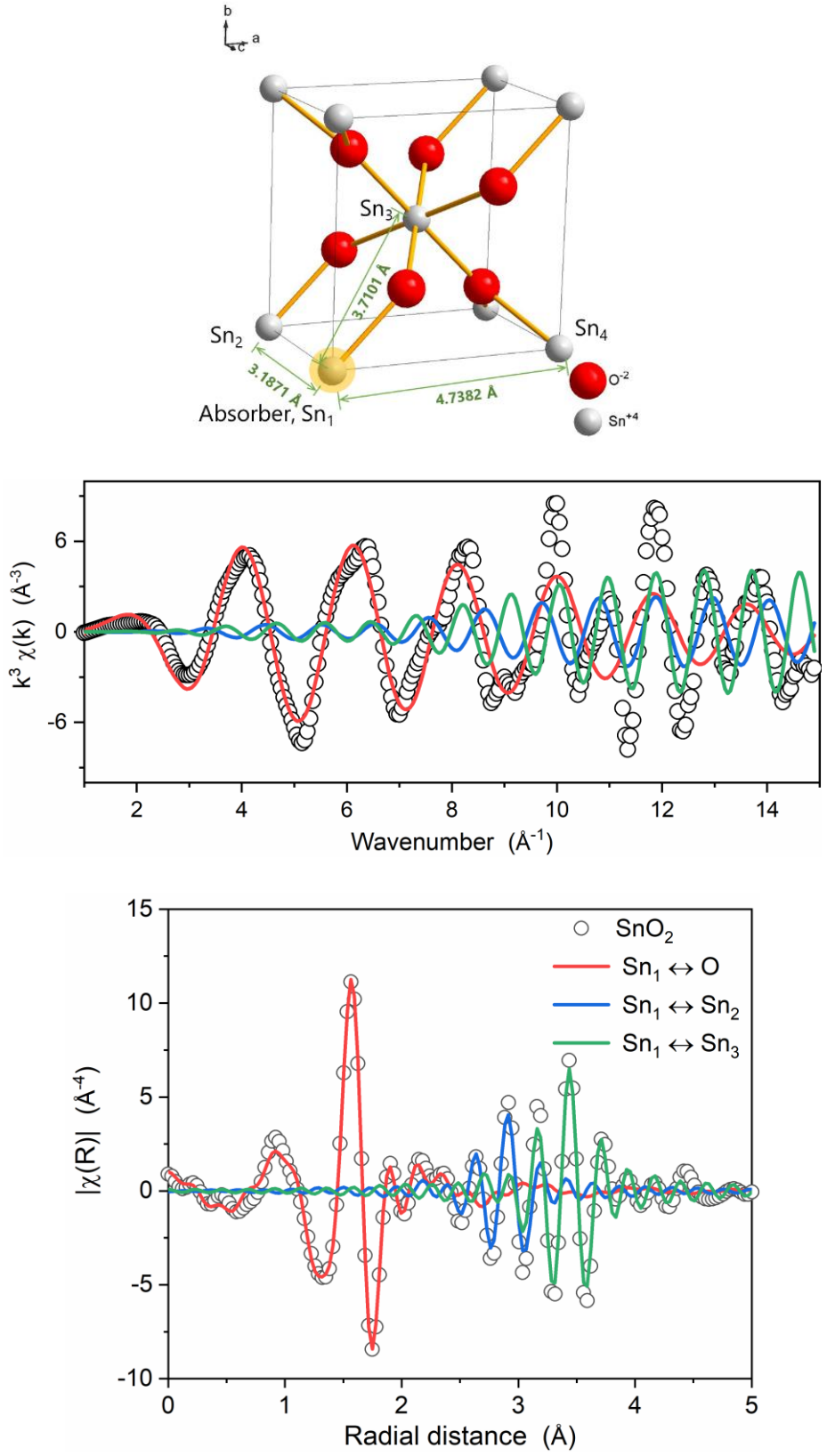

Figure S6-2 (top) A unit cell of rutile SnO_2 (ICSD 647469) and the EXAFS spectrum (middle) in k space and (bottom) in R-space (real part), showing the contribution of different scattering paths to the EXAFS spectrum.

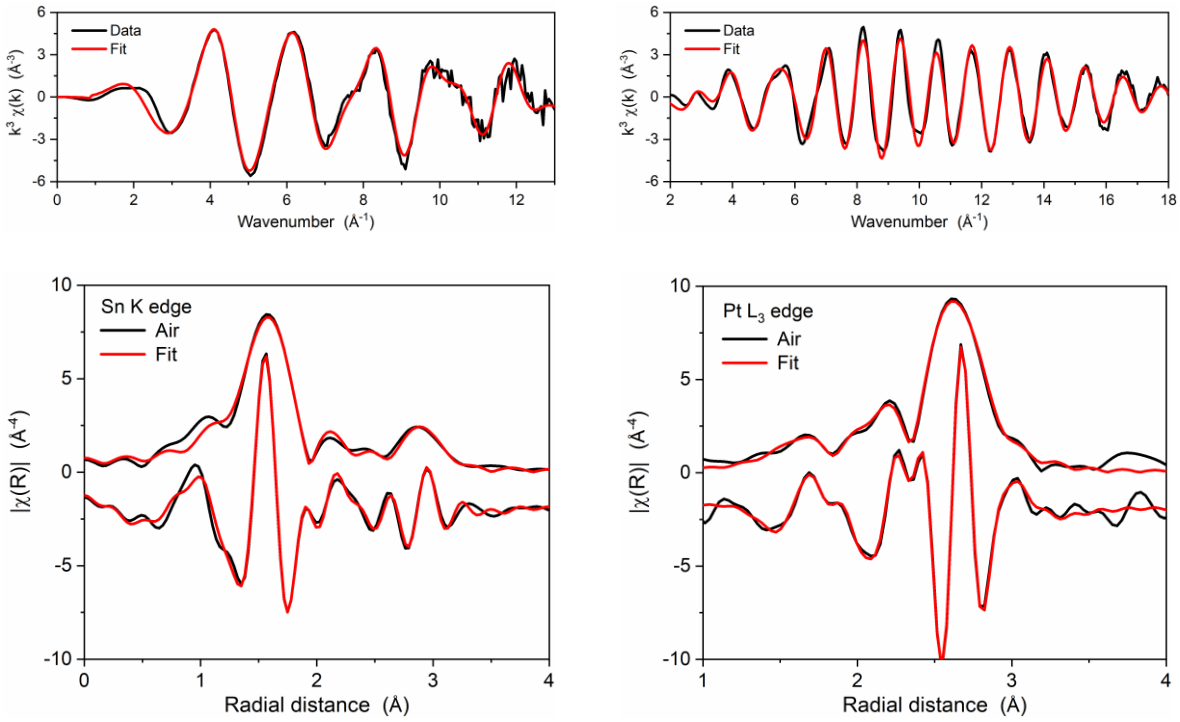

Figure S6-3 Same as Figure 6-4 but without a constraint in N(Sn–Pt). The fit yields an R-factor of 0.24% and the obtained structural parameters listed in Table S6-.

Table S6-1 Structural parameters obtained from individual double-dataset fits of the dealloyed Pt-Sn data collected in air, without a constraint in N(Sn–Pt). The fits use 18 variables out of ~27 independent points for the data collected in air.

Samples	Scattering path	*N*	*R* (Å)	σ^2 (×10³ Å²)	Δ*E* (eV)	*R*-factor (%)
Dealloyed Pt-Sn (air)	Pt – O	0.8(1)	1.996(6)	5(2)		0.24
	Pt – Pt	7.6(3)	2.757(2)	7.6(2)	7.3(4)	
	Pt – Sn	0.9(7)	2.83(2)*	19(11)*		
	Sn – O	5.0(7)	2.04(1)	5(2)		
	Sn – Pt	4(5)**	2.83(2)*	19(11)*	3(2)	
	Sn – Sn	1(1)	3.23(3)	6(7)		

* Pt – Sn and Sn – Pt scattering paths are set to have the same value in *R* and σ^2.

** not constrained.

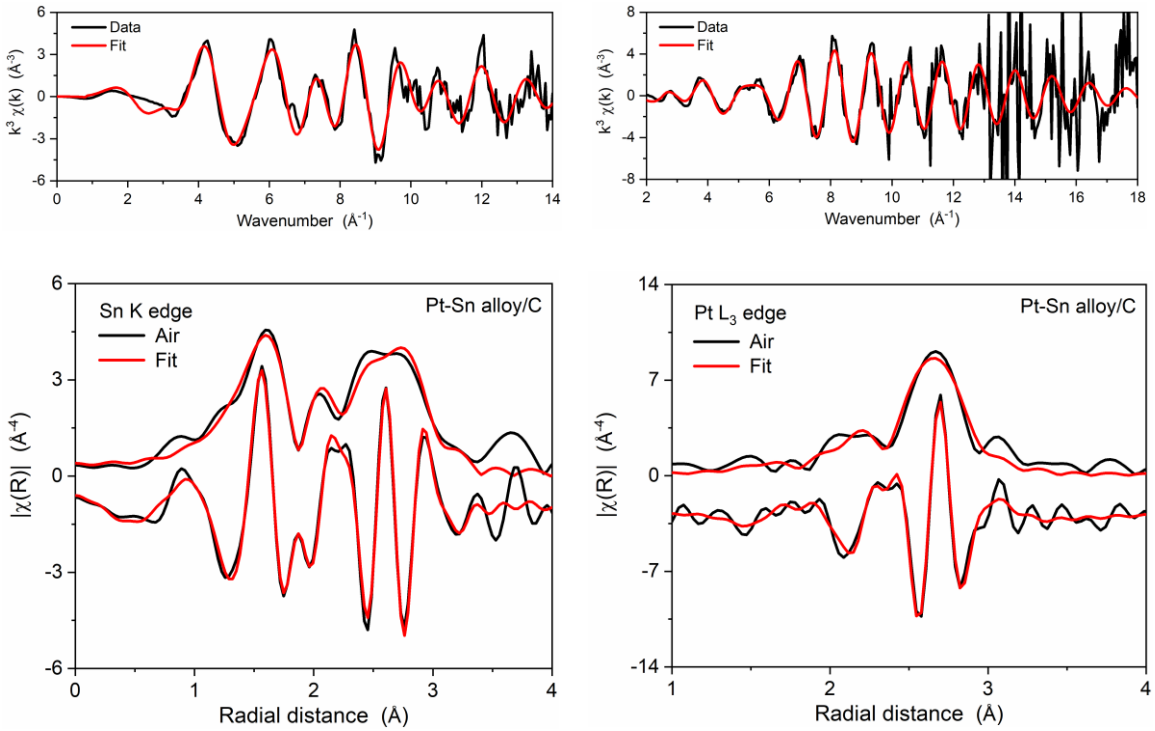

Figure S6-4 Same as Figure S6-3 but for Pt-Sn alloy data measured in air, and the Fourier transformation was carried out in a k-range of 3.6–13.7 Å^{-1} for the Sn K edge and 3.5–17.3 Å^{-1} for the Pt L_3 edge. The fit yields an R-factor of 1.13% and the obtained structural parameters listed in Table S6-2.

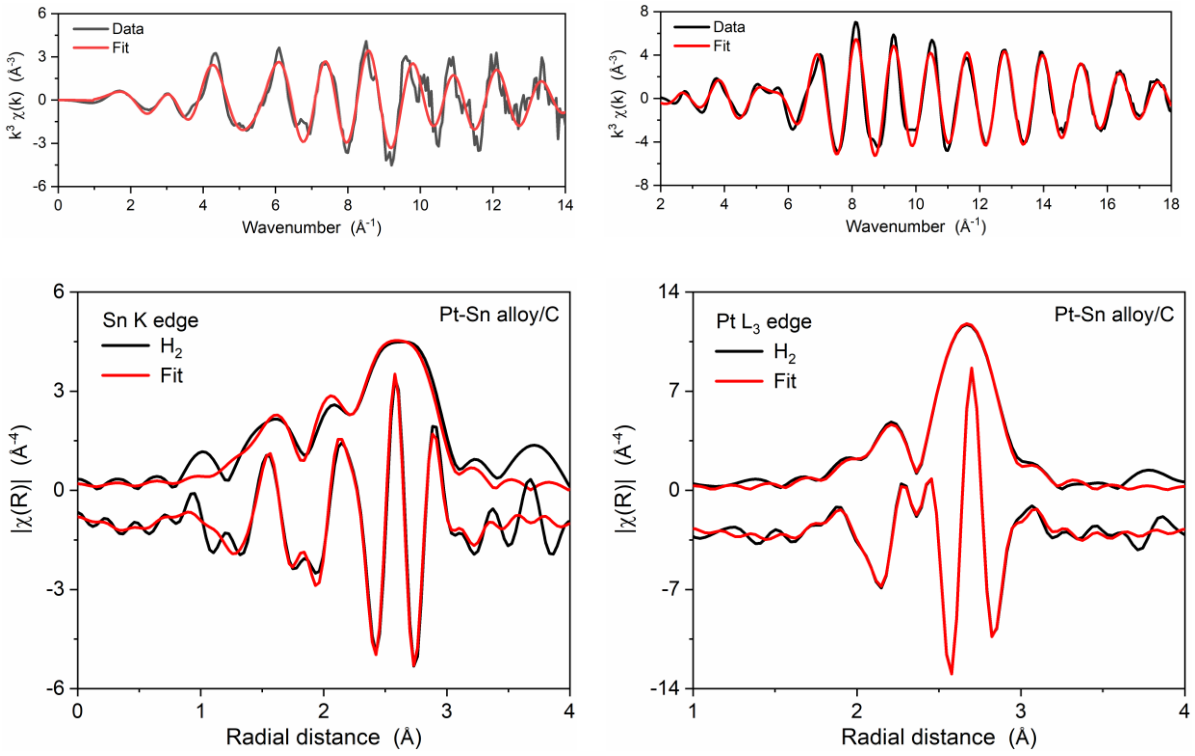

Figure S6-5 Same as Figure S6-4 but for Pt-Sn alloy data measured in H_2(g). The fit yields an R-factor of 0.56%.

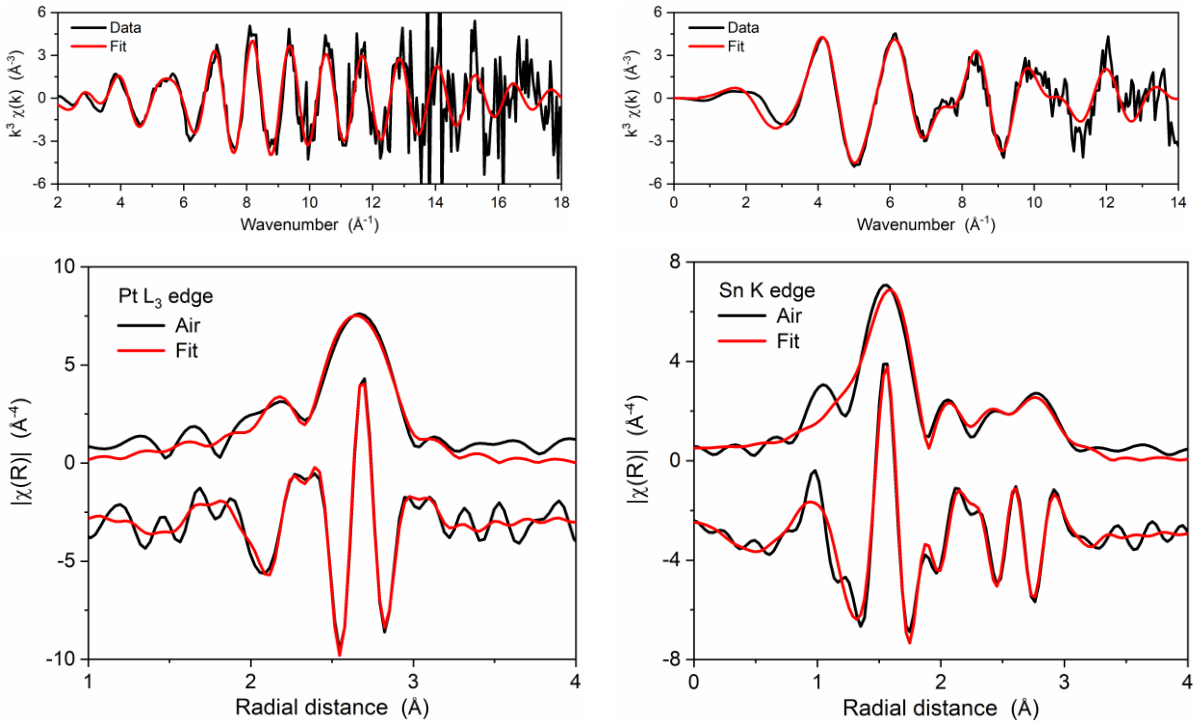

Figure S6-6 Same as Figure S6-3 but for partly alloyed Pt-Sn data measured in air, and the Fourier transformation was carried out in a k-range of 3.6–13.7 Å^{-1} for the Sn K edge and 3.5–16.2 Å^{-1} for the Pt L_3 edge. The fit yields an R-factor of 1.25% and the obtained structural parameters listed in Table S6-2.

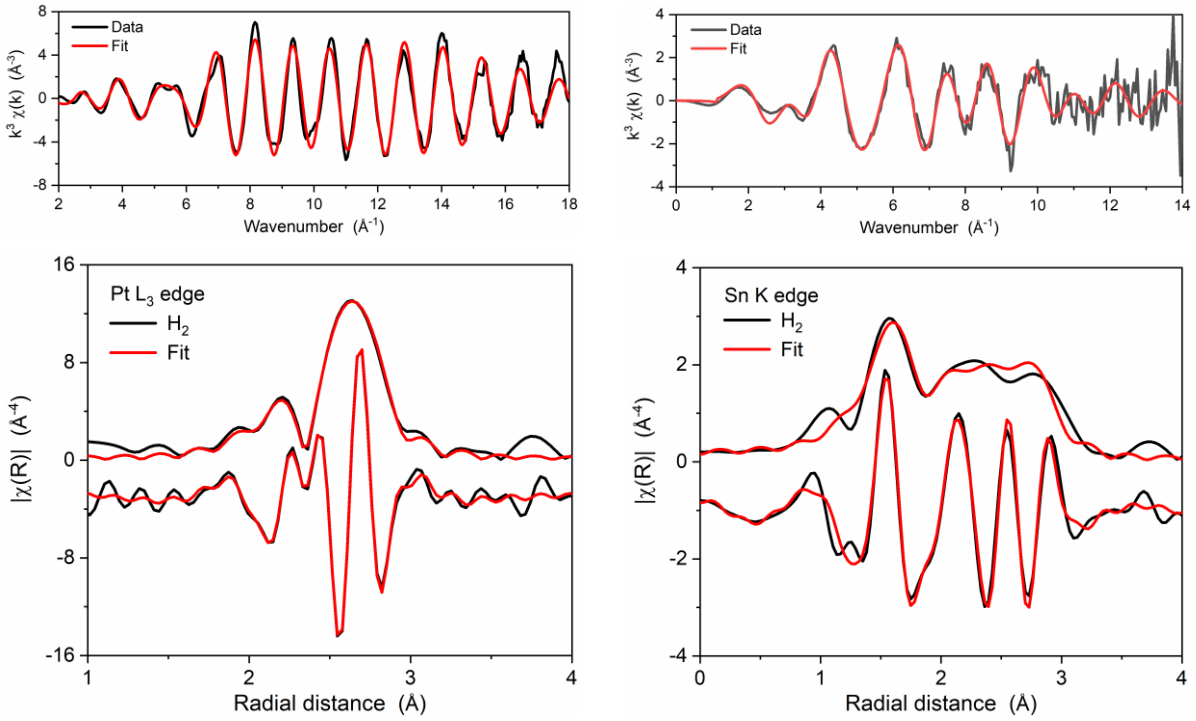

Figure S6-7 Same as Figure S6-3 but for partly alloyed Pt-Sn data measured in H_2, and the Fourier transformation was carried out in a k-range of 3.6–13.2 Å^{-1} for the Sn K edge and 3.5–17.3 Å^{-1} for the Pt L_3 edge. The fit yields an R-factor of 1.25% and the obtained structural parameters listed in Table S6-2.

Table S6-2 Structural parameters obtained from double-dataset fits for alloyed Pt-Sn and partly alloyed Pt-Sn samples measured in air and in H_2(g). For the fits of alloyed Pt-Sn, 18 variables were used out of ~28 independent points for the data collected in air and 12 out of ~28 for the data collected in H_2(g). For the fits of partly alloyed Pt-Sn, 18 variables were used out of ~27 independent points for the data collected in air and 12 out of ~24 for the data collected in H_2(g).

Samples	Scattering path	*N*	*R* (Å)	σ^2 (×10^3 Å^2)	Δ*E* (eV)	*R*-factor (%)
Alloyed Pt-Sn (air)	Pt – O	0.3(6)	1.99(8)	5(21)		1.13
	Pt – Pt	7(1)	2.77(1)	8(1)	5(2)	
	Pt – Sn	1.3(7)	2.808(4)*	9.7(7)*		
	Sn – O	2.9(2)	2.042(5)	6.3(8)		
	Sn – Pt	6.1(6)	2.808(4)*	9.7(7)*	2.5(6)	
	Sn – Sn	1.6(6)	3.28(2)	13(4)		
Alloyed Pt-Sn (H_2)	Pt – Pt	7.8(2)	2.778(2)	6.7(2)	4.8(3)	0.56
	Pt – Sn	2.0(2)	2.790(5)*	10(1)*		
	Sn – O	1.0(6)	2.03(3)	5(7)	4(1)	
	Sn – Pt	8(1)	2.790(5)*	10(1)*		
Partly alloyed Pt-Sn (air)	Pt – O	1(2)	2.0(1)	14(40)		1.25
	Pt – Pt	7(2)	2.77(2)	8(1)	7(3)	
	Pt – Sn	0.8(8)	2.802(8)*	10(2)*		
	Sn – O	4.4(3)	2.037(6)	5.6(7)		
	Sn – Pt	3.4(9)	2.802(8)*	10(2)*	1.7(9)	
	Sn – Sn	3(2)	3.25(3)	20(10)		
Partly alloyed Pt-Sn (H_2)	Pt – Pt	8.2(2)	2.764(2)	6.5(1)	5.0(3)	0.63
	Pt – Sn	1.3(2)	2.775(8)*	14(2)*		
	Sn – O	1.7(5)	2.04(2)	6(3)	5(1)	
	Sn – Pt	7(1)	2.775(8)*	14(2)*		

*The interatomic scattering paths are set to be equal in *R* and σ^2 for samples measured in the same atmosphere, that is, *R*(Pt–Sn) = *R*(Sn–Pt) and σ^2(Pt–Sn) = σ^2(Sn–Pt).

Table S6-3 The fitting model and guessed parameters, used in the 4-dataset fit of the dealloyed Pt-Sn sample.

Samples	**Scattering path**	***N***	**Δ*E***	**Δ*R***	**σ^2**
Pt L_3 in air	Pt – O	amppto	enotpt	delrpto	sspto
	Pt – Pt	amppt*		delrpt*	sspt*
	Pt – Sn	ampptsn*		delrptsn*,***	ssptsn*,***
Sn K in air	Sn – O	6×ampsno	enotsn	delrsno**	sssno**
	Sn – Pt	12×(1-ampsno)*		delrptsn*,***	ssptsn*,***
	Sn – Sn (2^{nd} shell)	ampsnsn		delrsnsn**	sssnsn**
Pt L_3 in H_2	Pt – Pt (core)	amppt*	enotpth2	delrpt*	sspt*
	Pt – Sn (core)	ampptsn*		delrptsn*	ssptsn*
	Pt – Pt (shell)	amppth2		delrpth2	sspth2
	Pt – Sn (shell)	ampptsnh2		delrptsnh2***	ssptsnh2***
Sn K in H_2	Sn – O	ampsnoh2	enotsnh2	delrsno**	sssno**
	Sn – Pt (core)	12×(1-ampsno)*		delrptsn*	ssptsn*
	Sn – Pt (shell)	ampsnpth2		delrptsnh2***	ssptsnh2***
	Sn – Sn (2^{nd} shell)	ampsnsnh2		delrsnsn**	sssnsn**

*Pt – Pt, Pt – Sn and Sn – Pt of the air data are set to have the same parameters as the core part of the H_2 data in terms of *N*, Δ*R* and σ^2;

** Sn – O and Sn – Sn (2^{nd} shell) of the Sn edge data are set to have same Δ*R* and σ^2;

*** Pt – Sn and Sn – Pt of data measured in the same atmosphere are set to have same Δ*R* and σ^2.

Supplementary note 1: XANES and EXAFS analysis on SnO_2-Pt/C

SnO_2-Pt/C, synthesized by hydrolysing SnO_3^{2-} on a commercial Pt/C, is a controlled sample to ascertain the shortened Pt-Sn bond distance on the surface and to support the *R*~CN correlation in Pt-Sn system. The Sn speciation of the SnO_2-Pt/C samples was characterized by XANES (Figure S6-8) and EXAFS (Figure S6-9). The XANES spectrum of the SnO_2-Pt/C samples at Sn K edge was compared with that of the standard SnO_2. Like the dealloyed Pt-Sn, the SnO_2-Pt/C largely follows SnO_2 reference in terms of major features and the edge position, but slightly higher whiteline intensity is found, 1.53 for SnO_2-Pt/C and 1.50 for SnO_2. On the EXAFS spectra, compared to the previous Pt-Sn samples, the SnO_2-Pt/C share the similar oscillations in phase with the SnO_2 in not only the first shell Sn–O region but also the higher shell Sn–Sn region, indicating that the ordered rutile SnO_2 structure is present. In terms of magnitude, these oscillations in these two regions are slightly weaker than those in SnO_2. The lower magnitude in the Sn–Sn region can be attributed to the smaller particle size of SnO_2 particles, but that in the Sn–O region could be from the lower CN, the lower extent of order, or both.

The corresponding EXAFS fitting (Figure S6-10 and Table S6-4) suggests that the CN of the Sn–O is 6.2±0.3, within the error with that of SnO_2, and the σ^2 (6.0±0.6×10^3 Å^2), which describes the disorder degree of the Sn-O bond, is significantly higher than that of SnO_2 (4.1±0.6×10^3 Å^2 for nanopowder, 2.5±0.9×10^3 Å^2 for bulk SnO_2, Figure S6-11) but close to the disordered [SnO_6] species on the Pt-Sn samples (5~6 ×10^3Å^2) (a disordered feature found in Sn-O, and an ordered feature found in Sn-Sn). Thus, the lower magnitude in the Sn–O region is due to a fraction of disordered structure, and both disorder [SnO_6] species and order SnO_2 nanocrystals coexist in the SnO_2-Pt/C.

Like the Pt-Sn samples, SnO_2-Pt/C can be partly reduced by H_2 (g) at room temperature, as indicated by changes in whiteline intensity and edge position. However, for the edge position, the change is not a simple shift but a broadened shoulder toward lower energy, which indicates that the extent of reduction is limited and a significant amount of tin oxide remains after H_2 reduction. The same indication can also be found in the EXAFS. The CN of the Sn–O decreased less than half to 3.4±0.2, lower than that of the Pt-Sn samples. In addition, in the Sn–Sn regions the oscillations are largely unchanged in terms of phase and magnitude. Thus, for the reduction of Sn^{IV} species in the SnO_2-

Pt/C, only part of the [SnO_6] species was participated and reduced into Sn-Pt bonds, and the crystalized SnO_2 was not involved. The distinct reactivity between the disordered [SnO_6] and crystalized SnO_2 is consistent with a study of tin oxide on Pt(111) by ambient pressure X-ray photoelectron spectroscopy study[S1]. In this study, the disordered tin oxide is found to be highly active and can be reduced by H_2 at low partial pressure of H_2 and low temperature, whilst other tin oxide film, ordered monolayers and multilayers, were found to show much lower reduction activity by 7 orders of magnitude.

For the EXAFS fit of the H_2 data, three scattering paths Sn–Pt and two Sn–Sn, are involved in a narrow *R* range of 2.5~3.5 Å, and 13 variables are required out of ~18 independent points fits (Figure S6-10 and Table S6-4). To have sufficient independent points and to obtain more precise structural parameters, a constrained fit was proposed. In this fitting model, the *R* and σ^2 of the inactive tin oxide phases are assumed to be unaffected by the H_2 reduction, which can be inferred from the individual. The double-data-set fit produces approximate structural parameters of the air data as compared to the individual fit, and yields a more reasonable parameter (Figure S6-12 and Table S6-5).

More importantly, a shortened and precise Sn-Pt bond (2.768±0.007 Å) is obtained. Assuming the residual tin oxide species in H_2 have a saturated O shell in H_2, the CN of the surface Sn atoms can be estimated to be 8.8±1.7. Same EXAFS analysis was also applied to a SnO_2-Pt/C sample from a different branch (SnO_2-Pt/C_2), and the CN of the shortened Sn-Pt (*R*=2.771±0.009 Å) is 9.2±2.4 (Figure S6-13 and Figure S6-14, Table S6-6 and Table S6-7).

Reference

[1] L.Y. Kraya, G.F. Liu, X. He, B.E. Koel, Structures and Reactivities of Tin Oxide on Pt(111) Studied by Ambient Pressure X-ray Photoelectron Spectroscopy (APXPS), Top. Catal., 59 (2016) 497-505.

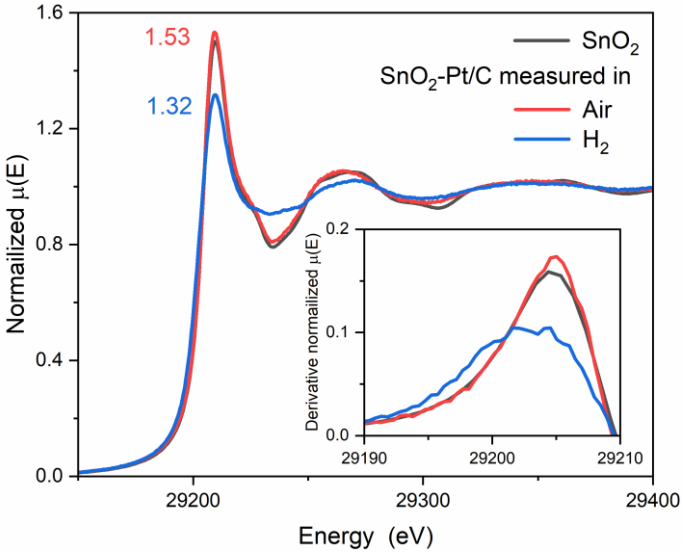

Figure S6-8 Sn K-edge XANES spectra of SnO_2-Pt/C samples collected in air and in H_2, along with (inset) the 1st derivative at the rising edge region. This figure shows the reduction of Sn species as suggested by the decreased intensity of whiteline and the negative shift of the rising edge.

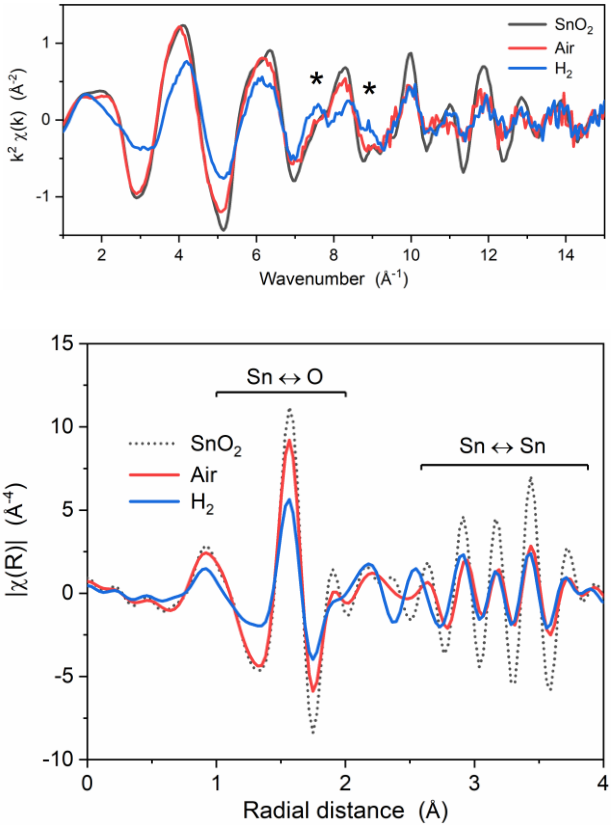

Figure S6-9 Sn K-edge EXAFS spectra of SnO_2-Pt/C samples in (top) k space and (bottom) the real part of R space. The samples collected in air and collected in H_2 are present, and the spectra are k^2-weighted. The comparison of the samples indicates the H_2 reduction induces a decreased intensity in low k-region (3–6 $Å^{-1}$) and low R-region (1–2 Å) and an added oscillation at 7–9 $Å^{-1}$ and 2–3 Å. This indicates the Sn coordination is altered due to the H_2 reduction.

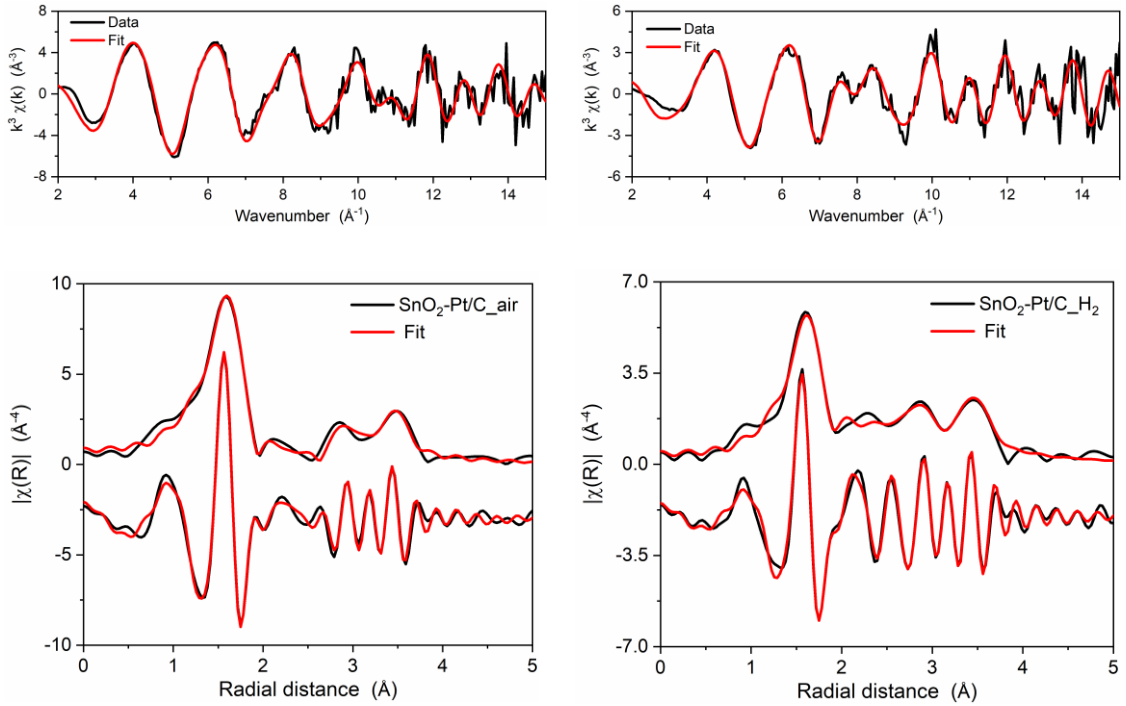

Figure S6-10 Individual fits for Sn K edge EXAFS spectra of SnO_2-Pt/C samples (measure in air and in H_2), plotted as k^3-weighted (top panels) k-space and (bottom panels) the magnitude and the real part of R-space. The Fourier transformation was performed in a k-range of 3.4–14.0 $Å^{-1}$, and the fitting was carried in an R-range of 1.0–3.7 Å, yielding R-factors of 0.57% for the air data and 0.76% for the H_2 data. The obtained structural parameters are listed in Table S6-4.

Table S6-4 Structural parameters obtained from the individual fits of SnO_2-Pt/C data. The fits use 10 variables out of ~18 independent points for the air data and 13 out of ~18 for the H_2 data.

Sample	**Scattering path***	**R (Å)**	**N**	**σ^2 ($\times10^3$ Å^2)**	**ΔE_0 (eV)**	**R factor (%)**
SnO_2-Pt/C (air)	Sn–O	2.052(5)	6.2(3)	6.0(6)	3.1(6)	0.57
	Sn–Sn (2nd shell)	3.23(1)	0.9(4)	5(2)		
	Sn–Sn (3rd shell)	3.721(9)	0.9(5)	2(2)		
SnO_2-Pt/C (H_2)	Sn–O	2.054(9)	3.4(2)	6(1)	5(1)	0.76
	Sn–Pt	2.77(1)	4(1)	11(2)		
	Sn–Sn(2nd shell)	3.22(3)	0.3(4)	4(6)		
	Sn–Sn(3rd shell)	3.72(1)	0.6(4)	1(3)		

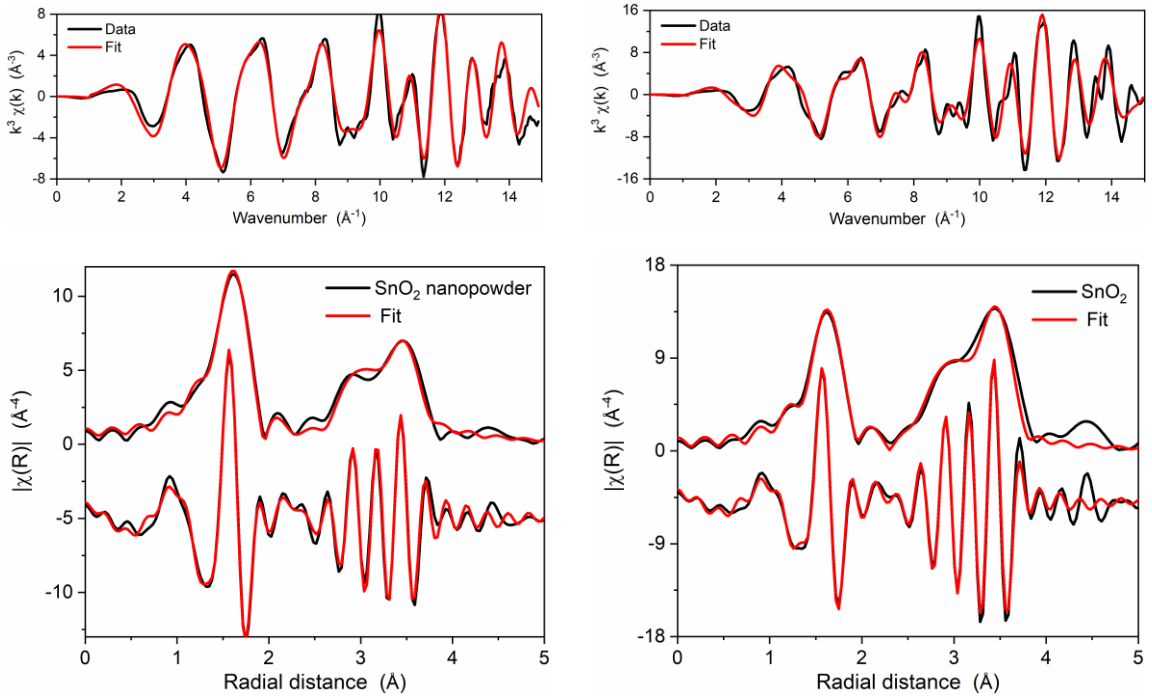

Figure S6-11 Fits of SnO_2 nanopowder and SnO_2 reference, plotted as k^3-weighted (top panel) k-space and (bottom panel) the magnitude and the real part of R-space. The Fourier transformation was performed in a k-range of 3.4–14.0 Å^{-1}, and the fitting was carried in an R-range of 1.0–3.7 Å, yielding R-factors of 0.70%.

Sample	**Scattering path***	**R (Å)**	**N**	**σ^2 (×10^3 Å^2)**	**ΔE_0 (eV)**	**R factor (%)**
SnO_2 nanopowder	Sn–O	2.053(5)	6.2(3)	4.1(6)	4.1(8)	0.70
	Sn–Sn (2nd shell)	3.199(9)	1.2(5)	3(2)		
	Sn–Sn (3rd shell)	3.726(6)	2.3(5)	2(1)		
SnO_2	Sn–O	2.055(8)	6*	2.5(9)	5(1)	1.34
	Sn–Sn(2nd shell)	3.198(8)	2*	1.8(8)		
	Sn–O	3.52(5)	4*	3(7)		
	Sn–Sn(3rd shell)	3.73(1)	8*	4.1(8)		

*set to be equal to the theoretic values obtained from rutile SnO_2 crystal structure (ICSD 647469).

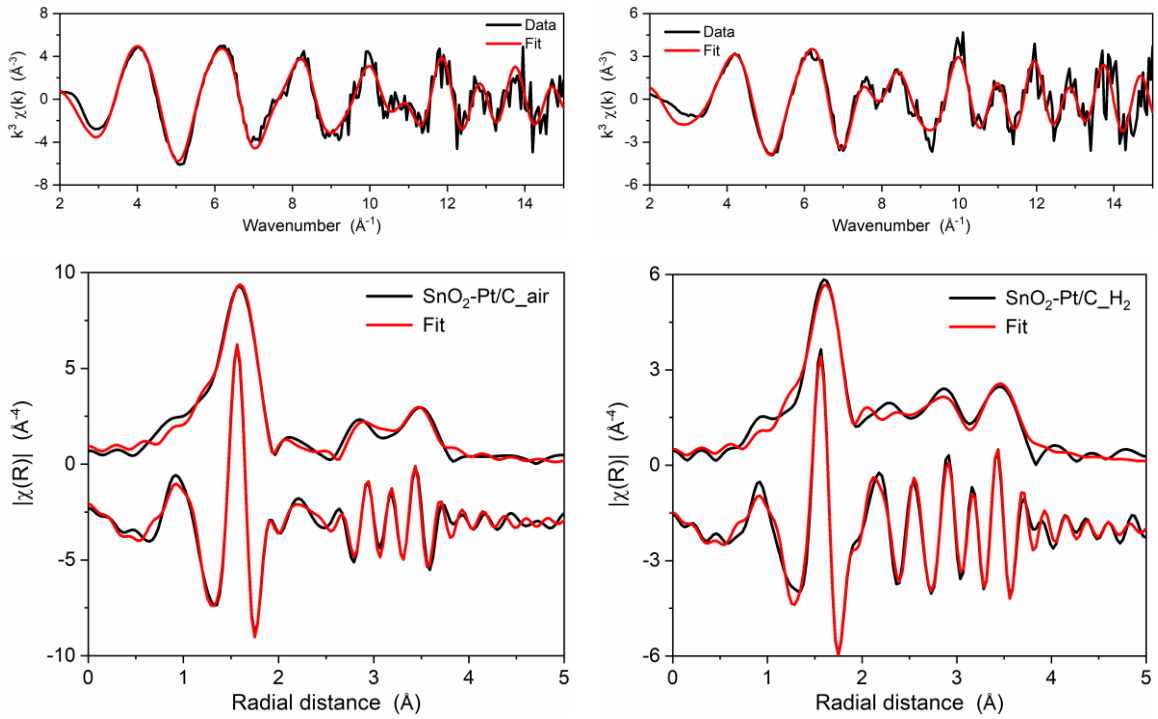

Figure S6-12 A double-dataset fit for Sn K edge EXAFS spectra of SnO_2-Pt/C samples, combining the data measured in air and that in H_2. The fit is plotted as k^3-weighted (top panels) k-space and (bottom panels) the magnitude and the real part of R-space. The Fourier transformation was performed in a k-range of 3.4–14.0 Å^{-1}, and the fitting was carried in an R-range of 1.0–3.7 Å, yielding an R-factor of 0.74% and the obtained structural parameters listed in Table S6-5.

Table S6-5 Structural parameters obtained from the combined dataset fit of SnO_2-Pt/C samples. The fit uses 17 variables out of ~36 independent points

Sample	Scattering path	R (Å)	N	σ^2 (×10^3 Å^2)	ΔE_0 (eV)	R factor (%)
SnO_2-Pt/C (air)	Sn–O*	2.053(4)	6.2(2)	5.9(4)	3.1(5)	
	Sn–Sn (2nd shell)*	3.23(1)	0.9(3)	5(2)		
	Sn–Sn (3rd shell)*	3.719(5)	0.8(3)	1(1)		
SnO_2-Pt/C (H_2)	Sn–O*	2.053(4)	3.4(1)	5.9(4)	5.1(6)	0.74
	Sn–Pt	2.768(7)	3.8(7)	11(1)		
	Sn–Sn (2nd shell)*	3.23(1)	0.4(2)	5(2)		
	Sn–Sn (3rd shell)*	3.719(5)	0.7(2)	1(1)		

* For SnO_2-related scattering paths, Sn–O, Sn–Sn_1(2nd shell) and Sn–Sn_1(3rd shell), each path is set to have the same *R* and σ^2 for both the air data and the H_2 data. Highlighted in blue.

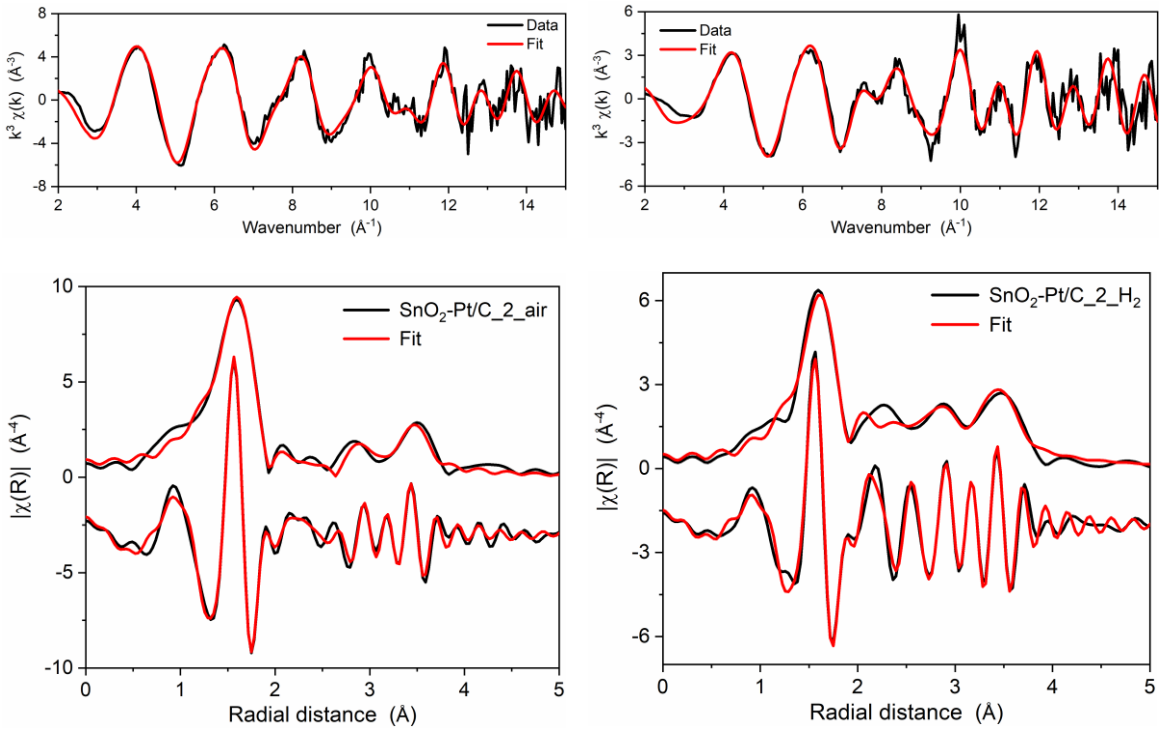

Figure S6-13 Same as Figure S6-10 but for SnO_2-Pt/C_2. The obtained parameters are listed in Table S6-6.

Table S6-6 Structural parameters obtained from the individual fits of SnO_2-Pt/C_2 data. The fits use 10 variables out of ~18 independent points for the air data and 13 out of ~18 for the H_2 data.

Sample	**Scattering path***	**R (Å)**	**N**	**σ^2 ($\times 10^3$ Å^2)**	**ΔE_0 (eV)**	**R factor (%)**
SnO_2-Pt/C_2 (air)	Sn–O	2.051(5)	6.2(3)	5.8(6)	3.2(6)	0.67
	Sn–Sn (2nd shell)	3.24(1)	1.1(5)	7(3)		
	Sn–Sn (3rd shell)	3.72(1)	1.0(5)	2(2)		
SnO_2-Pt/C_2 (H_2)	Sn–O	2.046(9)	3.2(3)	5(1)	5(2)	1.3
	Sn–Pt	2.77(1)	5(2)	13(3)		
	Sn–Sn(2nd shell)	3.20(5)	0.4(6)	5(8)		
	Sn–Sn(3rd shell)	3.72(1)	0.6(5)	0.3(30)		

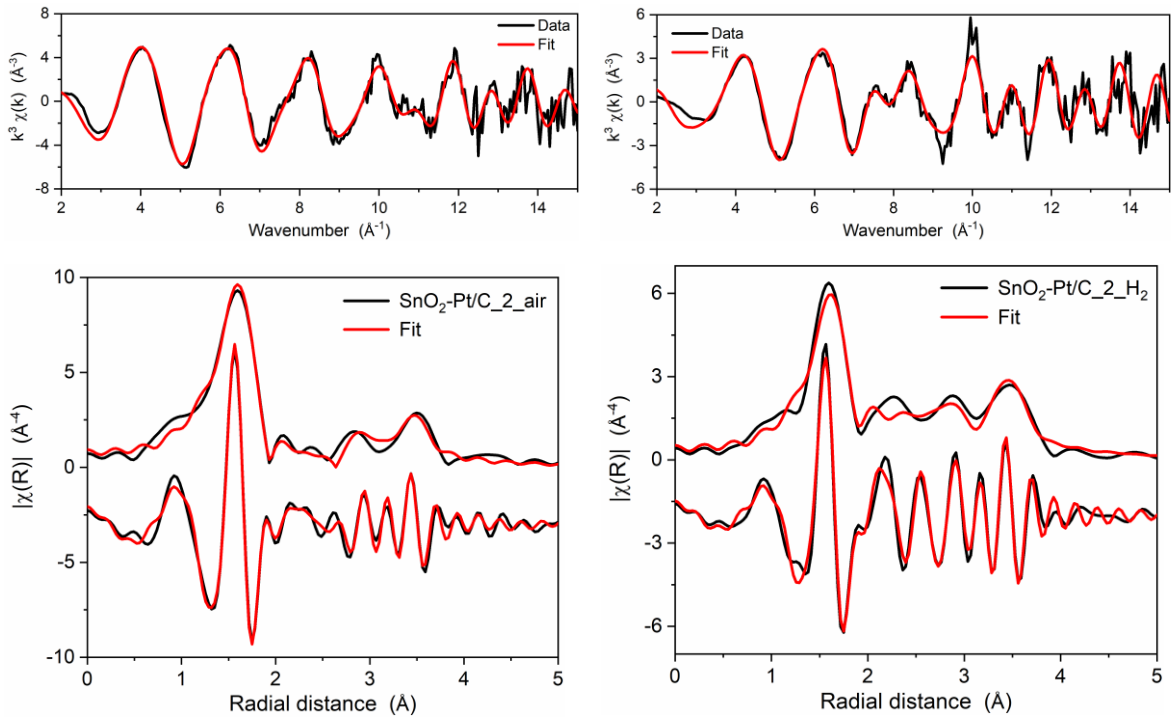

Figure S6-14 Same as Figure S6-12 but for SnO_2-Pt/C_2. The obtained parameters are listed in Table S6-7.

Table S6-7 Structural parameters obtained from the combined dataset fit of SnO_2-Pt/C samples. The fit uses 17 variables out of ~36 independent points

Sample	**Scattering path**	**R (Å)**	**N**	**σ^2 (×10^3 Å^2)**	**ΔE_0 (eV)**	**R factor (%)**
SnO_2-Pt/C_2 (air)	Sn–O*	2.050(4)	6.1(2)	5.5(5)	3.1(6)	
	Sn–Sn (2nd shell)*	3.23(1)	1.0(4)	6(3)		
	Sn–Sn (3rd shell)*	3.719(6)	0.7(3)	1(2)		
SnO_2-Pt/C_2 (H_2)	Sn–O*	2.050(4)	3.4(2)	5.5(5)	5.0(7)	1.2
	Sn–Pt	2.771(9)	4(1)	12(2)		
	Sn–Sn (2nd shell)*	3.23(1)	0.5(3)	6(3)		
	Sn–Sn (3rd shell)*	3.719(6)	0.8(3)	1(2)		

* For SnO_2-related scattering paths, Sn–O, Sn–Sn_1(2nd shell) and Sn–Sn_1(3rd shell), each path is set to have the same R and σ^2 for both the air data and the H_2 data. Highlighted in blue.